
Polyimido Sulfur Compounds as Promising Ligands in Molecular Magnets

Dissertation

zur Erlangung des mathematisch-naturwissenschaftlichen Doktorgrades

„Doctor rerum naturalium“

der Georg-August-Universität Göttingen

im Promotionsprogramm Chemie

der Georg-August University School of Science (GAUSS)

vorgelegt von

Jochen Jung

aus Zweibrücken

Göttingen, 2021

Thesis Committee:

Prof. Dr. Dietmar Stalke *Institute of Inorganic Chemistry, Georg-August-University, Göttingen*

Prof. Dr. Franc Meyer *Institute of Inorganic Chemistry, Georg-August-University, Göttingen*

Members of the Examination Commission:**Reviewer:**

Prof. Dr. Dietmar Stalke *Institute of Inorganic Chemistry, Georg-August-University, Göttingen*

Co-Reviewer:

Prof. Dr. Franc Meyer *Institute of Inorganic Chemistry, Georg-August-University, Göttingen*

Additional Members of the Examination Commission:

Prof. Dr. Manuel Alcarazo *Institute of Organic and Biomolecular Chemistry, Georg-August-University, Göttingen*

Jun.-Prof. Dr. Anna Krawczuk *Institute of Inorganic Chemistry, Georg-August-University, Göttingen*

Dr. Michael John *Institute of Organic and Biomolecular Chemistry, Georg-August-University, Göttingen*

Dr. Matthias Otte *Institute of Inorganic Chemistry, Georg-August-University, Göttingen*

Day of the Oral Examination:

09.11.2021

The work described in this doctoral thesis has been carried out under the guidance and supervision of Prof. Dr. Dietmar Stalke at the Institute of Inorganic Chemistry of the Georg-August-University, Göttingen between April 2016 and June 2021.

Publications

1. Jochen Jung, Annika Münch, Regine Herbst-Irmer and Dietmar Stalke, „*Tetraimido Sulfuric Acid $H_2S(NtBu)_4$ – Valence Isoelectronic to H_2SO_4* “, *Angew. Chem. Int. Ed.* **2021**, 60, 5679 – 5682.^[1]
2. Jochen Jung, Christina M. Legendre, Regine Herbst-Irmer and Dietmar Stalke, „*Exchange Coupling in Binuclear Manganese and Cobalt Complexes with the Tetraimido Sulfate Anion $[S(NtBu)_4]^{2-}$* “, *Inorg. Chem.* **2021**, 60, 2, 967 – 972.^[2]
3. Jochen Jung, Florian Benner, Regine Herbst-Irmer, Selvan Demir and Dietmar Stalke, „*Slow Magnetic Relaxation in Mono- and Bimetallic Lanthanide Tetraimido-Sulfate $S(NtBu)_4^{2-}$ Complexes*“, *Chem. Eur. J.* **2021**, 27, 12310 – 12319.^[3]
4. Jochen Jung, Christina M. Legendre, Serhiy Demeshko, Regine Herbst-Irmer and Dietmar Stalke, „*Trigonal Planar Iron(II) and Cobalt(II) Complexes Containing $[RS(NtBu)_3]^{n-}$ ($R = NtBu$, $n = 2$; CH_2PPh_2 , $n = 1$) as Acute Bite-Angle Chelating Ligands: Soft P Donor Proves Beneficial to Magnetic Co Species*“, *Inorg. Chem.* **2021**, 60, 13, 9580 – 9588.^[4]
5. Jochen Jung, Christina M. Legendre, Serhiy Demeshko, Regine Herbst-Irmer and Dietmar Stalke, „*Imido sulfonate scorpionate ligand in lanthanide single-molecule magnet design: slow magnetic relaxation and butterfly hysteresis in $[ClDy\{Ph_2PCH_2S(NtBu)_3\}_2]$* “, *Dalton Trans.* **2021**, 50, 17194 – 17201.^[5]

Table of Contents

Publications	V
Table of Contents.....	VII
Abbreviations.....	XIII
List of Compounds	XV
1. Introduction.....	1
1.1. Sulfur nitrogen chemistry	1
1.1.1. Sulfur nitrogen chemistry – historical background	1
1.1.2. Sulfur nitrogen chemistry – SN_x ligands and their coordination chemistry	3
1.2. Single-molecule magnetism.....	8
1.2.1. Single-molecule magnetism – historical background and applications.....	8
1.2.2. Single-molecule magnetism – theoretical background	10
1.2.3. Single-molecule magnetism – strategies and design basics	15
2. Research Scope	18
3. Results and Discussion	19
3.1. General procedures for the ligand syntheses.....	20
3.2. Sulfur imido ligands in d-block metal SMMs and SIMs	23
3.2.1. Exchange coupling in binuclear complexes of the tetraimido sulfate $[\text{S}(\text{NtBu})_4]^{2-}$	23
3.2.1.1. Synthesis of $[\text{Cl}_2\text{Mn}(\text{NtBu})_2\text{S}(\text{tBuN})_2\text{Mn}\{\text{CLi}(\text{thf})_3\}_2]$ (1)	23
3.2.1.2. Synthesis of $[(\text{acac})\text{Co}(\text{NtBu})_2\text{S}(\text{tBuN})_2\text{Co}(\text{acac})]$ (2)	27
3.2.1.3. Conclusion on exchange coupling in binuclear complexes of the tetraimido sulfate $[\text{S}(\text{NtBu})_4]^{2-}$	33
3.2.2. Synthesis and deprotonation of $[\text{Ph}_2\text{PCH}_2\text{S}(\text{NtBu})_2\text{NHtBu}]$ (4) for the isolation of the potassium compound $[\text{K}(\text{thf})_3\{\text{Ph}_2\text{PCH}_2\text{S}(\text{NtBu})_3\}]$ (5)	34
3.2.2.1. Synthesis of $[\text{Ph}_2\text{PCH}_2\text{S}(\text{NtBu})_2\text{NHtBu}]$ (4)	34
3.2.2.2. Synthesis of $[\text{K}(\text{thf})_3\{\text{Ph}_2\text{PCH}_2\text{S}(\text{NtBu})_3\}]$ (5)	37
3.2.2.3. Conclusion on the synthesis and deprotonation of $[\text{Ph}_2\text{PCH}_2\text{S}(\text{NtBu})_2\text{NHtBu}]$ (4) for the isolation of the potassium compound $[\text{K}(\text{thf})_3\{\text{Ph}_2\text{PCH}_2\text{S}(\text{NtBu})_3\}]$ (5)	41
3.2.3. Trigonal planar Fe(II) and Co(II) complexes of the tetraimido sulfate $[\text{S}(\text{NtBu})_4]^{2-}$ and the triimido sulfonate $[\{\text{Ph}_2\text{PCH}_2\text{S}(\text{NtBu})_3\}]^-$	42
3.2.3.1. Synthesis of the trigonal planar compounds $[(\text{thf})_2\text{Li}\{(\text{NtBu})_4\text{S}\}\text{M}\{\text{N}(\text{SiMe}_3)_2\}]$ with M = Fe (6) and Co (7)	42

3.2.3.2. Synthesis of the trigonal planar compounds $[M\{N(SiMe_3)_2\}\{Ph_2PCH_2S(NtBu)_3\}]$ with $M = Fe$ (8) and Co (9)	48
3.2.3.3. Structural comparison of the trigonal planar $Fe(II)$ and $Co(II)$ compounds $[(thf)_2Li\{(NtBu)_4S\}M\{N(SiMe_3)_2\}]$ and $[M\{N(SiMe_3)_2\}\{Ph_2PCH_2S(NtBu)_3\}]$ (6 – 9)	53
3.2.3.4. Magneto-structural correlation in the trigonal planar $Fe(II)$ and $Co(II)$ compounds $[(thf)_2Li\{(NtBu)_4S\}M\{N(SiMe_3)_2\}]$ and $[M\{N(SiMe_3)_2\}\{Ph_2PCH_2S(NtBu)_3\}]$ (6 – 9)	54
3.2.3.5. Conclusion on trigonal planar $Fe(II)$ and $Co(II)$ complexes of the tetraimido sulfate $[S(NtBu)_4]^{2-}$ and the triimido sulfonate $[\{Ph_2PCH_2S(NtBu)_3\}]^-$	63
3.3. Sulfur imido ligands in f-block metal SMMs and SIMs	64
3.3.1. f-block metal SMMs containing the tetraimido sulfate $[S(NtBu)_4]^{2-}$	64
3.3.1.1. Synthesis and structure	64
3.3.1.2. Magnetic properties	71
3.3.1.3. Conclusion on f-block metal SMMs containing the tetraimido sulfate $[S(NtBu)_4]^{2-}$	77
3.3.2. f-block metal SMMS containing the triimido sulfonate $[\{Ph_2PCH_2S(NtBu)_3\}]^-$	78
3.3.2.1. Synthesis and structure	78
3.3.2.2. Magnetic properties	85
3.3.2.3. Conclusion on f-block metal SMMs containing the triimido sulfonate $[Ph_2PCH_2S(NtBu)_3]^-$	91
3.4. Tetraimido sulfuric acid $H_2S(NtBu)_4$ – a valence isoelectronic analogue to H_2SO_4	92
3.4.1. Synthesis and characterization	92
3.4.2. Conclusion on tetraimido sulfuric acid $H_2S(NtBu)_4$ – a valence isoelectronic analogue to H_2SO_4	98
4. Summary and Outlook	99
5. Experimental Section	104
5.1. General procedures	104
5.2. Analytical methods	104
5.2.1. NMR spectroscopy	104
5.2.2. Mass spectrometry	104
5.2.3. Elemental analysis	105
5.2.4. Mössbauer spectroscopy	105
5.2.5. Magnetic measurements	105
5.2.6. Computational calculations	107
5.3. Synthesis and characterization	108

5.3.1. $[\text{Cl}_2\text{Mn}(\text{NtBu})_2\text{S}(\text{tBuN})_2\text{Mn}\{\text{ClLi}(\text{thf})_3\}_2]$ (1)	108
5.3.2. $[(\text{acac})\text{Co}(\text{NtBu})_2\text{S}(\text{tBuN})_2\text{Co}(\text{acac})]$ (2)	109
5.3.3. $\text{Ph}_2\text{PCH}_2\text{S}(\text{NtBu})_2\text{NHtBu}$ (4).....	110
5.3.4. $[\text{K}(\text{thf})_3\{\text{Ph}_2\text{PCH}_2\text{S}(\text{NtBu})_3\}]$ (5)	111
5.3.5. $[(\text{thf})_2\text{Li}\{(\text{NtBu})_4\text{S}\}\text{Fe}\{\text{N}(\text{SiMe}_3)_2\}]$ (6)	112
5.3.6. $[(\text{thf})_2\text{Li}\{(\text{NtBu})_4\text{S}\}\text{Co}\{\text{N}(\text{SiMe}_3)_2\}]$ (7).....	113
5.3.7. $[\text{Fe}\{\text{N}(\text{SiMe}_3)_2\}\{\text{Ph}_2\text{PCH}_2\text{S}(\text{NtBu})_3\}]$ (8).....	114
5.3.8. $[\text{Co}\{\text{N}(\text{SiMe}_3)_2\}\{\text{Ph}_2\text{PCH}_2\text{S}(\text{NtBu})_3\}]$ (9).....	115
5.3.9. $[\{\text{Cl}_2\text{Gd}(\text{NtBu})_2\text{S}(\text{NtBu})_2\text{Li}(\text{thf})_2\}_2\cdot\{\text{ClLi}(\text{thf})_2\}]$ (10a).....	116
5.3.10. $[\{\text{Cl}_2\text{Tb}(\text{NtBu})_2\text{S}(\text{NtBu})_2\text{Li}(\text{thf})_2\}_2\cdot\{\text{ClLi}(\text{thf})_2\}]$ (10b)	117
5.3.11. $[\{\text{Cl}_2\text{Dy}(\text{NtBu})_2\text{S}(\text{NtBu})_2\text{Li}(\text{thf})_2\}_2\cdot\{\text{ClLi}(\text{thf})_2\}]$ (10c)	118
5.3.12. $[\{\text{Cl}_2\text{Ho}(\text{NtBu})_2\text{S}(\text{NtBu})_2\text{Li}(\text{thf})_2\}_2\cdot\{\text{ClLi}(\text{thf})_2\}]$ (10d).....	119
5.3.13. $[\{\text{Cl}_2\text{Er}(\text{NtBu})_2\text{S}(\text{NtBu})_2\text{Li}(\text{thf})_2\}_2\cdot\{\text{ClLi}(\text{thf})_2\}]$ (10e).....	120
5.3.14. $[\{(\text{thf})_2\text{Cl}_2\text{Gd}(\text{NtBu})_2\text{S}(\text{NtBu})_2\text{Li}(\text{thf})_2\}_2]$ (11a).....	121
5.3.15. $[\{(\text{thf})_2\text{Cl}_2\text{Tb}(\text{NtBu})_2\text{S}(\text{NtBu})_2\text{Li}(\text{thf})_2\}_2]$ (11b)	122
5.3.16. $[\{(\text{thf})_2\text{Cl}_2\text{Dy}(\text{NtBu})_2\text{S}(\text{NtBu})_2\text{Li}(\text{thf})_2\}_2]$ (11c)	123
5.3.17. $[\{(\text{thf})_2\text{Cl}_2\text{Ho}(\text{NtBu})_2\text{S}(\text{NtBu})_2\text{Li}(\text{thf})_2\}_2]$ (11d).....	124
5.3.18. $[\{(\text{thf})_2\text{Cl}_2\text{Er}(\text{NtBu})_2\text{S}(\text{NtBu})_2\text{Li}(\text{thf})_2\}_2]$ (11e).....	125
5.3.19. $[\text{ClTb}\{\text{Ph}_2\text{PCH}_2\text{S}(\text{NtBu})_3\}_2]$ (12a)	126
5.3.20. $[\text{ClDy}\{\text{Ph}_2\text{PCH}_2\text{S}(\text{NtBu})_3\}_2]$ (12b).....	127
5.3.21. $[\text{ClHo}\{\text{Ph}_2\text{PCH}_2\text{S}(\text{NtBu})_3\}_2]$ (12c)	128
5.3.22. $[\text{ClEr}\{\text{Ph}_2\text{PCH}_2\text{S}(\text{NtBu})_3\}_2]$ (12d).....	129
5.3.23. $[\text{ClLu}\{\text{Ph}_2\text{PCH}_2\text{S}(\text{NtBu})_3\}_2]$ (12e).....	130
5.3.24. $\text{H}_2\text{S}(\text{NtBu})_4$ (13)	131
5.4. Crystallographic section.....	133
5.4.1. Crystal selection and handling.....	133
5.4.2. Data collection and processing.....	133
5.4.3. Structure solution and refinement.....	134

5.4.4. Treatment of disorder	135
5.5. Determined structures	136
5.5.1. $[\text{Cl}_2\text{Mn}(\text{NtBu})_2\text{S}(\text{tBuN})_2\text{Mn}\{\text{CLi}(\text{thf})_3\}_2]$ (1)	136
5.5.2. $[(\text{acac})\text{Co}(\text{NtBu})_2\text{S}(\text{tBuN})_2\text{Co}(\text{acac})]$ (2a)	137
5.5.3. $[(\text{acac})\text{Co}(\text{NtBu})_2\text{S}(\text{tBuN})_2\text{Co}(\text{acac})]$ (2b)	138
5.5.4. $[(\text{thf})_2\text{Li}\{(\text{NtBu})_4\text{S}\}\text{Co}(\text{acac})]$ (3)	139
5.5.5. $\text{Ph}_2\text{PCH}_2\text{S}(\text{NtBu})_2\text{NHtBu}$ (4)	140
5.5.6. $[\text{K}(\text{thf})_3\{\text{Ph}_2\text{PCH}_2\text{S}(\text{NtBu})_3\}]$ (5)	141
5.5.7. $[(\text{thf})_2\text{Li}\{(\text{NtBu})_4\text{S}\}\text{Fe}\{\text{N}(\text{SiMe}_3)_2\}]$ (6)	142
5.5.8. $[(\text{thf})_2\text{Li}\{(\text{NtBu})_4\text{S}\}\text{Co}\{\text{N}(\text{SiMe}_3)_2\}]$ (7)	143
5.5.9. $[\text{Fe}\{\text{N}(\text{SiMe}_3)_2\}\{\text{Ph}_2\text{PCH}_2\text{S}(\text{NtBu})_3\}]$ (8)	144
5.5.10. $[\text{Co}\{\text{N}(\text{SiMe}_3)_2\}\{\text{Ph}_2\text{PCH}_2\text{S}(\text{NtBu})_3\}]$ (9)	145
5.5.11. $[\{\text{Cl}_2\text{Gd}(\text{NtBu})_2\text{S}(\text{NtBu})_2\text{Li}(\text{thf})_2\}_2\cdot\{\text{CLi}(\text{thf})_2\}]$ (10a)	146
5.5.12. $[\{\text{Cl}_2\text{Tb}(\text{NtBu})_2\text{S}(\text{NtBu})_2\text{Li}(\text{thf})_2\}_2\cdot\{\text{CLi}(\text{thf})_2\}]$ (10b)	147
5.5.13. $[\{\text{Cl}_2\text{Dy}(\text{NtBu})_2\text{S}(\text{NtBu})_2\text{Li}(\text{thf})_2\}_2\cdot\{\text{CLi}(\text{thf})_2\}]$ (10c)	148
5.5.14. $[\{\text{Cl}_2\text{Ho}(\text{NtBu})_2\text{S}(\text{NtBu})_2\text{Li}(\text{thf})_2\}_2\cdot\{\text{CLi}(\text{thf})_2\}]$ (10d)	149
5.5.15. $[\{\text{Cl}_2\text{Er}(\text{NtBu})_2\text{S}(\text{NtBu})_2\text{Li}(\text{thf})_2\}_2\cdot\{\text{CLi}(\text{thf})_2\}]$ (10e)	150
5.5.16. $[\{(\text{thf})_2\text{Cl}_2\text{Gd}(\text{NtBu})_2\text{S}(\text{NtBu})_2\text{Li}(\text{thf})_2\}_2]$ (11a)	151
5.5.17. $[\{(\text{thf})_2\text{Cl}_2\text{Tb}(\text{NtBu})_2\text{S}(\text{NtBu})_2\text{Li}(\text{thf})_2\}_2]$ (11b)	152
5.5.18. $[\{(\text{thf})_2\text{Cl}_2\text{Dy}(\text{NtBu})_2\text{S}(\text{NtBu})_2\text{Li}(\text{thf})_2\}_2]$ (11c)	153
5.5.19. $[\{(\text{thf})_2\text{Cl}_2\text{Ho}(\text{NtBu})_2\text{S}(\text{NtBu})_2\text{Li}(\text{thf})_2\}_2]$ (11d)	154
5.5.20. $[\{(\text{thf})_2\text{Cl}_2\text{Er}(\text{NtBu})_2\text{S}(\text{NtBu})_2\text{Li}(\text{thf})_2\}_2]$ (11e)	155
5.5.21. $[\text{ClTb}\{\text{Ph}_2\text{PCH}_2\text{S}(\text{NtBu})_3\}_2]$ (12a)	156
5.5.22. $[\text{ClDy}\{\text{Ph}_2\text{PCH}_2\text{S}(\text{NtBu})_3\}_2]$ (12b)	157
5.5.23. $[\text{ClDy}\{\text{Ph}_2\text{PCH}_2\text{S}(\text{NtBu})_3\}_2]$ (12b_tol)	158
5.5.24. $[\text{ClHo}\{\text{Ph}_2\text{PCH}_2\text{S}(\text{NtBu})_3\}_2]$ (12c)	159
5.5.25. $[\text{ClEr}\{\text{Ph}_2\text{PCH}_2\text{S}(\text{NtBu})_3\}_2]$ (12d)	160
5.5.26. $[\text{CLu}\{\text{Ph}_2\text{PCH}_2\text{S}(\text{NtBu})_3\}_2]$ (12e)	161

5.5.27. $\text{H}_2\text{S}(\text{NtBu})_4$ (13)	162
5.5.28. $[\{\text{Cl}_2\text{Tb}(\text{NtBu})_2\text{S}(\text{NtBu})_2\text{Li}(\text{thf})_2\}_4]$ (14).....	163
5.5.29. $[\{\text{Ph}_2\text{PCH}_2\text{S}(\text{NtBu})_3\text{Dy}(\text{thf})\text{Cl}_3\text{K}(\text{thf})_2\}_2]$ (15).....	164
6. Appendix.....	165
7. References.....	188

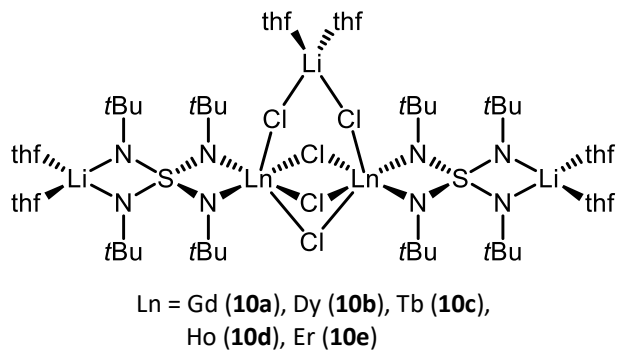
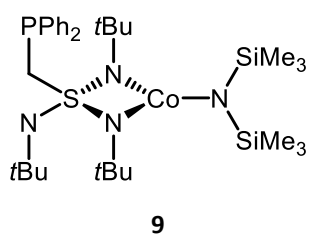
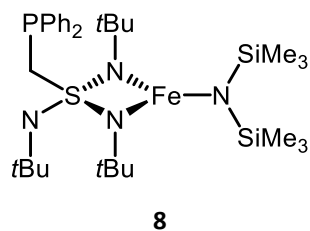
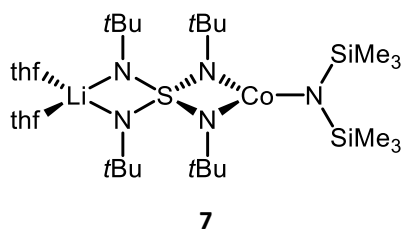
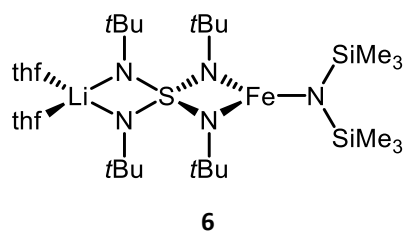
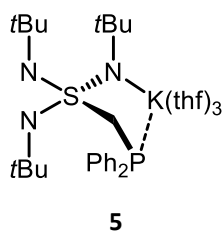
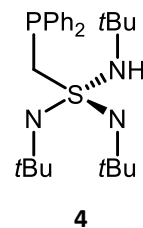
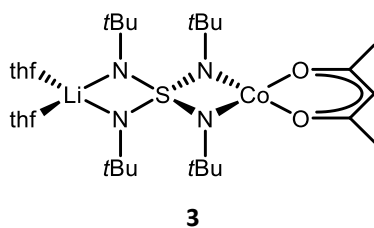
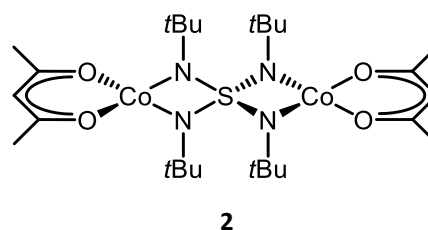
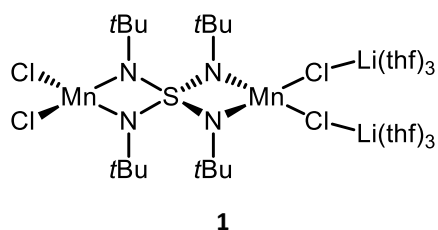
Abbreviations

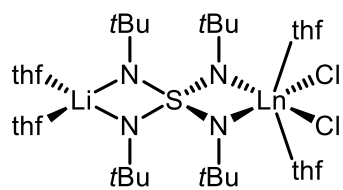
ac	Alternating Current
ADP	Anisotropic Displacement Parameters
AILFT	<i>ab initio</i> Ligand Field Theory
Bu	Butyl
CASSCF	COMPLETE Active Space Multiconfiguration Self Consistent Field
CCDC	Cambridge Crystallographic Data Center
COD	Cyclooctadiene
COSY	Correlation Spectroscopy
Cp	Cyclopentadienyl
Cp*	Pentamethylcyclopentadienyl
CSD	Cambridge Structural Database
δ	Chemical Shift
D	Zero-Field Splitting Parameter
dc	Direct Current
E	Rhombic Zero-Field Splitting Parameter
EI	Electron Ionization
emu	Electromagnetic Unit
EPR	Electron Paramagnetic Resonance
ESI	Electrospray Ionization
equiv.	Equivalent(s)
Et ₂ O	Diethyl ether
g	Landé Factor
HMBC	Heteronuclear Multiple Bond Correlation
HMDS	Bis(trimethylsilyl)amino
HSAB	Hard and Soft Acids and Bases
HSQC	Heteronuclear Single Bond Correlation
<i>i</i> Pr	<i>iso</i> -Propyl
IR	Infrared (Spectroscopy)
J	Magnetic Exchange Coupling Constant
KD	Kramers' Doublet
LIFDI	Liquid Injection Field Desorption Ionization
Ln	Lanthanides, also referred to as 4 <i>f</i> -elements
μ_{eff}	Effective Magnetic Moment
Me	Methyl
MeCN	Acetonitrile
MS	Mass Spectrometry
MW	Molecular Weight
m/z	Mass/Charge
<i>n</i> -BuLi	<i>n</i> -Butyllithium
NEVTP2	Second Order <i>n</i> -Electron Valence State Perturbation Theory
NMR	Nuclear Magnetic Resonance
OAM	Orbital Angular Momentum
Ph	Phenyl
PI	Paramagnetic Impurity
ppm	Parts per Million
QTM	Quantum Tunneling of the Magnetization
rt	Room Temperature
SMM	Single-Molecule Magnet
SIM	Single-Ion Magnet
SOC	Spin-Orbit Coupling

Abbreviations

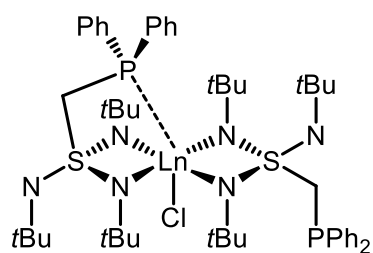
<i>tert</i> -Bu	<i>tertiary</i> Butyl
THF	Tetrahydrofuran
TMEDA	<i>N,N,N',N'</i> -tetramethylethylene-1,2-diamine
TMS	Trimethylsilyl (or Tetramethylsilane NMR reference only)
U_{eff}	Effective Thermal Energy Barrier to Spin Reversal
VTVH	Variable-Temperature Variable-Field
χ	Magnetic Susceptibility
X-ray	X-ray Radiation
XRD	X-ray Diffraction Analysis
<i>z</i>	Charge
ZFS	Zero-Field Splitting

List of Compounds

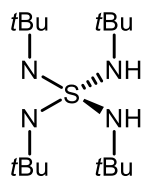




Ln = Gd (**11a**), Dy (**11b**), Tb (**11c**),
Ho (**11d**), Er (**11e**)



Ln = Dy (**12a**), Tb (**12b**), Ho (**12c**),
Er (**12d**), Lu (**12e**)



13

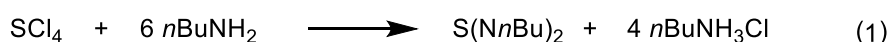
1. Introduction

1.1. Sulfur nitrogen chemistry

1.1.1. Sulfur nitrogen chemistry – historical background

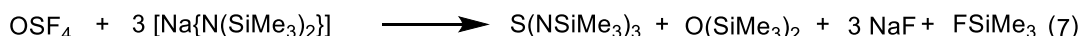
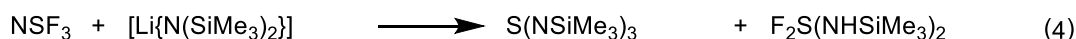
The beginning of sulfur nitrogen chemistry dates back to 1835 when GREGORY discovered tetrasulfur tetranitride (S_4N_4).^[6] The thermally unstable and shock-sensitive compound was obtained from a reaction of disulfur dichloride (S_2Cl_2) and ammonia (NH_3). Its stoichiometric composition, however, was only discovered in 1850^[7] and it took another 46 years until SCHENCK^[8] was able to specify the exact chemical formula. The early structural assumption of an eight-membered ring^[9] was supported by the research of GOEHRING^[10] in 1947 and finally confirmed by crystallographic X-ray analysis^[11,12]. After heating S_4N_4 for several hours over silver wool and under reduced pressure, BURT reported a blue inorganic polymer polythiazyl $(SN)_n$ in 1910.^[13] The same observation was reported by GOEHRING *et al.* in 1953^[14], when they confirmed the electrical conductivity of the polythiazyl, which was further investigated^[15,16] in later years. Additionally, they were able to isolate the room temperature instable and explosive disulfur dinitride (S_2N_2). Later, aside from electrical conductivity, the superconductive property of the polymer $(SN)_n$ at 0.26 K was discovered.^[17,18]

The first sulfur diimide was synthesized in 1956 by GOEHRING and WEIS from *n*-butylamine and sulfur tetrachloride in diethyl ether or chloroform at temperatures below $-65^\circ C$ (**Scheme 1-1 (1)**).^[19] After solvent evaporation, the residual pale yellow oil was distilled for purification. Afterwards, new routes to obtain sulfur diimides were published including their reactivity.^[20,21] CLEMENS, BELL and O'BRIEN presented an alternative synthesis that utilized *tert*-butylamine and the more stable SCl_2 in diethyl ether (**Scheme 1-1 (2)**).^[22] The initially obtained product is a polymeric compound which undergoes a pyrolysis (**Scheme 1-1 (3)**) upon slowly increasing the temperature to form $S(NtBu)_2$ (**SN-I**).^[22] The optimized synthesis made sulfur diimides quite accessible and sparked a growing interest in sulfur nitrogen chemistry.



Scheme 1-1 Synthetic routes to sulfur diimides. The first reaction was performed with SCl_4 and *n*-butylamine (1). The reaction of the more stable SCl_2 and *tert*-butylamine (2) initially resulted in a polymer that undergoes a slow pyrolysis under elevated temperatures (3).

In contrast, the synthesis of sulfur triimides proved to be more challenging. When the first sulfur diimide was synthesized, GLEMESER *et al.* worked on halogenated sulfur nitrogen compounds^[23,24] and isolated the gaseous sulfur nitride trifluoride (NSF₃)^[25] from a reaction of NSF and SN₂F₂ (synthetically accessible starting from S₄N₄) under the presence of AgF₂. Based on the gathered experience in sulfur imido chemistry, GLEMESER and WEGENER finally succeeded in the synthesis of the first sulfur triimide in 1970 (**Scheme 1-2** (4)).^[26] From a reaction of NSF₃ and lithium bis(trimethylsilyl)amide [Li{N(SiMe₃)₂}] in petroleum ether at 0°C, tris(*N*-trimethylsilylimido)sulfur S(NSiMe₃)₃ was isolated. At that time, it was the first molecule with a sulfur in oxidation state +VI and the coordination number 3 that did not polymerize.^[26,27] Seven years later, they were able to isolate tris(*tert*-butylimido)sulfur S(NtBu)₃ (**SN-III**). In contrast to the aforementioned synthesis, they used the precursor [Li{N(SiMe₃)(tBu)}] at –70°C, which first resulted in the isolation of (Me₃SiN)S(NtBu)₂ (5). At higher temperatures and with an excess of [Li{N(SiMe₃)(tBu)}], the molecule undergoes a transamidation (6) to form S(NtBu)₃ (**SN-III**).^[28] The modified procedure from LIDY and SUNDERMEYER alternatively utilized thionyl tetrafluoride (OSF₄) and sodium bis(trimethylsilyl)amide [Na{N(SiMe₃)₂}] to obtain S(NSiMe₃)₃ with improved yield.^[29] However, both NSF₃ and OSF₄ are hazardous gases and therefore difficult to handle. Consequently, the limited access to sulfur triimides hindered the expansion and evolution of sulfur triimido based chemistry.^[30]



Scheme 1-2 Synthesis of sulfur triimides. The first reaction was performed with NSF₃ and [Li{N(SiMe₃)₂}] (4) to yield S(NSiMe₃)₃. Performing the synthesis with [Li{N(SiMe₃)(tBu)}] resulted in (Me₃SiN)S(NtBu)₂ (5) that undergoes a transamidation upon excess of [Li{N(SiMe₃)(tBu)}] to form S(NtBu)₃ (6). An alternative reaction with OSF₄ and [Na{N(SiMe₃)₂}] also yielded S(NSiMe₃)₃ with improved yield (7).

It took more than 20 years for the field to develop, until FLEISCHER and STALKE reported a new route to sulfur triimides in 1996.^[31–33] It comprises the oxidation of [Li₄{(NtBu)₃S}]^[31] (**SN-II**) with Br₂, which resulted in easily controllable synthesis parameters and higher yields. Interestingly, an intense blue intermediate radical species forms at the beginning of the reaction, which was subsequently characterized by EPR spectroscopy.^[31,33] Due to the easier access to **SN-III**, STALKE *et al.* developed a fruitful SN chemistry and deeply investigated a large variety of novel sulfur imido ligands in the following years.^[34–37]

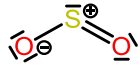
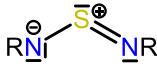
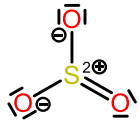
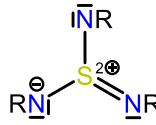

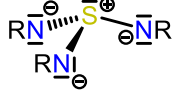
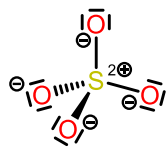
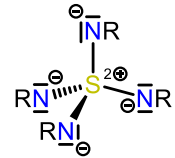

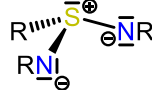
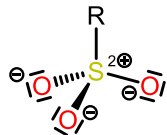
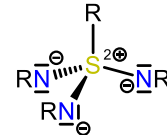
$S(NR)_2$ and $S(NR)_3$ are valence isoelectronic imido analogues to the sulfur oxides SO_2 and SO_3 . Therefore, they were regarded as compounds in which the central sulfur atom undergoes valence expansion with d-orbital participation, which involves that they do not obey to the eight-electron rule.^[38] This assumption was additionally fueled by the information gained from the structural characterization of $S(NtBu)_3$, which revealed relatively short sulfur imido bonds (around 1.5 Å) and led to the description of S–N double bonds.^[39] However, investigations from the 1980s demonstrated that d-orbitals do not participate in sulfur-nitrogen bonding, due to the large energy gap between the p- and d-orbitals.^[40–44] Theoretical studies on SO_2 and SO_3 revealed that the S–O bonds are highly ionic with bond orders close to one, which excludes hypervalency.^[45,46] Already in 1947, an alternative view on the debate was discussed by RUNDLE, as he stated that planar SN_x compounds should allow delocalized π -systems.^[47,48]

In order to get a deeper insight into SN bonding, STALKE *et al.* analyzed numerous sulfur imido systems by theoretical and experimental studies.^[34,36,49–55] In 2012, STALKE, GATTI and IVERSEN published their investigations on K_2SO_4 and characterized the S–O bonds as highly polarized, covalent $S^{\delta+}-O^{\delta-}$ bonds which are best described as single, rather than double bonds.^[56] In 2019, GRABOWSKY *et al.* confirmed these results.^[57] The deep understanding of S–O and S–N bonds seem to rule out hypervalency for sulfur. Nevertheless, hypervalency remains a matter of scientific discussions, until today.

1.1.2. Sulfur nitrogen chemistry – SN_x ligands and their coordination chemistry

The ligand systems used within the thesis are valence isoelectronic imido analogues to sulfur oxides. Replacing the oxygen atoms in classical sulfur oxides SO_n^{m-} with NR imido groups yields the polyimido sulfur species $S(NR)_n^{m-}$ ($n = 2, 3, 4$ and $m = 0, 2$).^[34,35] According to LANGMUIR^[58,59], (valence) isoelectronic species are supposed to be similar in their physical and chemical properties. However, sulfur oxides appear to have significantly different properties compared to their imido counterparts.^[60,61] In most cases, sulfur imides are not air stable at ambient conditions and decompose in water, while sulfur oxides do not. Furthermore, the lipophilic character of the $S(NR)_n^{m-}$ ligands due to the use of hydrocarbon residuals makes them highly soluble in common organic solvents. Some examples of sulfur oxides and imides are depicted in **Table 1-1** with sulfur in the oxidation state +IV and +VI, respectively.

Table 1-1 LEWIS diagrams of selected sulfur oxides in the oxidation states +IV and +VI and their valence isoelectronic imido analogues. Later on, molecular illustrations will be displayed without charges for clarity.

sulfur(IV) oxides	sulfur(IV) imides	sulfur(VI) oxides	sulfur(VI) imides
 sulfur dioxide SO ₂	 sulfur diimide S(NR) ₂	 sulfur trioxide SO ₃	 sulfur triimide S(NR) ₃
 sulfite SO ₃ ²⁻	 triimido sulfite S(NR) ₃ ²⁻	 sulfate SO ₄ ²⁻	 tetraimido sulfate S(NR) ₄ ²⁻
 sulfinic acid RSO ₂	 diimido sulfinic acid RS(NR) ₂	 sulfonic acid RSO ₃	 triimido sulfonic acid RS(NR) ₃

Due to the wide range of possible oxidation states for sulfur (–II to +VI) and the potential to bind one to four atoms, a huge number of ligand variations is possible, which makes them a versatile and tunable building block towards the design of various metal complexes.^[34,35,60–62]

When [Li₄{(NtBu)₃S₂}] (**SN-II**) was exposed to oxygen, intense blue radical intermediates were formed and analyzed by EPR investigations strongly supporting the assumption of the radical species [Li₃{(NtBu)₃S₂}][•].^[31,33,63] However, no such product could be isolated. Interestingly, reactions with halogens (Br₂, I₂) did not result in stable radicals but in the isolation of [(thf)₃Li₃(μ-X){(NtBu)₃S}] (X = Br or I).^[33] Just recently, the topic was revisited by the reduction of S(NtBu)₃ (**SN-III**) with elemental potassium.^[64] Surprisingly, it was possible to isolate the radical cage [K₃{(NtBu)₃S₂}][•], which was intensively analyzed by X-ray diffraction, UV-Vis spectroscopy and theoretical calculations.

Instead of oxidizing the sulfur(IV) atoms in the dimeric [Li₄{(NtBu)₃S₂}] (**SN-II**) to form S(VI) compounds, the system can alternatively be used as precursor for the synthesis of main^[65,66] and transition^[67] metal complexes. However, with group 14 metal(II) halides the ligand undergoes a decomposition redox reaction.^[66] This redox instability makes **SN-II** less attractive for the synthesis of new metal compounds.

Along with the easier access to S(NtBu)₃ (**SN-III**), the interest for the utilization of the molecule in subsequent reactions grew.^[34–37] However, **SN-III** is not versatile with regard to the coordination

properties of this planar, bulky molecule. Therefore, the introduction of a fourth side arm, resulting in a tetrahedrally coordinated sulfur (**Table 1-1**, sulfur(VI) imides), is more promising. With the ongoing debate about valence expansion in sulfur bonding, **SN-III** was intensively analyzed by experimental and theoretical charge density investigations, which revealed a 4-center-6-electron bonding with a distinct polarization of the π -system.^[50,51] Those results do not only underline the exclusion of hypervalency for sulfur, but give useful reactivity information for further synthesis. **Figure 1-1** shows the experimentally obtained reactive surface of **SN-III**. The π -electron density accumulation above and below the SN_3 plane renders a nucleophilic attack in these positions infeasible.

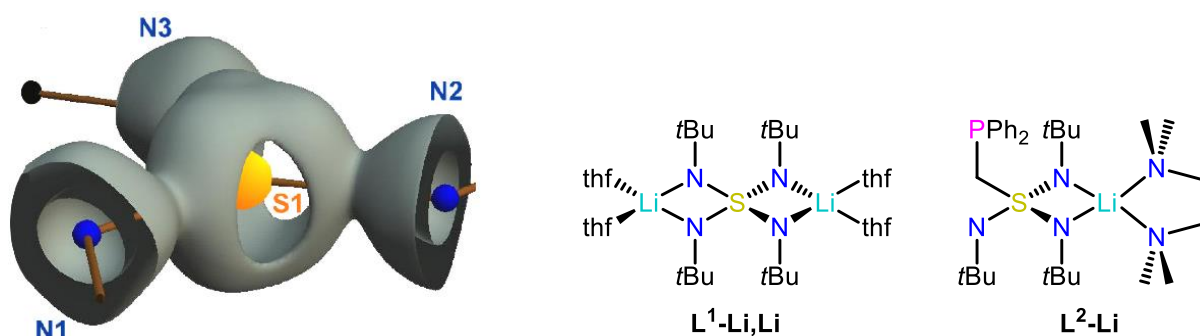


Figure 1-1 (left): Reactive surface of $\text{S}(\text{NtBu})_3$ (**SN-III**).^[50] Charge concentration is depicted in grey with a depletion located in the SN_3 plane between the NtBu groups at the sulfur atom. (middle): Lithium salt of the sulfate dianion $[(\text{thf})_4\text{Li}_2(\text{NtBu})_4\text{S}]$ (**L¹-Li,Li**) that was synthesized by FLEISCHER *et al.* in 1996.^[32] (right): The hetero-scorpionate $[(\text{tmeda})\text{Li}(\text{CH}_2\text{PPh}_2)]$ (**L²-Li**), isolated by CARL *et al.* in 2014.^[68]

The addition is only possible between two *tert*-butyl groups, where a charge depletion is localized. Therefore, only sterically less hindered organometallic reagents can be used. One of those ligand systems is the symmetric tetraimido sulfate $[\text{S}(\text{NtBu})_4]^{2-}$ (**L¹**) that features two identical coordination sides, allowing the synthesis of (hetero)bimetallic compounds. It can be seen as analogue to the sulfate dianion and was first isolated as the lithium salt $[(\text{thf})_4\text{Li}_2(\text{NtBu})_4\text{S}]$ (**L¹-Li,Li**) by FLEISCHER *et al.* in 1996 via the addition of two equiv. of $[\text{Li}\{\text{N}(\text{H})\text{tBu}\}]$ to **SN-III** (**Figure 1-1**, middle).^[32]

Another interesting system, featuring a phosphorus donor atom, was isolated by CARL *et al.* in 2014 from a reaction of $[(\text{tmeda})\text{Li}(\text{CH}_2\text{PPh}_2)]$ with **SN-III** (**Figure 1-1**, right).^[68] The obtained $[(\text{tmeda})\text{Li}\{\text{Ph}_2\text{PCH}_2\text{S}(\text{NtBu})_3\}]$ (**L²-Li**) is similar to the hetero-scorpionate $[(\text{tmeda})\text{Li}\{\text{Ph}_2\text{PCH}_2\text{S}(\text{NtBu})_2\}]$ (**SN-IV**) that was isolated by MEINHOLZ *et al.*, starting from the sulfur diimide **SN-I**.^[69] According to Trofimenko's^[70–73] poly(pyrazolyl)borates, a “scorpionate” ligand consists of two *N,N'*-chelating pyrazolyl claws in the equatorial plane and a third pseudo axial sting that bends towards the metal. Later, different substituent variations led to various ligand designs^[74–76], including phosphinoborates^[77,78], which only consist of phosphorus as donor atoms. In contrast to the aforementioned homo-scorpionates, the hetero-scorpionates^[69,79–81] consist of two identical claws and a sting with a different donor atom. Thus, the diimido sulfinates and the triimido sulfonates can be

referred to as scorpionate ligands. The introduction of a softer phosphorus offers a wide range of possible metal coordination, explainable by PEARSON'S HSAB concept.^[82–84] Furthermore, especially interesting for the synthesis of highly performing single molecule magnets (SMMs), an additional softer donor atom might be beneficial to boost the magnetic properties.^[85–96] More details on SMMs will be explained in the following chapters.

Aside from the presented compounds, a wide selection of polyimido sulfur ligands were synthesized.^[33,97–103] Due to the diverse functionalization properties of $S(NR)_2$ and $S(NR)_3$ via organometallic addition reactions, the synthesis of a broad SN ligand family is feasible. They possess an admirable adaptability towards various metals, primarily exploited in main group s-block^[98,104], p-block^[49,105] as well as transition metal^[68,87,106–109] compounds. So far, f-block metal complexes were only reported for S(IV) systems.^[110,111] Selected examples are depicted in **Scheme 1-3**. A remarkable compound was published in 2015 by CARL *et al.* (**Figure 1-2**).^[107]

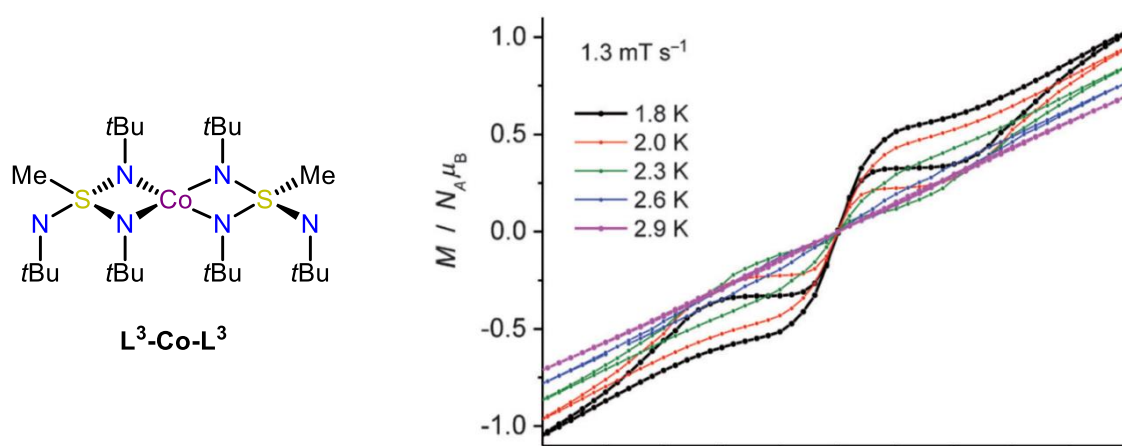
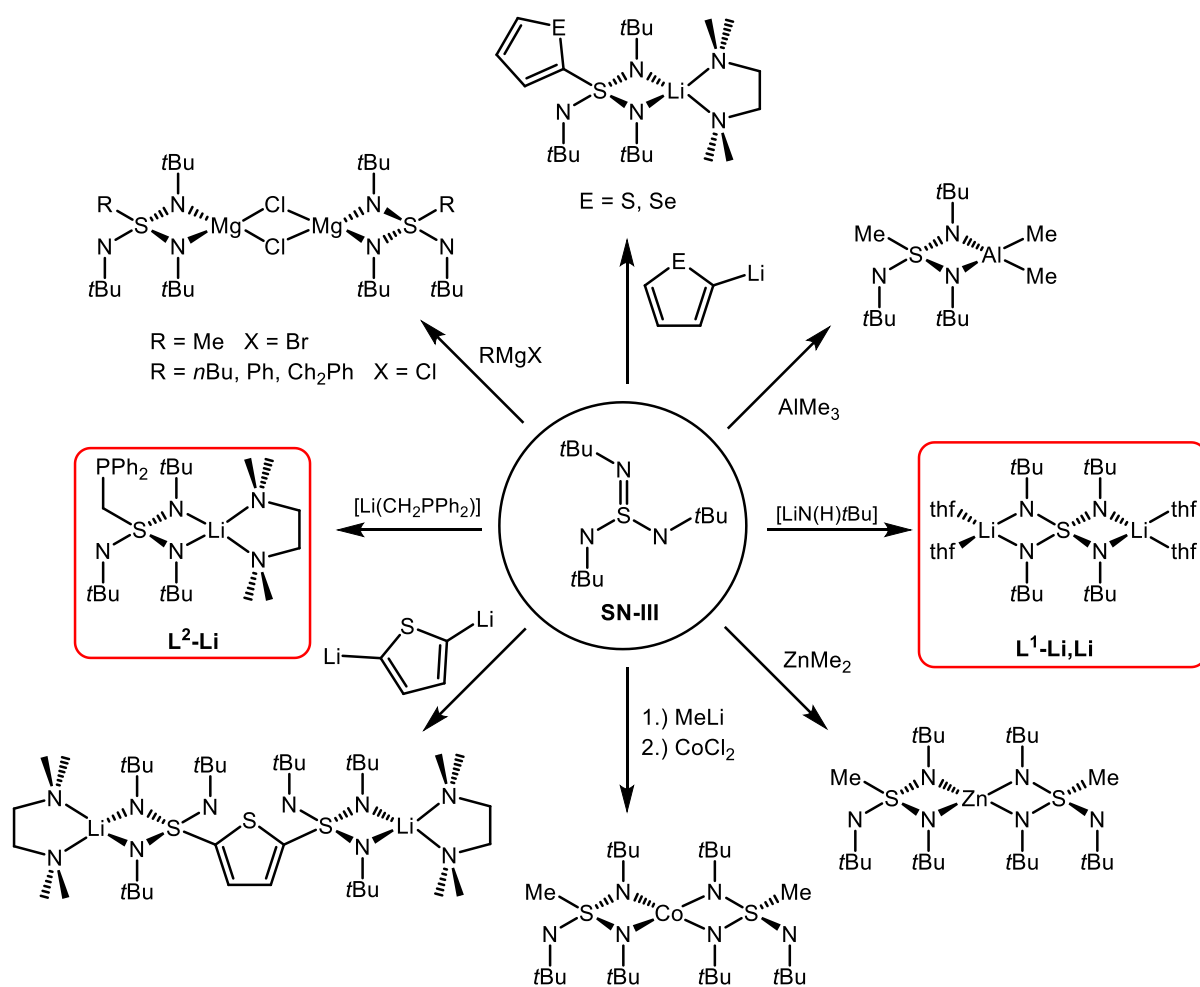


Figure 1-2 Depicted are the tetrahedrally coordinated Co(II) compound $[Co\{(NtBu)_3SMe\}_2]$ (L^3-Co-L^3) (left) and the respective butterfly hysteresis up to 2.6 K (right).^[107]

It possesses a tetrahedrally coordinated, polyimido sulfonate N,N' -chelated Co(II) ion. The compound shows slow relaxation of the magnetization under zero applied dc field, high magnetic anisotropy ($D = -58 \text{ cm}^{-1}$; $U_{\text{eff}} = 75 \text{ cm}^{-1}$) and a butterfly hysteresis up to 2.6 K. The polyimido sulfonate ligand is another example of the useful SN family that introduces an acute N–Co–N bite angle and is synthesized by the addition of methyllithium to the triimido sulfonate $S(NtBu)_3$ (**SN-III**).^[33]

Based on these first results, revealing the SN bonding motive to be a tunable platform for various ligands that can adapt to different electronic and geometric requirements, it seems promising to expand sulfur imido chemistry towards SMM application.^[34,35,60,61,112] The central sulfur atom provides the flexibility to adopt to various metal centers by shifting its position among the SN_x moiety, while the hard nitrogen atom gives the rigidity to the obtained coordination complexes. Furthermore, the acute

N–S–N bite angles found for the SN ligands enable the synthesis of pseudo-linear coordinated metal compounds. This structural characteristic is even more pronounced in sulfur(VI) systems and it seems desirable to exploit their properties. The advantage to introduce soft p-block elements, like phosphorus, in the ligand moiety (**Scheme 1-3**, **L²-Li**) gives the opportunity to investigate the influence of soft element donation on the magnetic performance. Furthermore, the tetraimido sulfonate (**Scheme 1-3**, **L¹-Li, Li**) is suitable for the synthesis of homo- and heterobimetallic compounds, which can be studied concerning magnetic coupling and synergies between paramagnetic centers. In summary, the well-established sulfur imido ligands show reasonable evidence for a vast potential in the field of molecular magnetism.^[87,107,110] However, they were not sufficiently investigated towards this particular aim and f-block metal chemistry is still underexplored, especially in S(VI) ligands.^[111] Altogether, the effort to breathe new life into the field of sulfur imido chemistry and to transfer this research field to the next chapter seems to be a fruitful alternative to classic SMM ligands.



Scheme 1-3 Overview of different ligands and metal complexes of the sulfur imido family. The two ligand systems, which were used as starting materials for the thesis, the tetraimido sulfate [S(NtBu)₄]²⁻ (**L¹**) and the triimido sulfonate [Ph₂PCH₂S(NtBu)₃]⁻ (**L²**) are highlighted in red and are depicted as lithium compounds.

1.2. Single-molecule magnetism

1.2.1. Single-molecule magnetism – historical background and applications

A single-molecule magnet (SMM) is a molecule that exhibits slow relaxation of the magnetization at low temperature.^[113] Thus, such compounds provide bistability of the magnetic states with a remanent magnetization even after the removal of an applied external field. They possess a microscopic magnetic memory which makes them promising alternatives in high density information storage.^[113–117] Moreover, applications in the field of quantum computing^[118–121] and as qubits for spintronics^[122–124] are imaginable.^[125] In contrast to macroscopic magnets, the relaxation is of true molecular origin without higher magnetic ordering.^[113,115,126,127]

The first compound that was found to display those SMM properties was the manganese cluster $[\text{Mn}_{12}\text{O}_{12}(\text{OAc})_{16}(\text{H}_2\text{O})_4]$ ^[115,128,129] (known as Mn_{12}). It was discovered by SESSOLI and GATTESCHI in 1993^[115], but the term SMM^[130] was coined three years later. Since then, the field of single-molecule magnetism has been a subject of growing interest and the strategies for the synthesis of highly anisotropic SMMs have experienced different developments. After the discovery of Mn_{12} , the relationship between the energy barrier to spin reversal U , the magnetic anisotropy D and the spin S was given by the equation $U = S^2 |D|$. Hence, the synthetic approach was to obtain the highest possible spin ground-state^[126,131] since the squaring of S has a large impact on the energy barrier.^[126,131] However, this equation does not give the right relation between the parameters. The actually crucial contribution of D can be seen considering the case of the manganese cluster that was presented from POWELL et al. in 2006.^[132] It possesses a record spin ground-state of $S = 83/2$, the highest at that time, but a negligible magnetic anisotropy and therefore, it did not display SMMs behavior. In contrast, the highest U_{eff} value was held for a time by a complex from BRECHIN et al. with only a spin of $S = 12$, but large magnetic anisotropy.^[133] The initially proposed relation between U , D and S is therefore more accurately described by $U = S^0 |D|$ ^[134] and the goal is to maximize D , while the total spin is less relevant.^[135] RUIZ *et al.* even doubted the coexistence of large magnetic anisotropy and a high spin ground-states.^[136] Moreover, D was actually found to be inversionally proportional to S .^[137]

Since then, the development in 3d transition metal SMMs led to the isolation of many remarkable compounds and the aim to achieve compounds with maximum spin systems went towards the synthesis of complexes containing less metal centers.^[137–140]

The first single-ion magnet (SIM), which is a compound with only one paramagnetic center, was isolated by CHANG, LONG *et al.* in 2010.^[141] It is the field-induced Fe(II) compound $\text{K}[(\text{tpa}^{\text{Mes}})\text{Fe}]$ (tpa^{Mes} = tris-mesityl tris-(2-pyrrolyl-methyl)amine), which displayed slow relaxation only under an applied dc field. The first SIM that showed magnetic relaxation even in the absence of an applied field

ist the Co(II) complex $[(\text{Ph}_4\text{P})_2][\text{Co}(\text{SPh})_4]$, which was published by ZADROZNY and LONG in 2011.^[90] With respect to that, it is now understood that tuning the magnetic anisotropy is crucial for the design of high-performance SMMs.^[142–148] However, a high spin ground-state is still mandatory for best magnetic properties.

In order to achieve higher anisotropies, the focus shifted towards f-element SMMs. The first lanthanide-based compounds with a single ion center were presented by ISHIKAWA *et al.* in 2003.^[149] They are double-decker phthalocyanine complexes with either Tb(III) or Dy(III) centers, resulting in energy barriers several times higher than the original Mn_{12} cluster. This discovery unambiguously showed that a single paramagnetic center with a smaller spin ground-state can clearly outperform metal ion clusters with a high total spin, in terms of reaching highest energy barriers to spin reversal (U_{eff}). In fact, lanthanides are well-suited for the design of molecular magnets for several reasons.^[150] The large anisotropy for lanthanides arises from their intrinsic spin-orbit coupling (SOC) created by the large unquenched orbital angular momentum (OAM) inherent to f-elements.^[143,151] Hence, they turned out to be promising candidates for the synthesis of SMMs^[152–155] and are even more successful in SIMs^[149,156–161]. The highest performing SMMs to date are dysprosocenium compounds^[156–160]. The best example of this class was presented by LAYFIELD *et al.* in 2018 (**Figure 1-3**).^[158]

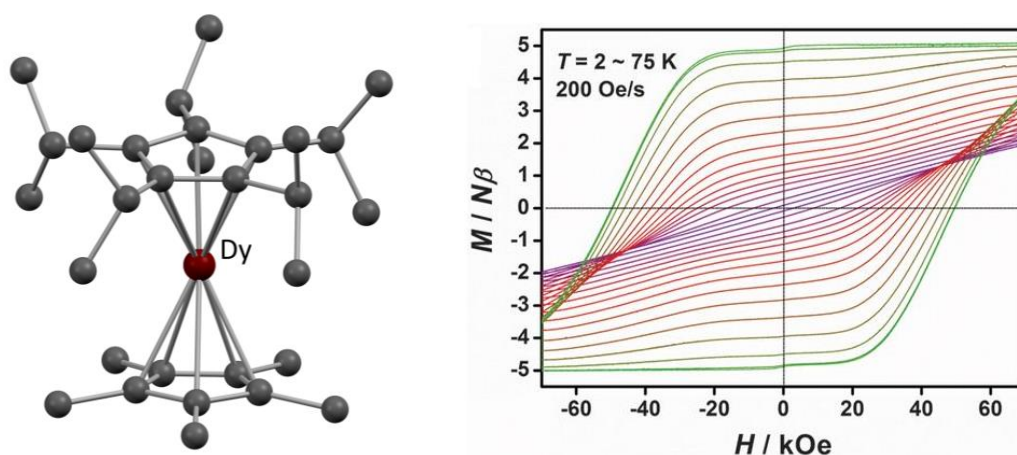


Figure 1-3 (left): Crystal structure of $[(\text{Cp}^{i\text{Pr}5})\text{Dy}(\text{Cp}^*)]^+$. Hydrogen atoms and counterion $[\text{B}(\text{C}_6\text{F}_5)_4]^-$ are omitted for clarity. (right): Hysteresis of $[(\text{Cp}^{i\text{Pr}5})\text{Dy}(\text{Cp}^*)][\text{B}(\text{C}_6\text{F}_5)_4]$ between 2 – 75 K.^[158] Reproduced with permission from the cited literature.

The compound consists of a dysprosium metallocene cation $[(\text{Cp}^{i\text{Pr}5})\text{Dy}(\text{Cp}^*)]^+$ ($\text{Cp}^{i\text{Pr}5}$ = penta-*iso*-propyl-cyclopentadienyl; Cp^* = pentamethylcyclopentadienyl) and a $[\text{B}(\text{C}_6\text{F}_5)_4]^-$ counterion and it displays a remarkable hysteresis even above the boiling point of liquid nitrogen, i.e. up to 80 K.

However, it seems possible that the structural optimization for this ligand class has reached a high-level plateau and that new approaches with rather underexplored compounds should come into focus to further develop the field of molecular magnetism.

1.2.2. Single-molecule magnetism – theoretical background

To display SMM behavior, a compound needs to possess at least one paramagnetic metal center with unpaired electrons resulting in a non-zero total spin ground-state, that needs to be doubly degenerated and bistable.^[126] For multinuclear systems, it is also necessary that the magnetic moments of the paramagnetic metal centers are oriented into the same direction (ferromagnetic coupling) or, if not, that they do not cancel out each individual contribution to the magnetic moment (antiferromagnetic coupling).^[127,162]

It was discussed in the previous chapter that the magnetic anisotropy is crucial for the magnetic performance of SMMs, which means that the magnetization has a preferred orientation. It arises from the interplay between the ligand field (LF), the orbital angular momentum (OAM) and the resulting spin-orbit coupling (SOC).^[163] The splitting of the magnetic sublevels in the absence of an external magnet field is called zero-field splitting (ZFS), which results from the spin-spin interaction of unpaired electrons. For transition metal compounds, considering the d-orbital splitting is sufficient to qualitatively predict the magnetic anisotropy. This does not work for the f-orbitals of lanthanides and in the following, explanations will mainly focus on transition metals. While lanthanides benefit from an intrinsic OAM^[146] giving rise to huge magnetic anisotropy, transition metals require a suitable ligand field^[140] to prevent full quenching of the OAM. However, both 3d- and 4f-elements require a specific LF to display SMM behavior, even though 4f-orbitals do not interact much with the ligands, while this is the case for 3d-orbitals.

It is known that a circulating current creates a magnetic field, which, as a consequence, will affect any other magnetic center nearby. Thus, a circulating electron in an orbital induces a magnetic field which can be associated with the OAM.^[164] The effect of the electrons' internal magnetic field on the angular momentum of the spin is called spin-orbit coupling, which creates a preferred spin orientation. Whether OAM is quenched or unquenched can be predicted by determining the matrix elements $\langle \Psi_i | \hat{L}_u | \Psi_j \rangle$ ($u = x, y, z$). \hat{L}_u is the orbital angular momentum operator and Ψ_i is one of the wavefunctions associated with the irreducible representation $^{2S+1}\Gamma$. First-order OAM is unquenched, if a non-zero matrix element for $i = j$ exists. If not, then OAM is quenched. In this case, if a non-zero matrix element for $i \neq j$ exists, an effect called second-order OAM can occur.^[127]

For 3d-metals, it is also possible to distinguish between a quenched or unquenched first- or second-order OAM by considering the d-orbital splitting (**Figure 1-4**).^[140,146,163]

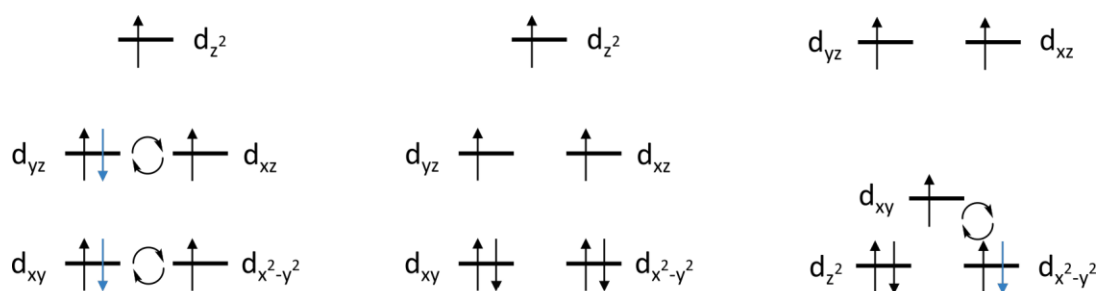


Figure 1-4 Example for an unquenched first-order OAM in a linear coordination environment with a d^7 electron configuration (left), a quenched OAM (middle) and a partially unquenched second-order OAM for a distorted tetrahedral geometry (right).

OAM is here associated with the orbital pairs sharing the same magnetic quantum number $m_l = \pm 2$ or ± 1 . An odd electron number in either (d_{xy} , $d_{x^2-y^2}$) or (d_{xz} , d_{yz}) will contribute with an OAM of $L = 2$ or 1 (**Figure 1-4**, left). Thus, the idealized linear geometry for a d^7 electron configuration results in a huge OAM largely contributing to the magnetic anisotropy. In the case of an even electron number in those orbitals, the OAM will be fully quenched due to Pauli Exclusion Principle (**Figure 1-4**, middle). However, real molecules barely display ideal geometries and the degeneracy of the orbitals is lifted. The distorted tetrahedral coordination geometry in a d^7 electron configuration (**Figure 1-4**, right), still provides a second-order OAM, due to a small energy gap between $d_{x^2-y^2}$ and d_{xy} . Therefore, the OAM is not fully quenched and the electrons in the $d_{x^2-y^2}$ orbital are allowed to interact with the higher lying d_{xy} .^[140] The smaller the energy gap between the involved orbitals, the larger the OAM will be. Nevertheless, it is always smaller compared to first-order OAM, found for lanthanides. This will then affect the magnetic states (M_S or M_J) by splitting the energy levels at zero applied magnetic field.

When a compound has no first-order OAM, L is not a good quantum number. Therefore, it is assumed that only the spin with the corresponding M_S states is relevant. The M_S states split due to second-order OAM and can be described with the zero-field splitting parameters D and E .^[165] A large axial parameter D is associated with a large energy splitting of the pure M_S states, while the rhombic parameter E accounts for transverse anisotropy, mixes the M_S states with $\Delta M_S = \pm 2$ and hinders magnetic properties. The functioning of a SMM, the energy splitting of the spin states and the respective energy barrier to spin reversal U is best displayed by a double-well potential model (**Figure 1-5**).^[166]

The depicted model describes the first SMM, the cluster compound Mn_{12} and can be adopted for other molecules, depending on the specific spin ground-state value. Since D is negative, the maximum M_S state must be stabilized and Mn_{12} possesses a bistable ground-state of $M_S = \pm 10$. Each pair of M_S with the same absolute value is called a Kramers doublet (KD).^[167]

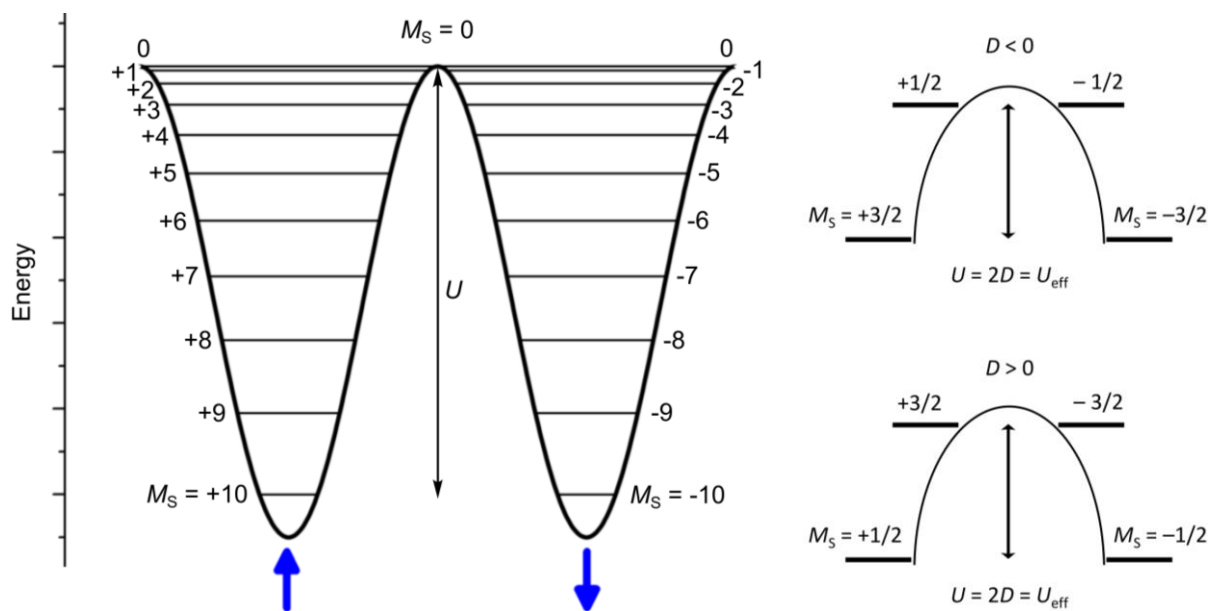


Figure 1-5 (left): Double-well potential model for the Mn_{12} system with an $S = 10$ ground state for a negative D value with ZFS. The molecule can either be trapped spin up or spin down and a sequential Orbach transition has to overcome the energy barrier to spin reversal U . (right): Double-well potential model for a $S = 3/2$ spin system. When D is negative, the maximum ground-state is stabilized while a positive D requires the stabilization of the $M_S = \pm 1/2$ magnetic state.

With this representation, it can be explained how a SMM works. Once the molecule is magnetized, the magnetic moment is trapped in the lowest lying magnetic state, here for example $M_S = +10$. In order to reverse the spin into the opposite direction, the system requires a sequential transition over every excited state (+9, +8, ...), as the selection rule for phonon absorption only allows $\Delta M_S = \pm 1$.^[166] Thus, for an ideal thermal transition (Orbach relaxation) from $M_S = +10$ to -10 , the system has to overcome the energy barrier of spin reversal U . This explains the possible application as high-density data storage devices, since the two $M_S = \pm 10$ states correspond to the binary states (1, 0) in computer operations. To erase the information that is stored with the magnetization, a certain amount of energy is required. Otherwise, the system stays in the defined state and represents a safe data-storage device.

The axial ZFS parameter D and the rhombic parameter E describe the separation of the single M_S states and are related to the symmetry of the system. While D is associated with a pure, axial splitting of the M_S states, E determines the mixing of different states with $\Delta M_S = \pm 2$, which induces transverse anisotropy, an obstacle for SMM behavior. A good SMM should have a large, negative D value (maximum M_S is stabilized) and a negligible amount of E . In contrast, a stabilization of the lowest M_S state would result in a positive D value (**Figure 1-5**, right). However, in systems with first-order angular momentum and strong SOC, D and E are no longer valid for a proper description. Therefore, the quantum number S , which only takes the spin into account, needs to be replaced by the quantum number J , a combination of the spin and the OAM ($J = |S \pm L|$).^[126]

The ultimate goal for every high-performance SMM is the presence of a hysteresis loop at temperatures as high as possible (**Figure 1-6**). The SMM starts at zero field without any degree of magnetization (A). When a dc field is applied, the magnetization first increases rapidly with the field strength and finally reaches a saturation (B). If the field is then slowly reduced up to zero, the magnetization is higher than the initial amount, which is called remanence (C). Upon gradually increasing the field into the opposite direction, the magnetization reaches zero (D), which is called the coercive field. Further increase of the field strength will finally result in saturation again, but with the opposite direction (E). From here, the same procedure as described above results in a hysteresis loop. For SMMs, the temperature beyond which the hysteresis is closed, is called hysteresis temperature T_{Hys} .^[126]

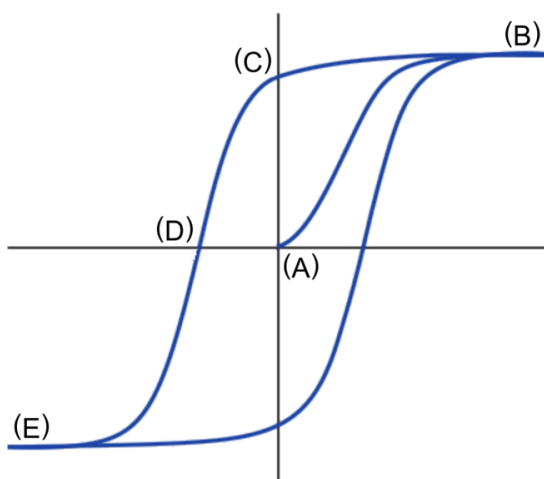


Figure 1-6 Example of magnetic hysteresis with the remnant magnetization at zero field and the coercive field, which describes the amount that is required to demagnetize the compound.

The sequential transition over the different magnetic M_S states (Orbach process) within the double-well potential is desirable for high-performance SMMs. However, in real compounds, there are several other processes that hinder the systems to exhaust the whole potential energy barrier (**Figure 1-7**).^[137,165,168]

In addition to the ideal thermal Orbach relaxation, there are three spin-lattice relaxation mechanisms that are all temperature-dependent and minimize the SMM performance due to a lowering of the effective energy barrier.^[137] The direct process (between adjacent M_S states) includes the emission or absorption of a single phonon (lattice vibration) with the exact energy required for the transition.^[169] The Orbach Relaxation^[170] is a concerted two phonon process, with the absorption of a phonon that causes an excitation into a higher-lying state and the subsequent deexcitation by phonon emission.

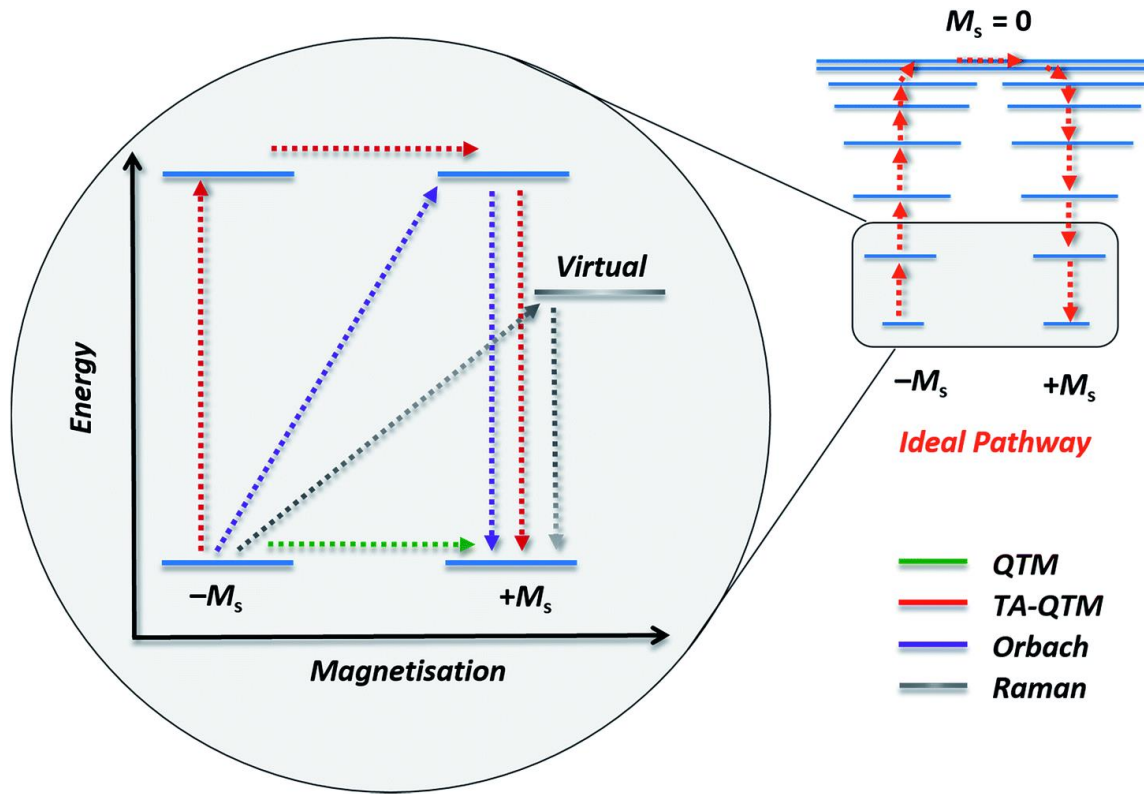


Figure 1-7 Illustration of different relaxation processes.^[137] An ideal pathway (ideal Orbach process) as sequential transition over the whole energy barrier. An Orbach process (blue arrows) from the M_s ground-state, a Raman transition (grey arrows) including a virtual state, quantum tunneling of the magnetization (green arrow), thermally assisted QTM (red arrow) and a direct process (red arrows) between adjacent states. For detailed explanation see the description in the main text. Reproduced with permission from the cited literature.

The Orbach process follows the Arrhenius law and describes the height of the energy barrier to spin reversal by the following equation:

$$\frac{1}{\tau_{\text{obs}}} = \tau_0^{-1} \exp\left(-U_{\text{eff}}/k_B T\right) \quad (\text{Eq. 1-1})$$

Where τ_{obs} is the observed relaxation time, τ_0 the relaxation rate for the Orbach process, U_{eff} the effective energy barrier to spin reversal and k_B the Boltzmann constant.

Here, the effective energy barrier U_{eff} (experimentally measured value) can be lower or equal compared to U (energy between the highest and lowest M_s state). For example, in a d^7 spin system with $M_s = 3/2$ a transition is only possible between $M_s = \pm 3/2$ and $\pm 1/2$, hence U and U_{eff} are equal (**Figure 1-5**, right). For f-elements, both values are often different, since more than two Kramers' doublets offer the possibility for a transition through excited states.

A Raman process works in the same manner, but it includes the transition into a virtual state.^[171] Another important process is the temperature-independent quantum tunneling of the magnetization

(QTM). It describes the bypassing of the energy barrier by “tunneling” between the M_S ground states at the same energy level. Thermally assisted quantum tunneling (TAQTM) includes the previous excitation (usually by rising the temperature) into higher states followed by a transition through the barrier. An important challenge for high-temperature SMMs is the minimization of QTM. Therefore, one should focus on the use of Kramers’ ions and the required LFs (e.g. axial for oblate ions and for Co(II)).^[137] This reduces the amount of transverse anisotropy that causes the mixing of M_S states, which supports QTM.^[168]

1.2.3. Single-molecule magnetism – strategies and design basics

In chapter 1.2.2 it was discussed that the OAM in 3d transition metals is often quenched by the ligand field, which prevents large ZFS. Consequently, 3d SMMs are rather field induced SMMs, which means that they require an external dc field for displaying SMM behavior. The diffuse 3d orbitals are more strongly affected by the ligand field, while 4f orbitals hardly participate in ligand bonding.^[151] Lanthanides possess a large, intrinsic OAM that favors SOC and gives rise to high anisotropies and energy barriers to spin reversal.^[143,172] Since the free lanthanide ions are highly anisotropic, they need a non-disturbing ligand field to display well-performing SMM behavior.

Lanthanides have received their name from the first element in the series, lanthanum. They are also referred to as “rare-earth metals”, however, this is misleading since some of them have similar abundances to common industrial metals and are significantly less rare compared to precious metals like gold and platinum.^[168] With the increasing atomic number along the 4f period, the radii of the respective metals gradually decrease going from lanthanum to lutetium. This correlation is known as “lanthanide contraction”. The electron configuration of lanthanides is $[\text{Xe}]4f^{n-1}5d^16s^2$, with the 4f orbitals being shielded by the 5s and 5p orbitals. This enables a highly stable +III oxidation state and hinders the 4f orbitals from covalent bonding.^[151] Furthermore, it provides them similar chemical properties and they are therefore difficult to separate from each other.

In general, Kramers’ ions^[167] are the preferred choice for the design of high-performance SMMs. According to the Kramers’ degeneracy theorem, this ensures two M_S (M_J for f-elements) ground-states with the same energy. Those two states are called Kramers’ doublets (KDs). Furthermore, for f-elements it is essential to design the ligand field with regard to the shape of the electron density of the free metal ions. There are oblate-shaped^[143] elements, e.g. Tb(III) and Dy(III), that require an axial ligand field, and prolate^[173,174] ions, e.g. Er(III), that need to be incorporated into an equatorial LF. Since

the presentation of the first lanthanide-based SMM in 2003, many remarkable compounds have been synthesized.^[149,150,155–160]

At first sight, 3d transition metals have some disadvantages compared to f-elements. However, in recent years, many remarkable 3d metal SMMs^[137–140] with high anisotropies were synthesized, displaying the importance of ligand field design.^[137–140,175–177] They include linear Fe(I)^[175–177] and Co(II)^[163] and tetrahedral Co(II)^[90,107,178–181] compounds. Additionally, some of them have even been analyzed by high-resolution X-ray diffraction to determine the d-orbital population.^[163,181] Among those examples, trigonal planar Fe(II)^[92,93,182] and Co(II)^[93,183,184] complexes are rather rare in literature and have not been sufficiently explored in the field of single molecule magnetism.^[183,184] One of the first examples of a three-coordinate Fe(II) high-spin complex with large orbital angular momentum was already reported by HOLLAND *et al.* in 2002 using β -diketiminato ligands.^[182] The trigonal planar Co(II) complexes [Li(15-crown-5)][Co{N(SiMe₃)₂}₃], [Co{N(SiMe₃)₂}₂(thf)] and [Co{N(SiMe₃)₂}₂(PCy₃)] all display slow relaxation of the magnetization under an applied dc field.^[93] In contrast, the isostructural Fe(II) complexes [Li(15-crown-5)][Fe{N(SiMe₃)₂}₃] and [Fe{N(SiMe₃)₂}₂(thf)]^[93] do not show SMM behavior. Interestingly, the only exception for this series of compounds is [Fe{N(SiMe₃)₂}₂(PCy₃)]^[92], which might benefit from the influence of a softer phosphorus donor, displaying SMM behavior under an applied dc field.

The introduction of soft main-group elements to enhance the magnetic properties in the design of SMMs has indeed proven its potential.^[185] However, the influence of main group elements on the magnetic performance is still not sufficiently investigated. Some rare examples reported that the presence of softer elements boosted the magnetic properties, probably due to enhanced spin orbit coupling.^[85–96] For transition metal SMMs, various examples demonstrate how the introduction of heavier and softer p-block donor atoms positively impact the magnetic properties. For example, the influence of a phosphorus donor ligand in trigonal planar Fe(II)^[92,93] and Co(II)^[93] complexes significantly raised the effective energy barriers to spin reversal. Moreover, a strong spin orbit coupling was found in a heterobimetallic Mn(II)-Bi(III) complex.^[94] Other investigations demonstrated that the magnetic anisotropy can be enhanced by the heavy-atom effect. A series of Fe(II) complexes were synthesized varying both the coordinated halides (Br, I) and the group 14 elements (Ge, Sn).^[186] The variation increased the zero-field splitting with increasing halide mass, due to a stronger spin-orbit coupling. Additionally, this observation was also discussed in a series of tetrahedral Co(II) complexes with EPh ligands (E = O, S and Se) that exhibit increasing zero-field splitting (*D*) values descending down the row.^[90,95]

The beneficial influence of main group elements on the SMMs performance is not only limited to transition metals, but is also observable in f-element systems.^[187,188] Lanthanide-based SMMs including heavier donor atoms are still rare and one remarkable compound is the phospholyl Er(III) complex $[(\text{Dsp})\text{Er}(\text{COT})]^{[96]}$ (COT^{2-} = cyclooctatetraenide; Dsp^- = 3,4-dimethyl-2,5-bis(trimethylsilyl)-phospholyl), which benefits from phosphorus donation and superior relaxation performance compared to the phosphorus free compound $[(\text{Cp}^*)\text{Er}(\text{COT})]^{[189]}$. In contrast, the bis-monophospholyl dysprosium SMM $[\text{Dy}(\text{Dtp})_2][\text{Al}\{\text{OC}(\text{CF}_3)_3\}_4]^{[91]}$ ($\text{Dtp} = \{\text{P}(\text{C}(\text{tBu})\text{C}(\text{Me}))_2\}$) does not exceed its carbon-based counterparts with the cationic $[\text{Dy}(\text{Cp}^{3-\text{tBu}})_2]^{+[156,157]}$ ($\text{Cp}^{3-\text{tBu}} =$ penta-iso-propylcyclopentadienyl) or $[(\text{Cp}^{i\text{Pr5}})\text{Dy}(\text{Cp}^*)]^{+[158]}$. However, a series of group 15 bridged dysprosocenes with the soft donor in the equatorial positions and a strong axial crystal field generated by cyclopentadienyl ligands, revealed increasing anisotropy barriers from phosphorus to antimony.^[85,88,89] Those results clearly show the necessity to reduce the equatorial crystal field for the development of high-temperature dysprosium SMMs, but also demonstrate the possibility to improve molecular magnetism on the basis of softer donor atoms. Recently, the use of softer main group elements was even applied to strongly couple paramagnetic transition metals and lanthanide ions, which opens the possibility to synthesize promising heterometallic SMMs.^[86] In this context, the strength of magnetic exchange interactions can be quantified by the magnetic exchange coupling constant J .

Heavier p donor atoms do not only contribute to the spin-orbit coupling. They were also found to mediate exchange coupling^[86] in $\text{Cr}(\text{II})^{[190]}$ and $\text{Mn}(\text{II})^{[191]}$ compounds. However, literature examples are mainly based on μ -bridging nitrogen or oxygen atoms. Cyanate ligands are found in compounds bridging between $\text{Mn}(\text{II})$ and $\text{Fe}(\text{III})^{[192]}$ or in $\text{W}(\text{V})^{[193]}$. Oxo bridges are common in literature and supported the communication between $\text{Mn}(\text{III})$ and $\text{Dy}(\text{III})^{[194]}$ or $\text{Mn}(\text{II})$ and $\text{Bi}(\text{III})^{[94]}$. Further ligand mediated exchange-coupling were found between lanthanides and $\text{Co}(\text{II})^{[195]}$, $\text{Ni}(\text{II})^{[196]}$. Additionally, superexchange coupling^[197] is found in chloride-bridged bimetallic lanthanide compounds.^[198–200] Another strategy, which offers the possibilities to reduce under-barrier relaxation processes, is the direct exchange coupling that is mediated by using radical ligands.^[153,154,201–212] Since SN_x ligands were found to stabilize radicals, this might be a promising tool in order to further tune the SMM properties in polyimido sulfur complexes.^[33,64,110]

2. Research Scope

The scope of this thesis is to open a new chapter in SN chemistry and establish polyimido sulfur(VI) ligands in the field of molecular magnetism, especially through their marriage with f-block metals. In order to reach this goal, novel 3d- and 4f-element complexes of known polyimido sulfur centered ligands (in the oxidation state +VI) were synthesized and characterized by crystal structure X-ray diffraction and magnetic measurements. The first part of this work focusses on the symmetric tetraimido sulfate $[S(NtBu)_4]^{2-}$ (L^1), which contains two identical coordination sites that may enable the formation of (hetero)bimetallic exchange coupled systems. The second part investigates the chemistry of the triimido sulfonate $[Ph_2PCH_2S(NtBu)_3]^-$ (L^2). Although this ligand only possesses one coordination site, it additionally has the opportunity to bound through a softer phosphorus donor atom in a scorpionate-like fashion, which may be beneficial to the magnetic properties of the target compounds. The influence of such ligand designs on the magnetic properties were thoroughly studied and are presented in the following chapters.

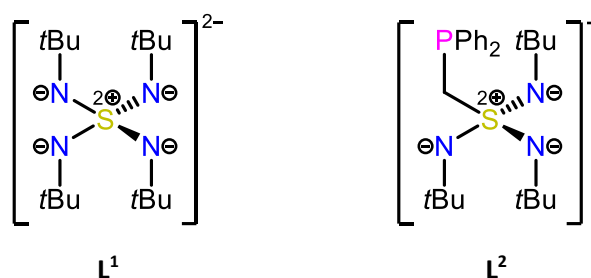


Figure 2-1 Depicted are the two S(VI) centered polyimido ligands that were used within this work. (left): The double negatively charged tetraimido sulfate $[S(NtBu)_4]^{2-}$ (L^1) with two identical coordination sites. (right): The triimido sulfonate $[Ph_2PCH_2S(NtBu)_3]^-$ (L^2) that provides a soft phosphorus donor instead of four nitrogen atoms and a total ligand charge of minus one.

The first studies were performed on d-block elements with large magnetic anisotropy like cobalt, iron and manganese, commonly used for their magnetic properties. Furthermore, based on the results obtained with 3d transition metals, the suitability of ligands L^1 and L^2 towards SMM design with lanthanide ions, more especially Tb(III) and Dy(III) has been probed. This was so far unexplored to this class of ligands. Due to their inherent, unquenched OAM and large spin-orbit coupling, lanthanides are promising candidates towards the synthesis of single molecule magnets (SMMs) and single ion magnets (SIMs).

3. Results and Discussion

Major parts of this chapter have been published in:

1. Jochen Jung, Annika Münch, Regine Herbst-Irmer and Dietmar Stalke, „*Tetraimido Sulfuric Acid $H_2S(NtBu)_4$ – Valence Isoelectronic to H_2SO_4* “, *Angew. Chem. Int. Ed.* **2021**, 60, 5679 – 5682.^[1]
2. Jochen Jung, Christina M. Legendre, Regine Herbst-Irmer and Dietmar Stalke, „*Exchange Coupling in Binuclear Manganese and Cobalt Complexes with the Tetraimido Sulfate Anion $[S(NtBu)_4]^{2-}$* “, *Inorg. Chem.* **2021**, 60, 2, 967 – 972.^[2]
3. Jochen Jung, Florian Benner, Regine Herbst-Irmer, Selvan Demir and Dietmar Stalke, „*Slow Magnetic Relaxation in Mono- and Bimetallic Lanthanide Tetraimido-Sulfate $S(NtBu)_4^{2-}$ Complexes*“, *Chem. Eur. J.* **2021**, 27, 12310 – 12319.^[3]
4. Jochen Jung, Christina M. Legendre, Serhiy Demeshko, Regine Herbst-Irmer and Dietmar Stalke, „*Trigonal Planar Iron(II) and Cobalt(II) Complexes Containing $[RS(NtBu)_3]^{n-}$ ($R = NtBu$, $n = 2$; CH_2PPh_2 , $n = 1$) as Acute Bite-Angle Chelating Ligands: Soft P Donor Proves Beneficial to Magnetic Co Species*“, *Inorg. Chem.* **2021**, 60, 13, 9580 – 9588.^[4]
5. Jochen Jung, Christina M. Legendre, Serhiy Demeshko, Regine Herbst-Irmer and Dietmar Stalke, „*Imido sulfonate scorpionate ligand in lanthanide single-molecule magnet design: slow magnetic relaxation and butterfly hysteresis in $[ClDy\{Ph_2PCH_2S(NtBu)_3\}_2]$* “, *Dalton Trans.* **2021**, 50, 17194 – 17201.^[5]

3.1. General procedures for the ligand syntheses

The historical development of the synthetic routes to obtain sulfur diimides and triimides were already presented in chapter 1.1.1. The most convenient reaction paths for the still challenging synthesis that were chosen for the thesis are depicted in **Figure 3-1**. The syntheses will be explained in detail and sometimes differ from the cited literature.

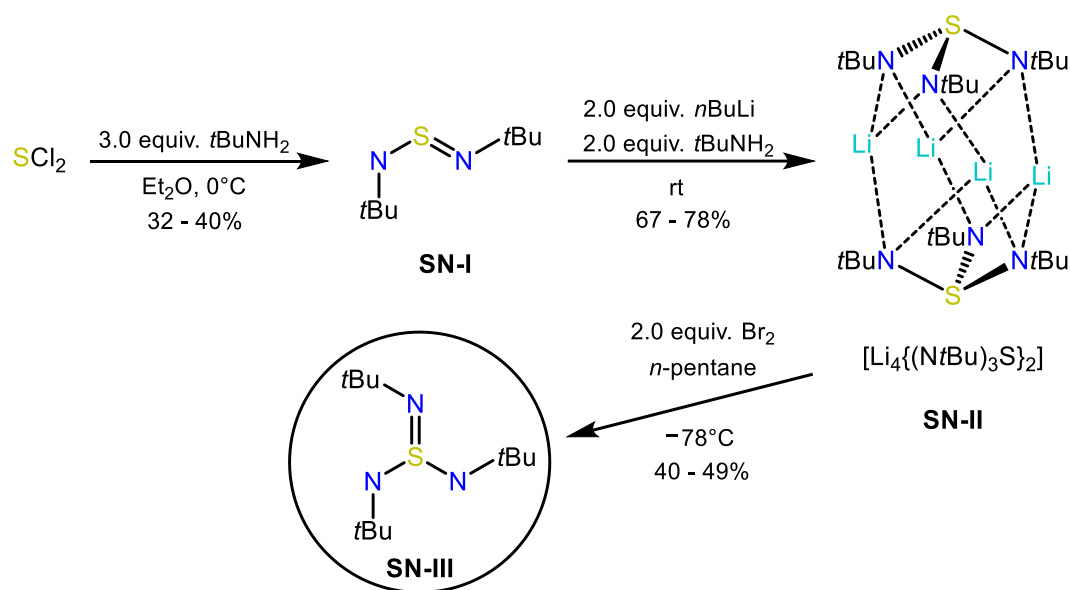


Figure 3-1 Synthetic route to the sulfur diimide $\text{S}(\text{N}t\text{Bu})_2$ (**SN-I**) and the sulfur triimide $\text{S}(\text{N}t\text{Bu})_3$ (**SN-III**) over the intermediate and cap-shaped dimer $[\text{Li}_4\{(\text{N}t\text{Bu})_3\text{S}\}_2]$ (**SN-II**). Synthetic details are described in the text.

The synthesis of SCl_2 , a common precursor for organosulfur compounds, started directly from elemental sulfur and chlorine.^[213] Sulfur was placed in a reaction flask without the need of an additional solvent. Under a constant chlorine gas flow, the solid element slowly turned into a red liquid over time. Due to the equilibrium between sulfur dichloride and disulfur dichloride ($2 \text{SCl}_2 \rightleftharpoons \text{S}_2\text{Cl}_2 + \text{Cl}_2$), a purification distillation was required to obtain pure SCl_2 . Freshly distilled SCl_2 was then reacted with *tert*-butylamine in diethyl ether.^[22] The highly exothermic reaction required a slow addition under cooling with an ice bath. After two days at room temperature, the solid byproduct *tert*-butylamine hydrochloride was filtered off and washed with Et_2O . Evaporation of the solvent yielded a yellow liquid, that was distilled under reduced pressure and under a continuous temperature increase up to 160°C . Thereby, the formed polymeric $(\text{SN}t\text{Bu})_x$ undergoes a slow pyrolysis from which a pale-yellow liquid was obtained. Subsequent purification distillation yielded pure $\text{S}(\text{N}t\text{Bu})_2$ (**SN-I**). The sulfur diimide was then reacted with $[\text{Li}\{\text{N}(\text{H})t\text{Bu}\}]$, synthesized at -78°C in situ from *n*-BuLi in *n*-hexane and *tert*-butylamine.^[31]

Slow addition of **SN-I** at room temperature gave the cap shaped dimer $[\text{Li}_4\{(\text{NtBu})_3\text{S}\}_2]$ (**SN-II**). After removal of the reaction solvent, the residue was dissolved in a minimum amount of hot toluene and stored for crystallization at -30°C . The isolated crystals were washed with cold *n*-pentane and the mother liquor was reduced in volume and crystallized again to improve yields. The sulfur(IV) atoms in **SN-II** can be further oxidized by elemental bromine in *n*-pentane at -78°C .^[32] Upon addition of the Br_2 solution, the color of the reaction mixture instantly turned into an intense, deep blue, indicative of the formation of radical^[31,33,63] intermediate species. The reaction mixture's color evolved upon further oxidant addition from colorless, over green to orange. The reaction was finished when all colors vanished resulting in a white suspension. Removal of the formed LiBr precipitates by filtration improved the purification process. Otherwise, the product stuck to the surface of the side product and subsequent sublimation was less efficient. The solvent was carefully removed under reduced pressure, since **SN-III** is volatile, too. The product was then sublimed at temperatures up to 70°C and collected in a cold trap that was cooled with liquid nitrogen. During the sublimation process, partial crystallization of **SN-III** as colorless blocks was observed in the connector between the reaction flask and the cold trap. The remaining *n*-pentane was used to dissolve the product and the solution was transferred in a Schlenk flask to enable proper crystallization at -35°C . Prior to that, *n*-pentane was concentrated to a minimum amount, since the product is highly soluble in organic solvents. The use of *n*-pentane instead of *tert*-butylamine is handy, because it is more volatile and did not stick to the surface of the formed crystals.

The isolated **SN-III** possesses a central sulfur atom in the oxidation state +VI and can be further functionalized by the addition of a fourth side-arm. An example is the reaction of **SN-III** with $[\text{Li}\{\text{N}(\text{H})\text{tBu}\}]$, which gives the symmetric tetraimido sulfate $[\text{S}(\text{NtBu})_4]^{2-}$ (**L¹**). The ligand contains two identical coordination sites and can be seen as analogue to the sulfate dianion. The synthesis of the lithium salt $[(\text{thf})_4\text{Li}_2(\text{NtBu})_4\text{S}]$ (**L¹-Li, Li**) is depicted in **Figure 3-2**.^[32] Two equiv. of $[\text{Li}\{\text{N}(\text{H})\text{tBu}\}]$ were first synthesized by adding *n*-BuLi solution to *tert*-butylamine at -78°C . Subsequent addition of a thf solution of **SN-III** at room temperature and crystallization directly from the reaction medium yielded colorless crystals after two days at -35°C . The mother liquor can be reduced in volume and crystallized twice to improve yields. The isolated $[(\text{thf})_4\text{Li}_2(\text{NtBu})_4\text{S}]$ (**L¹-Li, Li**) is highly sensitive towards oxygen exposure and would turn blue if oxidized, even under the smallest concentrations of O_2 (e.g. over time when stored in an inert glovebox).

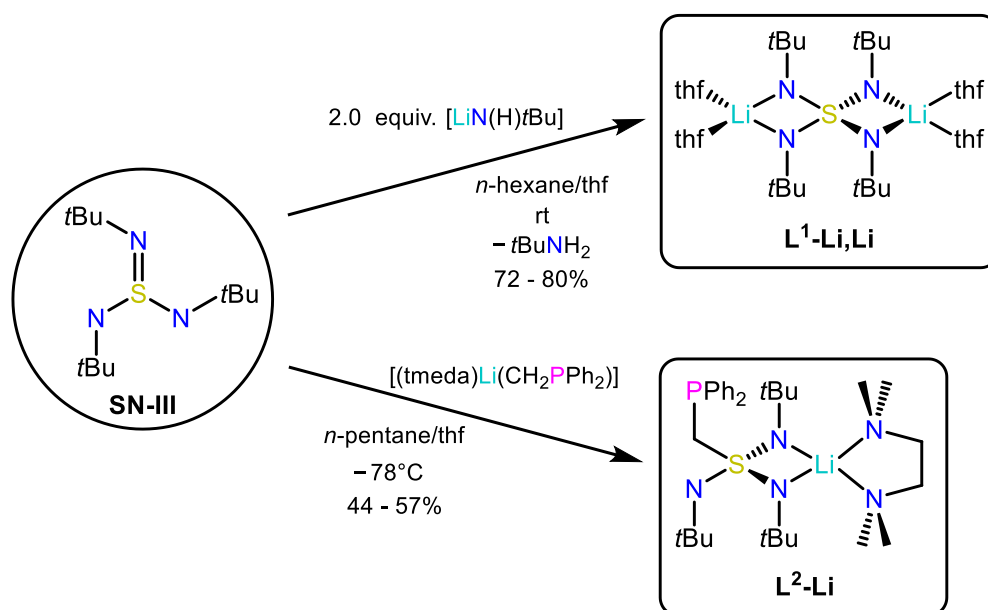


Figure 3-2 Synthesis of the tetraimido sulfate ligand $[\text{S}(\text{NtBu})_4]^{2-}$ (**L¹**) as the lithium salt $[(\text{thf})_4\text{Li}_2(\text{NtBu})_4\text{S}]$ (**L¹-Li, Li**) and the formation of the triimido sulfonate $[\{\text{Ph}_2\text{PCH}_2\text{S}(\text{NtBu})_3\}]^-$ (**L²**) based lithium compound $[(\text{tmeda})\text{Li}\{\text{Ph}_2\text{PCH}_2\text{S}(\text{NtBu})_3\}]$ (**L²-Li**).

The synthesis of the scorpionate-like ligand **L²** required the previous formation of the phosphorus side-arm $[(\text{tmeda})\text{Li}(\text{CH}_2\text{PPh}_2)]$ that was isolated as pale-yellow to white powder.^[69,214,215] A solution of *n*-BuLi in *n*-hexane was added with 1 equiv. of tetramethylethylenediamine (tmeda) and 1 equiv. of methyldiphenylphosphine (MePPH_2). After stirring for half an hour, a colorless precipitate in the yellow reaction mixture was formed. The solvent was removed by filtration and the residue was washed several times with *n*-pentane to yield $[(\text{tmeda})\text{Li}(\text{CH}_2\text{PPh}_2)]$. For the subsequent ligand synthesis, $[(\text{tmeda})\text{Li}(\text{CH}_2\text{PPh}_2)]$ was suspended in *n*-pentane and a solution of **SN-III** in thf was added at -78°C .^[68] A yellow precipitate was formed, which was dissolved by the addition of a minimum amount of thf, and the reaction mixture was stored at -35°C for crystallization. Colorless crystals were collected, washed with *n*-pentane and dried under reduced pressure.

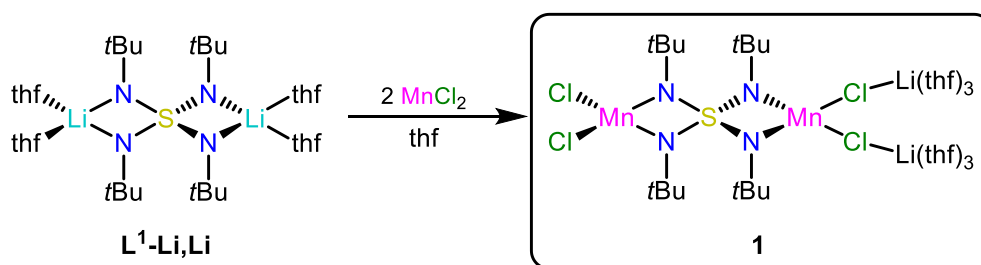
3.2. Sulfur imido ligands in d-block metal SMMs and SIMs

3.2.1. Exchange coupling in binuclear complexes of the tetraimido sulfate $[S(NtBu)_4]^{2-}$

In order to synthesize novel complexes using the SN ligand family, several strategies were followed. One was the use of the polydentate tetraimido sulfate $[S(NtBu)_4]^{2-}$ (**L¹**), which is a promising candidate for magnetic exchange coupled systems. It allows the synthesis of (hetero)bimetallic molecules and may enhance the magnetic communication between paramagnetic metal ions, due to a relatively short S–N distance. The results on d-block metal SMMs with Mn(II) and Co(II) are presented in the following.

3.2.1.1. Synthesis of $[Cl_2Mn(NtBu)_2S(tBuN)_2Mn\{ClLi(thf)_3\}_2]$ (**1**)

The binuclear manganese compound $[Cl_2Mn(NtBu)_2S(tBuN)_2Mn\{ClLi(thf)_3\}_2]$ (**1**) was synthesized from the dilithium tetraimido sulfate $[(thf)_4Li_2(NtBu)_4S]$ (**L¹-Li, Li**) that was combined with 2 equiv. of $MnCl_2$ and dissolved in thf at room temperature (**Scheme 3-1**). Crystallization was possible directly from the reaction mixture at $-34^\circ C$ upon filtration and solvent concentration under reduced pressure. The product was isolated in 67% yield as orange crystals, suitable for single crystal X-ray diffraction analysis.



Scheme 3-1 Synthetic route to the binuclear manganese compound $[Cl_2Mn(NtBu)_2S(tBuN)_2Mn\{ClLi(thf)_3\}_2]$ (**1**). Combination of the dilithium tetraimido sulfate $[(thf)_4Li_2(NtBu)_4S]$ (**L¹-Li, Li**) and 2 equiv. of $MnCl_2$ in thf at room temperature resulted in the isolation of the LiCl co-coordinated compound **1** in 67% yield.

The elemental analysis of $[Cl_2Mn(NtBu)_2S(tBuN)_2Mn\{ClLi(thf)_3\}_2]$ (**1**) was performed several times under different conditions as they showed a significant deviation from the theoretical values for a compound with six coordinated thf molecules. They obviously bind only weakly turning the crystalline material into a powder upon partial solvent loss over time, accompanied by a loss of mass. Therefore, the elemental analysis even of freshly isolated **1** has a broad deviation from the calculated composition. Drying the powder under reduced pressure for several hours to force thf to evaporate, resulted in a compound with approximately two thf molecules corresponding to the elemental analysis

(for more details see chapter 5.3.1). **1** crystallizes in the monoclinic space group $C2/c$ with half a molecule in the asymmetric unit (**Figure 3-3**).

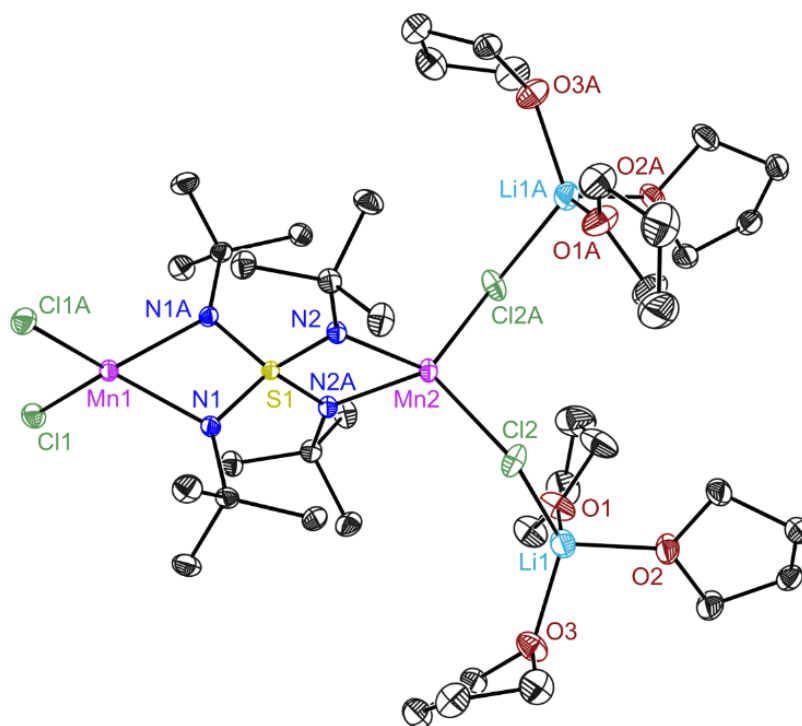


Figure 3-3 Crystal structure of $[\text{Cl}_2\text{Mn}(\text{NtBu})_2\text{S}(\text{tBuN})_2\text{Mn}\{\text{ClLi}(\text{thf})_3\}_2]$ (**1**). Anisotropic displacement parameters are depicted at the 50% probability level. Hydrogen atoms are omitted for clarity. Selected bond lengths [Å] and angles [°]: Mn1–Cl1 2.3597(4), Mn2–Cl2 2.3727(6), Mn1–N1 2.1148(10), Mn2–N2 2.0783(9), S1–N1 1.5898(9), S1–N2 1.5982(9), Cl1–Mn1–Cl1A 108.01(2), Cl2–Mn2–Cl2A 109.98(3), N1–Mn1–N1A 67.19(5), N2–Mn2–N2A 68.33(5), N1–S1–N1A 94.80(7), N2–S1–N2A 93.82(7), N1A–S1–N2 117.40(5), N1–S1–N2 117.69(5).

Both manganese ions show a distorted tetrahedral coordination environment by two chlorine atoms and the N,N' chelating tetraimido sulfate ligand. The elimination product LiCl from the metal exchange reaction did not precipitate and remained co-coordinated in **1** for charge compensation.^[106] Since the influence of a heavy atom to the magnetic properties was detected, predominantly from metal bonded heavy halides^[216–218] and rationalized by theory,^[219] this finding is also considered as potentially beneficial for the magnetic performance of **1**.

Interestingly, both lithium ions coordinate on one side of the compound, each one to a single chlorine atom. The coordination sphere of each lithium is saturated by three thf solvent molecules. This bonding induces two asymmetric Mn(II) ions, one on each coordination sites of the imido ligand and it was assumed that the different metal environments results in enhanced magnetic properties.

The Mn1–Cl1/Cl1A bond distances with 2.3597(4) Å are 0.013 Å shorter than the Mn2–Cl2/Cl2A bonds with 2.3727(6) Å, while the Mn–N bond is elongated by 0.037 Å from 2.0783(9) Å (Mn2–N2/N2A) to 2.1148(10) Å (Mn1–N1/N1A). This can be explained by the reduced halide electron density that can be donated to Mn2, which is due to the coordination of the (electro)positive lithium ions by Cl2 and Cl2A, respectively. To compensate for this, the Mn2–N2/N2A interaction is stronger than Mn1–N1/N1A, resulting in a significant shorter bond distance. However, the lower electron density on N2/N2A compared to N1/N1A only slightly influences the polar S–N single bonds by an elongation of 0.008 Å.

Interestingly, all S–N bond distances sum up to 6.376 Å and thereby fall in the reported range between 6.343 Å for [(acac)Cu(NtBu)₂S(tBuN)₂Cu(acac)] (**L¹-Cu,Cu**)^[106] and 6.405 Å for the lithium complex^[32] **L¹-Li,Li**.

Since lithium-bound thf starts to evaporate once crystalline **1** is isolated, magnetic investigations were performed with roughly dried crystals by evaporating the remaining crystallization medium (thf) at ambient temperature and pressure. To prevent crystal-bound thf molecules to evaporate, the freshly crystalized compound was “dried” for only a few minutes, just until the crystalline material was about to lose its shape. The problem of solvent evaporation was discussed earlier. The exact molecular composition, upon solvent loss, is unclear and so a reproducible sample with a predictable composition is synthetically not accessible. In this context, the relatively high diamagnetic impurity percentage (13.6%) can be explained, since the crystals were not completely dry.

The measurements and data processing for **1** (and **2**, next chapter) was done by Dr. C. M. Legendre. Full information on the data processing can be found in the PhD thesis of Dr. C. M. Legendre^[64] or in the publication (2).^[2]

Temperature-dependent dc magnetic susceptibility data for **1** were collected in the temperature range between 2 – 210 K and under an applied dc field of $H_{dc} = 0.5$ T. The observed $\chi_M T$ value at 210 K of 7.45 cm³mol⁻¹K is significantly smaller than the expected value of 8.75 cm³mol⁻¹K for two uncoupled Mn(II) ions with a spin of $S=5/2$ (**Figure 3-4**). The problem of potential solvent loss, and the remaining solvent molecules due to the roughly dried sample are a good explanation for this deviation. The $\chi_M T$ value gradually declines with increasing slope starting at 210 K and tends to reach zero at low temperatures. This is an indication for an overall $S = 0$ ground state due to antiferromagnetic coupling between the Mn(II) ions, resulting in magnetic quenching.^[220]

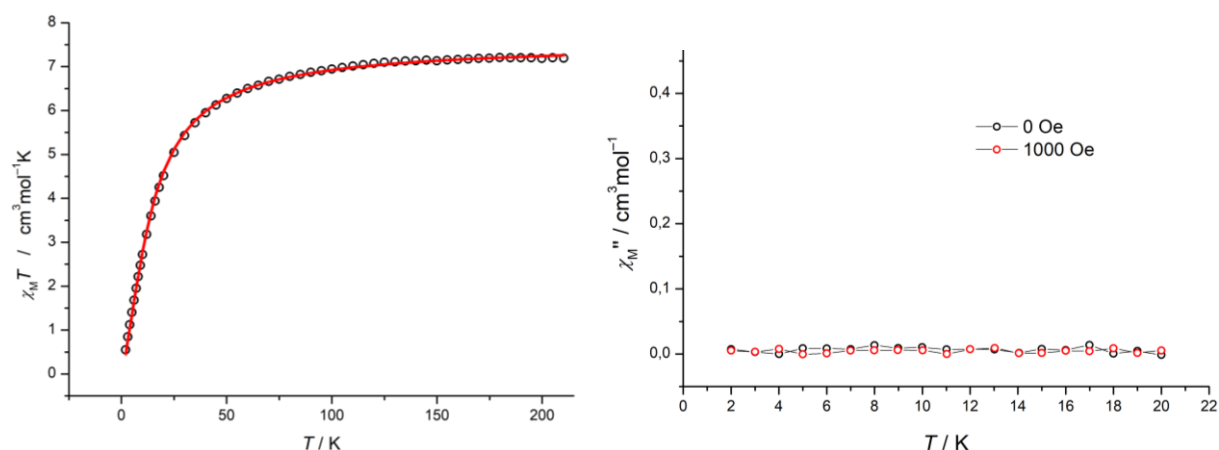


Figure 3-4 (left): Temperature-dependent dc magnetic susceptibility measurement $\chi_M T$ vs. T for **1** at 0.5 T with the obtained fitting parameters $g = 2.0$ (fixed), $D = 0 \text{ cm}^{-1}$, $J = -1.00 \text{ cm}^{-1}$ TIP = $1805 \cdot 10^{-6} \text{ cm}^3 \text{ mol}^{-1}$ and PI = 13.6%. (right): Temperature-dependent out-of-phase (χ_M'') ac susceptibility measurement for **1** under zero applied dc field (black) and under $H_{dc} = 1000 \text{ Oe}$ (red).

Indeed, the best data fit resulted in a small and negative coupling constant of $J = -1.00 \text{ cm}^{-1}$ together with a fixed $g = 2.0$ and a zero-field splitting parameter $D = 0 \text{ cm}^{-1}$. Such a small antiferromagnetic coupling is comparable to those of other compounds with both symmetrically and asymmetrically coordinated manganese(II) ions.^[220–222]

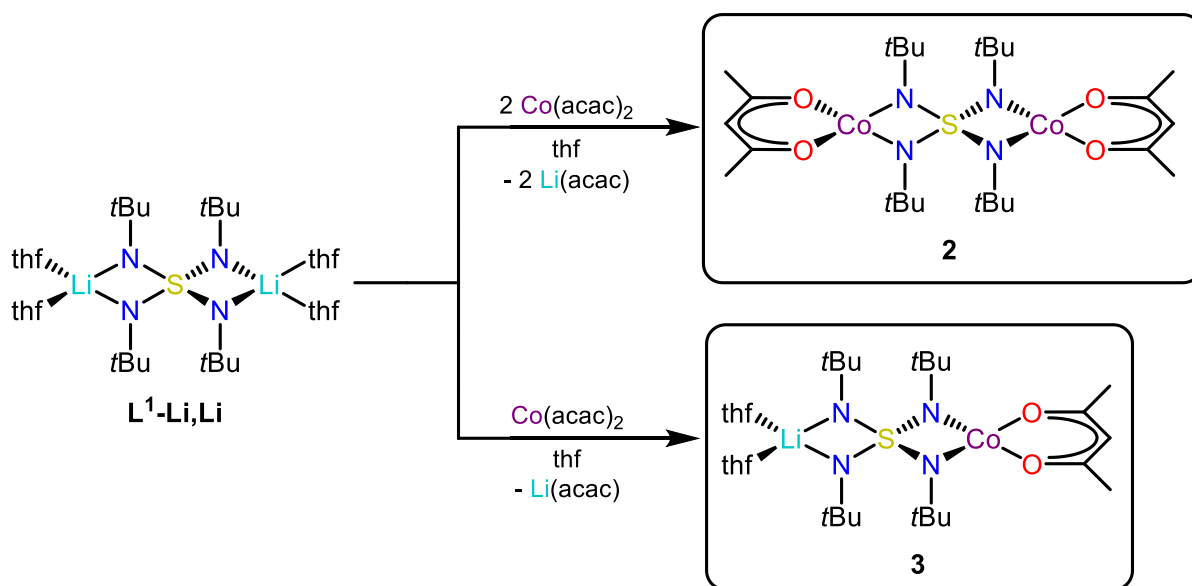
Similar to all the metal complexes of the tetraimido sulfate $[\text{S}(\text{NtBu})_4]^{2-}$ (**L**¹), a remarkable acute N–M–N' bite angle was observed for **1** (N1–Mn1–N1A $67.19(5)^\circ$ and N2–Mn2–N2A $68.33(5)^\circ$). The unusual, highly distorted tetrahedral geometry around the metal centers prescribed by the ligand is expected to be beneficial for the magnetic properties of the compound.^[107] To probe this hypothesis, out-of-phase (χ_M'') temperature-dependent ac magnetic susceptibility data were collected at the maximum frequency of 1488 Hz, while ranging the temperature from 2 – 20 K. First, the measurement was performed without an applied dc field and then at $H_{dc} = 1000 \text{ Oe}$ (**Figure 3-4**). Nevertheless, since no characteristic peak maximum for slow magnetic relaxation was observed, neither without nor under an applied external dc field, compound **1** does not show any single-molecule magnet behavior.

3.2.1.2. Synthesis of $[(\text{acac})\text{Co}(\text{NtBu})_2\text{S}(\text{tBuN})_2\text{Co}(\text{acac})]$ (**2**)

An alternative approach to the pathway of metal exchange via transition metal halides explored the utilization of M(II) acetylacetonate (acac) complexes. The reaction is triggered by Li(acac) formation, which is hardly soluble in common organic solvents.

The homonuclear bimetallic cobalt compound $[(\text{acac})\text{Co}(\text{NtBu})_2\text{S}(\text{tBuN})_2\text{Co}(\text{acac})]$ (**2**) was synthesized by combining $[(\text{thf})_4\text{Li}_2(\text{NtBu})_4\text{S}]$ (**L¹-Li, Li**) with two equivalents of $\text{Co}(\text{acac})_2$ in thf at room temperature (**Scheme 3-2**). After stirring for 1 d, Li(acac) precipitates were formed and removed by filtration. Extraction with a small amount of *n*-pentane and crystallization at -34°C yielded red crystals in 81% yield, suitable for single crystal X-ray diffraction analysis.

Employing the same synthesis with one equivalent $\text{Co}(\text{acac})_2$ in thf at room temperature led to the hetero bimetallic $[(\text{acac})\text{Co}(\text{NtBu})_2\text{S}(\text{tBuN})_2\text{Li}(\text{thf})_2]$ (**3**), isolated as red crystalline needles (**Scheme 3-2**). As expected, only one lithium ion is substituted by cobalt.



Scheme 3-2 Synthetic routes to the hetero bimetallic cobalt complex $[(\text{acac})\text{Co}(\text{NtBu})_2\text{S}(\text{tBuN})_2\text{Li}(\text{thf})_2]$ (**3**) and the homo bimetallic $[(\text{acac})\text{Co}(\text{NtBu})_2\text{S}(\text{tBuN})_2\text{Co}(\text{acac})]$ (**2**). Starting from the lithium precursor $[(\text{thf})_4\text{Li}_2(\text{NtBu})_4\text{S}]$ (**L¹-Li, Li**), **2** is obtained by the reaction with 2 equiv. of $\text{Co}(\text{acac})_2$ followed by a metal exchange and $\text{Li}(\text{acac})$ elimination in 81% yield. If only one equiv. of $\text{Co}(\text{acac})_2$ is used, the hetero bimetallic complex **3** is formed instead, with only one lithium exchange.

For the homo binuclear cobalt complex **2**, two polymorphs, **2a** (monoclinic, space group $P2_1/n$) (**Figure 3-5**) and **2b** (orthorhombic, $Pna2_1$), were isolated with rather small structural differences, basically limited to the Co-acetylacetonate angles (see chapter 6, **Figure 6-1**).

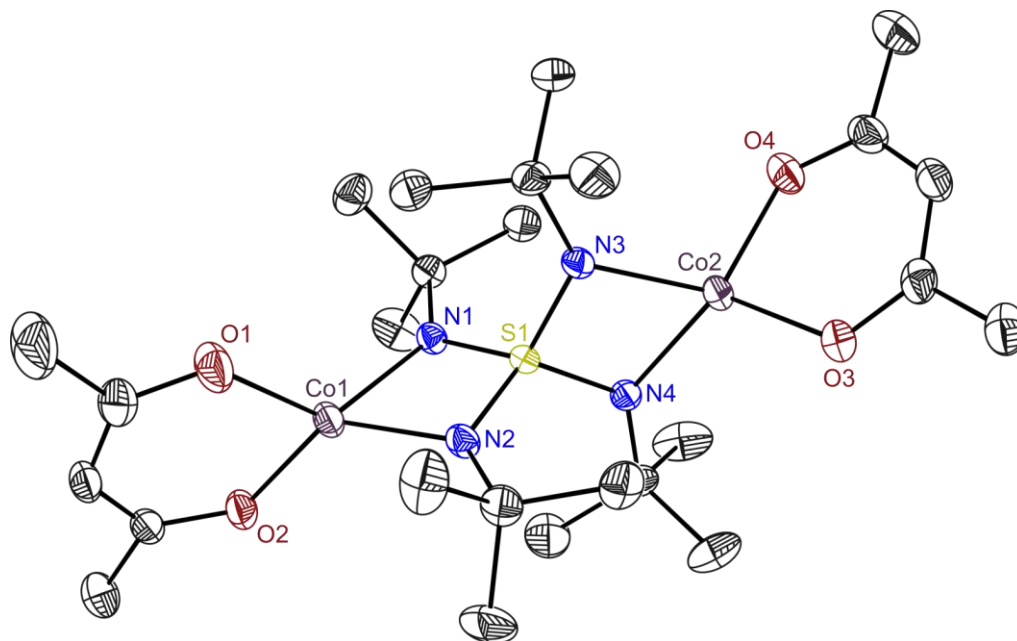


Figure 3-5 Crystal structure of **2a** (100 K). Anisotropic displacement parameters are depicted at the 50% probability level. Hydrogen atoms are omitted for clarity. Selected bond lengths [Å] and angles [°] for the polymorphs **2a,b**: Co1–O1 1.9443(14), 1.9512(15); Co1–O2 1.9433(13), 1.9505(16); Co2–O3 1.9453(14), 1.9349(15); Co2–O4 1.9352(14), 1.9462(15); Co1–N1 1.9839(15), 1.9726(17); Co1–N2 1.9772(15), 1.9796(17); Co2–N3 1.9713(15), 1.9742(17); Co2–N4 1.9703(14), 1.9713(13); O1–Co1–O2 93.25(6), 94.06(6); O3–Co2–O4 94.35(6), 94.91(6); N1–Co1–N2 71.71(6), 71.85(7), N3–Co2–N4 72.08(6), 72.08(7); N1–S1–N2 93.55(8), 93.41(9); N3–S1–N4 93.47(7), 93.53(9).

Since both cobalt ions in **2** have the same coordination environment, only averaged values will be discussed. The Co–O distances of 1.942 Å in **2a** and 1.946 Å in **2b**, as well as the Co–N distances of 1.976 Å (**2a**) and 1.974 Å (**2b**) are almost identical. A more pronounced but still small difference can be found for the O–Co–O angles. In both structures, there is one side in which this angle is significantly larger than the one on the other side of the SN_4 -ligand. The two bite angles have values of 93.25° and 94.35° in **2a**, and 94.06° and 94.91° in **2b**. Hence, there is a significant difference for each of the two sides, and additionally the average value of 93.80° for **2a** is 0.66° smaller than 94.46° in **2b**. Due to the symmetrical coordination, no significant difference in the S–N bond lengths and the N–S–N angles can be found with averaged values of 1.592 Å and 93.49°, respectively.

$[(\text{acac})\text{Co}(\text{NtBu})_2\text{S}(\text{tBuN})_2\text{Co}(\text{acac})]$ (**2**) is structurally similar to the bimetallic copper complex $[(\text{acac})\text{Cu}(\text{NtBu})_2\text{S}(\text{tBuN})_2\text{Cu}(\text{acac})]$ (**L¹-Cu,Cu**) that was obtained in a comparable reaction of $[(\text{thf})_4\text{Li}_2(\text{NtBu})_4\text{S}]$ (**L¹-Li,Li**) and $\text{Cu}(\text{acac})_2$.^[106] While the Co(II) ions in **2** are strongly distorted tetrahedrally coordinated, the Cu(II) ions are coordinated in a nearly square planar environment. However, the different geometry has only a small influence on the M–O and M–N bonds with averaged 1.923 Å and 1.958 Å in **L¹-Cu,Cu** and slightly larger values in **2** of 1.944 Å and 1.975 Å, respectively. This is probably rather explainable by smaller ionic radii for later transition metals than by geometrical

differences. The overall S–N bond sum in **2** is with 6.370 Å again almost identical to 6.343 Å in the copper compound **L¹-Cu,Cu**.

Since Co(II) complexes are strongly paramagnetic, NMR investigations can be challenging. Due to this paramagnetic character, the NMR signals are broader and shifted over a wide range compared to common organic molecules. Nevertheless, the integration of the compound's signals as well as the signal splitting reveals the molecule to be stable in solution and confirms the formation on a large scale. The ¹H-NMR spectrum of **2** in C₆D₆ is depicted in **Figure 3-6**. As it was expected for the symmetric SN₄ ligand environment, the four chemically identical *tert*-butyl groups can be identified as one broad singlet that resonates at $\delta = -33.02$ ppm. Since the [S(NtBu)₄]²⁻ ligand only possesses *tert*-butyl groups, the remaining signals can only arise from the acetylacetonate H₂C(C(O)Me)₂ (acac) ligands. The four methyl groups of the two acac ligands can be found in a smaller and sharper singlet at $\delta = 23.52$ ppm and the two CH protons have a chemical shift of $\delta = 72.35$ ppm. The ¹³C{¹H}-NMR spectrum revealed five signals at $\delta = 353.21$, 372.75, 653.88, 710.94 and 1172.73 ppm (see chapter 6, **Figure 6-2**). That fits to the assumption of one signal for the quaternary and one for the primary carbon atom of the *tert*-butyl groups accompanied by three signals for the acetylacetonate ligands.

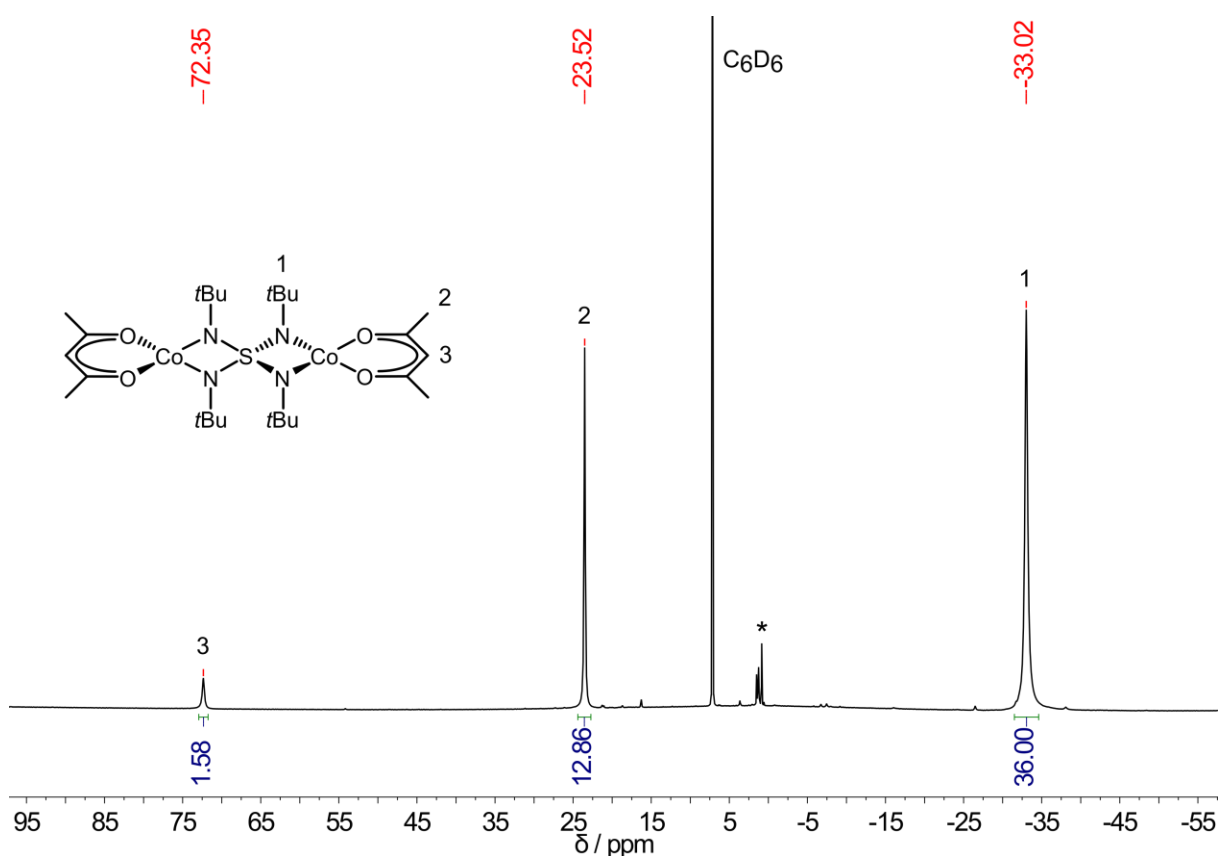


Figure 3-6 ¹H-NMR (500.13 MHz, 298 K, C₆D₆) of **2**. δ [ppm] = -33.02 (s br, 36H, 4 NC(CH₃)₃), 23.52 (s br, 12H, 4 acac-CH₃), 72.35 (s br, 2H, 2 acac-CH). (*): Refers to residual solvent and decomposition signals.

The performed LIFDI mass spectrometry of **2** with an m/z value of 632.2 for the positively charged molecule ion peak $[M]^+$ and the obtained isotope pattern is in good agreement with the expected molecular mass (see chapter 6, **Figure 6-3**).

From the reaction of $[(\text{thf})_4\text{Li}_2(\text{NtBu})_4\text{S}]$ (**L¹-Li,Li**) with only one equivalent of $\text{Co}(\text{acac})_2$ in thf at room temperature, the hetero bimetallic structure **3** was isolated (**Scheme 3-2**). Consequently, only one lithium ion is substituted by cobalt. The second lithium is tetrahedrally coordinated by two thf molecules and two nitrogen atoms of the imido ligand, just like in the starting material **L¹-Li,Li**. At the opposite side of the SN_4 moiety, the tetrahedrally coordinated cobalt is N,N' -chelated by the $[\text{S}(\text{NtBu})_4]^{2-}$ ligand and O,O' -chelated by acetylacetonate, the same coordination environment that was found for the hetero-bimetallic cobalt complex **2**.

In order to isolate **3**, the reaction mixture was filtered and volatiles were removed under reduced pressure. The raw product was then extracted with *n*-pentane and crystallized at -34°C . However, upon recrystallization attempts, **3** started to become more and more insoluble and a solid started to precipitate. Compared to the high solubility of **2** and the insolubility of **L¹-Li,Li** in *n*-pentane, it was assumed that compound **3** is not stable enough in solution. Instead, it is likely that two molecules of **3** react to form the starting material $[(\text{thf})_4\text{Li}_2(\text{NtBu})_4\text{S}]$ (**L¹-Li,Li**) and one molecule of **2**. Nevertheless, the isolation of **3** reveals the opportunity to selectively replace lithium step by step. First, one lithium ion could be replaced by different transition metals like Mn(II) or Co(II), followed by a second substitution by heavy main group elements like Bi(III), to give magnetic anisotropy by spin-orbit coupling^[94]. Alternatively, lithium could be exchanged with highly paramagnetic lanthanides like Dy.^[194]

Compound **3** crystallizes in the monoclinic space group $C2/c$ with half a molecule in the asymmetric unit (**Figure 3-7**). Since this compound is halfway from the starting material $[(\text{thf})_4\text{Li}_2(\text{NtBu})_4\text{S}]$ (**L¹-Li,Li**) to compound **2**, the different influence of the coordinated metals and the flexibility features of the SN_4 moiety is well displayed upon comparing all three compounds (**Table 3-1**). While the sum of all S–N bonds in the double lithiated $[(\text{thf})_4\text{Li}_2(\text{NtBu})_4\text{S}]$ is highest with 6.405(3) Å, it only slightly decreases to 6.381(2) Å in **3** and finally reaches 6.370(2) Å in **2**. However, these differences are particularly small and thus the overall S–N bond sum is almost unaffected by different metal coordination. This means that the rising electropositive charge by substitution of lithium with cobalt and the larger demand for electron density from the SN_4 ligand has almost no effect on the overall S–N bond sum. This characteristic is also illustrated by the S–N bond sum (6.354(1) Å) of the tetraimido sulfur acid $\text{H}_2\text{S}(\text{NtBu})_4$ (**13**), which will be discussed in chapter 3.4. The second feature is not only the flexibility of the S–N bond itself due to electrostatic interaction, but the position of the central sulfur within the SN_4 moiety and the direct influence of a larger positive charge density concentration at the ligand's coordination sphere through metal interaction.

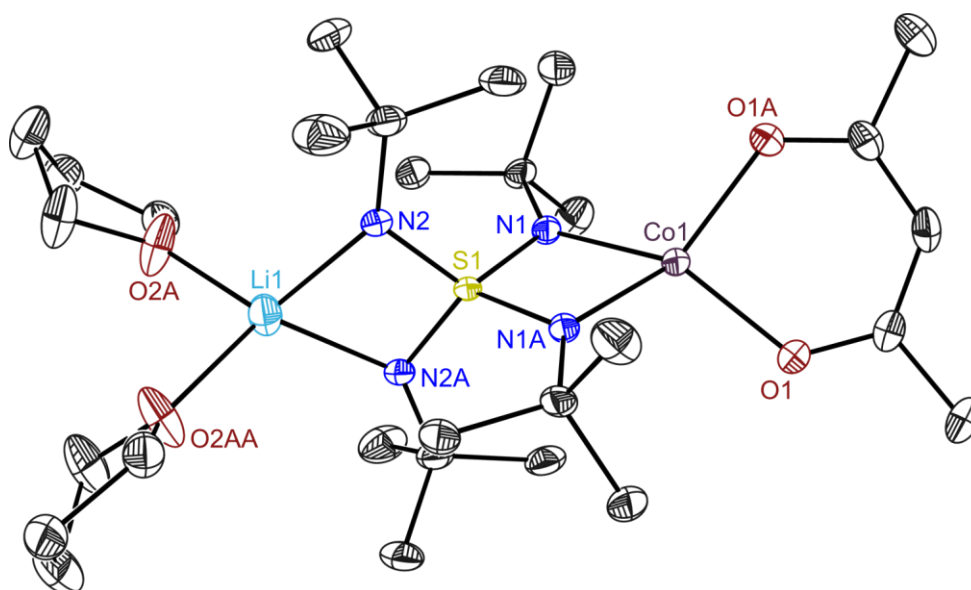


Figure 3-7 Crystal structure of **3**. Anisotropic displacement parameters are depicted at the 50% probability level. Hydrogen atoms and minor part of the disordered thf are omitted for clarity. Selected bond lengths [Å] and angles [°] with averaged thf: Co1–O1 1.9668(13), Co1–N1 1.9541(15), Li1–O2 1.997(3), Li1–N2 1.990(4), S1–N1 1.6231(15), S1–N2 1.5672(15), O1–Co1–O1A 92.02(8), N1–Co1–N1A 72.70(8), O2–Li1–O2A 92.8(2), N2–Li1–N2A 72.65(17), N1–S1–N1A 91.05(10), N2–S1–N2A 97.53(11).

Table 3-1 Selected bond lengths [Å] for **2**, **3** and **L¹-Li₂Li**. The Co–N, Co–O, Li–N and Li–O bonds are averaged values for **2** and **L¹-Li₂Li**.

compound	2	3	L¹-Li₂Li
S1–N1	1.5929(17)	1.6231(15)	1.608(3)
S1–N2	1.5921(17)	1.5672(15)	1.600(3) Å
S1–N3	1.5915(18)	–	1.600(3)
S1–N4	1.5940(17)	–	1.597(3)
Co–N	1.975	1.9541(15)	–
Co–O	1.944	1.9668(13)	–
Li–N	–	1.990(4)	1.957
Li–O	–	1.997(3)	2.025
S–N bond sum	6.370	6.381	6.405

In general, it can be stated that with a rising demand for electron density and with a larger withdrawal from the nitrogen atoms the S–N bond lengths increase within one compound.

However, this is only true for unsymmetrical compounds. The four S–N bonds in $[(\text{thf})_4\text{Li}_2(\text{NtBu})_4\text{S}]$ ($\text{L}^1\text{-Li,Li}$) are found between 1.597(3) Å and 1.608(3) Å and split to 1.6231(15) Å (Co site) and 1.5672(15) Å (Li site) in **3**. The larger positive charge concentration reduces the electron density at the nitrogen atom, which elongates the appropriate S–N bond due to lower electrostatic interaction. For compensation, the S–N bonds at the opposite side (Li side) with smaller positive charge concentration get shorter as a result of stronger SN interaction. In response to the electronic depletion and reduced interaction, the sulfur atom shifts towards the lithium, which reduces the appropriate S–N bond length. Even though a larger charge concentration was supposed to be found at the Li side (compared to Co), the Li–N bonds elongate to 1.990(4) Å from av. 1.957 Å in $\text{L}^1\text{-Li,Li}$. As a compensation, the Li–O bonds in average shorten by 0.028 Å. The second lithium substitution then results in averaged bond distances for S–N of 1.593 Å and Co–N of 1.975 Å. This shows that after the symmetric charge expansion at the outside of the SN_4 tetrahedron the sulfur shifts back towards equilibrium with an almost unchanged overall S–N bond length sum. Furthermore, it illustrates the flexibility and the electrostatic response of the SN moiety to charge changes in the coordination sphere of this ligand class.^[49]

Temperature-dependent dc magnetic susceptibility data were collected in the temperature range between 2 – 210 K and under an applied dc field of $H_{\text{dc}} = 0.5$ T (**Figure 3-8**). The observed high temperature $\chi_{\text{M}}T$ value of 5.1 $\text{cm}^3\text{mol}^{-1}\text{K}$ is considerably higher than the expected spin-only value (3.75 $\text{cm}^3\text{mol}^{-1}\text{K}$) for two non-interacting Co(II) ions with a spin of $S = 3/2$. This suggests a significant contribution of unquenched orbital angular momentum.^[90,107] The $\chi_{\text{M}}T$ value decreases right upon cooling with an increasing slope and tends to reach zero at low temperatures. At lower temperatures, $\chi_{\text{M}}T$ indeed decreases more slowly, finally reaching 0.31 $\text{cm}^3\text{mol}^{-1}\text{K}$ at 5 K. This behavior is an indication for antiferromagnetic coupling as found for other compounds.^[220] The best fit of the $\chi_{\text{M}}T$ vs. T data over the whole temperature range, based on the spin Hamiltonian $H = -2J S_1 S_2$ gives the coupling constant $J = -6.1 \text{ cm}^{-1}$ with $g = 2.59$ and a zero-field splitting parameter $D = -56.9 \text{ cm}^{-1}$. Like in the manganese complex **1**, both cobalt atoms in **2** are antiferromagnetically coupled. Also similar to **1**, a remarkable acute N–Co–N bite angle (71.93(6)°) is found in **2**, which results in a strongly distorted tetrahedral geometry. To probe the magnetic relaxation dynamics, out-of-phase (χ_{M}'') temperature-dependent ac magnetic susceptibility data were collected at 1488 Hz while ranging the temperature from 2 – 22 K under zero and under $H_{\text{dc}} = 1000$ Oe applied dc fields (**Figure 3-8**). However, the characteristic peak maximum for slow magnetic relaxation in the out-of-phase signal (χ_{M}'') is not observed and compound **2** does not show any single-molecule magnet behavior, neither without nor under an applied external

dc field. Nevertheless, the magnetic analysis of **2** revealed antiferromagnetic exchange coupling, which was already found for the manganese complex **1**.

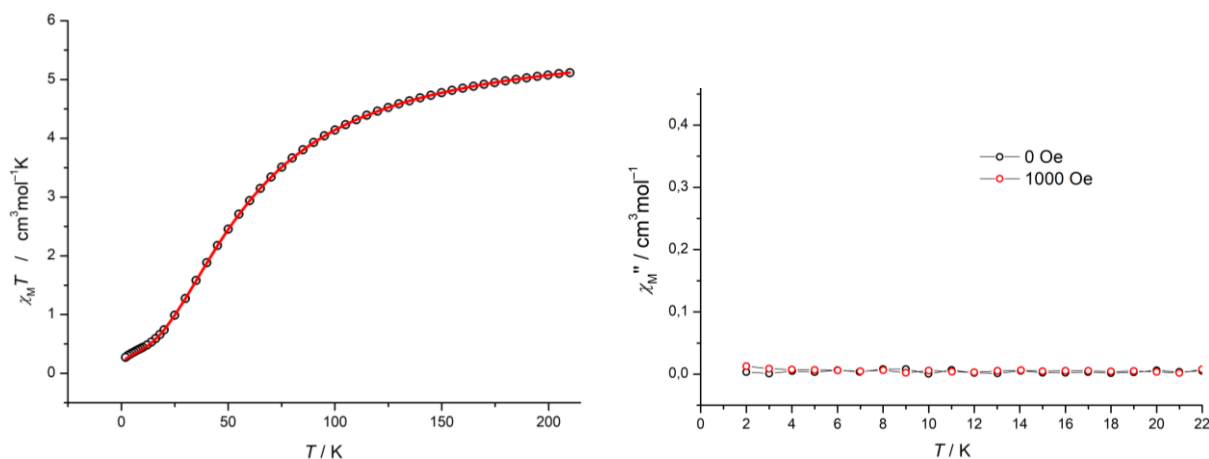


Figure 3-8 (left): Temperature-dependent dc magnetic susceptibility measurement $\chi_M T$ vs. T for **2** at 0.5 T with the obtained fitting parameters $g = 2.59$, $D = -56.9 \text{ cm}^{-1}$, $J = -6.1 \text{ cm}^{-1}$, $\text{TIP} = 244 \cdot 10^{-6} \text{ cm}^3 \text{ mol}^{-1}$. (right): Temperature-dependent out-of-phase (χ_M'') ac susceptibility measurement for **2** under zero applied dc field (black) and an applied dc field of $H_{dc} = 1000 \text{ Oe}$ (red).

3.2.1.3. Conclusion on exchange coupling in binuclear complexes of the tetraimido sulfate $[\text{S}(\text{NtBu})_4]^{2-}$

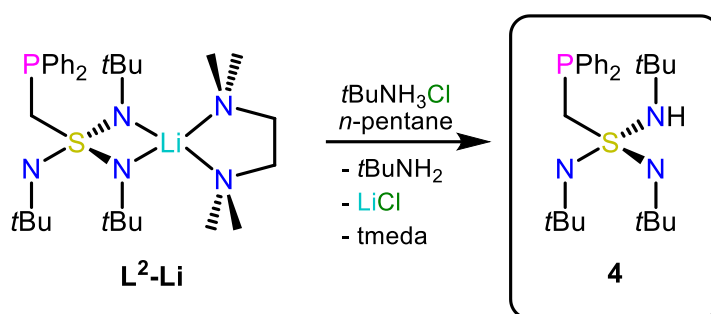
The focus of the last chapter was on the synthesis of new compounds containing the tetraimido sulfate ligand $[\text{S}(\text{NtBu})_4]^{2-}$ (**L**¹) to evaluate whether this ligand offers the opportunity to support communication between paramagnetic centers. Two new bimetallic compounds, the asymmetric $[\text{Cl}_2\text{Mn}(\text{NtBu})_2\text{S}(\text{tBuN})_2\text{Mn}\{\text{ClLi}(\text{thf})_3\}_2]$ (**1**) and the symmetric $[(\text{acac})\text{Co}(\text{NtBu})_2\text{S}(\text{tBuN})_2\text{Co}(\text{acac})]$ (**2**) were synthesized. Indeed, both compounds display an antiferromagnetic coupling of $J = -1.0$ and -6.1 cm^{-1} , respectively, which proves the $[\text{S}(\text{NtBu})_4]^{2-}$ (**L**¹) ligand to be a promising candidate to enhance magnetic communication between metal centers. The next step comprises further ligand tuning to afford ferromagnetic coupling. This could be achieved by the use of radical SN ligands^[33,64,110] in order to induce a direct exchange, a promising strategy to further develop the coupling abilities of SN compounds. Furthermore, with the crystallization of $[(\text{acac})\text{Co}(\text{NtBu})_2\text{S}(\text{tBuN})_2\text{Li}(\text{thf})_2]$ (**3**), it has been proven that a single lithium cobalt exchange in $[(\text{thf})_4\text{Li}_2(\text{NtBu})_4\text{S}]$ (**L**¹-**Li**,**Li**) is feasible. This suggests that $[\text{S}(\text{NtBu})_4]^{2-}$ (**L**¹) can be a building block for heteronuclear metal complexes with heavy main-group elements or lanthanides.

3.2.2. Synthesis and deprotonation of $[\text{Ph}_2\text{PCH}_2\text{S}(\text{NtBu})_2\text{NHtBu}]$ (**4**) for the isolation of the potassium compound $[\text{K}(\text{thf})_3\{\text{Ph}_2\text{PCH}_2\text{S}(\text{NtBu})_3\}]$ (**5**)

3.2.2.1. Synthesis of $[\text{Ph}_2\text{PCH}_2\text{S}(\text{NtBu})_2\text{NHtBu}]$ (**4**)

The second system of the S(VI) polyimido sulfur ligand family used in this thesis is the sulfonate-like $[\{\text{Ph}_2\text{PCH}_2\text{S}(\text{NtBu})_3\}]^-$ (**L²**). It is formed as the lithium salt $[(\text{tmeda})\text{Li}\{\text{Ph}_2\text{PCH}_2\text{S}(\text{NtBu})_3\}]$ (**L²-Li**) from a reaction of $\text{S}(\text{NtBu})_3$ and $[(\text{tmeda})\text{LiCH}_2\text{PPh}_2]$ in a solvent mixture of *n*-pentane and thf.^[68] Since lithium halide co-complexation is synthetically challenging to prevent in metal exchange reactions, premature elimination of this potential problem was achieved with the exchange of lithium for a non-metallic proton. Therefore, the protonated species $[\text{Ph}_2\text{PCH}_2\text{S}(\text{NtBu})_2\text{NHtBu}]$ (**4**) was synthesized to use this metal free compound in a subsequent deprotonation reaction with different hexamethyldisilazane (HMDS) complexes (see chapters 3.2.2.2 and 3.2.3.2). It should be noted that the protonation reaction and some analysis data of **4** has already been published in doctoral thesis of Elena Carl.^[223] Nevertheless, new results have just been published recently with an optimized synthesis along with new analytical data.^[4]

To obtain the lithium-free and protonated compound $[\text{Ph}_2\text{PCH}_2\text{S}(\text{NtBu})_2\text{NHtBu}]$ (**4**), 1 equiv. of **L²-Li** and 1 equiv. of *t*BuNH₃Cl were suspended in *n*-pentane and stirred at room temperature for 1 d (**Scheme 3-3**).



Scheme 3-3 Synthesis of the protonated imido species $[\text{Ph}_2\text{PCH}_2\text{S}(\text{NtBu})_2\text{NHtBu}]$ (**4**). A suspension of **L²-Li** and 1 equiv. of *tert*-butylamine in *n*-pentane enables proper LiCl abstraction and the isolation of pure **4** in 87% yield.

Since **4** is perfectly soluble in *n*-pentane, LiCl can directly be filtered off from the reaction mixture. The solvent was reduced in volume under reduced pressure and the residue was stored for crystallization that started within hours at -34°C . The solvent was removed and pure **4** was isolated as colorless crystals in 87% yield.

Compound **4** crystallizes from pure *n*-pentane directly from the reaction mixture, but the crystal selected and grown for the single crystal X-ray diffraction analysis presented in here, derived from a solvent mixture of *n*-pentane and thf. **4** is found in the monoclinic space group $P2_1/n$ with one molecule of the compound and half a molecule of thf in the asymmetric unit (**Figure 3-9**).

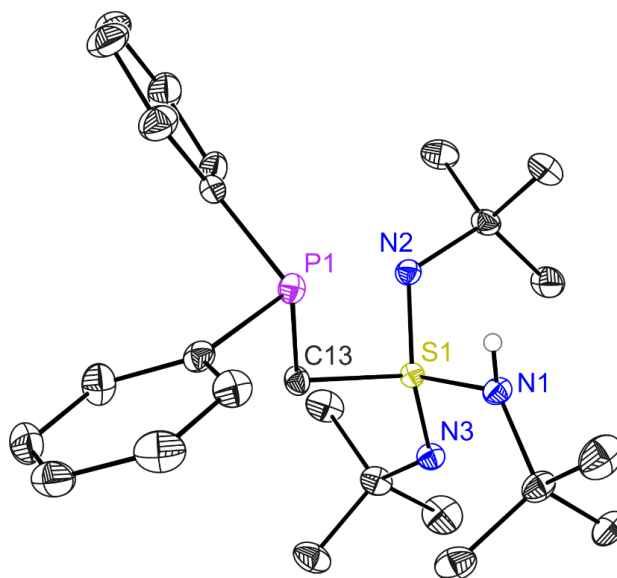


Figure 3-9 Crystal structure of **4**. Anisotropic displacement parameters are depicted at the 50% probability level. Hydrogen atoms and thf molecule are omitted for clarity. Selected bond lengths [Å] and angles [°]: S1–N1 1.6498(13), S1–N2 1.5210(13), S1–N3 1.5144(13), S1–C13 1.8167 (15), N1–S1–N2 108.88(7), N1–S1–N3 101.33(7), N2–S1–N3 127.84(7), N1–S1–C13 105.27(7), N2–S1–C13 97.37(7), N3–S1–C13 114.56(7), S1–C13–P1 110.05(8).

The two chemically identical imido bonds S1–N2/N3 have almost the same length of 1.5210(13) Å and 1.5144(13) Å, respectively, while the amido S1–N1 bond is significantly longer with 1.6498(13) Å. This difference might be taken as an indication for one longer single amido (S–NH) bond and two shorter imido (S–N) double bonds. However, both types are strongly polarized $S^{\delta+}$ – $N^{\delta-}$ single bonds with higher electrostatic contribution in the imido than in the amido bond.^[50,51] This was also confirmed by the isolation and characterization of $H_2S(NtBu)_4$ (**13**), the valence isoelectronic imido analogue of sulfuric acid.^[1] This molecule is also part of the thesis and the difference of amido and imido bonds will be discussed more precisely in chapter 3.4.

Even though higher-resolution data would be required for a detailed examination, the crystal structure does not show any N(H)/N hydrogen atom disorder. Those results can further be supported by the NMR-spectroscopic analysis of **4**. The influence on the chemical shifts as a consequence of protonation is observable in the 1H -NMR spectrum (**Figure 3-10**). It shows two large singlets at $\delta = 1.29$ ppm

(NH*t*Bu) and 1.47 ppm (N*t*Bu), that match with the different *tert*-butyl groups. The NH proton signal at $\delta = 4.05$ ppm splits into a doublet due to 4J P-H coupling (5 Hz), while the singlet of the two methylene protons resonates at $\delta = 3.86$ ppm. The remaining phenyl signals can be found in the normal range for aromatic protons accompanied by the ortho (7.61 – 7.65 ppm), meta (7.09 – 7.12 ppm) and para (7.03 – 7.07 ppm) splitting. The ^{31}P signal is set at -16.98 ppm and the $^{15}\text{N}/^1\text{H}$ -NMR correlation analyses support the idea that a proton exchange is not observable. This induces two different S–N bonds with signals at -249.4 ppm (NC(CH₃)₃) and -269.4 ppm (HNC(CH₃)₃) (see chapter 6, **Figure 6-9** and **Figure 6-10**).

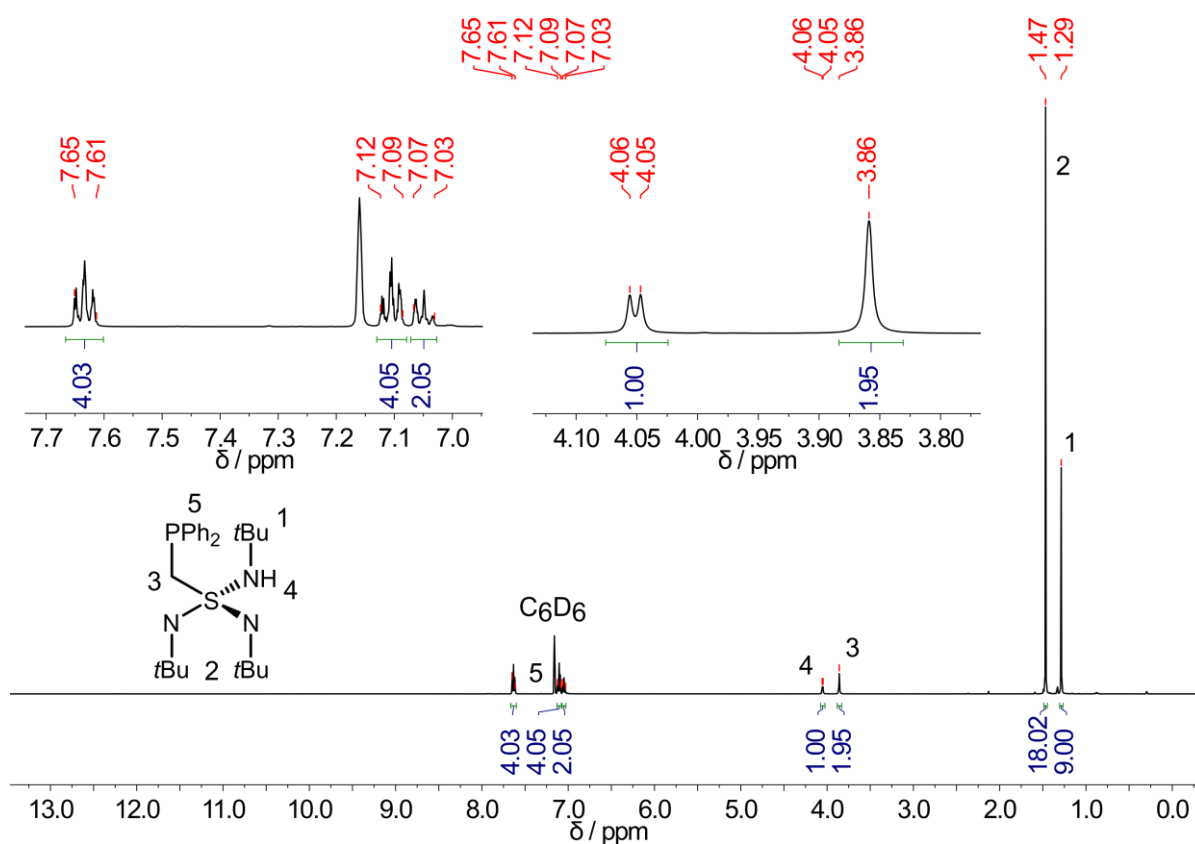


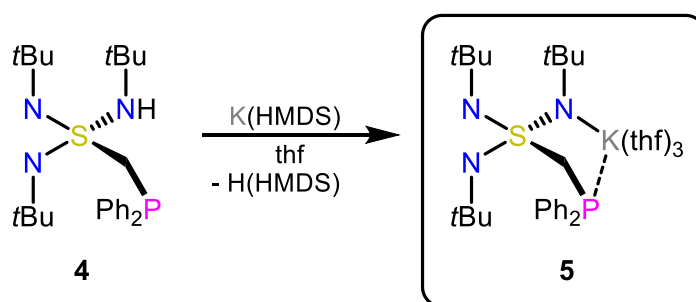
Figure 3-10 ^1H -NMR spectrum of **4** at 298 K in C_6D_6 . δ [ppm] = 1.29 (s, 9H, HNC(CH₃)₃), 1.47 (s, 18H, 2 NC(CH₃)₃), 3.86 (s, 2H, PCH₂), 4.05 (d, $^4J_{\text{HP}} = 5$ Hz, HN(CH₃)₃), 7.03–7.07 (m, 2H, *p*-Ph-H), 7.09–7.12 (m, 4H, *m*-Ph-H), 7.61–7.65 (m, 4H, *o*-Ph-H).

3.2.2.2. Synthesis of $[K(thf)_3\{Ph_2PCH_2S(NtBu)_3\}]$ (**5**)

In chapter 3.2.2.1 it was described that the overall target behind the synthesis of the protonated sulfonate-like compound **4** was the subsequent deprotonation with different metal hexamethyldisilazide $M^x\{N(SiMe_3)_2\}_x$ reagents to form novel complexes of ligand **L**². Because they are strong, non-nucleophilic bases that are highly soluble in organic solvents, they are ideal candidates to achieve that goal.^[224–236] In this context, the potassium complex $[K(thf)_3\{Ph_2PCH_2S(NtBu)_3\}]$ (**5**) was not only synthesized for the proof of concept, but will be useful for exchange reaction under the exclusion of potential lithium-halide contamination by co-complexation.

Even though previous efforts indicated the proton not to be acidic enough to be removed by HMDS compounds^[223], the potential benefit of employing this chemistry was reason enough to reassume this synthetic path. During the work with the utilized ligands, it always turned out that synthetic nuances can considerably trigger a successful synthesis. This means that sometimes only a narrow window makes the difference between success and failure. Still, due to the unique properties of these ligands, it is desirable to overcome those difficulties. However, deprotonation of **4** has not been successful, until now.

For the synthesis of **5**, a solution of $K\{N(SiMe_3)_2\}$ in thf was added to $[Ph_2PCH_2S(NtBu)_2NHtBu]$ (**4**) dissolved in thf and stirred at room temperature for 1 d (**Scheme 3-4**). The reaction solvent was removed under reduced pressure and the residue redissolved in a 5:1 mixture of thf and *n*-pentane, which was a suitable mixture to crystallize $[K(thf)_3\{Ph_2PCH_2S(NtBu)_3\}]$ (**5**) after filtration. Crystallization started within minutes upon storage at $-34\text{ }^\circ\text{C}$, yielding colorless crystals suitable for single crystal X-ray diffraction analysis in 88% yield.



Scheme 3-4 Synthesis of the potassium complex $[K(thf)_3\{Ph_2PCH_2S(NtBu)_3\}]$ (**5**). A deprotonation reaction of **4** with 1 equiv. $K\{N(SiMe_3)_2\}$ in thf at room temperature resulted in the isolation of crystalline **5** in 88% yield.

It turned out that $[\text{K}(\text{thf})_3\{\text{Ph}_2\text{PCH}_2\text{S}(\text{NtBu})_3\}]$ (**5**) loses the coordinating thf molecules over time when stored at room temperature over time and that all thf molecules can be removed under reduced pressure (see chapter 5.3.4). Nevertheless, the crystalline material is coordinated by three thf molecules. **5** crystallizes in the monoclinic space group $P2_1/n$ with one molecule in the asymmetric unit (**Figure 3-11**).

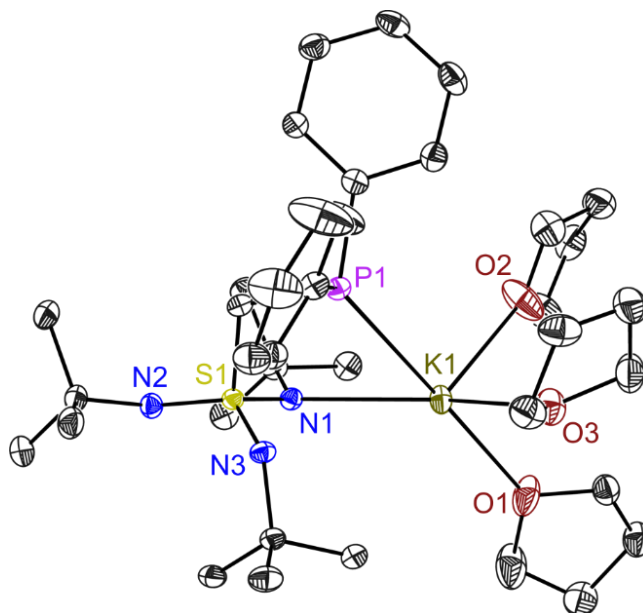


Figure 3-11 Crystal structure of **5**. Anisotropic displacement parameters are depicted at the 50% probability level. Hydrogen atoms, disorder at thf1/2 (O2/3) and 3 are omitted for clarity. Disordered thf1 with three different oxygen positions are omitted as well. Selected bond lengths [Å] and angles [°]: K1–N1 2.7434(14), K1–P1 3.3301(7), K1–O1A 2.703(14), K1–O1B 2.881(17), K1–O2 2.7511(14), K1–O3 2.6844(14), S1–N1 1.5685(14), S1–N2 1.5461(14), S1–N3 1.5588(14), S1–C13 1.8314(16), N1–S1–N2 109.56(7), N1–S1–N3 110.32(7), N2–S1–N3 122.66(7), N1–S1–C13 108.68(7), N2–S1–C13 108.07(7), N3–S1–C13 96.13(7), N1–K1–P1 69.44(3), O2–K1–O3 92.61(5), N1–K1–O2 114.02(5), N1–K1–O3 145.79(4), P1–K1–O2 104.77(4), P1–K1–O3 83.73(3), N1–S1–C13 108.68(7), N2–S1–C13 108.07(7), N3–S1–C13 96.13(7).

The potassium ion is fivefold coordinated by one nitrogen and one phosphorus atom, both from the imidosulfonate ligand **L**² and additionally three thf solvent molecules. In contrast to other structure motifs of **L**², it does not function as an *N,N'* chelating ligand, which was the case for the lithium species **L**²-Li and is also true for the transition metal complexes **8** and **9** and for the lanthanide compounds **12a-e**. According to PEARSON'S HSAB concept^[82–84], the large potassium is probably more attracted by the softer phosphorus than by the harder nitrogen atom.

The S1–N bond distances for **5** are similar with an average value of 1.558 Å, but due to potassium coordination, the S1–N1 bond (1.5685(14) Å) is slightly elongated. For comparison, the protonated S–NH bond in the starting material **4** is considerably longer with 1.6498(13) Å. This clearly shows that metal coordination has a smaller impact on the S–N bond properties and lengths than the direct bonding to a hydrogen atom. The K1–P1 bond distance is with 3.3301(7) Å in the normal range for a

potassium phosphorus bond. For comparison, the P...Li distance in [(tmeda)Li{Ph₂PCH₂S(NtBu)₃}] (**L²-Li**)^[68] is with 3.718 Å too long to be considered a bond, while the K1–N1 bond distance falls with 2.7434(14) Å in the normal range for a fivefold coordinated potassium ion.

The lithium ion in **L²-Li** is *N,N'*-chelated by the ligand, while it seems to be more favorable for the potassium in **5** to be coordinated by the softer phosphorus atom. The coordination sphere of the potassium is saturated by three thf solvent molecules. The oxygen atom O1 has been refined on three positions with an averaged value of 2.744 Å for the K1–O1 bond. The oxygen atoms of the remaining thf molecules do not display any disorder and the appropriate bond distances were found with values of 2.648(5) Å (K1–O1) and 2.7511(14) Å (K1–O2). A closer look at the angles between the donor atoms around the potassium reveals a strong distortion for a trigonal bipyramidal as well as for a square pyramidal geometry. All O–K1–N1 angles deviate significantly from the ideal geometries with values of 92.61(5)° (O2–K1–O3), 114.02(5)° (O2–K1–N1) and 145.79(4)° (O3–K1–N1). The same deviation is found for the angles including the phosphorus donor with 69.44(3)° (P1–K1–N1), 104.77(4)° (P1–K1–O2) and 83.73(3)° (P1–K1–O3). Since the three S–N bond distances are similar, it could be anticipated that the different N–S1–C13 angles would follow this trend. The N1–S1–C13 (108.68(7)°) and N2–S1–C13 (108.07(7)°) angles are marginally different. In comparison the N3–S1–C13 angle (96.13(7)°) is around 12° narrow. This can be explained as a result of the phosphorus potassium interaction accompanied by a phosphorus shift towards the metal. The phosphorus acts like a scorpionate's sting^[70,237] and thereby bends over to N3. Nevertheless, this interaction has only a small influence on the S1–C13 bond distance of 1.8314(16) Å, when compared to the protonated compound [Ph₂PCH₂S(NtBu)₂NHtBu] (**4**) (1.8167(15) Å) and the lithium species [(tmeda)Li{Ph₂PCH₂S(NtBu)₃}] (**L²-Li**) (1.8181(12) Å). The S1–C13–P1 angles in **4** (110.05(8)°), **5** (113,17(8)°) and in **L²-Li** (111.75(6)°) are similar and the three N–S1–C13 angles for the considered structures span a range from 95.90° to 114.56(7)°. Therefore, one can deduce that the ligand flexibility and the capability of P–donation arises rather from the SN orientation than from a significant flexibility in the S–C–P angle.

To gain further analytical information, NMR investigations were performed. The ¹H-NMR spectra of **5** is shown in **Figure 3-12**. Since virtually all thf molecules can be removed under reduced pressure, no thf solvent molecule is observable in the spectrum. Nevertheless, thf free **5** [K{Ph₂PCH₂S(NtBu)₃}] is actually entirely insoluble in pure C₆D₆ or other unpolar solvents like toluene. In order to show that the thf molecule are no longer incorporated into the structure, NMR measurements cannot be performed in pure thf-*d*₈. To solve this problem, only a few drops of deuterated thf were added to form the soluble thf complex of **5**.

All three -NtBu groups are equal in solution with a chemical shift of $\delta = 1.65$ ppm. The two methylene protons of the phosphorus side arm resonate at $\delta = 3.94$ ppm as doublet that is generated by a $^2J_{\text{HP}}$ coupling of 5.0 Hz. The phenyl signals can be found in the normal range for aromatic protons and are splitted into the ortho (7.07 – 7.09 ppm), meta (7.15 – 7.18 ppm) and para (7.84 – 7.87 ppm) multiplets.

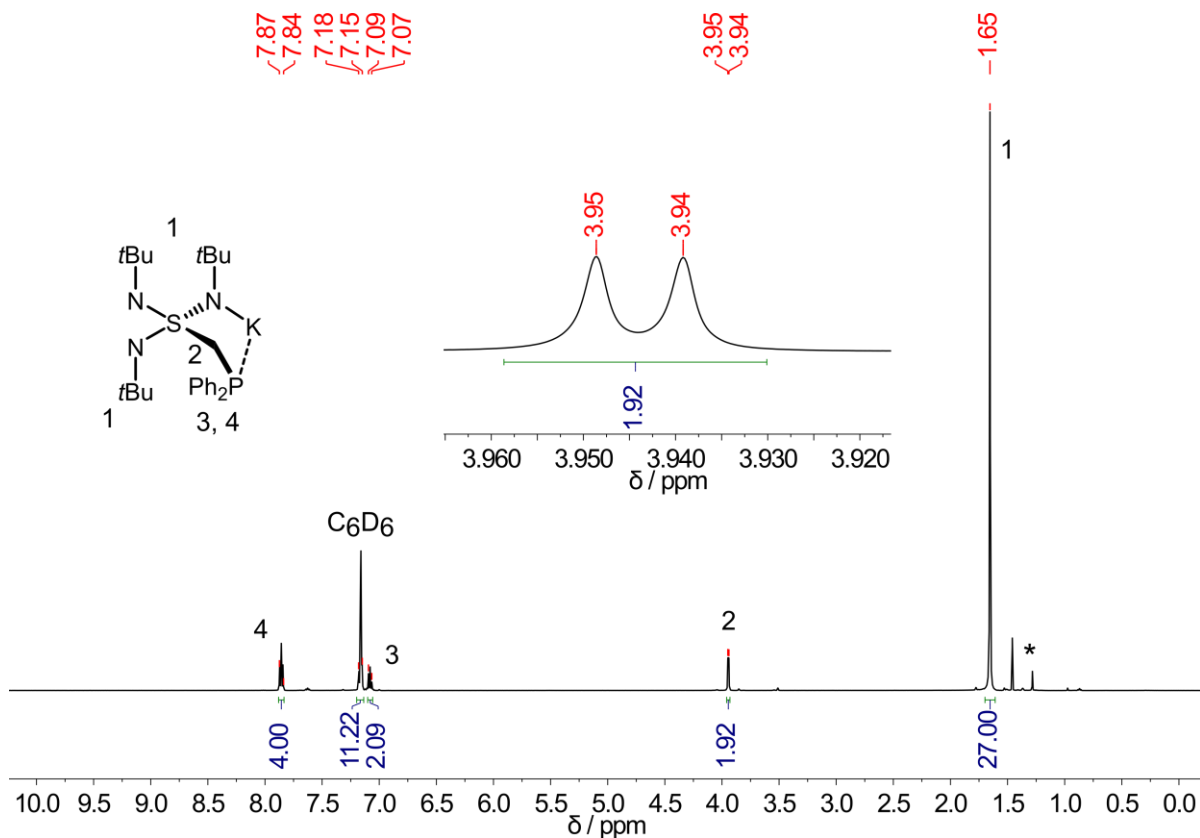


Figure 3-12 ^1H -NMR spectrum of **5** at 298 K in C_6D_6 . δ [ppm] = 1.65 (s, 27H, 3 $\text{NC}(\text{CH}_3)_3$), 3.94 (d, $^2J_{\text{HP}} = 5.0$ Hz, 2H, PCH_2), 7.07 – 7.09 (m, 2H, 2 *p*-Ph-H), 7.15 – 7.18 (m, 4H, 2 *m*-Ph-H), 7.84 – 7.87 (s, 2H, *o*-Ph-H). (*): Refers to signals of **4**, due to the decomposition of **5**.

A comparison of the protonated compound **4** (turquoise) and the deprotonated potassium complex **5** (red) is depicted in **Figure 3-13** (top). The small amount of **4** present in the sample of **5** is due to its high reactivity towards small traces of H_2O and the reprotonation to form **4** again. However, the signal splitting into one smaller HNtBu singlet (1.29 ppm) and one larger NtBu singlet (1.47 ppm) for **4** relative to only one signal for **5** is illustrated. The disappearance of the NH proton signal, which is a doublet in **4** with a chemical shift of $\delta = 4.05$ ppm ($^4J_{\text{HP}} = 5$ Hz) is, upon deprotonation, observable for the potassium compound **5**. The superimposed ^{31}P -NMR spectrum (**Figure 3-13**, bottom) displays a signal shift from -16.98 ppm (**4**) to -18.14 ppm (**5**), which further confirms the formation of **5** by NMR analyses. For more analytical details see chapter 5.3.4 and chapter 6, **Figure 6-11** to **Figure 6-18**.

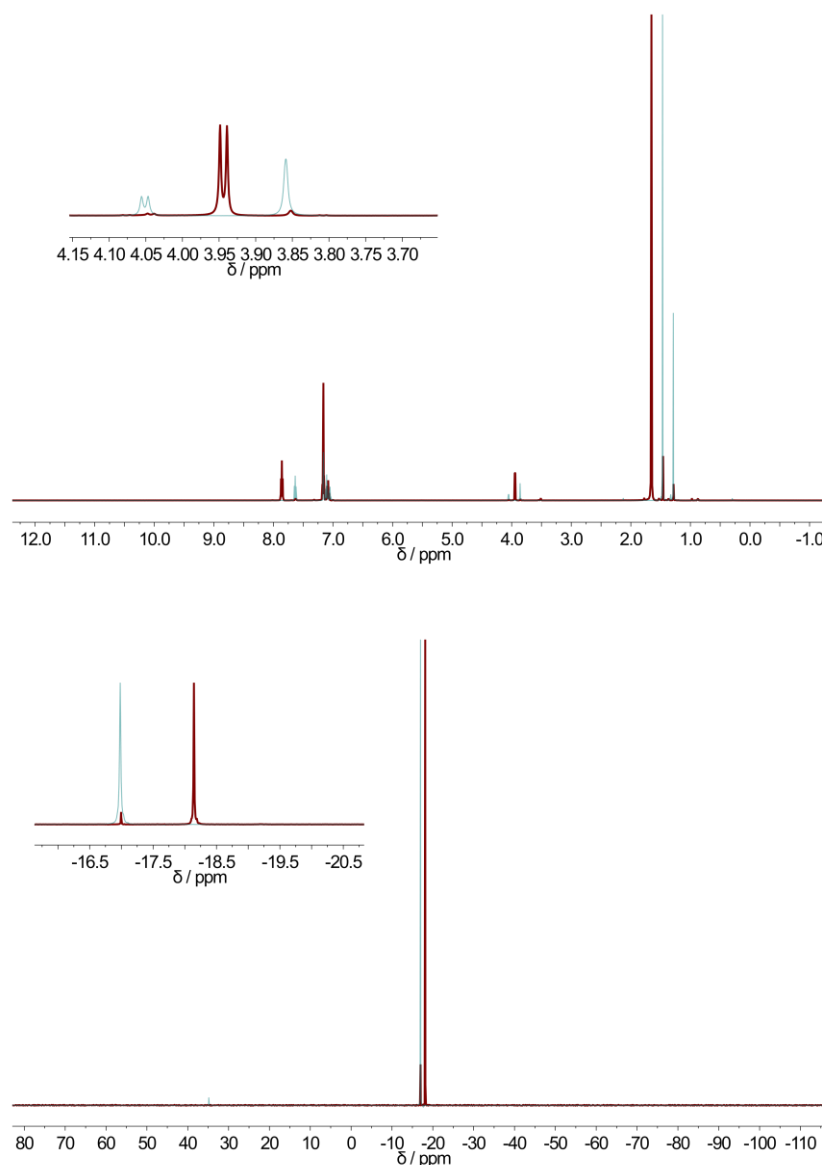


Figure 3-13 (top): Superimposed ^1H -NMR spectra of **4** (turquoise) and **5** (red) at 298 K in C_6D_6 . (bottom): Superimposed ^{31}P -NMR spectra of **4** (turquoise) and **5** (red) at 298 K in C_6D_6 .

3.2.2.3. Conclusion on the synthesis and deprotonation of $[\text{Ph}_2\text{PCH}_2\text{S}(\text{NtBu})_2\text{NHtBu}]$ (**4**) for the isolation of the potassium compound $[\text{K}(\text{thf})_3\{\text{Ph}_2\text{PCH}_2\text{S}(\text{NtBu})_3\}]$ (**5**)

In the last chapter, the protonated $[\text{Ph}_2\text{PCH}_2\text{S}(\text{NtBu})_2\text{NHtBu}]$ (**4**) was synthesized and characterized. Furthermore, it was possible for the first time, to subsequently deprotonate **4** under the utilization of $\text{K}\{\text{N}(\text{SiMe}_3)_2\}$, forming the potassium compound $[\text{K}(\text{thf})_3\{\text{Ph}_2\text{PCH}_2\text{S}(\text{NtBu})_3\}]$ (**5**). Lithium halide co-complexation in a transmetallation reaction with lanthanides is challenging to prevent. To exclude this potential contamination, **5** was synthesized with the ultimate goal to utilize this compound in subsequent reactions, since potassium halide co-complexation is less probable.

3.2.3. Trigonal planar Fe(II) and Co(II) complexes of the tetraimido sulfate $[S(NtBu)_4]^{2-}$ and the triimido sulfonate $[\{Ph_2PCH_2S(NtBu)_3\}]^-$

Another strategy for new sulfur imido ligands $RS(NtBu)_3^{n-}$ ($R = -NtBu, -CH_2PPh_2$; $n = 2, 1$) based SMMs comprises the synthesis of trigonal planar complexes with Fe(II) and Co(II) centers. In order to achieve this goal, two different synthetic strategies utilizing the appropriate hexamethyldisilazane $M\{N(SiMe_3)_2\}_2$ compounds were followed. One is based on a metal exchange reaction with the lithiated tetraimido sulfate anion $[S(NtBu)_4]^{2-}$ (**L¹**), while the other one exploits the strong basicity of $M\{N(SiMe_3)_2\}_2$ compounds and follows the route to deprotonate $[Ph_2PCH_2S(NtBu)_2NHtBu]$ (**4**) that was already presented for the potassium complex $[K(thf)_3\{Ph_2PCH_2S(NtBu)_3\}]$ (**5**) (see chapter 3.2.2.2).

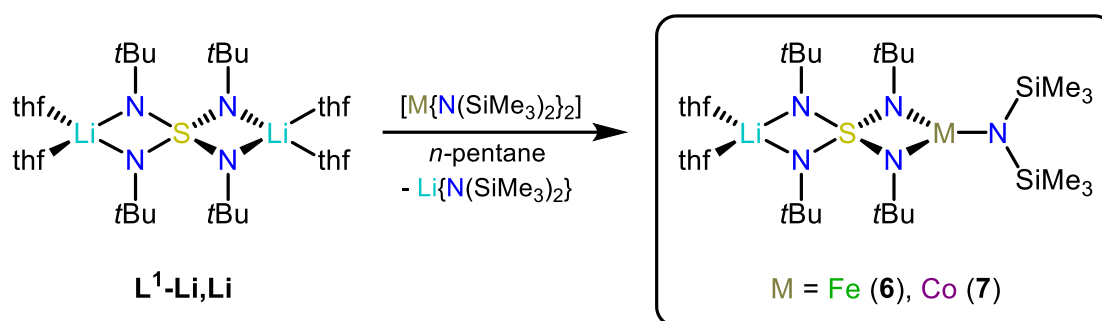
In recent years, many remarkable 3d-block element SMMs with high anisotropies were synthesized.^[137–140] Among them, trigonal planar Fe(II)^[92,93,182] and Co(II)^[93,183,184] complexes are rare in literature and not sufficiently explored in the field of single ion magnets.^[140] However, due to the low coordination number, trigonal planar complexes are promising in terms of SMM design. The acute N–S–N bite angle in **L¹** and **L²** offers the opportunity to synthesize pseudo-linear, heteroleptic complexes in a trigonal planar coordinated fashion, which will be presented in the following chapters.

3.2.3.1. Synthesis of the trigonal planar compounds $[(thf)_2Li\{(NtBu)_4S\}M\{N(SiMe_3)_2\}_2]$ with $M = Fe$ (**6**) and Co (**7**)

In this part, the synthesis containing the tetraimido sulfate anion $[S(NtBu)_4]^{2-}$ (**L¹**) will be discussed. For the targeted metal exchange reaction, the appropriate $M\{N(SiMe_3)_2\}_2$ complexes had to be synthesized. The iron compound was obtained according to a literature procedure from HOLLAND and coworkers.^[236] Anhydrous $FeCl_2$ was suspended in Et_2O , cooled to $0^\circ C$ and subsequently a solution of $Li\{N(SiMe_3)_2\}$ in Et_2O was slowly added. The reaction mixture was warmed to room temperature and stirred for 1 d. All volatiles were removed under reduced pressure and the residue was extracted with *n*-pentane. The raw product was purified via distillation to afford a green oil that solidified upon storage at $-34^\circ C$. The cobalt compound was synthesized according to the literature procedure from POWER *et al.*^[235] Similar to the synthesis of the iron compound, anhydrous $CoCl_2$ was suspended in Et_2O and cooled to $0^\circ C$. Subsequently, a solution of $Li\{N(SiMe_3)_2\}$ in Et_2O was slowly added. The reaction mixture was warmed to room temperature and stirred for 1 d. After the solvent was removed under reduced pressure, the residue was extracted with *n*-hexane. For purification, the raw product was

sublimated to form a brown solid. In order to receive a higher purity, the compound was recrystallized from *n*-pentane at -34°C .

For the general synthesis of the trigonal planar iron and cobalt compounds $[(\text{thf})_2\text{Li}\{(\text{NtBu})_4\text{S}\}\text{M}\{\text{N}(\text{SiMe}_3)_2\}]$, with $\text{M} = \text{Fe}$ (**6**) and Co (**7**), the lithiated precursor $[(\text{thf})_4\text{Li}_2(\text{NtBu})_4\text{S}]$ (**L¹-Li,Li**) was dissolved with one equiv. of the appropriate transition metal compound $\text{M}\{\text{N}(\text{SiMe}_3)_2\}_2$ in *n*-pentane and stirred for 1 d. After concentration of the reaction solvent under reduced pressure, the mixture was stored at -34°C . Crystallization started within minutes and yielded yellow (iron) and purple (cobalt) crystals that were suitable for single crystal X-ray diffraction analysis (**Scheme 3-5**).



Scheme 3-5 Synthesis of the $[\text{S}(\text{NtBu})_4]^{2-}$ (**L¹**) ligand based metal complexes $[(\text{thf})_2\text{Li}\{(\text{NtBu})_4\text{S}\}\text{M}\{\text{N}(\text{SiMe}_3)_2\}]$ with $\text{M} = \text{Fe}$ (**6**), Co (**7**). They are synthetically accessible through a metal exchange reaction of the lithiated precursor $[(\text{thf})_4\text{Li}_2(\text{NtBu})_4\text{S}]$ (**L¹-Li,Li**) with one equiv. of the appropriate $\text{M}\{\text{N}(\text{SiMe}_3)_2\}_2$ in *n*-pentane. Crystals were isolated in 79% (**6**) and 78% (**7**) yields.

The two isomorphous complexes **6** (iron) and **7** (cobalt) were, after recrystallization, isolated in 79% and 78% yields, respectively. They crystallize in the monoclinic space group $C2/c$ with half a molecule in the asymmetric unit (**Figure 3-14**).

Like in the starting material **L¹-Li,Li**, the unsubstituted lithium ion remains tetrahedrally coordinated by two thf molecules and *N,N'* chelated by the imido ligand $[\text{S}(\text{NtBu})_4]^{2-}$. The larger positive charge concentration at the ligand's opposite coordination side, which is a result of the metal exchange by lithium for transition metal(II) ions, only marginally influences the lithium bonding. The averaged Li–N (1.957 Å) bonds in **L¹-Li,Li** only have a minor decrease to 1.986(3) Å for **6** and 1.990(4) Å for **7**. Larger structural deviations can be found for the ligand itself where the N–S–N angle at the lithium side in **L¹-Li,Li** is with 94.70° significantly wider than with $97.54(10)^\circ$ in **6** and $97.49(12)^\circ$ in **7** (**Table 3-2**). In contrast, the averaged angles between the two edges of the ligand's tetrahedron are almost identical with 117.08° (**L¹-Li,Li**), 117.53° (**6**) and 117.91° (**7**).

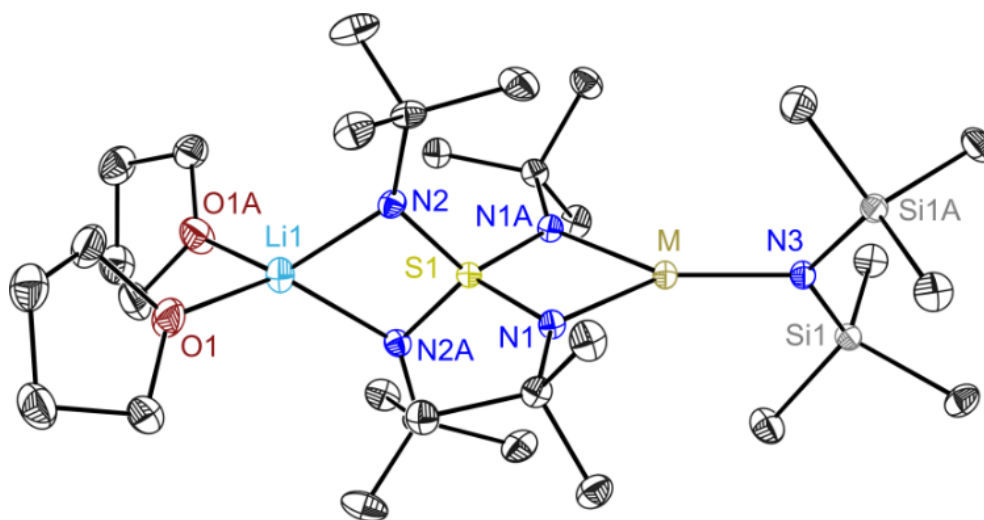


Figure 3-14 Crystal structure of **6** and **7**. Anisotropic displacement parameters are depicted at the 50% probability level for the iron complex. Hydrogen atoms are omitted for clarity. Selected bond lengths [Å] and angles [°] for **6**: Fe1–N1 1.9690(13), Fe1–N3 1.9196(18), S1–N1 1.6336(13), S1–N2 1.5648(12), Li1–N2 1.986(3), N1–S1–N1A 90.97(9), N2–S1–N2A 97.54(10), N1–S1–N2 117.79(6), N1–S1–N2A 117.26(6), N1–Fe1–N1A 72.54(7), N1–Fe1–N3 143.73(4); for **7**: Co1–N1 1.9275(16), Co1–N3 1.901(2), S1–N1 1.6356(16), S1–N2 1.5632(16), Li1–N2 1.990(4), N1–S1–N1A 89.57(11), N2–S1–N2A 97.49(12), N1–S1–N2 118.09(8), N1–S1–N2A 117.72(8), N1–Co1–N1A 73.42(9), N1–Co1–N3 143.29(5).

Another response of the imido ligand to the unsymmetrical coordination is the adaptation of the S–N bonds to the influence of different positive charge concentration at the two coordination sides of the ligand. The sum for all S–N bond distances (6.405 Å in **L¹-Li,Li**) is almost unaffected by a metal exchange with values of 6.397 Å (**6**) and 6.398 Å (**7**). However, the different S–N bonds do not display the same behavior. While they range between 1.596(3) Å and 1.608(3) Å in the symmetric bi-lithium complex **L¹-Li,Li**, a splitting to 1.6356(13) Å and 1.5632(13) Å in **6** and 1.6356(16) Å and 1.5632(13) Å in **7** is observable, with the larger value for the transition metal coordinated side of the ligand. The phenomenon of electrostatic response as a consequence of metal interaction was already discussed for the cobalt complexes **2** and **3** and will be part of the discussion for other metal complexes of the tetraimido sulfate [S(NtBu)₄]²⁻, that will be presented later in the thesis. The higher charges of the d-element ions pull the imido substituents away from the electropositive sulfur atom. For compensation, the ligand reduces the S–N(Li) bond lengths and the total S–N bond sum remains almost unchanged.

Small deviations without a clear trend in structural changes upon d-block metal exchange can be found when **6** and **7** are compared to the already published isostructural zinc compound [(thf)₂Li{(NtBu)₄S}Zn{N(SiMe₃)₂}] (**L¹-Li,Zn**).^[106] However, the aforementioned behavior is similar with 1.6312(14) Å for the S–N(Zn) and 1.5661(14) Å for the S–N(Li) bonds. The two crystallographically identical M–N1 bonds for all three compounds range from 1.9690(13) Å (**6**) to 1.9275(16) Å (**7**), while the M–N(SiMe₃)₂ bonds are similar with 1.9196(18) Å (**6**), 1.901(2) Å (**7**) and 1.880(2) Å in the zinc

complex **L¹-Li,Zn**. Interestingly, the N1–M–N1A bite angles are considerably acute and range between 72.54(7)° (**6**) and 73.42(9)° (**7**). In contrast, the angles between the imido ligand and the hexamethyldisilazide anion N1–M–N3 span between 143.73(4) (**6**) to 143.29(5)° (**7**), which displays the strong distortion from an idealized trigonal planar angle of 120°.

Table 3-2 Selected bond lengths [Å] and angles [°] for **6**, **7**, **L¹-Li,Zn** and **L¹-Li,Li**. Li–N and N–S–N (at the lithium side) are averaged for **L¹-Li,Li**. N–S–N (angles between the two edges of the ligand's tetrahedron) are averaged values for all compounds.

compound	6	7	L¹-Li,Zn	L¹-Li,Li
S1–N1	1.6356(13)	1.6356(13)	1.6312(14)	1.608(3)
S1–N2	1.5632(13)	1.5632(13)	1.5661(14)	1.600(3)Å
S1–N3	–	–	–	1.600(3)
S1–N4	–	–	–	1.597(3)
M1–N1	1.9690(13)	1.9275(13)	1.9580(14)	–
M1–N3	1.9196(18)	1.901(2)	1.880(2)	–
Li–N	1.986(3)	1.990(4)	1.988(3)	1.957
N1–M–N1A	72.54(7)	73.42(9)	73.19(8)	–
N1–M–N3	143.73(4)	143.29(5)	143.41(4)	–
N–S–N (Li)	97.54(10)	97.49(12)	96.80(11)	94.70
N–S–N (edges)	117.53	117.91	117.63	117.08
S–N bond sum	6.397	6.398	6.395	6.405

Additionally, the compounds were analyzed by NMR spectroscopy and elemental analysis. The latter fits well to the calculated values (see chapter 5.3.5 and 5.3.6). The challenges of NMR characterization of paramagnetic compounds were already discussed in chapter 3.2.1. Nevertheless, ¹H- and ⁷Li-NMR data were collected for **6** and **7**, while an interpretable ¹³C-NMR spectrum was only obtainable for **7**. The ¹H-NMR spectrum of the cobalt compound **7** is depicted in **Figure 3-15**.

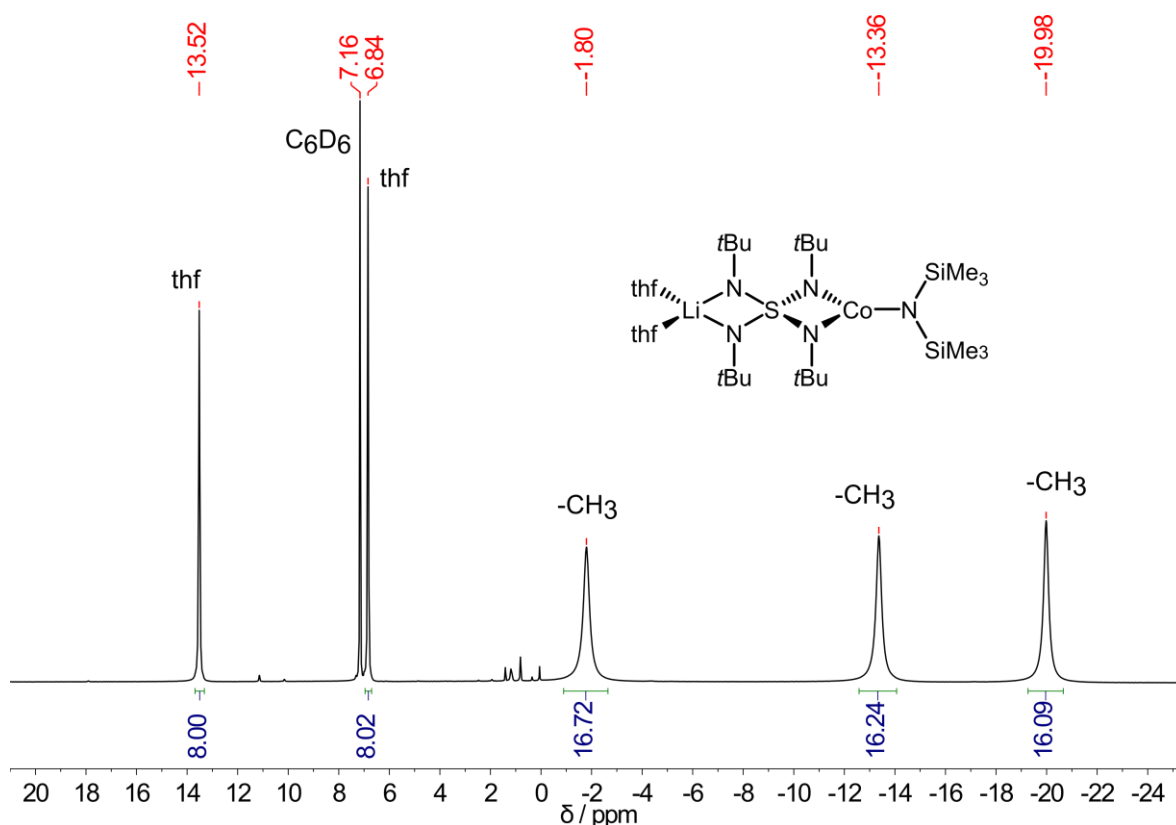


Figure 3-15 ^1H -NMR spectrum of **7** at 298 K in C_6D_6 . δ [ppm] = -19.98 (s br, 18H, 6 CH_3), -13.36 (s br, 18H, 6 CH_3), -1.80 (s br, 18H, 6 CH_3), 6.84 (s, 8H, thf-*H*), 13.52 (s, 8H, thf-*H*).

The proton signals display a strong broadening and the resonances were found over a wide range. Due to the discussed problems, the integral values of the three singlets ($\delta = -19.98$; -13.36 , -1.80 ppm), that can be attributed to the methyl groups CH_3 , are less than the expected value of 18 protons.

Without a further distinction, each signal represents either two chemically independent *tert*-butyl (*t*Bu) groups of the imido ligand or the two trimethylsilyl (SiMe_3) groups of the hexamethyldisilazide. The signals for the two lithium coordinating thf molecules are significantly sharper, but in contrast to unbound molecules (multiplets at $\delta = 1.43$ and 3.57 ppm),^[238] displaying singlets at $\delta = 6.84$ and 13.52 ppm. The corresponding spectrum for the iron complex **6** reveals even broader signals, which additionally makes integration more difficult (see chapter 6, **Figure 6-19**).

The ^7Li -NMR spectra of **6** (green) and **7** (purple) in C_6D_6 are shown in **Figure 3-16** (top), with chemical shifts of $\delta = 88.77$ (s) and 6.42 (s) ppm, respectively. **Figure 3-16** (bottom) shows the $^{13}\text{C}\{^1\text{H}\}$ -NMR spectrum of **7** in C_6D_6 . Seven signals were identified ranging from $\delta = 24.87$ to 973.52 ppm. That fits to the assumption of each one signal for the quaternary and the primary carbon of the *tert*-butyl groups at the lithium and at the 3d- metal side, two signals for the thf molecules and one signal for the methyl groups of the hexamethyldisilazide.

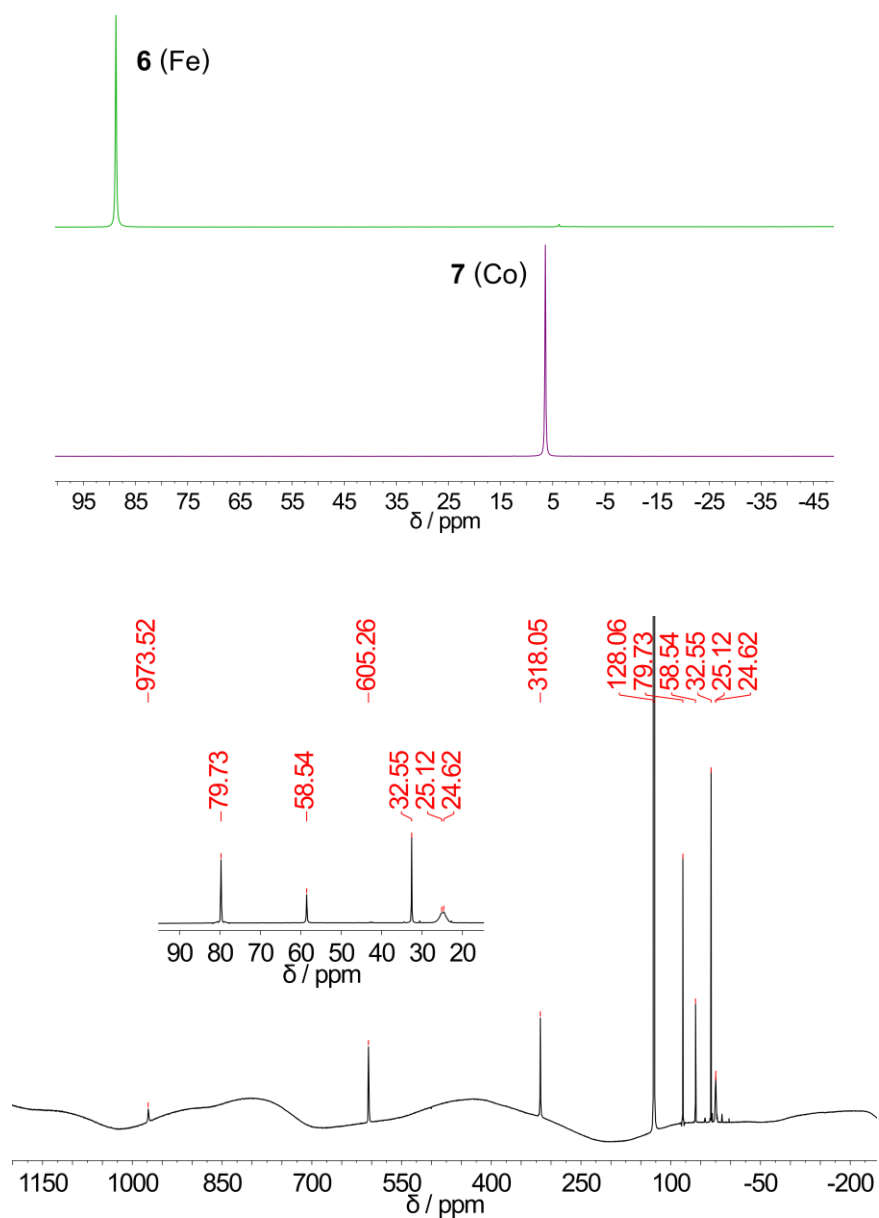
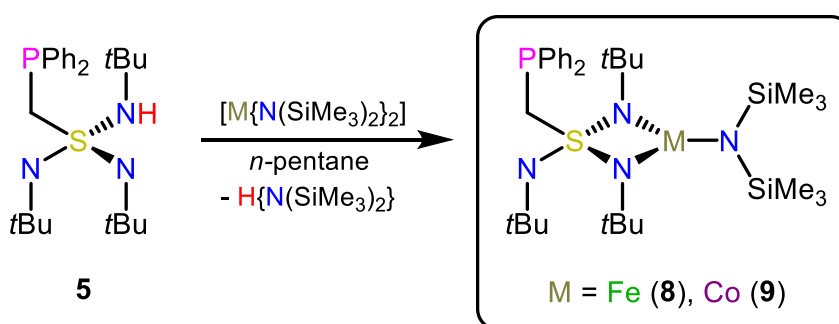


Figure 3-16 (top): ${}^7\text{Li}$ -NMR spectrum of **6** (green) and **7** (purple) at 298 K in C_6D_6 . δ [ppm] = 88.77 (s), 6.42 (s). (bottom): ${}^{13}\text{C}\{{}^1\text{H}\}$ -NMR spectrum of **7** at 298 K in C_6D_6 . δ [ppm] = 24.87 (s, CH_3), 32.55 (s, thf-C), 58.54 (s, $\text{NC}(\text{CH}_3)_3$), 79.73 (s, thf-C), 318.05 (s, CH_3), 605.26 (s, CH_3), 973.52 (s, $\text{NC}(\text{CH}_3)_3$).

3.2.3.2. Synthesis of the trigonal planar $[M\{N(SiMe_3)_2\}\{Ph_2PCH_2S(NtBu)_3\}]$ with $M = Fe$ (**8**) and Co (**9**)

In addition to a lithium metal exchange, the route of exploiting the strong basicity of hexamethyldisilazide transition metal compounds $M\{N(SiMe_3)_2\}_2$ with $M = Fe(II)$ and $Co(II)$ was followed. The deprotonation of the N-bound proton in $[Ph_2PCH_2S(NtBu)_2NHtBu]$ (**4**) with $K\{N(SiMe_3)_2\}$ is possible and was presented in chapter 3.2.2.2. This opportunity was then extended to the paramagnetic transition metals. The synthetic benefits of a deprotonation in contrast to a metal exchange reaction are the exclusion of potential lithium co-complexation and the improved purification, which is due to the convenient removal of $HN(SiMe_3)_2$, a volatile side product of the synthesis.

In order to synthesize $[M\{N(SiMe_3)_2\}\{Ph_2PCH_2S(NtBu)_3\}]$ with $M = Fe$ (**8**), Co (**9**), a mixture of $Ph_2PCH_2S(NtBu)_2NHtBu$ (**4**) and one equiv. of the appropriate $M\{N(SiMe_3)_2\}_2$ reactant were dissolved in *n*-pentane and stirred at room temperature (**Scheme 3-6**). After one day, the reaction mixture was reduced in volume and stored at $-34^\circ C$ from which crystals, suitable for single crystal X-ray diffraction analysis, were isolated in 89% (**8**, orange) and 92% (**9**, green) yields. In contrast to the synthesis of compounds **6** and **7**, an additional recrystallization was not required.



Scheme 3-6 Synthesis of $[Ph_2PCH_2S(NtBu)_3]^-$ (L^2) based metal complexes $[M\{N(SiMe_3)_2\}\{Ph_2PCH_2S(NtBu)_3\}]$ with $M = Fe$ (**8**) and Co (**9**). They can be synthesized through a deprotonation of the protonated precursor $[Ph_2PCH_2S(NtBu)_2NHtBu]$ (**4**) with one equiv. of the appropriate $M\{N(SiMe_3)_2\}_2$ in *n*-pentane. Crystals were isolated in 89% (**8**) and 92% (**9**) yields.

Both compounds can geometrically be compared to the complexes **6** and **7**. However, the imido sulfonate ligand $[Ph_2PCH_2S(NtBu)_3]^-$ (L^2) has a scorpionate-like and flexible fourth side-arm. Thus, apart from N,N' -chelation, this ligand system provides the opportunity of additional phosphorus donation. In contrast, a threefold chelation (N,N',N'') by the tetraimido sulfate ligand $[S(NtBu)_4]^{2-}$ (L^1) has not been observed for any of its coordination complexes and L^1 rather does N,N' chelation upon metal coordination with a large angle between the two coordination sides, than coordination over

three nitrogen atoms to the same metal ion.^[36,106] Hence, besides a trigonal planar geometry, distorted tetrahedral geometries with beneficial p-block element donor interaction are potentially feasible in the compounds containing the sulfonate ligand (L^2) $[M\{N(SiMe_3)_2\}\{Ph_2PCH_2S(NtBu)_3\}]$, with $M = Fe$ (**8**), Co (**9**).

The two isomorphous compounds **8** and **9** crystallize in the monoclinic space group $P2_1/c$ with one molecule in the asymmetric unit (**Figure 3-17**).

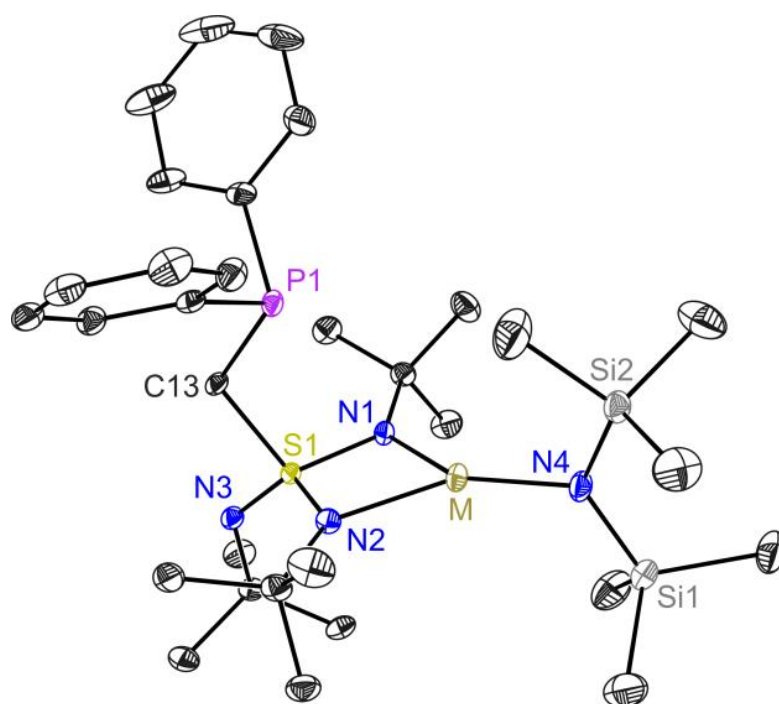


Figure 3-17 Crystal structure of **8** and **9**. Anisotropic displacement parameters are depicted for the iron complex at the 50% probability level. Hydrogen atoms are omitted for clarity. Selected bond lengths [Å] and angles [°] for **8**: S1–N1 1.6012(16), S1–N2 1.6095(16), S1–N3 1.5106(17), S1–C13 1.8082(19), Fe1–N1 2.0029(16), Fe1–N2 1.9949(16), Fe1–N4 1.9081(17), N1–S1–N2 93.52(8), N1–Fe1–N2 71.62(6), N1–Fe1–N4 143.80(7), N2–Fe1–N4 144.23(7), S1–C13–P1 110.78(10); for **9**: S1–N1 1.6051(13), S1–N2 1.6099(13), S1–N3 1.5085(14), S1–C13 1.8101(15), Co1–N1 1.9581(13), Co1–N2 1.9551(14), Co1–N4 1.8912(14), N1–S1–N2 92.60(7), N1–Co1–N2 72.88(5), N1–Co1–N4 140.68(6), N2–Co1–N4 141.32(6), S1–C13–P1 110.08(8).

The metal centers are trigonal planar coordinated by two chemically identical nitrogen atoms from the imido ligand $[Ph_2PCH_2S(NtBu)_3]^-$ (L^2) and one from the $\{N(SiMe_3)_2\}^-$ anion. The third sulfur bound nitrogen (N3) points into the opposite direction and does not bind, while the phosphorus is oriented towards the metal in the apical position of the coordination sphere with $M\cdots P1$ distances of 3.733 Å (**8**) and 3.532 Å (**9**). The orientation of the phosphorus into the unsaturated coordination sphere of the transition metal and the significant difference between the iron and cobalt compounds with a 0.2 Å shorter $P\cdots M$ distance in **9** is a clear indication for a metal to phosphorus interaction. Even though the ligand's geometry is indicative of a weak coordination, the distance between the phosphorus and the

metal is too long to be considered a bond (normally ranging from 2.0 to 2.5 Å). For comparison, the Li...P distance in the lithiated species [(tmeda)Li{Ph₂PCH₂S(NtBu)₃}] (**L²-Li**) has a value of 3.718 Å (**Table 3-4**). The averaged M–N1/N2 bond lengths for the imido ligands with values of 2.003 Å (**8**) and 1.958 Å (**9**), as well as the coordination by the {N(SiMe₃)₂}[–] anion M–N4 with 1.9081(17) Å (**8**) and 1.8912(14) Å (**9**) are quite similar for both compounds. Like in other isostructural metal complexes of the SN_x ligand family, chemically similar S–N bonds are almost invariant, while S–N bonds with other coordination environments display significant deviations. In average for **8** and **9**, the S–N bond distances for the *N,N'* chelating nitrogen atoms were found to be around 1.606 Å. In contrast, as a result of the larger positive charge concentration upon transition metal coordination, the uncoordinated nitrogen is more attracted by the positive sulfur(VI) resulting in shorter bond distances of averaged 1.510 Å.

Pronounced differences in the compound geometry of **8** and **9** can be found for the angles including the heteroleptic ligands and the metals. The acute L² centered N1–M–N2 angles are rather similar for **8** (71.62(6) Å) and **9** (72.88(5) Å). Furthermore, the N1–M–N4 and N2–M–N4 angles stay unchanged within one metal complex, but differ significantly upon exchange from iron to cobalt with averaged values of 144.23° and 140.68°, respectively.

The astonishing flexibility of the SN_x ligand is further demonstrated through N–S–N angle comparison. While only a small difference is found for **8** and **9**, a huge variation is observable for the different ligand angles. The angles between the coordinating nitrogen atoms and the pendent residual N1/N2–S–N3 are similar with an averaged value of 124.01°. Interestingly, this is much larger than the N1–S1–N2 angle of 93.06°. Although the M...P distances were found to be significantly different, the S1–C13–P1 angles do not follow this trend and are almost identical with 110.78(10)° (**8**) and 110.08(8)° (**9**).

Additionally, the compounds were analyzed by elemental analysis and NMR spectroscopy. The elemental analysis fits well to the calculated values (see chapters 5.3.7 and 5.3.8). The difficulties of NMR investigations on paramagnetic iron and cobalt compounds was already discussed for **6** and **7**. Nevertheless, collecting ¹H-NMR data was successful for both compounds, but the ¹³C-NMR investigation for the iron complex **8** are limited by the paramagnetic metal center. The ¹H NMR spectrum of the cobalt compound **9** in C₆D₆ is depicted in **Figure 3-18**.

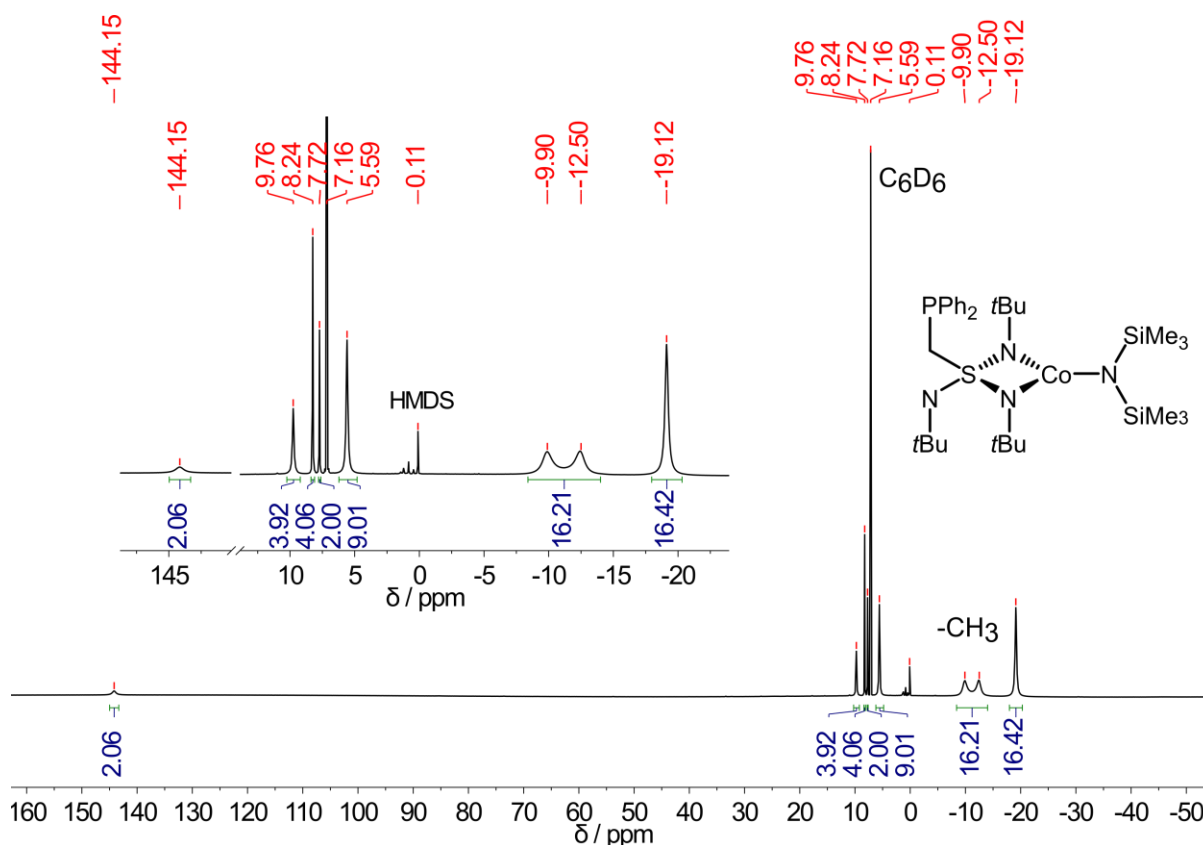


Figure 3-18 ^1H -NMR spectrum of **9** at 298 K in C_6D_6 . δ [ppm] = -19.12 (s br, 18H, 6 CH_3), -12.50 (s br, 9H, 3 CH_3), -9.90 (s br, 9H, 3 CH_3), 5.59 (s br, 9H, 3 CH_3), 7.72 (s, 2H), 8.24 (s, 4H, Ph-H), 9.76 (s br, 4H, Ph-H), 144.15 (s, 2H).

In comparison to **7**, the $[\text{Ph}_2\text{PCH}_2\text{S}(\text{N}t\text{Bu})_3]^-$ (L^2) ligand in **9** is less symmetric and more signals were expected. However, even though paramagnetic NMR prediction is challenging, the signals resonating at $\delta = -19.12$, -12.50 , -9.90 and 5.59 ppm can be attributed to the methyl groups (CH_3). Due to peak broadening as a result of the paramagnetic cobalt ion, integration of the corresponding signals reveals less than the expected values of 18 and 9 protons, respectively.

Even though the analysis does not allow an exact distinction between the different methyl groups, increasing the temperature to 323K merged the two signals at $\delta = -12.50$ and -9.90 ppm into one broad signal located at $\delta = -10.13$ ppm (see chapter 6, **Figure 6-25**). Therefore, it can be concluded that the signal of the pendent $\text{N}t\text{Bu}$ group can be identified as the resonance at $\delta = 5.59$ ppm. Nevertheless, it is still not possible to address whether the remaining signals belong to the trimethylsilyl (SiMe_3) groups of the hexamethyldisilazide or to the *tert*-butyl ($t\text{Bu}$) groups of the imido ligand. The signals for the phenyl groups are significantly sharper and in the region that is regularly attributed to diamagnetic compounds. However, since no correlation measurements were achievable, it is not absolutely certain, which of the two signals ($\delta = 7.72$ and 144.15 ppm) belongs to the *para*-phenyl protons and which one to the methylene group (CH_2).

The corresponding spectrum for the iron complex **8** shows even broader peaks, but the analysis is similar to **9** (see chapter 5.3.7 and chapter 6 **Figure 6-23**).

The $[\text{Ph}_2\text{PCH}_2\text{S}(\text{NtBu})_3]^-$ (L^2) based compounds **8** and **9**, in contrast to the $[\text{S}(\text{NtBu})_4]^{2-}$ (L^1) based **6** and **7**, do not contain a lithium ion that is coordinated by the ligand, but possess a phosphorus atom that is potentially acting as additional donor in a scorpionate-like fashion. Thus, ^{31}P -NMR measurements were performed. However, a signal was only detectable for the cobalt complex **9** with a chemical shift of $\delta = 540.01$ ppm (**Figure 3-19**, left), displaying the strong impact of the paramagnetic compound by signal broadening. The $^{13}\text{C}\{^1\text{H}\}$ -NMR spectrum of **9** in C_6D_6 is shown in **Figure 3-19** (right).

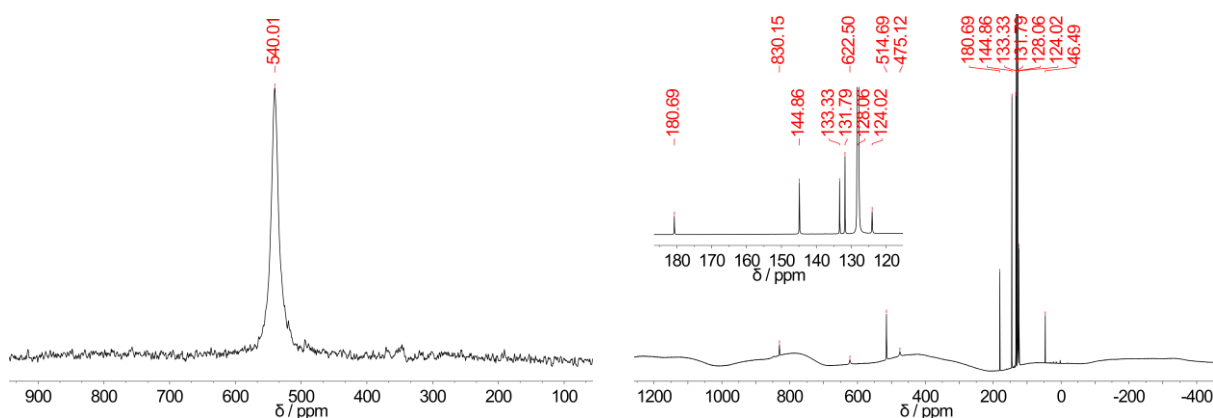


Figure 3-19 (left) $^{31}\text{P}\{^1\text{H}\}$ -NMR spectrum of **9** at 298 K in C_6D_6 . δ [ppm] = 540.01 (s). (right) $^{13}\text{C}\{^1\text{H}\}$ -NMR spectrum of **9** at 298 K in C_6D_6 . δ [ppm] = 46.49 (s), 124.02 (s), 131.79 (s), 133.33 (s), 144.87 (s), 180.69 (s), 475.12 (s), 514.69 (s), 622.50 (s), 830.15 (s).

Ten signals were identified ranging from $\delta = 46.49$ to 830.15 ppm. That fits to the assumption of each one signal for the quaternary and the primary carbon of the *tert*-butyl groups at the cobalt side, two different signals for the *tert*-butyl group bound to the pendent nitrogen and one signal for the methylene bridge. Four signals are attributed to the phenyl groups and the remaining represents the methyl groups of the hexamethyldisilazide.

3.2.3.3. Structural comparison of the trigonal planar Fe(II) and Co(II) compounds $[(\text{thf})_2\text{Li}\{(\text{NtBu})_4\text{S}\}\text{M}\{\text{N}(\text{SiMe}_3)_2\}]$ and $[\text{M}\{\text{N}(\text{SiMe}_3)_2\}\{\text{Ph}_2\text{PCH}_2\text{S}(\text{NtBu})_3\}]$ (**6** – **9**)

The astonishing flexibility of the SN_x ligands has already been discussed. To obtain further insight into the structural differences that are induced by the choice of ligand, compounds **6** to **9** should be compared. Since it is most interesting for the magnetic performance, this will mainly focus on the coordinated metal that is located within the $N,N,N(P)$ coordination pocket. Interestingly, the iron and cobalt ions in complexes **6** and **7** are found to be perfectly coplanar within the N,N,N plane (**Figure 3-20**). Even more, this can be expanded to the central sulfur atom of the ligand, following this coplanar arrangement. Such a finding cannot be observed in **8** and **9**. While the iron in **8** is only lifted by 0.058 Å, the cobalt in **9** is located 0.224 Å above the N,N,N plane. This difference could explain, why the M–P1 distance for cobalt is around 0.2 Å shorter compared to iron. It was discussed that the orientation of the phosphorus indicates an interaction with the metals in the apical position of its unsaturated coordination environment. Even if the interaction between the phosphorus and the metal might be weak, the orientation of the donor atom could be the reason for the observed structural differences between the $[\text{S}(\text{NtBu})_4]^{2-}$ (L^1) and the $[\text{Ph}_2\text{PCH}_2\text{S}(\text{NtBu})_3]^-$ (L^2) based metal compounds. In contrast to the metal ions in **8** and **9**, the sulfur atoms are found to be slightly below the N,N,N plane with 0.011 Å (**8**) and 0.020 Å (**9**). However, further geometrical differences of the transition metals' coordination sphere are marginal. The averaged bond distances between the imido ligands and the metal N–M range from 1.928 Å to 1.999 Å, while hexamethyldisilazide bond distances range from 1.891 Å to 1.920 Å. The N–M–N angles through N,N' chelation by L^1 and L^2 are considerably acute and range between 71.62° to 73.42°.

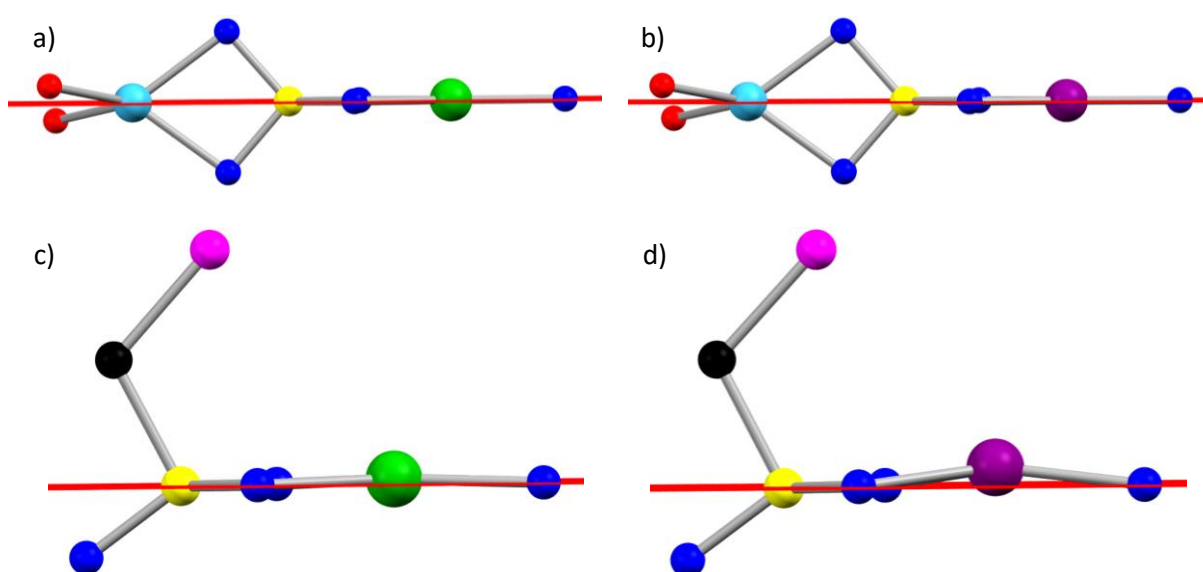


Figure 3-20 Sideways view on the N,N,N plane for $[(\text{thf})_2\text{Li}\{(\text{NtBu})_4\text{S}\}\text{M}\{\text{N}(\text{SiMe}_3)_2\}]$ with a) $\text{M} = \text{Fe}$ (**6**), b) $\text{M} = \text{Co}$ (**7**) and $[\text{M}\{\text{N}(\text{SiMe}_3)_2\}\{\text{Ph}_2\text{PCH}_2\text{S}(\text{NtBu})_3\}]$ with c) $\text{M} = \text{Fe}$ (**8**), d) $\text{M} = \text{Co}$ (**9**). Iron (green), cobalt (purple), lithium (turquoise), sulfur (yellow), phosphorus (pink), nitrogen (blue), oxygen (red) and carbon atoms (black).

3.2.3.4. Magneto-structural correlation in the trigonal planar Fe(II) and Co(II) compounds $[(\text{thf})_2\text{Li}\{\text{N}(\text{tBu})_4\text{S}\}\text{M}\{\text{N}(\text{SiMe}_3)_2\}]$ and $[\text{M}\{\text{N}(\text{SiMe}_3)_2\}\{\text{Ph}_2\text{PCH}_2\text{S}(\text{NtBu})_3\}]$ (**6** – **9**)

The structural differences for the complexes containing either **L**¹ or **L**² are rather small, while a imido ligand exchange alters the position of the metal relatively to *N,N,N* plane, which is generated by the *N,N'* chelating imido ligands and the hexamethyldisilazide anion. In **8** and **9**, the iron and cobalt ions are lifted out of the plane, which may be a consequence of the phosphorus interaction and the different substituent orientations around the central sulfur of the ligands. The magneto-structural correlations will be discussed in pairs for the two iron and cobalt compounds. Finally, the structural influence to the magnetic anisotropy that arises from the different imido ligands will be pointed out.

The measurements and data processing were done by Dr. C. Legendre and Dr. S. Demeshko. Full information on the data processing and the calculations can be found in the PhD thesis of Dr. C. M. Legendre^[64] or in the publication (4).^[4]

The crystal structure analysis of **6** to **9** have already confirmed that the metal ions are in the oxidation state +II in a strongly distorted trigonal planar coordination geometry. The measurement of the temperature-dependent magnetic susceptibility further revealed that both **6** and **8** are high spin Fe(II) (*d*⁶; *s* = 2) systems (**Figure 3-21**).

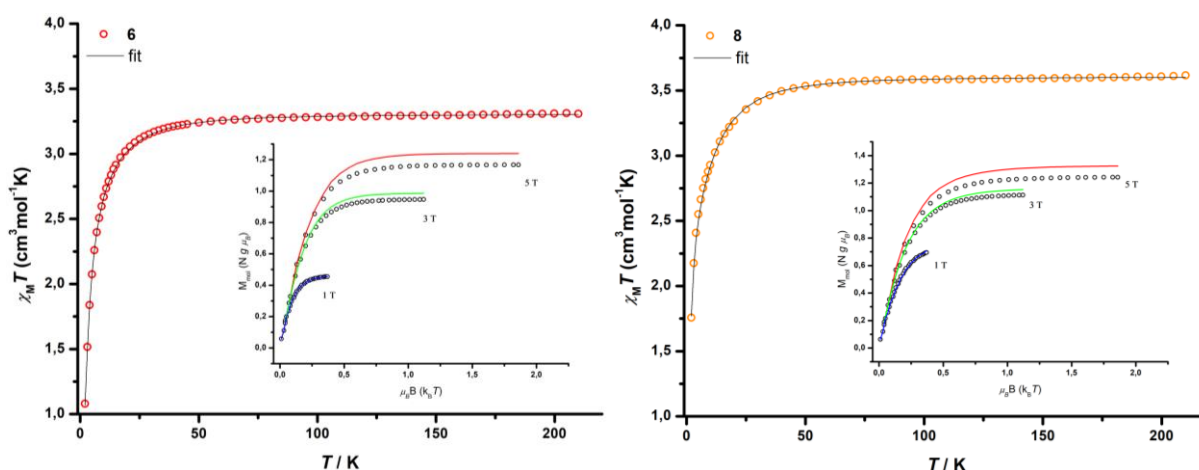


Figure 3-21 Temperature-dependent dc magnetic susceptibility measurements $\chi_M T$ vs. T at 0.1 T and variable temperature variable field (VTVH) measurements at 1, 3 and 5 T for **6** (left) and **8** (right).

Going from high to low temperature, the $\chi_M T$ value first gradually declines. Then, at around 50 K it sharply drops to reach at 2 K low temperature values of 1.08 (**6**) and 1.76 $\text{cm}^3\text{mol}^{-1}\text{K}$ (**8**). The extracted $\chi_M T$ values at 210 K are 3.31 and 3.62 $\text{cm}^3\text{mol}^{-1}\text{K}$, respectively, which are higher than the spin-only value of 3.00 $\text{cm}^3\text{mol}^{-1}\text{K}$, indicative of a significant amount of unquenched orbital angular momentum.^[140]

However, both compounds do not show strong axial magnetic anisotropy. The $\chi_M T$ vs. T together with the variable temperature variable field (VTVH) data, were fitted according to **Eq. 3-1** with isotropic g values. The calculated zero-field splitting parameter D yielded values of +10.3 (**6**) and -9.2 cm^{-1} (**8**) and a large rhombicity was found for both compounds with the rhombic parameter of $E/D = 0.16$ for **6** and the maximum possible value of 0.33 for **8** (**Table 3-3**). To probe the magnetic relaxation dynamics, out-of-phase (χ_M'') temperature-dependent ac magnetic susceptibility data were collected under zero and applied dc fields. However, the characteristic peak maximum for slow magnetic relaxation was not observed. Thus, **6** and **8** do not display SMM properties, even under an applied dc field.

Table 3-3 Selected structural characteristics and magnetic data for compounds **6** and **8**.

compound	N–Co–N (°)	M···(N,N,N)-plane (Å)	g	D (cm^{-1})	E/D (cm^{-1})
6	72.54	0	2.10	+10.3	0.16
8	71.62	0.058	2.13	-9.2	0.33

Even though structural differences are small, ligand variation influences the magnetic performance with a noticeable change in the sign of the zero-field splitting parameter D . Here, a negative D is accompanied by a stabilization of the maximum magnetic ground-state ($M_S = \pm 3/2$), while a positive D is associated with the stabilization of $M_S = \pm 1/2$. The iron in **8** is found to be slightly lifted out of the N,N,N plane, while in **6** all four atoms are coplanar (**Table 3-3**). The phosphorus metal interaction in **8** might explain the observed differences, even though it is assumed to be weak. The influence of the phosphorus donation and the strictly planar coordination geometry will be discussed more precisely later on.

In order to obtain more information about the Fe(II) centers, compounds **6** and **8** were further characterized by ^{57}Fe Mössbauer spectroscopy at 80 K. The two spectra are depicted in **Figure 3-22** and show a quadrupole doublet with an isomer shift of $\delta = 0.52 \text{ mms}^{-1}$ for **6** and $\delta = 0.60 \text{ mms}^{-1}$ for **8**, which are typical values for low coordination numbers.^[239] Since the metal ions are incorporated in a trigonal planar coordination fashion, those values fit well to the solid state and magnetic analysis. The quadrupole splitting values are $|\Delta E_Q| = 1.84$ and 1.41 mms^{-1} , respectively. In general, higher coordination numbers can be associated with larger δ values and observed values for the isomeric shift δ are typical for low-coordination iron.^[240] Therefore, the larger sigma value for **8** supports the

assumption that the phosphorus atom in the compounds with the sulfonate ligand $[\text{Ph}_2\text{PCH}_2\text{S}(\text{NtBu})_3]^-$ interacts with the coordinated iron metal. More precisely, the phosphorus interaction would rise the coordination number and the isomer shift would tend for higher values.

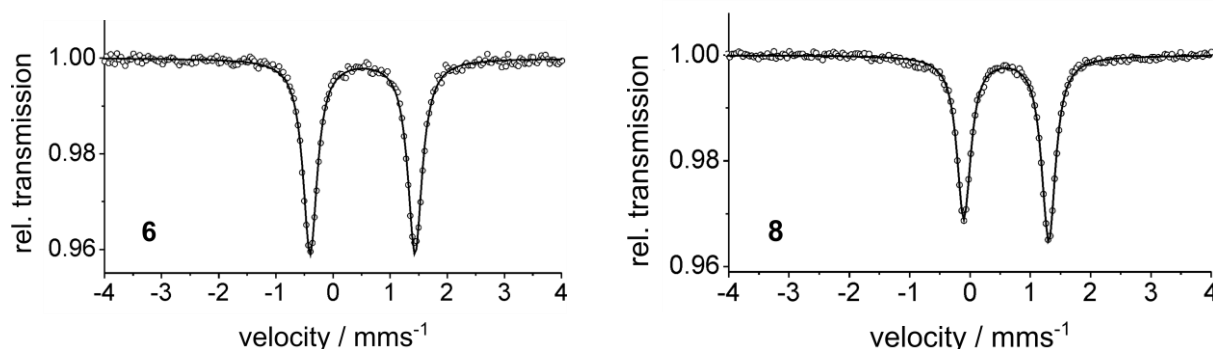


Figure 3-22 ^{57}Fe Mössbauer spectrum of **6** (left) and **8** (right) at 80 K. Both spectra show a quadrupole doublet with an isomer shift of $\delta = 0.52 \text{ mm s}^{-1}$ (**6**) and $\delta = 0.60 \text{ mm s}^{-1}$ (**8**). The quadrupole splitting values are $|\Delta E_Q| = 1.84$ and 1.41 mm s^{-1} , respectively.

The measurement of the temperature-dependent magnetic susceptibility for the cobalt compounds **7** and **9** revealed $\chi_M T$ values of 2.66 and $3.05 \text{ cm}^3 \text{ mol}^{-1} \text{ K}$ at 210 K, which are significantly larger than the expected spin-only value of $1.875 \text{ cm}^3 \text{ mol}^{-1} \text{ K}$ (**Figure 3-23**). This significant deviation suggests a considerable contribution of unquenched orbital angular momentum as observed in other cobalt complexes.^[93,107,140,183,184] In contrast to **6** and **8**, the decline in the $\chi_M T$ curve starts already at higher temperatures, indicative for a pronounced influence of the zero-field splitting. First attempts to fit the $\chi_M T$ vs. T data with an isotropic g value did not produce useful results. Therefore, the $\chi_M T$ vs. T and the VTVH data were simultaneously fitted according to the following anisotropic spin Hamiltonian, which includes Zeeman splitting and zero-field splitting (ZFS):

$$\hat{H} = \mu_B (S_x g_x B_x + S_y g_y B_y + S_z g_z B_z) + D \left[\hat{S}_z^2 - \frac{1}{3} S(S+1) + \frac{E}{D} (\hat{S}_x^2 - \hat{S}_y^2) \right] \quad (\text{Eq. 3-1})$$

The best fit-to-data values are summarized in **Table 3-4** and the obtained zero-field splitting parameters $D = +43 \text{ cm}^{-1}$ (**7**) and -80 cm^{-1} (**9**) are comparable to other compounds.^[93,107,140,183,184] Remarkably, the high negative value of **9** is one of the largest known for trigonal planar cobalt SIMs. Both compounds display large rhombic magnetization with E/D values of 0.33 and 0.10 , which is, in the case of **7**, as high as the theoretical limit of $1/3$. However, the large negative D value for **9** indicates that, at low temperatures, only the lowest kramers doublet ($M_S = \pm 3/2$) is populated. Consequently, a

sizeable energy barrier to spin reversal and SIM properties are expected. Nevertheless, frequency-dependent ac magnetic susceptibility measurements without an applied dc field did not show the characteristic signals in the out-of-phase (χ_M'') signal. This could be explained by the high rhombicity, which suggests the presence of under-barrier relaxation processes (e.g. a Raman process or quantum tunneling of the magnetization) that hamper the SMM performance.

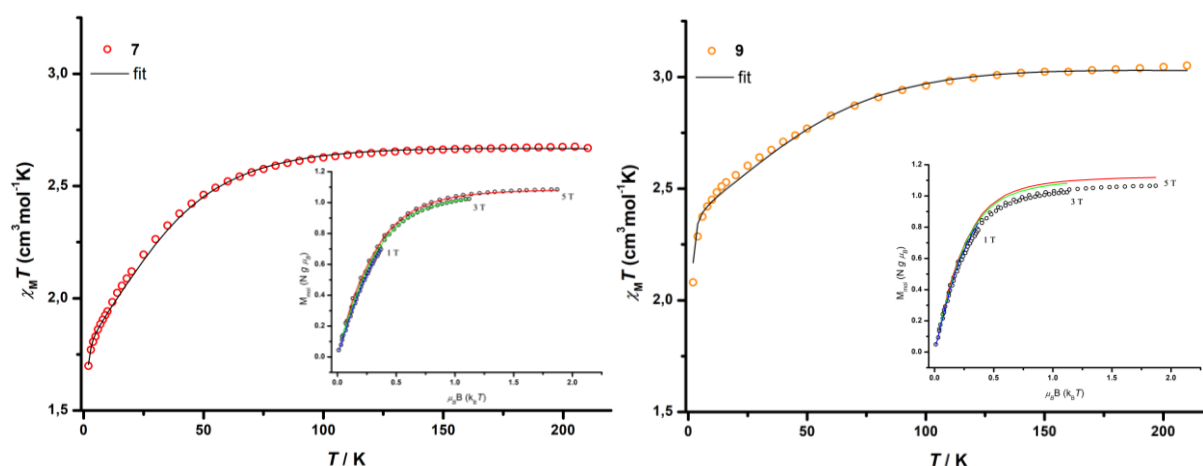


Figure 3-23 Temperature dependent susceptibility measurements at 0.1 T and variable temperature variable field (VTVH) measurements at 1, 3 and 5 T for **7** (left) and **9** (right).

To probe the magnetic properties under an applied dc field, field-dependent ac magnetic susceptibility data at constant temperature were measured. Here, the characteristic maxima in the out-of-phase (χ_M'') signal were observed at 1000 Oe (**7**) and 2000 Oe (**9**). The variable-frequency variable-temperature in-phase (χ_M') and out-of-phase (χ_M'') ac magnetic susceptibility measurements under these dc fields then revealed that both cobalt compounds show field-induced slow magnetic relaxation (**Figure 3-24** and **Figure 3-25**).

Table 3-4 Selected structural characteristics and magnetic data for compounds **7** and **9**. For compound **9**, two relaxation processes were found.

compound	N–Co–N (°)	M···(N,N,N) (Å)	$g_x = g_y$; g_z	D (cm ⁻¹)	E/D (cm ⁻¹)	H_{dc} (Oe)	$U_{eff,Orbach}$ (cm ⁻¹)
7	73.42	0	1.92; 2.55	+43	0.33	1000	33.0
9	72.88	0.224	2.44; 2.91	–80	0.10	2000	21.9, 17.7

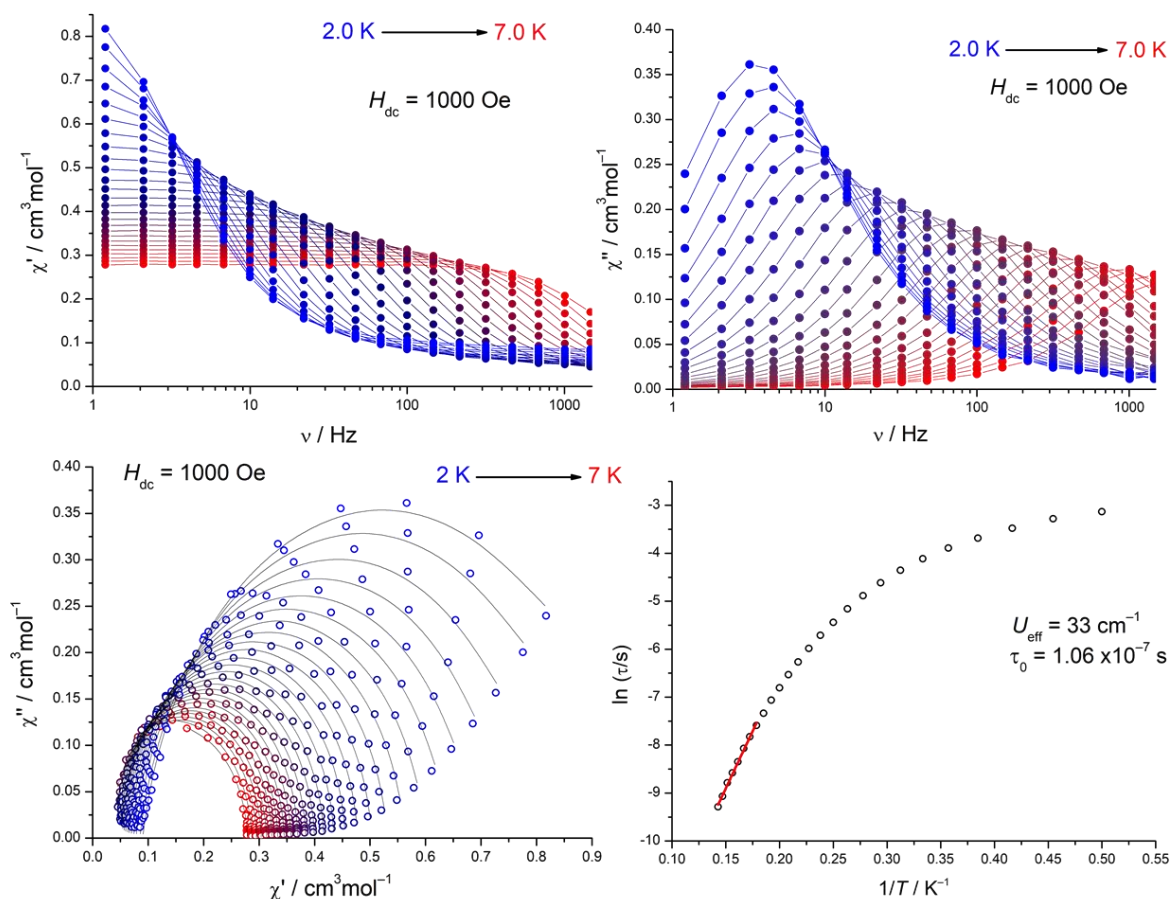


Figure 3-24 (top): In-phase (χ') and out-of-phase (χ'') ac susceptibility measurement under an applied dc-field of $H_{dc} = 1000$ Oe for **7**. The solid lines are guide for the eyes. (bottom): Corresponding Cole-Cole plot and Arrhenius plot for **7**. The solid lines represent a fit to the data.

With the data obtained from the frequency measurement, Cole-Cole plots were constructed. The extracted relaxation times (τ_{obs}) at given temperatures were then plotted as a value of the natural logarithm against the inverse temperature to obtain the Arrhenius plots. A linear fit in the high temperature region ultimately resulted in the estimation of the energy barrier to spin reversal U_{eff} , according to the Arrhenius law using **Eq. 1-1**.

The Cole-Cole and especially the Arrhenius plots for **7** indicated several relaxation processes, including Raman and QTM. For **9**, the normally semicircular Cole-Cole plots display a small shoulder at higher values of χ' , indicative for a second relaxation process^[241,242] and mirrored in the corresponding Arrhenius plot. The lifetime of the first process is calculated to be much shorter ($\tau_{0,1} = 3.5 \cdot 10^{-7}$ s and $\tau_{0,2} = 1.0 \cdot 10^{-4}$ s), but the estimated U_{eff} values are similar for both processes (21.9 and 17.7 cm^{-1}). In comparison, only one relaxation process was found for **7** and the obtained values are similar to **9** with $U_{eff} = 33 \text{ cm}^{-1}$ and $\tau_0 = 1.06 \cdot 10^{-7}$ s. To model the under-barrier relaxation processes, full fits according to **Eq. 3-2** were performed (**Figure 3-26** and **Figure 3-27**). The equation includes Orbach, Raman and QTM relaxation processes, where τ_0 is the relaxation rate for the Orbach process, U_{eff} is the effective

energy barrier to spin reversal, k_B the Boltzmann constant, C and n are Raman parameters and τ_0 is the relaxation rate for QTM. However, they did not produce a significant increase in the energy barriers (Table 3-5).

$$\frac{1}{\tau_{\text{obs}}} = \tau_0^{-1} \exp\left(-U_{\text{eff}}/k_B T\right) + CT^n + \frac{1}{\tau_{\text{QTM}}} \quad (\text{Eq. 3-2})$$

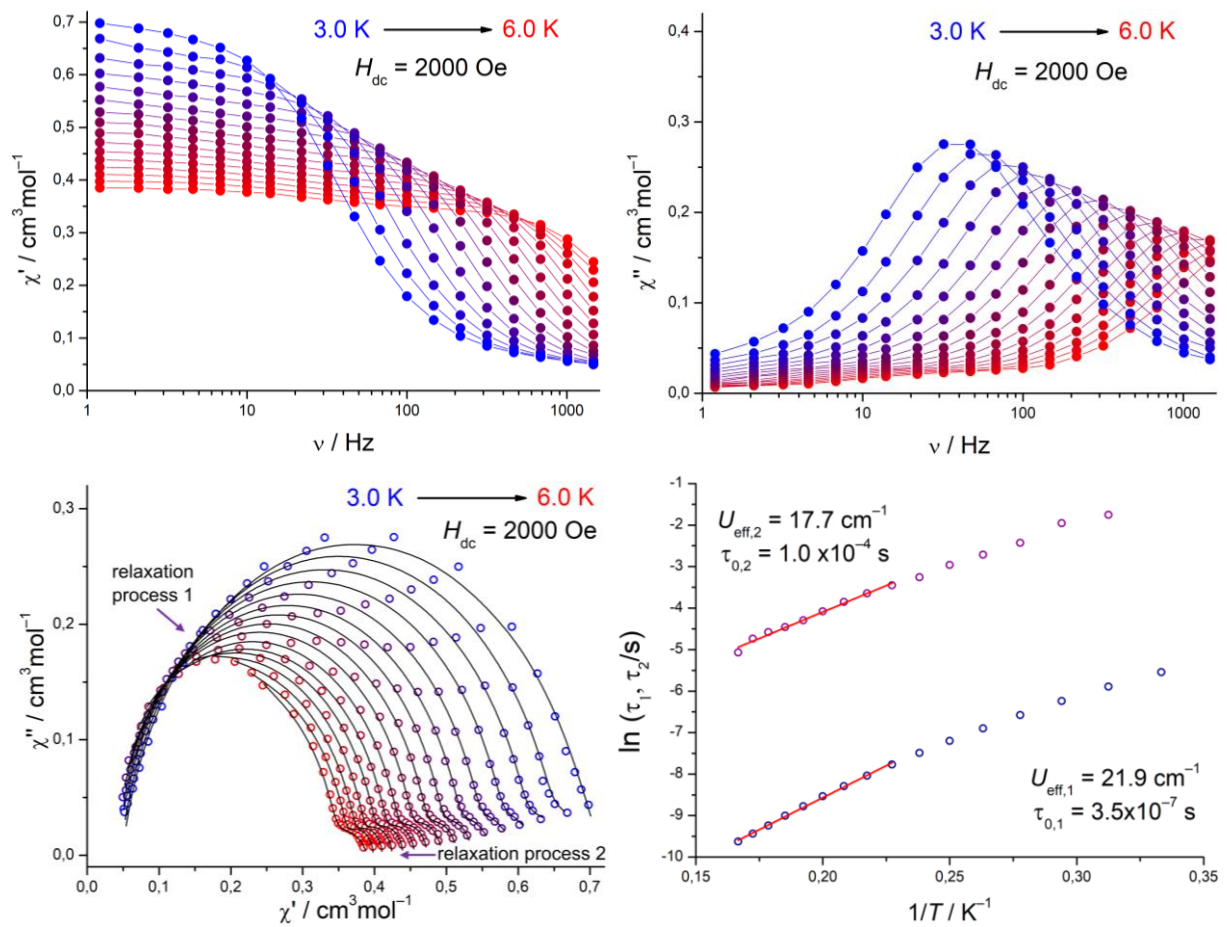
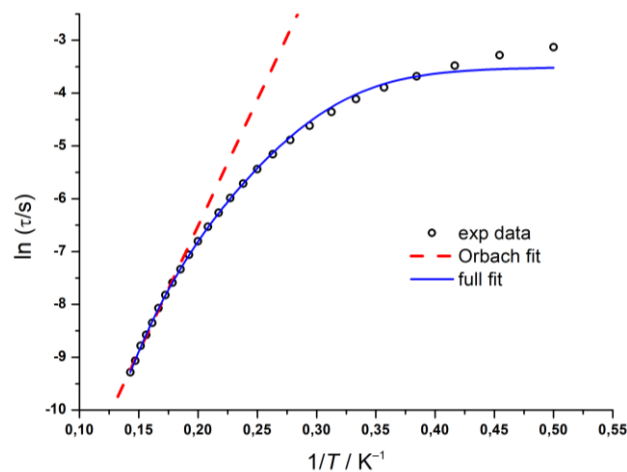
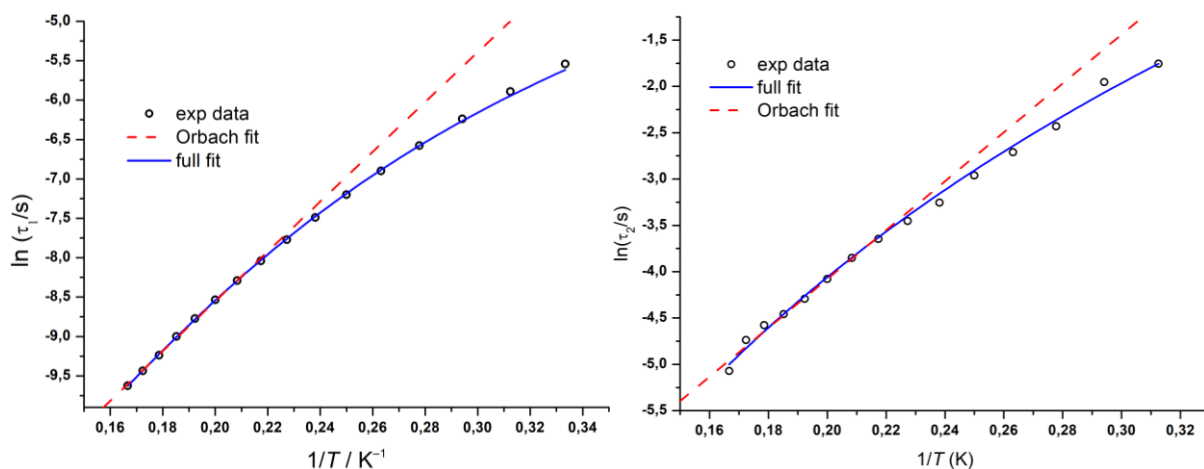


Figure 3-25 (top): In-phase (χ') and out-of-phase (χ'') ac susceptibility measurement under an applied dc-field of $H_{\text{dc}} = 1000$ Oe for **9**. The solid lines are guide for the eyes. (bottom): Corresponding Cole-Cole plot and Arrhenius plot with two different relaxation processes for **9**. The solid lines represent a fit to the data.

Table 3-5 Full relaxation fits for compounds **7** and **9** according to Eq. 3-2. The best parameters obtained are depicted.

compound	$U_{\text{eff,fullfit}} (\text{cm}^{-1})$	$\tau_0 (\text{s})$	C parameter (Raman)	n (Raman)	$\tau_{\text{QTM}} (\text{s})$
7	17.4	$1.58 \cdot 10^{-5}$	$1.2 \cdot 10^{-5}$	9.3	$3.00 \cdot 10^{-2}$
9 (relaxation 1)	27.8	$1.62 \cdot 10^{-7}$	1.65	4.6	—
9 (relaxation 2)	34.2	$1.00 \cdot 10^{-3}$	0.014	5.2	—

**Figure 3-26** Full relaxation fits for **7**. The red dashed line represents the Orbach fit while the blue solid line represents the relaxation fit including Orbach, Raman and QTM relaxation processes.**Figure 3-27** Full relaxation fits for **9**, with the first relaxation (left) and the second relaxation (right). The red dashed line represents the Orbach fit while the blue solid line represents the fit including Orbach and Raman relaxation processes.

In addition to the magnetic measurements, CASSCT/NEVPF2 calculations were carried out to support the experimental data. The calculations gave, for the iron complexes **6** and **8**, small and negative ZFS values of $D = -18$ and -25 cm^{-1} . The absolute values of those result are comparable to the experimental data. The calculated transverse anisotropies are lower, but still large with an E/D ratio of 0.12 and 0.08, respectively. The difference in the sign for the calculated value of the zero-field splitting parameter D in **6** compared to the experimental result (**Table 3-6**) can be explained by the large rhombicity. In general, the sign prediction is less reliable for system with large transverse anisotropy and hence, the results may be different.^[140]

Table 3-6 Selected structural characteristics and theoretical magnetic parameters for compounds **6** and **9**.

compound	N–Co–N (°)	M···(N,N,N) (Å)	$g_x; g_y;$ g_z	D (cm^{-1})	E/D (cm^{-1})	ΔE (d-orbitals) (cm^{-1})	ΔE (KD) (cm^{-1})
6	72.54	0	1.99; 2.08; 2.40	–18	0.12	1821	–
7	73.42	0	1.98; 2.55; 2.93	+59	0.31	1882	133.4
8	71.62	0.058	1.98; 2.08; 2.54	–25	0.08	2441	–
9	72.88	0.224	1.86; 2.39; 3.33	–105	0.13	1130	215.7

The calculated rhombicities for the cobalt compounds **7** and **9** are high (0.31 and 0.13) and in good agreement with the experimental measurements. The D values are $+59 \text{ cm}^{-1}$ and -105 cm^{-1} , and hence consistent with the experimental data. The energy gap between the two lowest lying Kramers' doublets $\Delta E(\text{KD}) = 133.4$ and 215.7 cm^{-1} are large, but efficient slow relaxation of the magnetization is probably prevented by the high mixing of the M_s states ($E/D = 0.31$ and 0.13 , respectively).

Furthermore, *ab initio* ligand field theory (AFLT) calculations gave access to the orbital energy splitting in the distorted trigonal planar cobalt complexes **7** and **9** (**Figure 3-28**).

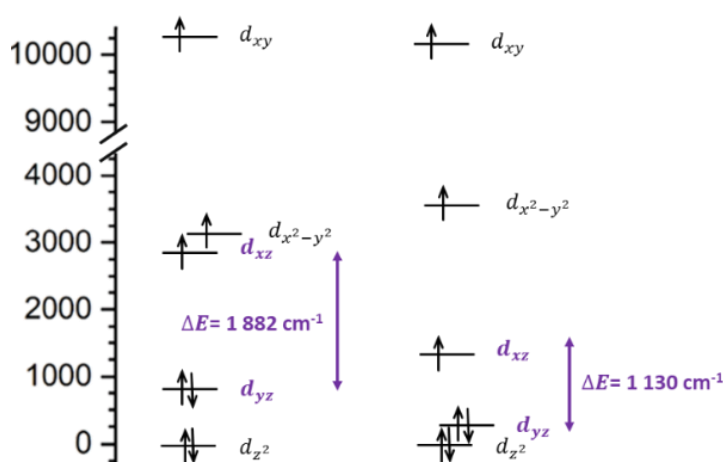


Figure 3-28 d-orbital energy-splitting in the cobalt complexes **7** (left) and **9** (right).

The splitting predicts that the two lowest lying orbitals are the d_{z^2} and d_{yz} and that the energy splitting between d_{yz} and d_{xz} is crucial for the orbital angular momentum (OAM). For a maximum OAM and hence magnetic anisotropy, both orbitals should be degenerated. This would maximize the spin orbit coupling and hence the splitting of the degenerated M_s magnetic states. The smaller the gap between d_{yz} and d_{xz} , the larger the second-order spin-orbit coupling. The energy gaps between those two orbitals are relatively large with $\Delta E = 1821, 1882, 2441$ and 1130 cm^{-1} (**6** - **9**). However, it explains why **9** (1130 cm^{-1}) displays a better magnetic performance, compared to **7** (1882 cm^{-1})

To further elucidate the influence of the ligand differences on the magnetic performances, especially the phosphorus interaction and the relative position of the metal to the N,N,N plane, CASSCF/NEVPT2 calculations on modified structures were carried out. To determine the influence of the phosphorus atom, the whole phosphine group was removed and replaced by a hydrogen atom, which resulted in a slightly lower ZFS parameter of $D = -90 \text{ cm}^{-1}$. Alternatively, the whole group was orientated away from the metal, which resulted in marginally lower D of -87 cm^{-1} . A pronounced difference is found when the metal ion is placed coplanar to the N,N,N plane. This simulates the bonding situation in the tetraimido sulfate $[\text{S}(\text{NtBu})_4]^{2-}$ (**L**¹) system and dramatically lowers the ZFS giving a positive value of $+63 \text{ cm}^{-1}$ and an E/D ratio of 0.10.

Altogether, those findings underline the initial assumption that the phosphorus supported ligand beneficially influences the magnetic properties of the compounds.

3.2.3.5. Conclusion on trigonal planar Fe(II) and Co(II) complexes of the tetraimido sulfate $[S(NtBu)_4]^{2-}$ (L^1) and the triimido sulfonate $[Ph_2PCH_2S(NtBu)_3]^-$ (L^2)

In the last chapters, the synthesis of four trigonal planar Fe(II) and Co(II) complexes featuring the tetraimido sulfate $[S(NtBu)_4]^{2-}$ (L^1) and the triimido sulfonate $[Ph_2PCH_2S(NtBu)_3]^-$ (L^2) were presented. Compounds **6**, **7**, **8** and **9** were further characterized by crystallographic analysis, NMR-investigations, magnetic studies and additionally for the iron complexes Mössbauer spectroscopy. The cobalt species showed slow magnetic relaxation under applied dc fields with zero-field splitting parameters D of $+43\text{ cm}^{-1}$ (**7**) and -80 cm^{-1} (**9**) and effective energy barriers to spin reversal U_{eff} of 33.0 and 21.9 cm^{-1} , respectively. Even though they possess some of the largest ZFS parameters observed for three-coordinated cobalt SIMS^[140], the huge amount of transverse anisotropy hampers efficient slow relaxation of the magnetization and high values for the effective energy barriers. To investigate the influence of the phosphorus donation in the sulfonate compounds, theoretical ligand variations were made and calculations revealed an appreciable influence to the magnetic performance. However, the direct interaction to the metal is only weak and slightly enhances the magnetic properties. Nevertheless, the position of the metal relatively to the N,N,N plane seems to be crucial for the magnetic performance. Even though the interaction between the phosphorus and the metal might be small, the substitution of one $NtBu$ group for the CH_2PPh_2 residue triggers the geometry changes in the coordination sphere of the appropriate metal ions in **6**, **7**, **8** and **9**. The very acute $N-M-N$ bite angles lead to considerable deviation from idealized trigonal planar geometry, which seems to be advantageous due to the high anisotropies found for those compounds.

3.3. Sulfur imido ligands in f-block metal SMMs and SIMs

Molecular magnetism has first been discovered in a 3d-element metal cluster containing manganese ions. However, due to their large unquenched orbital angular momentum and sizeable spin-orbit coupling that results in high magnetic anisotropies, f-metals are well-suited for the design of highly performing SMMs, even under elevated temperatures. Until the isolation of the following compounds, f-metal chemistry has been unexplored for the ligand systems that have been used in this thesis. Hence, this chapter will focus on the first f-metal compounds based on the two sulfur center ligands in the oxidation state VI, the tetraimido sulfate $[S(NtBu)_4]^{2-}$ (**L**¹) and the triimidosulfonate $[Ph_2PCH_2S(NtBu)_3]^-$ (**L**²). Some of the isolated complexes turned out to perform as single molecule magnets (SMMs).

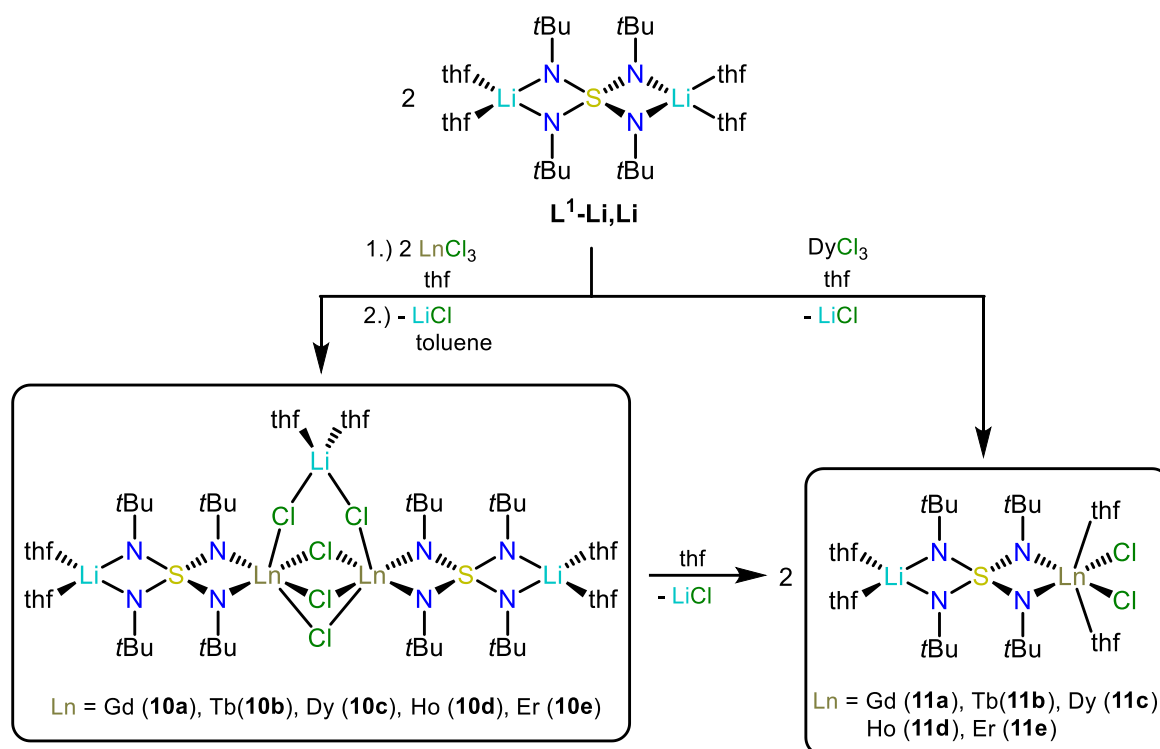
3.3.1. f-block metal SMMs containing the tetraimido sulfate $[S(NtBu)_4]^{2-}$

3.3.1.1. Synthesis and structure

In the previously presented tetraimido sulfate $[S(NtBu)_4]^{2-}$ (**L**¹) based Fe(II) and Co(II) complexes, synthesized under the utilization of the appropriate hexamethyldisilazides, a lithium to metal exchange was achieved. Since a similar reaction pathway on lanthanide(III) hexamethyldisilazides was not feasible, the route over lanthanide(III) chlorides has been made accessible.

For the desired lithium lanthanide metal exchange, the precursor $[(thf)_4Li_2(NtBu)_4S]$ (**L**¹-Li, Li) and the appropriate lanthanide(III) chlorides were combined and dissolved in thf. After stirring for several hours, the reaction mixture was concentrated in volume, filtered and the solvent was subsequently removed under reduced pressure. The residue was then dissolved in toluene from which crystallization started within minutes to hours at room temperature. The obtained crystals were suitable for single crystal X-ray diffraction analysis and the obtained binuclear lanthanide(III) compounds $[{(thf)_2Li(NtBu)_2S(tBuN)_2LnCl_2}_2 \cdot ClLi(thf)_2]$ **10a-e** (Ln = **a**: Gd, **b**: Tb, **c**: Dy, **d**: Ho, **e**: Er) were isolated in 17% to 45% yields (**Scheme 3-7**).

It should be emphasized, that attention must be paid to the extraction of the raw material after thf removal. During synthesis optimization, it turned out that this is the key to trigger the subsequent crystallization. The optimal extraction with toluene was achieved, when the raw product was dissolved right after turning into a powder upon removal of the reaction solvent (thf) under reduced pressure. Otherwise, crystallization of **10** was not always observable. If **10** did not crystalize from the toluene solution after several hours at room temperature, then the extraction process went wrong at some point.



Scheme 3-7 Synthesis of the lanthanide complexes $[\{\text{Cl}_2\text{Ln}(\text{N}^t\text{Bu})_2\text{S}(\text{N}^t\text{Bu})_2\text{Li}(\text{thf})_2\}\{\text{ClLi}(\text{thf})_2\}]$ (**10a-e**) in the row from gadolinium to erbium after dissolving $[(\text{thf})_4\text{Li}_2(\text{N}^t\text{Bu})_4\text{S}]$ ($L^1\text{-Li, Li}$) and the appropriate LnCl_3 in thf. From an extraction with toluene, crystals in 17% to 45% yields were obtained. Dissolving **10a-e** in thf yielded the isolation of $[\{(\text{thf})_2\text{Li}(\text{N}^t\text{Bu})_2\text{S}(\text{N}^t\text{Bu})_2\text{LnCl}_2(\text{thf})_2\}]$ (**11a-e**) in 60% to 77% yields. Additionally, a direct lithium dysprosium exchange from the starting material was performed.

Further attempts to achieve a double lithium exchange with two equiv. of the lanthanide(III) chlorides or changing the reaction solvent to toluene have remained unsuccessful under these conditions.

After the formation and isolation of the dimeric complexes, they cannot be redissolved in toluene, neither at room nor at elevated temperatures. It was found that they are most soluble in thf, but it was impossible to recrystallize the compounds. Instead, it turned out that when only small amounts of thf were used, the dissolved compounds crystallize to form the non $\mu\text{-LiCl}$ -bridged monomeric species $[\{(\text{thf})_2\text{Li}(\text{N}^t\text{Bu})_2\text{S}(\text{N}^t\text{Bu})_2\text{LnCl}_2(\text{thf})_2\}]$ **11a-e** ($\text{Ln} = \text{a: Gd, b: Tb, c: Dy, d: Ho, e: Er}$) in good yields (60% – 77%) and purity. In order to maximize yields the reaction mixture can be stored at lower temperature for several hours to days.

Instead of isolating the dysprosium dimer **11c** via the extraction with toluene in a first reaction, the monomeric species **10c** can also be obtained directly from the filtered reaction mixture upon being layered with *n*-pentane or by vapor diffusion. However, since this crystallization approach requires a narrow window of parameters and since the final product is actually insoluble in thf and even more in *n*-pentane, the product rather precipitates than crystallizes. Therefore, the previous isolation of the dimers seemed to be more advantageous and further research was focused on the optimization of the

synthetic route to obtain the μ -LiCl-bridged dimers **10a-e**. They crystallize in the monoclinic space group $C2/c$ with half a molecule in the asymmetric unit (**Figure 3-29**).

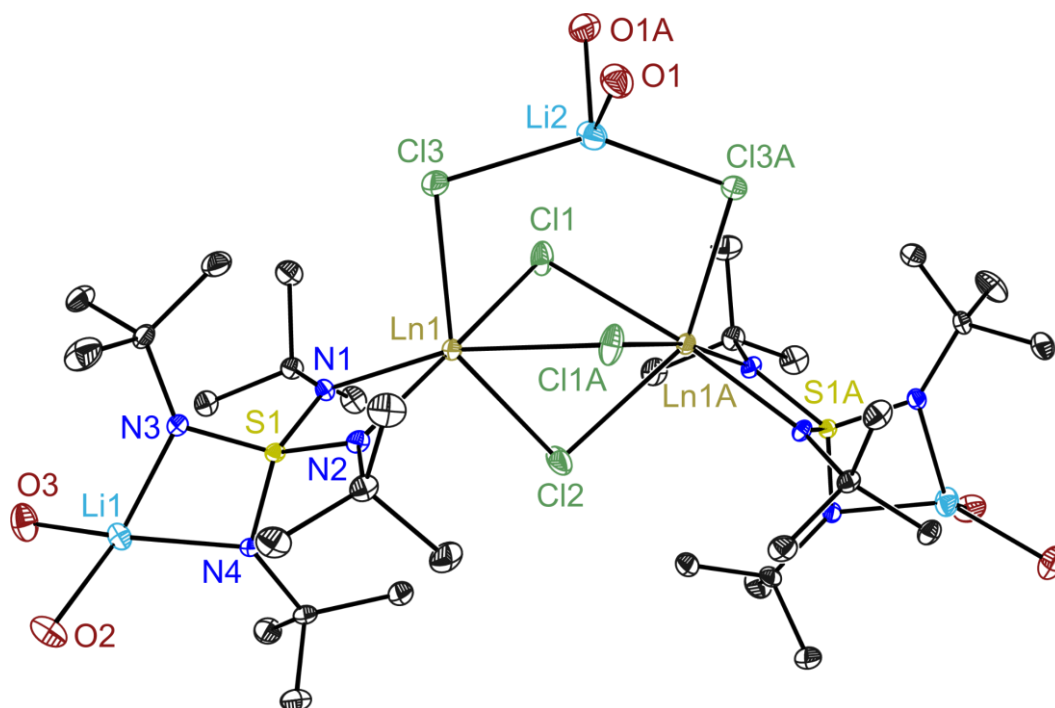


Figure 3-29 Crystal structure of **10a-e** (Ln = **a**: Gd, **b**: Tb, **c**: Dy, **d**: Ho, **e**: Er). Anisotropic displacement parameters are depicted at the 50% probability level for the dysprosium complex (for the others see chapter 5.5, **Figure 5-11** to **Figure 5-15**). The thf molecules are reduced to the coordinating oxygen atoms. Hydrogen atoms and disordered toluene molecule at lattice position are omitted for clarity. Selected bond length [Å] and angles [°] in average for **10a-e**. Ln1–N1 2.262, Ln1–N2 2.285, Ln1–Cl1 2.808, Ln1–Cl1A 2.759, Ln1–Cl2 2.698, Ln1–Cl3 2.644, S1–N1 1.624, S2–N2 1.629, S1–N3 1.569, S1–N4 1.566, Ln1···Ln1A 3.796, N1–Ln1–N2 61.61.

The lanthanide ions are coordinated in a distorted octahedral geometry. One equatorial coordination sides is occupied by the N,N' -chelating nitrogen atoms from the $[S(NtBu)_4]^{2-}$ ligand, while the four remaining ligands are chlorine atoms. Three chlorides bridge the two lanthanide ions forming the dimeric species of the two hetero bimetallic tetraimido sulfate moieties. The fourth chloride provides the Cl–Li–Cl link over the co-complexed lithium cation. All four Ln–Cl distances differ ranging for **10a** from 2.6707(5) Å to 2.8343(9) Å, and constantly shorten with decreasing ionic radii proceeding the period to **10e** (2.6171(8) Å to 2.7835(11) Å). The same trend can be found for the Ln–N distances that decrease from an average value of 2.299 Å in **10a** to 2.253 Å in **10e**. As seen for other complexes of the tetraimido sulfate ligand $[S(NtBu)_4]^{2-}$ (**L**¹), the S–N bond distances for all metal complexes are almost identical. Nevertheless, it should be mentioned that the averaged S–N1/N2 bond distances from the lanthanide site of the ligand (1.626 Å) are significantly longer than the S–N3/N4 distances from the lithium site (1.567 Å). That mirrors the two opposite coordination sides of the tetrahedral

ligand, which are unsymmetrically coordinated by a lithium ion at the site with shorter S–N bonds and the lanthanide(III) ions at the opposite site.

This difference can be explained by the strong ability of the triply positive charged lanthanides, which are obviously in much stronger demand of the negative charge at the nitrogen atoms, compared to lithium. This charge deficiency reduces the interaction between the positively charged sulfur and the nitrogen. A stronger demand of the charge located at nitrogen atoms causes a longer S–N bond. The reduced steric demand with decreasing lanthanide radii is also displayed in the reduction of the Ln1...Ln1A distances that ranges from 3.8347(5) Å in **10a** to 3.7517(5) Å in **10e**. Interestingly, the reduced radii have the opposite effect on the N1–Ln1–N2 angles, which increase from 60.91(4)° (**10a**) to 62.24(7)° (**10e**). Even though all Cl–Ln–Cl angles for one specific metal are different, they stay almost identical upon lanthanide exchange. The same trend was found for the N–S1–N angles.

A comparable coordination exists in a series of rare earth metal complexes with β -diketiminato ligands. Substitution at the nitrogen position with 2,6-dimethylphenyl,^[243] 2,6-diisopropylphenyl^[244–247] and mesityl^[248] resulted in binuclear complexes with unsymmetrically coordinated metal ions. Each one is attached to one β -diketiminato ligand and three bridging chlorines. One metal is additionally coordinated by a terminal chlorine atom, while the second one binds a thf molecule. The averaged Dy– μ -Cl bond distances of the tetra-chloro coordinated dysprosium in the complex with the mesityl substituted ligand^[248] display a value of 2.767 Å, hence close to those in **10c** with 2.726 Å. The same was found for the Dy–N bond length of 2.314 Å and 2.270 Å, respectively.

The non μ -LiCl-bridged monomeric species **11a–e** can be obtained by dissolving the appropriate dimer in small amounts of thf, from which they crystallize at room temperature. Alternatively, **11c** has also been obtained directly from the filtered reaction mixture at reduced temperature after the addition of *n*-pentane or by vapor diffusion. Since this synthesis was less efficient compared to the route along the previous isolation of the dimers, the synthetic route was not further developed for the other monomeric compounds. **11a–e** crystallize in the orthorhombic space group *Pca*2₁ with one molecule in the asymmetric unit (**Figure 3-30**). Compounds **10a–e** are almost monomeric to **11a–e** and from a theoretical elimination of 1 equiv. LiCl and the addition of 4 thf molecules, two monomers of **10a–e** would be obtained.

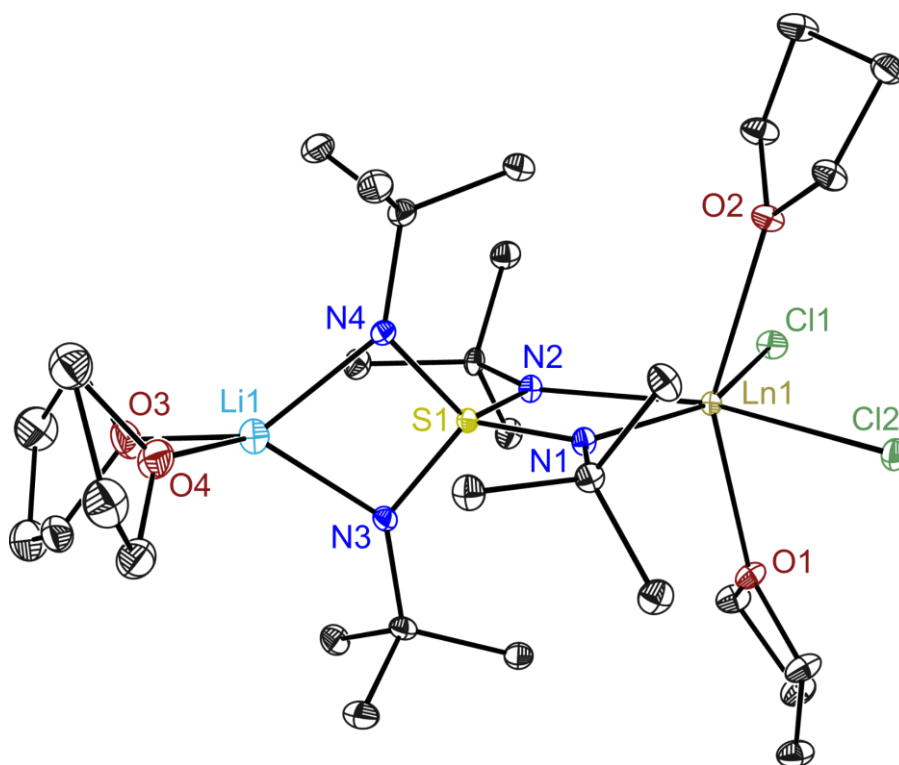


Figure 3-30 Crystal structure of **11a-e** (**a**: Ln = Gd, **b**: Tb, **c**: Dy, **d**: Ho, **e**: Er). Anisotropic displacement parameters are depicted at the 50% probability level for the dysprosium complex (for the others see chapter 5.5, **Figure 5-16** to **Figure 5-20**). Hydrogen atoms are omitted for clarity. Selected bond length [Å] and angles [°] in average for **11a-e**. Ln1–N1 2.330, Ln1–N2 2.325, Ln1–Cl1 2.648, Ln1–Cl2 2.639, Ln1–O1 2.418, Ln1–O2 2.418, S1–N1 1.629, S1–N2 1.633, S1–N3 1.567, S1–N4 1.565, N1–Ln1–N2 61.84, O1–Ln1–O2 149.88, N1–Ln1–N2 61.00, Cl1–Ln1–Cl2 108.05 (**11a**) 106.59 (**11b-e**).

The lanthanide ions are incorporated into a considerably distorted octahedral coordination geometry. One equatorial coordination sites is occupied by the *N,N'*-chelating nitrogen atoms from the $[S(NtBu)_4]^{2-}$ ligand, while two by chlorine atoms are bound at the opposite side. To saturate the coordination sphere, two thf molecules coordinate the lanthanide ions in the apical positions. To reduce steric hinderance, both are oriented away from the ligand's sterically demanding *tert*-butyl substituents.

The averaged Ln–N bond distances are slightly shorter compared to **10a-e** and range from 2.354 Å (**11a**) to 2.304 Å (**11e**). That mirrors the overall trend of stronger interaction for the smaller metal ions in the row from Gd to Er. The Ln1–Cl bond distances in **11a-e** (2.643 Å) are best comparable to the chlorine atoms in **10a-e** (2.644 Å) co-coordinated by the $Li(thf)_2$ unit. The Ln1–O distances are in the normal range for Ln–thf bonds. The O1–Ln1–O2 angle, that only slightly increases from **11a** to **11e**, has an averaged value of 149.88° and displays the strong distortion from an idealized octahedron, which is the result of the thf molecules trying to avoid the *t*Bu groups. The different S1–N bonds in **11a-e** are almost identical for all compounds and do not significantly differ from those in **10a-e**. Like in **10a-e**, a very acute N1–Ln1–N2 bite angle is found in **11a-e** (from 60.27(10)° to 61.61(5)°). This is promoted by

the N1–S1–N2 angle that is with averaged 92.83° far away from the ideal tetrahedral angle (109.5°) assumed from an idealized T_d symmetrical $[S(NtBu)_4]^{2-}$ dianion. The remarkable flexibility of this ligand, which has been noticed in other metal compounds before, supports the ligands adaptability to different electronic and steric requirements. The unoccupied space in the equatorial plane ultimately leads to a widening of the Cl1–Ln–Cl2 angle, largest for **11a** ($108.05(4)^\circ$) and with averaged 106.59° almost identical in **11b–e**.

In the synthesis of complex **10b**, a small amount of a tetranuclear side product $[\{(thf)_2Li(NtBu)_2S(tBuN)_2LnCl_2\}_4]$ (**14**) was isolated (**Figure 3-31**). It consists of four units of **11b** where the thf molecules at the terbium are replaced by two chlorine ions of the next unit, enabling the formation of a tetrameric tetra-nuclear species.

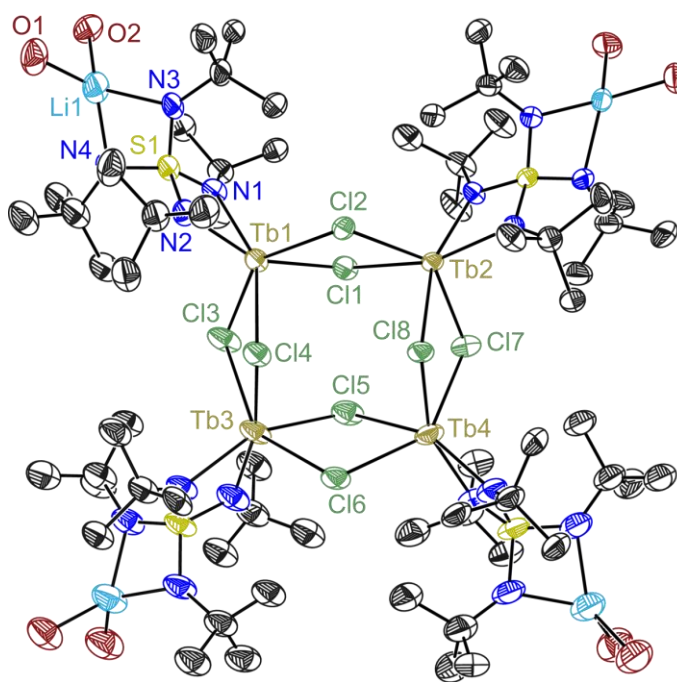


Figure 3-31 Crystal structure of **14**. Anisotropic displacement parameters are depicted at the 50% probability level. Hydrogen atoms and disordered ligands are omitted for clarity. Solvent molecules at lattice positions have not been refined. Selected bond length [Å] and angles [°] in averaged values: Tb–N 2.309, Tb–Cl 2.736, Tb⋯Tb 4.307, N1–Tb–N2 61.10° , N1–S1–N2 92.60° , N3–S1–N4 98.05° .

It should be mentioned that the product was only detected when the target molecule could not be isolated as a result of crystallization issues. Unfortunately, **14** is seriously disordered and the resulting X-ray data quality is rather poor. Similar crystals could not be found for dysprosium to erbium. In the case of gadolinium, a very poorly scattering crystal with very poor quality was found, which had cell parameters indicating that a similar structure might exist for Gd, too.

Still, it cannot entirely be excluded that in all syntheses this structural motive is formed as side product in small amounts. Nevertheless, due to crystallization process optimization, it is rather unlikely that the formation is realized in significant amounts since it is not promoted by the current crystallization strategy.

Besides poor data quality for the tetranuclear **14**, a structural comparison with the binuclear **10b** and the mononuclear **11b** is reasonable due to their similar structural core motifs (Table 3-9). For **14** the discussion will only focus on the structure parts at Tb1 and Tb2 that are not disordered.

The averaged Tb–N distances are close for all compounds with 2.283 Å (**10b**), 2.335 Å (**11b**) and 2.309 Å (**14**). All Tb–Cl bond distances are in a similar range, even though the terbium in **10b** and **14** are four-fold chlorine coordinated, while it is only two-fold in **11b**. The Tb–Cl bond distance for the two non-bridging chlorine atoms (2.655 Å) are comparable the lithium co-coordinated Cl in **10b** (2.6540(7) Å). In contrast, the Tb–Cl distances for the bridging chlorine atoms in **10b** (2.767 Å) and **14** (2.736 Å) are similar but longer than the aforementioned. With the rising nuclei number in **14**, the Tb···Tb distance increases to 4.307 Å compared to 3.8307(5) Å in **10b**. The acute N1–Tb–N2 bite angles of 61.22(8)° (**10b**) 60.67(7)° (**11b**) and 61.10° (**14**) are insignificantly different and evidently independent from the number of nuclei. The same is valid for the N1–S1–N2 angles of the *N,N'* chelating ligand at the Tb (91.47(11)°, 92.77(10)° and 92.60°) as well as for N3–S1–N4 at the Li side (96.54(11)°, 96.74(11)° and 98.05°).

Table 3-7 Selected bond lengths [Å] and angles [°] for **10b**, **11b** and **14**. For **14** only the structure parts at Tb1 and Tb2 were discussed. All bond lengths and angles are averaged if rational. More details can be found in the main text.

compound	10b	11b	14
Tb–N	2.283	2.335	2.309
Tb–Cl	–	2.6553	–
Tb–Cl (Li)	2.6540(7)	–	–
Tb–Cl (bridging)	2.7666	–	2.7363
Tb···Tb	3.8307(5)	–	4.307
N1–Tb–N2	61.22(8)	60.67(7)	61.10
N1–S1–N2 (Tb)	91.47(11)	92.77(10)	92.60
N3–S1–N4 (Li)	96.54(11)	96.74(11)	98.05

3.3.1.2. Magnetic properties

The magnetic data were collected and processed from both Prof. Dr. S. Demir and F. Benner. Full information on the data processing can be found in the publication (3).^[3] Temperature-dependent dc magnetic susceptibility data for the dimeric lanthanide complexes **10a-e** were collected in the temperature range between 2 – 300 K (**Figure 3-32**).

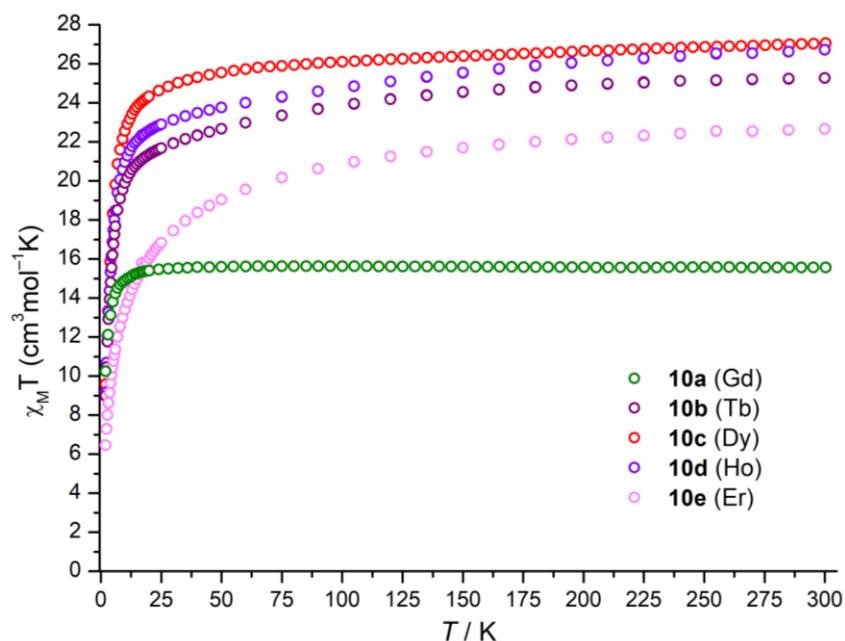


Figure 3-32 Temperature-dependent dc magnetic susceptibility measurement $\chi_M T$ vs. T for the lanthanide complexes **10a-e** collected under 1 T.

The room temperature $\chi_M T$ values at 1 T applied field for **10a-e** (15.56, 25.27, 27.06, 26.71 and 22.67 $\text{cm}^3 \text{mol}^{-1} \text{K}$) are in good agreement with the expected values for two uncoupled, triply positive Ln(III) ions (15.76, 23.62, 28.34, 28.12 and 22.96 $\text{cm}^3 \text{mol}^{-1} \text{K}$). For compounds **10b-e**, a gradual decline for $\chi_M T$ was found proceeding from high to low temperatures. At around 15 K, the values drop with increasing slope to reach low-temperature values (10.24, 8.99, 9.57, 9.14 and 6.46 $\text{cm}^3 \text{mol}^{-1} \text{K}$) at 2 K, which can be explained by the Zeeman effect or low intermolecular interactions. In comparison, the temperature dependence is much higher for the erbium compound **10e**, which indicates that the metal is strongly anisotropic in that particular coordination environment. Interestingly, the temperature dependence of $\chi_M T$ looks different for **10a**. Until 10 K is reached, the value almost stays the same. Below, it rapidly drops to reach a low temperature value of 10.24 $\text{cm}^3 \text{mol}^{-1} \text{K}$. This behavior indicates a small antiferromagnetic coupling of the two chloride bridged gadolinium ions. A useful characteristic of the triply positive gadolinium ion is the nature of a half-filled f-orbital valence shell. This allows to accurately calculate the anticipated coupling between the metal centers in **10a**. The coupling was

calculated according to the spin-only Hamiltonian $\hat{H} = -2J\hat{S}_{\text{Gd}(1)} + -2J\hat{S}_{\text{Gd}(2)}$ with the intramolecular coupling constant J and the spin operator \hat{S} . The fitted $\chi_M T$ vs. T data revealed a weak and antiferromagnetic coupling with the coupling constant $J = -0.045(1) \text{ cm}^{-1}$ (**Figure 6-27**). However, antiferromagnetic superexchange coupling in general is weak as it was found for other compounds.^[198]

Besides the investigations on the dimeric compounds, temperature-dependent dc magnetic susceptibility measurements were performed for the monomeric mononuclear species **11b-e** (**Figure 3-33**).

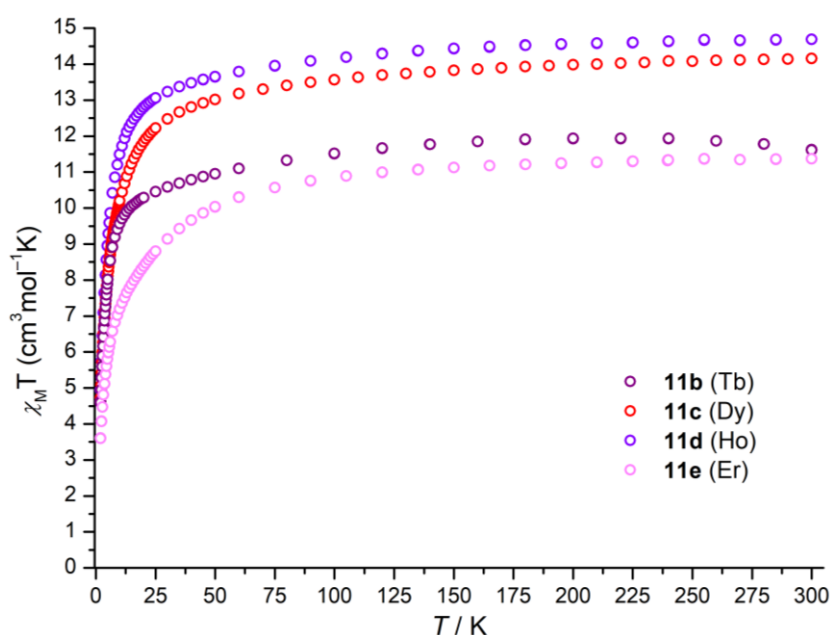


Figure 3-33 Temperature-dependent dc magnetic susceptibility measurement $\chi_M T$ vs. T for the lanthanide complexes **11b-e** collected under 1 T.

In this case, the gadolinium compound **11a** was not measured, since the half-filled electron shell does not promote magnetic anisotropy. The room temperature $\chi_M T$ values for **11b-e** are 16.62, 14.15, 14.69 and 11.37 $\text{cm}^3 \text{mol}^{-1} \text{K}$, hence marginally lower than the expected values for triply positive Ln(III) ions (11.81, 14.17, 14.06 and 11.48 $\text{cm}^3 \text{mol}^{-1} \text{K}$). Upon decreasing the temperature, **11b-e** show a similar temperature-dependent behavior as already discussed for **10b-e**.

To probe the presence of slow magnetic relaxation in **10b-e** and **11b-e** in-phase (χ_M') and out-of-phase (χ_M'') variable-frequency variable-temperature ac magnetic susceptibility data, under zero and under applied dc fields, were collected. The measurements revealed that compounds **10b,d,e** and **11d,e** do not display characteristic signals for χ_M'' , even under applied dc fields.

An exciting result was found for the dimeric dysprosium compound **10c**, which shows frequency dependent χ_M'' signals even under zero applied dc field and can therefore be classified as a true single molecule magnet SMM (**Figure 3-34**).

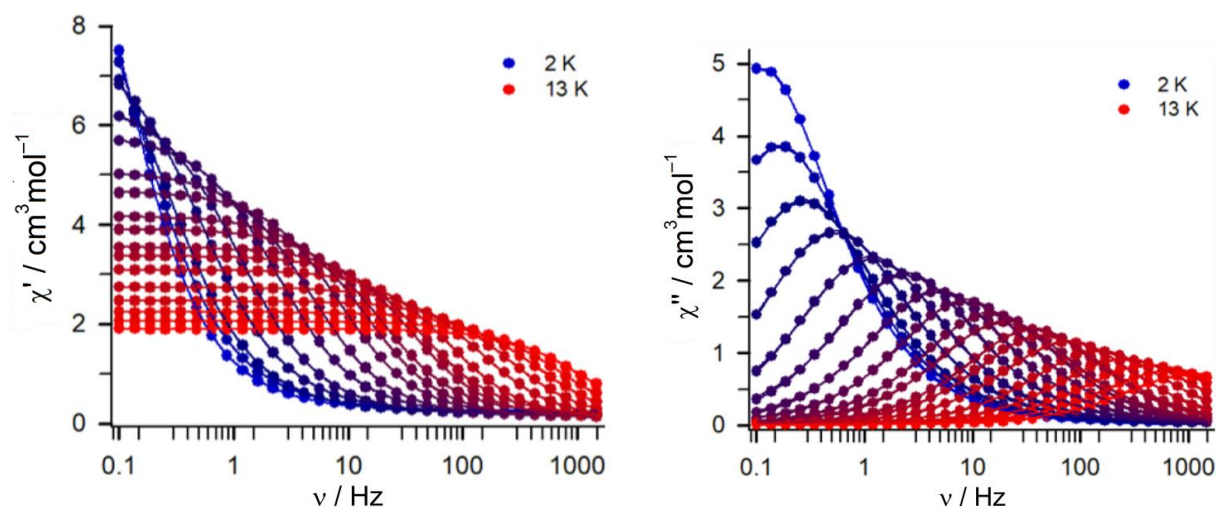


Figure 3-34 Variable temperature variable frequency in-phase (χ_M') and out-of-phase (χ_M'') ac susceptibility measurements for **10c** at zero applied dc field in the temperature range from 2 K to 13 K.

Full variable frequency variable temperature data were collected under zero applied dc field in the temperature range between 2 – 13 K. At 2 K, the out-of-phase (χ_M'') signal has its maximum at 0.1 Hz that shifts for higher temperatures to higher frequencies and gradually decreases in intensity. Cole-Cole plot construction and extraction of the corresponding relaxation times yielded the Arrhenius plots. The linear fit in the high temperature region yielded an effective thermal energy barrier to spin reversal of $U_{\text{eff}} = 43.9(8) \text{ cm}^{-1}$ with the relaxation time $\tau_0 = 1.1(1) \cdot 10^{-6} \text{ s}$ (**Figure 3-35** and **Table 3-8**).

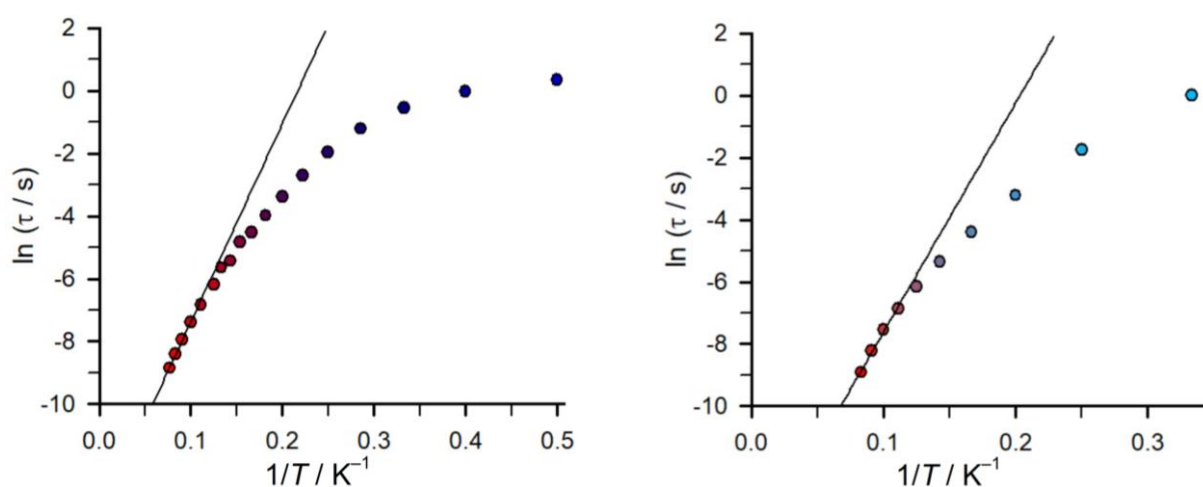


Figure 3-35 Arrhenius plot of **10c** at zero applied dc field in the temperature range from 2 K to 13 K with a fit for the data from 10 to 13 K (left) and under $H_{\text{dc}} = 500 \text{ Oe}$ applied dc field in the temperature range from 3 K to 12 K with a fit for the data from 9 to 12 K (right).

Interestingly, almost the same value was achieved under applying a dc field of $H_{dc} = 500$ Oe with $U_{eff} = 45.7(3) \text{ cm}^{-1}$. For comparison, when quantum tunneling and Raman processes were included according to **Eq. 3-2**, a significantly smaller value of $U_{eff} = 28.0(2) \text{ cm}^{-1}$ was calculated (**Figure 3-36**).

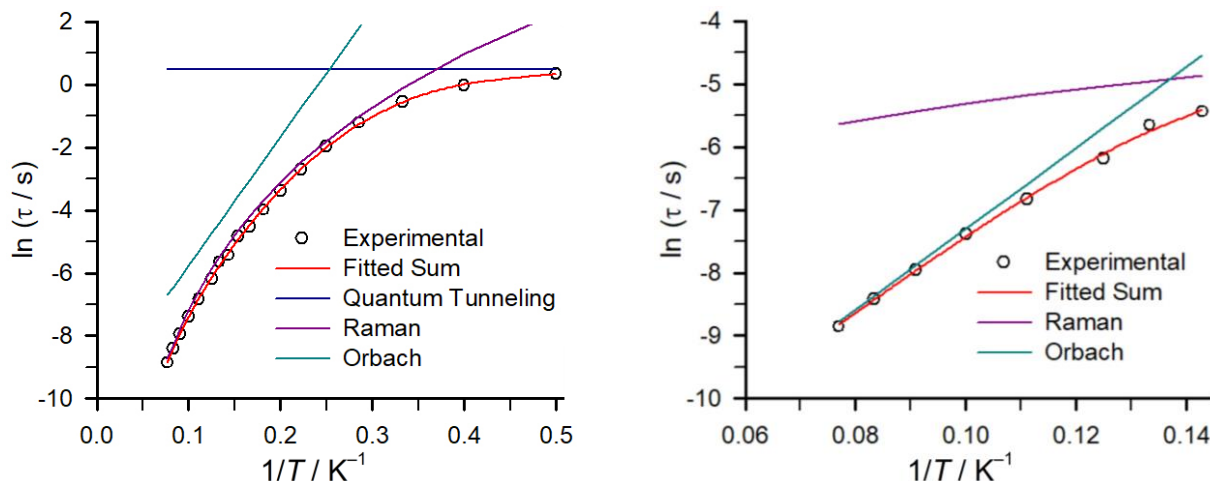


Figure 3-36 Individual contribution of the Quantum Tunneling, Raman and Orbach relaxation pathways to the Arrhenius plot for **10c** at zero applied dc field and in the temperature range between 7 K to 13 K (left) and under $H_{dc} = 500$ Oe applied dc field between 7 and 8 K (right).

Notably, a data fit including only Raman and Quantum tunneling processes yielded reasonable results, which may suggest that the energy barrier is underestimated, considering Orbach, Raman and Quantum tunneling processes.

A fit to an Orbach and Raman process yielded a higher value for the effective spin reversal barrier $U_{eff} = 44.8(1) \text{ cm}^{-1}$, which is comparable to the value obtained for only fitting the high temperature data (**Table 3-8**).

To suppress under-barrier relaxation processes, **10c** was additionally analyzed by applying the optimal external dc field of $H_{dc} = 500$ Oe. The high temperature linear fit of the Arrhenius plot yielded $U_{eff} = 45.7(3) \text{ cm}^{-1}$, comparable to the zero-field data. The best fit for the whole temperature range assuming an Orbach and Raman process ultimately revealed the highest value for the spin reversal barrier $U_{eff} = 64.9(1) \text{ cm}^{-1}$ with a relaxation time $\tau_0 = 5.2(8) \cdot 10^{-7} \text{ s}$ (**Figure 3-36**).

In contrast to the dimeric dysprosium compound **10c**, out-of-phase (χ_M'') signals were not observable for the monomeric terbium and dysprosium complexes **11b,c** under zero field. Nevertheless, since χ_M'' signals are sometimes observable under applied dc fields, frequency-dependent susceptibility data ranging from zero to 2400 Oe were collected. Indeed, the measurements revealed resonance maxima and optimal fields were found to be 2000 Oe (**11b**) and 500 Oe (**11c**).

Table 3-8 Selected magnetic parameters for compounds **10c**, **11b** and **11c** under zero and the optimal applied dc fields (H_{dc}). While $U_{eff,Orbach}$ only represents a linear fit to the high temperature data, $U_{eff,fullfit}$ includes Direct, Raman and Orbach relaxation processes according to **Eq. 3-3** for the whole data sets.

compound	10c	10c	11b	11c
H_{dc} (Oe)	0	500	2000	500
$U_{eff,Orbach}$ (cm^{-1})	43.9(8)	45.7(3)	–	11.1(1)
$U_{eff,fullfit}$ (cm^{-1})	28.0(2)	64.9(1)	42.8(6)	–
$\tau_{0,Orbach}$ (s)	$1.1(1) \cdot 10^{-6}$	$6.4(4) \cdot 10^{-7}$	–	$7.0(1) \cdot 10^{-7}$
$\tau_{0,fullfit}$ (s)	$5.7(1) \cdot 10^{-5}$	$5.2(8) \cdot 10^{-7}$	$2.2(4) \cdot 10^{-6}$	–
C ($\text{s}^{-1}\text{K}^{-n}$)	0.0017(1)	0.001(1)	68.21	–
n	5.89(1)	6.272(1)	1.686(7)	–
A ($\text{K}^{-1}\text{s}^{-1}$)	–	–	31.6(7)	–
τ_{QTM} (s)	1.63(1)	–	–	–

Variable frequency variable temperature ac susceptibility data were then collected at these optimum fields (**Figure 3-37**). **11b** shows χ_M'' signals in the temperature range between 2 K to 9 K. The extracted relaxation times from the Cole-Cole plot could be fitted according to **Eq. 3-3** that includes a Direct, Raman and Orbach relaxation process resulting in an energy barrier of $U_{eff} = 42.8(6) \text{ cm}^{-1}$.

$$\frac{1}{\tau_{obs}} = AH^4T + CT^n + \tau_0^{-1} \exp\left(-\frac{U_{eff}}{k_B T}\right) \quad (\text{Eq. 3-3})$$

The dysprosium compound **11c** only shows χ_M'' signals under an applied dc field of $H_{dc} = 500$ Oe between 1.8 – 2.4 K. The narrow window already indicates a small energy barrier for spin reversal and a linear fit of the Arrhenius plot yielded $U_{eff} = 11.1(1) \text{ cm}^{-1}$. The ultimate goal within the field of molecular magnetism is the presence of an open hysteresis loop with high remnant magnetization. Unfortunately, even at 1.8 K, only **10c** has a slightly opened butterfly-shaped hysteresis that is closed at zero dc field (see chapter 6, **Figure 6-28**). Within all other compounds, none showed any opening of the magnetization loop, even at higher fields.

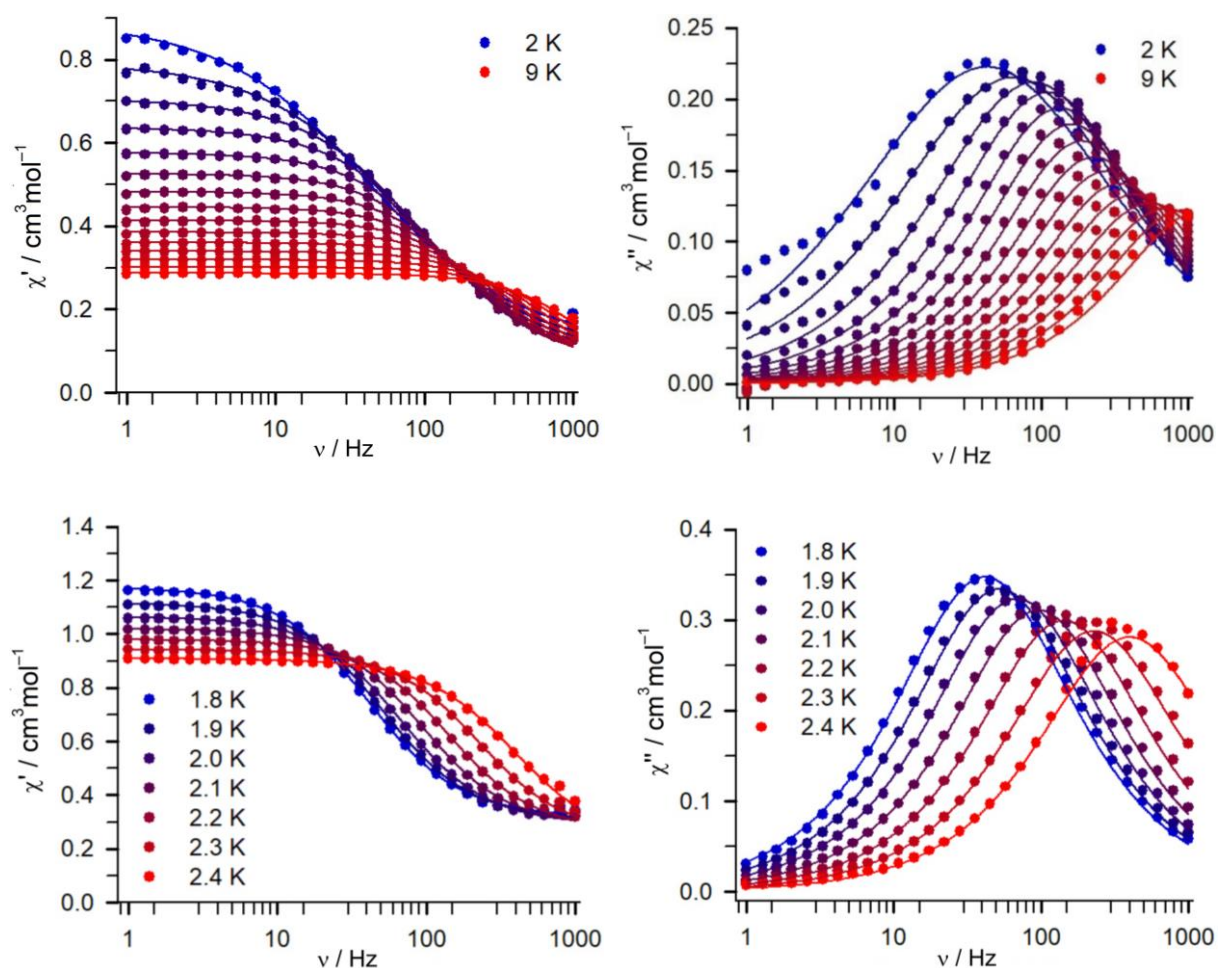


Figure 3-37 (top): Variable temperature variable frequency in-phase (χ_M') and out-of-phase (χ_M'') ac susceptibility measurements for **11b** under $H_{dc} = 2000$ Oe applied dc field in the temperature range from 2 K to 9 K. (bottom): Variable temperature variable frequency in-phase (χ_M') and out-of-phase (χ_M'') ac susceptibility measurements for **11c** under $H_{dc} = 500$ Oe applied dc field in the temperature range from 1.8 K to 2.4 K. Solid lines represent a fit to the data.

Furthermore, the orientation of the main magnetic axes of the ground-state for the dysprosium compounds **10c** and **11c** were calculated (**Figure 3-38**).

In **10c**, the main magnetic axes for the symmetry equivalent dysprosium ions was found between the bridging lithium ion and the most distant *tert*-butyl group. For **11c**, the main axes are located across the ligand through the lithium, the central sulfur atom and the dysprosium ion. Since both oxygen atoms in **11c** are perpendicular to the magnetic axes, it is likely that they introduce transverse anisotropy that hinders the magnetic performance. The crystal structure analysis already revealed both coordination motives to offer neither a strictly axial, nor a strictly equatorial ligand field. Due to their oblate shaped electron density, Tb(III) and Dy(III) ions require an axial LF in order to display the best magnetic performance. Thus, the removal of chloride anions or thf molecules might be a key to improve the SMM performance of **10c** and **11c**.^[145]

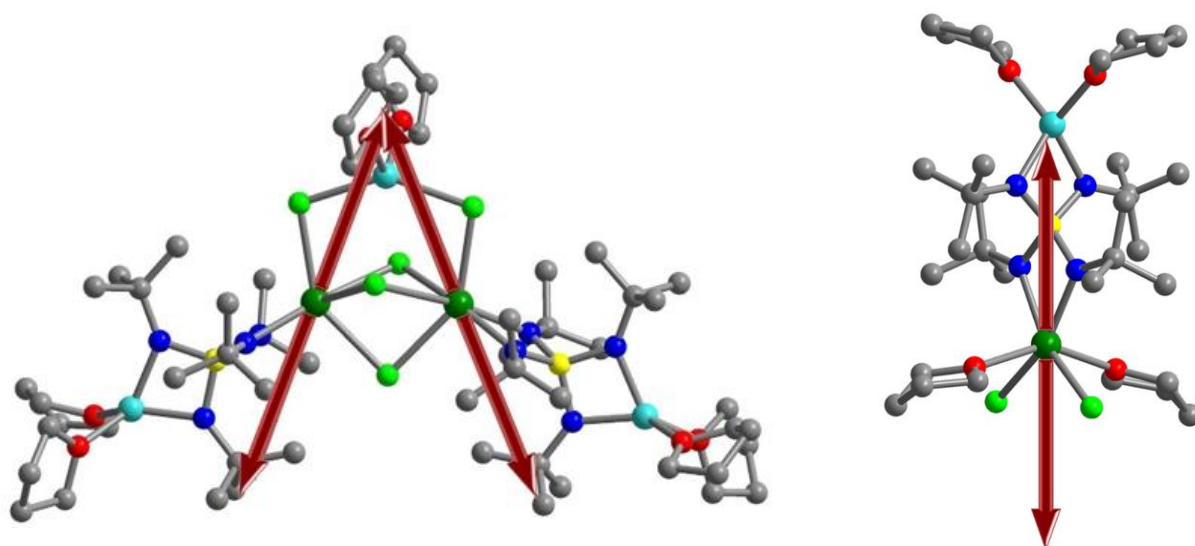


Figure 3-38 Main magnetic axes of **10c** (left) and **11c** (right). Dysprosium (dark green), chloride (pale green), nitrogen (blue), sulfur (yellow), lithium (turquoise), oxygen (red) and carbon (gray). Hydrogen atoms are omitted for clarity.

3.3.1.3. Conclusion on f-block metal SMMs containing the tetraimido sulfate $[S(NtBu)_4]^{2-}$

In the last chapter, the synthesis and the crystallographic and magnetic characterization of the first tetraimido sulfate $[S(NtBu)_4]^{2-}$ based f-element complexes $[{(thf)_2Li(NtBu)_2S(tBuN)_2LnCl_2}_2 \cdot ClLi(thf)_2}]$ (**10a-e**) and $[{(thf)_2Li(NtBu)_2S(tBuN)_2LnCl_2(thf)_2}]$ (**11a-e**) ($Ln = \mathbf{a: Gd, b: Tb, c: Dy, d: Ho, e: Er}$) in a series from gadolinium to erbium were presented. They were further characterized by crystallographic and magnetic studies. The monomeric terbium and dysprosium species $[{(thf)_2Li(NtBu)_2S(tBuN)_2LnCl_2(thf)_2}]$ **11b,c** show slow relaxation of the magnetization under applied dc fields. Therefore, they can be classified as field induced SMMs with $U_{eff} = 42.8(6) \text{ cm}^{-1}$ and $11.1(1) \text{ cm}^{-1}$, respectively. Furthermore, the binuclear dimeric dysprosium complex $[{(thf)_2Li(NtBu)_2S(tBuN)_2DyCl_2}_2 \cdot ClLi(thf)_2]$ **10c** was found to behave as a true single molecule magnet under zero applied dc field with a slow magnetic relaxation between 2 – 13 K and a energy barrier to spin reversal of $U_{eff} = 64.9(1) \text{ cm}^{-1}$.

3.3.2. f-block metal SMMS containing the triimido sulfonate $[\{\text{Ph}_2\text{PCH}_2\text{S}(\text{NtBu})_3\}]^-$

3.3.2.1. Synthesis and structure

The results in chapter 3.3.1 confirmed that the presence of lithium in the precursor for the synthesis with lanthanide halides results in an incorporation of LiCl into the structure, displayed by the binuclear dimeric compounds $[\{(\text{thf})_2\text{Li}(\text{NtBu})_2\text{S}(\text{tBuN})_2\text{LnCl}_2\}_2 \cdot \text{ClLi}(\text{thf})_2]$ (**10a-e**). Furthermore, the results demonstrated that a substitution of both Li ions in **L**¹ was not possible, at least for the chosen reaction conditions. To overcome the problem of lithium co-complexation in the synthesis of lanthanide complexes of the triimidosulfonate ligand $[\text{Ph}_2\text{PCH}_2\text{S}(\text{NtBu})_3]^-$ (**L**²), the potassium compound $[\text{K}(\text{thf})_3\{\text{Ph}_2\text{PCH}_2\text{S}(\text{NtBu})_3\}]$ (**5**) was synthesized in a previous reaction (chapter 3.2.2.2).

The potentially formed KCl from salt elimination is less soluble in common organic solvents compared to LiCl, which should result in an additional driving force to trigger the reaction. Furthermore, the large ionic radius^[249] of potassium should additionally support the persuaded metal exchange. The subsequent metal exchange reaction was done in pure thf, which did not produce any desired product at first. After storing the reaction mixture for several months at -34° , a small amount of crystalline $[\{\text{Ph}_2\text{PCH}_2\text{S}(\text{NtBu})_3\text{Dy}(\text{thf})\text{Cl}_3\text{K}(\text{thf})_2\}_2]$ (**15**) was formed that was isolated and suitable for single crystal X-ray diffraction analysis. Nevertheless, this reaction pathway was not further investigated for several reasons. The precipitation of KCl was not observable, which was indicative for a co-complexation rather than a salt elimination. Instead, an alternative reaction in toluene was performed and optimized in the meantime, which led to the desired product containing two ligands of $[\text{Ph}_2\text{PCH}_2\text{S}(\text{NtBu})_3]^-$. However, since the isolated amount of **15** was sufficient to perform XRD analysis and since the formation and the observed reaction behavior were key findings for facilitating the subsequent reaction, the structure will briefly be described.

The mixed metal compound $[\{\text{Ph}_2\text{PCH}_2\text{S}(\text{NtBu})_3\text{Dy}(\text{thf})\text{Cl}_3\text{K}(\text{thf})_2\}_2]$ (**15**) crystallizes in the triclinic space group $P\bar{1}$ with half a molecule of the compound and two disordered thf molecules at lattice positions in the asymmetric unit (**Figure 3-39**).

Expected KCl elimination and precipitation from the reaction mixture was not detected. Instead, two KCl were incorporated into the structure that bridge between the two $\{\text{Ph}_2\text{PCH}_2\text{S}(\text{NtBu})_3\text{Dy}(\text{thf})\text{Cl}_2\}$ subunits. Each Dy is found six-fold coordinated in a distorted octahedron coordination regime by three chlorine atoms, one thf molecule and *N,N'* chelated by the imido ligand. The chlorine atoms, in addition, bind the potassium atoms that for their part bridge to the second subunit. The Dy1–Cl bonds are almost identical with an averaged value of 2.6312 Å and an insignificant variation in bond length was found for the Dy–N1/2 bonds with averaged 2.3369 Å, too. The Dy1–O1 bond for the disordered thf molecule has a value of 2.3775 Å, which is in the normal range for a Dy(III) ion with six ligands.

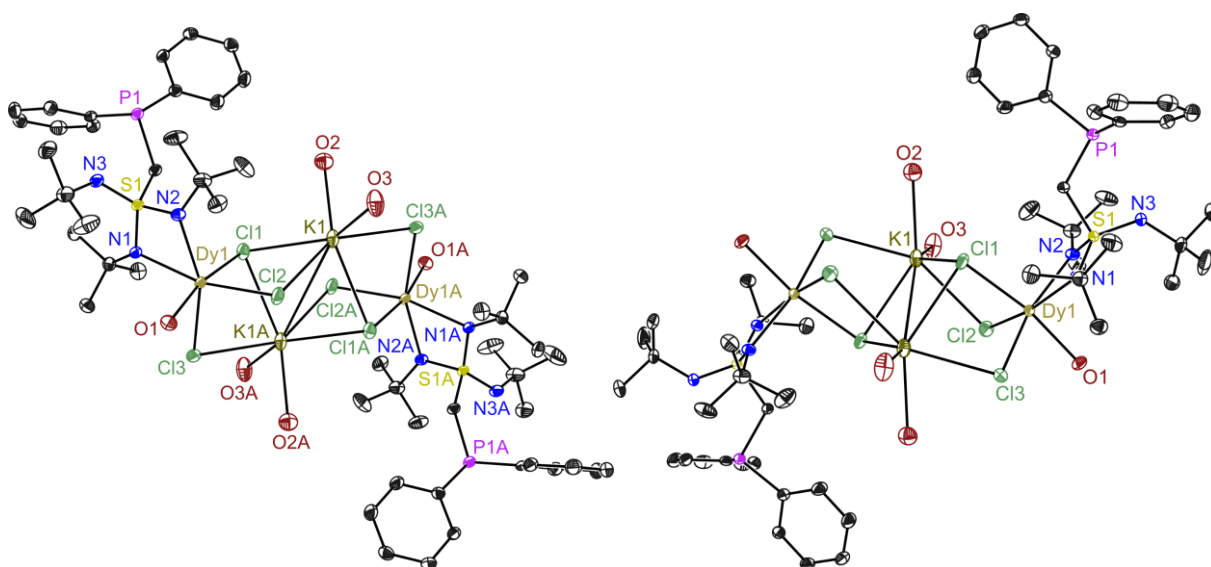


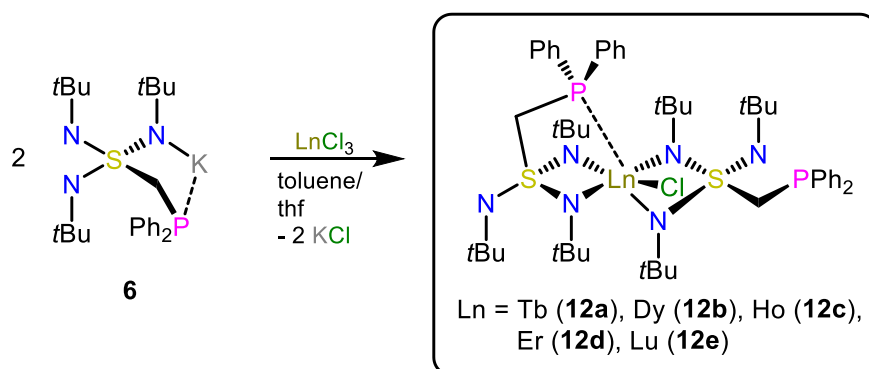
Figure 3-39 Crystal structure of **15**. Anisotropic displacement parameters are depicted at the 50% probability level. The thf molecules are reduced to the coordinating oxygen atoms. Hydrogen atoms and disordered thf molecules at lattice positions are omitted for clarity. Selected bond lengths [Å] and angles [°]: Dy1–Cl1 2.6334(6), Dy1–Cl2 2.6374(9), Dy1–Cl3 2.6228(9), Dy1–N1 2.3494(14), Dy1–N2 2.3243(15), Dy1–O1 2.3775(17), S1–N1 1.5989(14), S1–N2 1.5969(14), S1–N3 1.5195(14), N1–S1–N2 95.36(7), N1–Dy1–N2 60.74(5), Cl2–Dy1–Cl3 98.14(2), Cl1–Dy1–O1 170.2(9).

A closer examination of the $[\text{Ph}_2\text{PCH}_2\text{S}(\text{NtBu})_3]^-$ (L^2) ligand itself illustrates the adaptability of the S–N bonds and the flexible response to different coordination requirements, which is immanent for this ligand class. The sulfur imido bonds S1–N1/2 at the dysprosium side are almost identical with 1.598 Å. In contrast, the pendent nitrogen has a much shorter S1–N3 bond length of 1.5195(14) Å. All three N–S1–N angles are different with the smallest between N1–S1–N2 (95.36(7)°) as a result of metal coordination. The two angles that span to the metal's averted side are similar with 122.29(8)° (N1–S1–N3) and 121.51(8)° (N2–S1–N3).

The Dy ions display a distorted octahedral coordination with a Cl1–Dy1–O1 angle of 170.2(9)°. A pronounced deviation from ideal geometry is found in the equatorial plane that includes the N,N' chelating ligand. The N1–Dy1–N2 bite angle of 60.74(5)° is found to be remarkable acute, which is a common feature of this ligand and comparable to 60.22° in **12b** (which will be discussed in the following), while the Cl2–Dy1–Cl3 angle spans 98.14(2)°.

KCl precipitation could not be observed from a reaction in thf, which was a first indication, that an alternative synthesis was required. This was later confirmed by the isolation of the above described $[\{\text{Ph}_2\text{PCH}_2\text{S}(\text{NtBu})_3\text{Dy}(\text{thf})\text{Cl}_3\text{K}(\text{thf})_2\}_2]$ (**15**). Therefore, to trigger KCl elimination, the less polar solvent toluene was chosen. It was discussed in chapter 3.2.2.2 that the precursor $[\text{K}(\text{thf})_3\{\text{Ph}_2\text{PCH}_2\text{S}(\text{NtBu})_3\}]$ (**5**) loses the coordinating thf molecules over time when stored at room temperature, and that all thf molecules can be removed under reduced pressure. (For more details see chapter 3.2.2.2). As a result, when thoroughly dried, the thf-free **5** becomes insoluble in toluene. Since **5** was subsequently used for complexation reactions, it was mandatory to add thf in order to form the soluble thf complex of **5** and to ensure the completeness of the reaction. Without the addition of thf, no reaction product could be isolated.

For the synthesis of **12a-e**, thf-free **5** was suspended in toluene and approximately two volume percentage of thf were added to form the soluble $[\text{K}(\text{thf})_3\{\text{Ph}_2\text{PCH}_2\text{S}(\text{NtBu})_3\}]$ (**5**). After addition of the appropriate lanthanide(III) chloride, the reaction mixture was stirred for one day to form the desired complexes $[\text{LnCl}\{\text{Ph}_2\text{PCH}_2\text{S}(\text{NtBu})_3\}_2]$ **12a-e** (Ln = **a**: Gd, **b**: Tb, **c**: Dy, **d**: Ho, **e**: Er) (**Scheme 3-8**).



Scheme 3-8 Synthesis of the lanthanide complexes $[\text{LnCl}\{\text{Ph}_2\text{PCH}_2\text{S}(\text{NtBu})_3\}_2]$ **12a-e** (Ln = **a**: Tb, **b**: Dy, **c**: Ho, **d**: Er, **e**: Lu). From a reaction of the thf free $[\text{K}(\text{thf})_3\{\text{Ph}_2\text{PCH}_2\text{S}(\text{NtBu})_3\}]$ (**5**) with the appropriate lanthanide(III) chlorides in a mixture of toluene and approximately 2% thf, compounds **12a-e** were isolated in 30 to 51% yields.

Subsequently, the formed KCl was filtered off and all volatiles were removed under reduced pressure. The raw product was then dissolved in thf and carefully layered with *n*-pentane. After a few days at room temperature, crystals were formed that were suitable for single crystal X-ray diffraction analysis. Interestingly, the same product (only attempted for Dy) was isolated when only one equiv. of $[\text{Ph}_2\text{PCH}_2\text{S}(\text{NtBu})_3]^-$ was used instead.

12a-e are isomorphous and crystallize in the monoclinic space group $C2/c$ with one molecule of the compound and a thf/*n*-pentane disorder in the asymmetric unit (**Figure 3-40**).

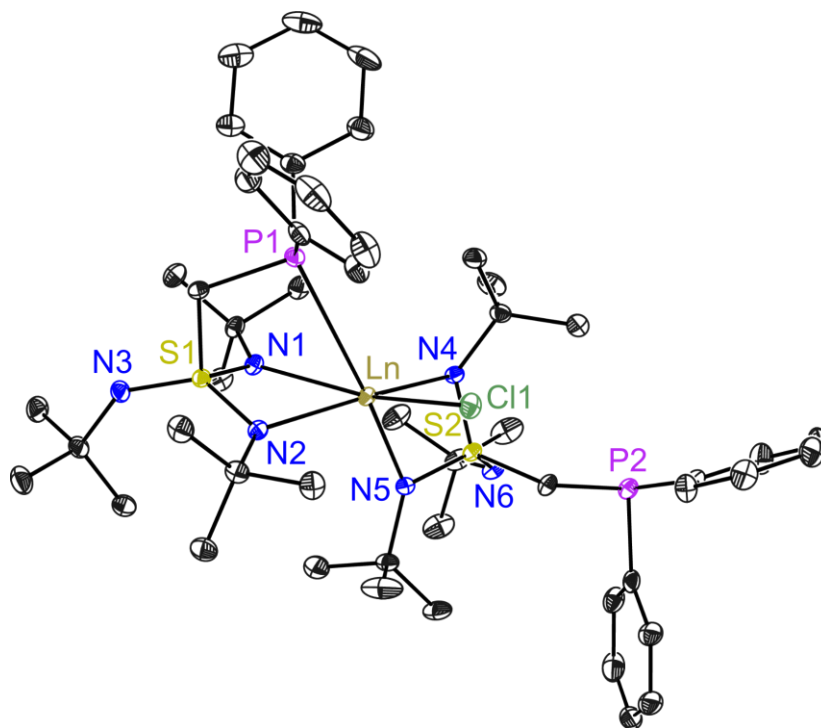


Figure 3-40 Crystal structure of **12a-e**. Anisotropic displacement parameters are depicted at the 50% probability level for the terbium complex **12a** (for the others see chapter 5.5, **Figure 5-22** to **Figure 5-26**). Hydrogen atoms and thf/*n*-pentane disordered molecules are omitted for clarity. Selected bond lengths [Å] and angles [°] are given for **12a**: Tb1–N1/2/4/5 2.365, Tb1–Cl1 2.6174(7), Tb1–P1 3.2291(6), Tb1–S1/2 3.099, N1–Tb1–N2 59.69(6), N4–Tb1–N5 59.97(6), N1–Tb1–P1 66.60(4), N2–Tb1–P1 67.47(4), P1–Tb1–Cl1 89.635(18), P1–Tb1–N5 171.62(4), N3–S1–C13 98.89(10); **12e**: Lu1–N1/2/4/5 2.300, Lu1–Cl1 2.5467(6), Lu1–P1 3.1900(5), Lu1–S1/2 3.022, N1–Lu1–N2 61.78(4), N4–Tb1–N5 62.15(6), N1–Lu1–P1 67.63(3), N2–Tb1–P2 68.73(3), P1–Lu1–Cl1 87.665(14), P1–Tb1–N5 172.37(3), N3–S1–C13 98.95(6).

As it was found for the KCl bridged $[\{\text{Ph}_2\text{PCH}_2\text{S}(\text{N}t\text{Bu})_3\text{Dy}(\text{thf})\text{Cl}_2\}_2]$ (**15**), the lanthanide(III) ions in **12a-e** are also six-fold coordinated. One $[\text{Ph}_2\text{PCH}_2\text{S}(\text{N}t\text{Bu})_3]^-$ ligand coordinates *N,N,P*-tripodal, while the second **L**² only chelates in a *N,N'* fashion with a phosphorus that is directed away from the metal. The coordination sphere is saturated by a chlorine atom and the geometry around the metal describes a strongly distorted octahedron. The Ln–Cl1 bond distance decreases from 2.6174(7) Å in **12a** to 2.5467(6) Å in **12e** as anticipated for decreasing ion radii proceeding the period. The four coordinating nitrogen atoms are crystallographically independent, even those connected to the same sulfur center.

The Ln–N distances range for **12a** from 2.3259(17) Å (Ln–N5) up to 2.4085(18) Å (Ln–N2) and follow the trend of decreasing bond lengths for smaller metal ions reaching in **12e** values of 2.2577(11) Å (Ln–N5) to 2.3393(11) Å (Ln–N2).

The four *N,N'* chelating S–N bonds are almost identical, even for the different compounds **12a–e** with an averaged value of 1.604 Å. In contrast, the pendent S1–N3 and S2–N6 bonds are significantly shorter of in average 1.515 Å. The opportunity of the ligand to flexibly respond to metal coordination by adopting the S–N bond lengths has already been discussed in the previous chapters.

The Ln–P1 bond distance decreases descending the period from 3.2291(6) Å in the terbium compound **12a** to 3.1900(5) Å in the lutetium complex **12e**. Even though those distances are at the end of the range found for other lanthanide phosphorus bonds, the geometries of the ligands are a clear indication for a pronounced P···Ln interaction. A similar observation was found for compounds **8** and **9** (see chapter 3.2.3). The attraction between P and Ln can especially be pointed out by the fact that the phosphorus atom from the second ligand points in the opposite direction. The flexibility of the ligand should principally offer the possibility for both phosphorus substituents to bend away from the metal, which would open a coordination site for a thf molecule, used as solvent. Since oxygen (thf) normally binds well to lanthanides, it can be assumed that the interaction in **12** is strong enough to prevent solvent coordination.

Remarkably acute are the almost identical N1–Ln1–N2 and N4–Ln1–N5 angles for one particular compound that slightly increase from 59.83° (**12a**) to 61.97° (**12e**). The N–S–N angles are almost unaffected by metal exchange and only marginally differ for the two ligands with averaged values of 95.43° (N1–S1–N2) and 94.17° (N4–S2–N5).

Attempts to characterize the paramagnetic lanthanide compounds **12a–d** via NMR-spectroscopy did not produce any utilizable spectra due to broad signals that extend over several tens of ppm. Instead, the diamagnetic lutetium compound **12e** was analyzed and the ¹H-NMR spectra in C₆D₆ is shown in **Figure 3-41**. A comparison with the protonated ligand [Ph₂PCH₂S(NtBu)₂NHtBu] (**4**) and the thf-free potassium precursor [K(thf)₃{Ph₂PCH₂S(NtBu)₃}] (**5**) further confirms the formation of the desired [LuCl{Ph₂PCH₂S(NtBu)₃}₂] (**12e**) by NMR-spectroscopy (**Figure 3-42**). The former singlet at δ = 1.65 ppm (for **5**) splits into two singlets. One resonates at δ = 1.50 ppm and corresponds to the *t*Bu groups, which are directed away from the metal. The larger signal at δ = 1.65 ppm can be attributed to the *t*Bu groups at the nitrogen atoms that coordinate to the lutetium ion. The methylene protons in **5** (doublet, δ = 3.94) shifted in the form of a multiplet to δ = 4.77 – 5.06. The phosphorus bound phenyl signals can be found in the normal region for aromatic protons and are different to the precursor. Due to a strong reactivity towards protonation, small amounts of **4** are present in the NMR sample of **5**. Nevertheless, **5** is not present, at least not above the detection level, in the ¹H-NMR spectrum of the lutetium complex **12e**, where only minor traces of **4** are visible.

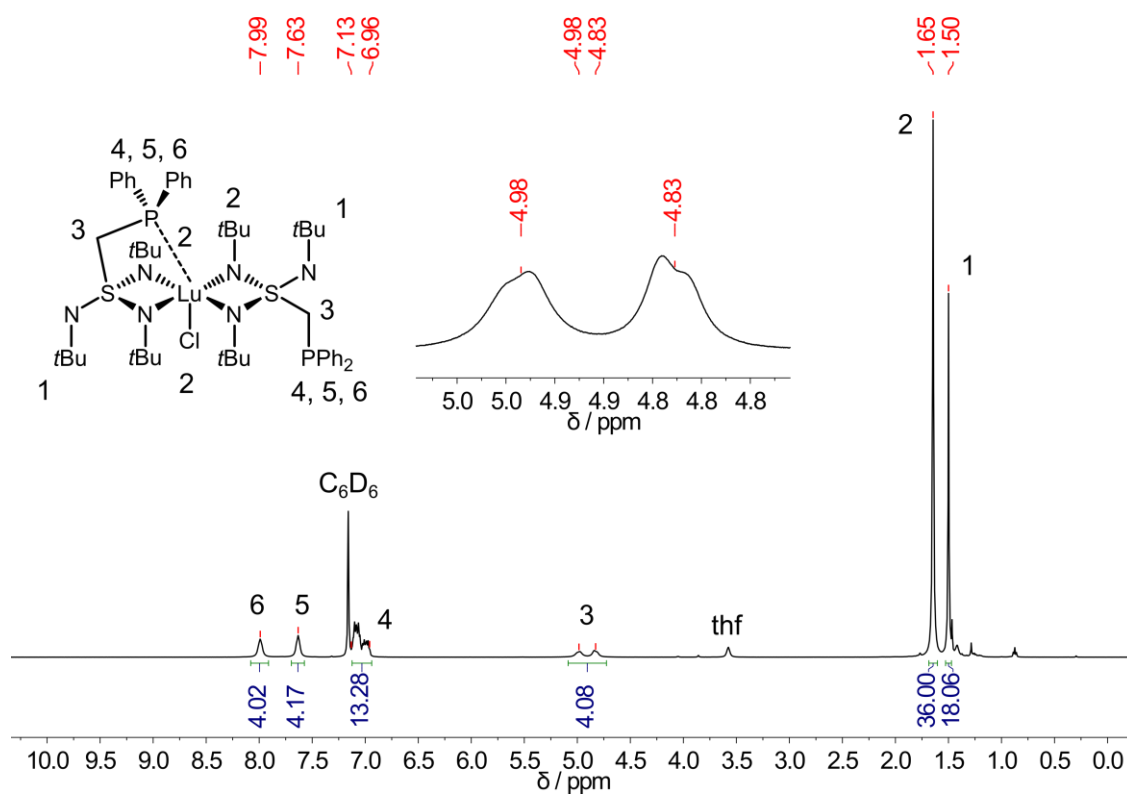


Figure 3-41 ^1H -NMR of **12e** at 298 K in C_6D_6 . δ [ppm] = 1.50 (s, 18H, 2 $\text{NC}(\text{CH}_3)_3$), 1.65 (s, 36H, 4 $\text{Lu-NC}(\text{CH}_3)_3$), 4.77–5.06 (m, 4H, 2 PCH_2), 6.96–7.13 (m, 12H, *m,p*-Ph-H), 7.63 (s, 4H, *o*-Ph-H), 7.99 (s, 4H, *o*-Ph-H).

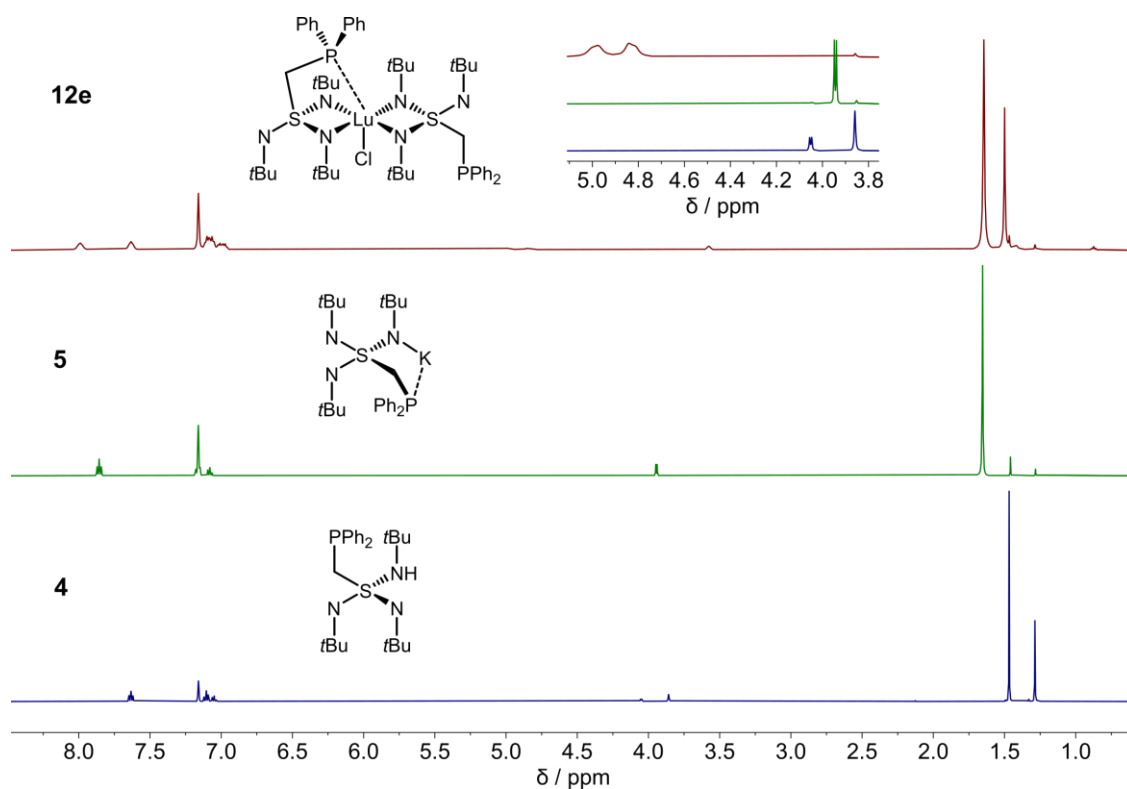


Figure 3-42 Comparison of the ^1H -NMR of **4** (bottom, blue), **5** (middle, green) and **12e** (top, red) at 298 K in C_6D_6 .

This is further confirmed by the ^{31}P -NMR comparison of all compounds (**Figure 3-43**). The ^{31}P -NMR spectrum of **12e** displays only one large singlet at $\delta = -24.59$ ppm, and in relation a very small signal that can be attributed to the protonated species **4** (at -16.98 ppm). The small amount of **4** can be explained as impurities, that arise from the high reactivity towards protonation. This was observed for all compounds containing the triimido sulfonate ligand $[\text{Ph}_2\text{PCH}_2\text{S}(\text{NtBu})_3]^-$ (**L²**), especially in solution.

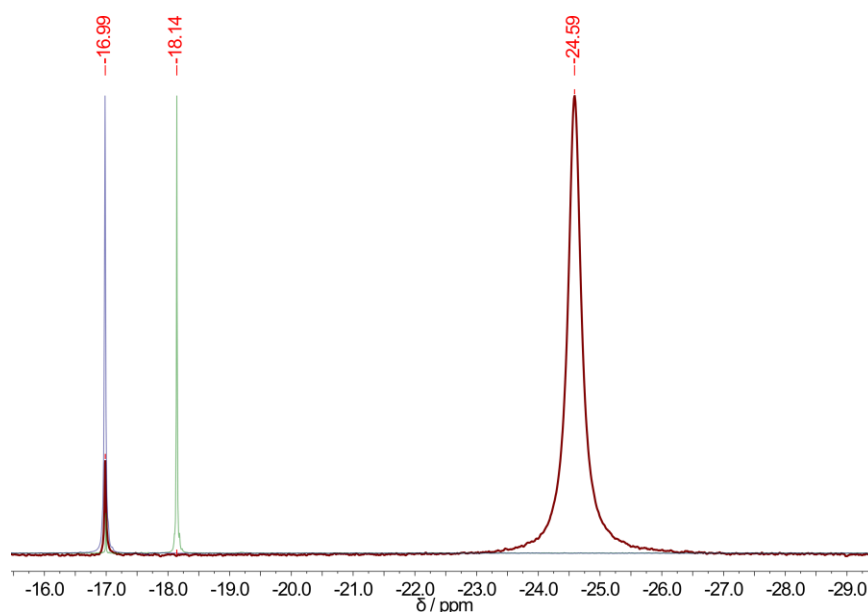


Figure 3-43 Superimposed $^{31}\text{P}\{^1\text{H}\}$ -NMR at 298 K in C_6D_6 of: **12e** (red) δ [ppm] = -24.59 (s); **4** (blue) and **5** (green).

Additionally, a $^{15}\text{N}/^1\text{H}$ -HMBC correlation spectrum was measured that reveals three different nitrogen signals (see chapter 6, **Figure 6-34**). The two metal chelating nitrogen atoms (tBu groups with a singlet at $\delta = 1.65$ ppm) have slightly different ^{15}N resonances with $\delta = -216.5$ and -218.7 ppm. In contrast, the pendent nitrogen is significantly different with $\delta = -255.2$ ppm.

The performed LIFDI mass spectrometry for **12a** was done from a thf solution with an expected m/z value of 1063.6 for $[\text{M-Cl}]^+$. The experiment and the corresponding isotope pattern are in good agreement with the calculations (**Figure 6-35**). The elemental analysis, which was done on crystalline material containing solvent molecules from the crystal lattice, fits well to the theoretical values for the atom composition derived from the crystal structure analysis.

The $^{13}\text{C}\{^1\text{H}\}$ -NMR as well as several two-dimensional $^{13}\text{C}/^1\text{H}$ -NMR spectra can be found in the attachment. For more analytical details of all lanthanide compounds $[\text{LnCl}\{\text{Ph}_2\text{PCH}_2\text{S}(\text{NtBu})_3\}_2]$ **12a-e** (Ln = **a**: Tb, **b**: Dy, **c**: Ho, **d**: Er, **e**: Lu) see chapter 5.3 and chapter 6, **Figure 6-29** to **Figure 6-34**.

3.3.2.2. Magnetic properties

The measurements and data processing were done by Dr. C. Legendre and Dr. S. Demeshko. Full information on the data processing and the calculations can be found in the PhD thesis of Dr. C. Legendre^[64] or in the publication (5).^[5] Temperature-dependent dc magnetic susceptibility data for the lanthanide complexes **12a-d** were collected in the temperature range between 2 – 210 K (**Figure 3-44**).

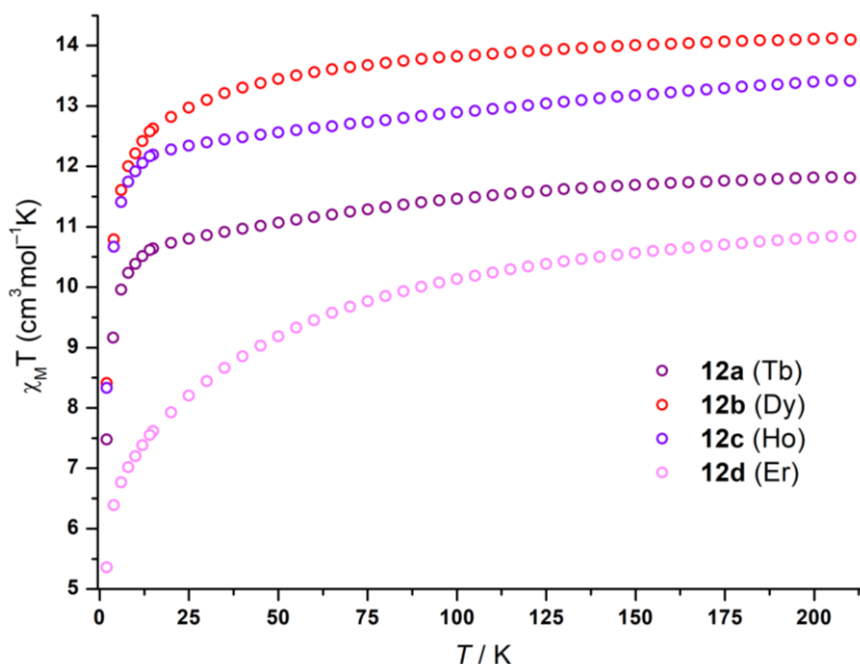


Figure 3-44 Temperature-dependent dc magnetic susceptibility measurement $\chi_M T$ vs. T for the lanthanide complexes (**12a-d**) at 0.5 T.

The $\chi_M T$ values at 210 K (11.81, 14.09, 13.41 and 10.86 cm³ mol⁻¹ K) (**12a-d**) are slightly lower than the expected values (11.82, 14.17, 14.04 and 11.48 cm³ mol⁻¹ K) for the triply positive lanthanide ions. Proceeding from high to low temperatures, the $\chi_M T$ values gradually decrease until around 15 K. Below, $\chi_M T$ drops rapidly to reach at 2 K low-temperature values of 7.46, 8.43, 8.29 and 5.39 cm³ mol⁻¹ K. The rapid decline can generally be explained by the Zeeman effect or low intermolecular interactions. The gradual decrease in $\chi_M T$ is most pronounced for **12d**, which can be associated with a highly anisotropic Er(III) in this particular coordination environment.

To probe the magnetic performance of **12a-d**, in-phase (χ_M') and out-of-phase (χ_M'') variable-frequency variable-temperature ac magnetic susceptibility data were collected. First, temperature-dependent χ_M'' measurements at dc fields of $H_{dc} = 0$ and 1000 Oe were performed, which revealed characteristic signals for **12a** (terbium), **12b** (dysprosium) and **12d** (erbium). For **12c** (holmium), the measurements revealed an optimal field of $H_{dc} = 1500$ Oe. However, a peak maximum in the frequency-dependent

χ_M'' measurement was only observable at 2 K. For higher temperatures, it shifted beyond the frequency limit of the magnetometer (see chapter 6, **Figure 6-42**).

Full data were then collected for the dysprosium complex **12b** under zero applied dc field in the temperature range between 2.0 – 12 K and at $H_{dc} = 1000$ Oe between 5.6 – 12.0 K.

For **12a** (Tb) and **12d** (Er), slow relaxation of the magnetization was observable under an applied dc field of $H_{dc} = 1000$ Oe for both compounds and up to temperatures of 25 K and 5 K, respectively (see chapter 6, **Figure 6-41** and **Figure 6-43**). The obtained χ_M'' data were plotted against χ_M' to construct Cole-Cole plots. From the extracted relaxation times, Arrhenius plots were obtained. The linear fit in the high temperature region yielded effective thermal energy barriers to spin reversal for a Orbach-type relaxation with $U_{eff} = 121$ cm⁻¹ (**12a**) and 20.5 cm⁻¹ (**12d**). This classifies both compounds as field induced SMMs. Calculations taking QTM, Raman and Orbach Relaxation processes into account (**Eq. 3-2**) yielded significantly higher values of $U_{eff} = 235$ and 34.5 cm⁻¹, respectively (**Figure 3-45** and **Table 3-9**).

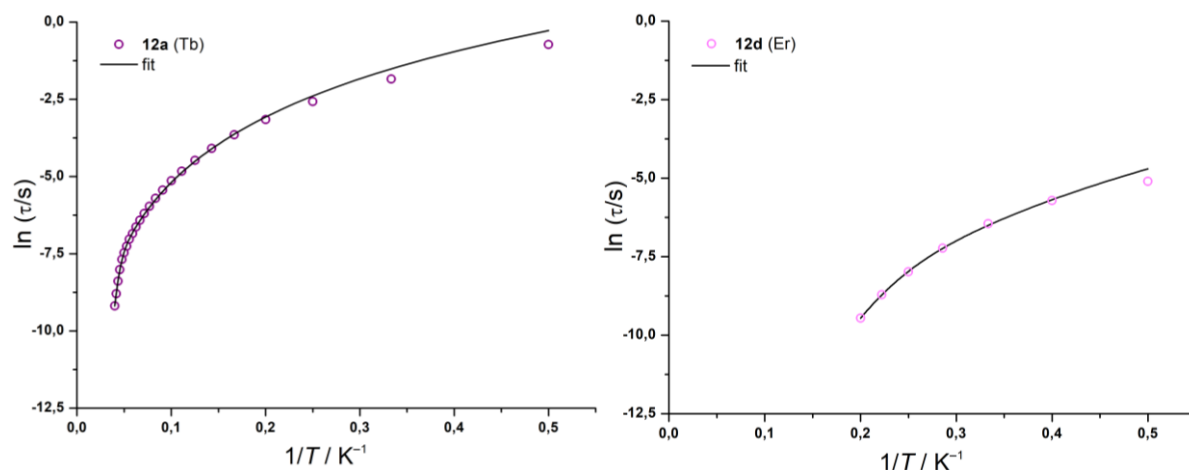


Figure 3-45 Arrhenius plots fitted according to **Eq. 3-2** under an applied dc field $H_{dc} = 1000$ Oe for **12a** (left) and **12d** (right). Solid lines represent a fit to the data

Particularly interesting results in the ac dynamic susceptibility were found for the dysprosium compound **12b** (**Figure 3-46**). Even without an applied dc field, peaks in the out-of-phase χ_M'' signal were observed up to 12 K. At low temperatures, no frequency dependence is observable. Instead, only a decreasing peak intensity was found until the temperature of around 5.6 K is reached, indicative of tunneling processes. In contrast, with an applied dc field of $H_{dc} = 1000$ Oe, the χ_M'' peak maxima are gradually shift to higher frequencies with lower intensities when the temperature was increased. This behavior strongly suggests that quantum tunneling is suppressed (**Figure 3-46**, bottom right).

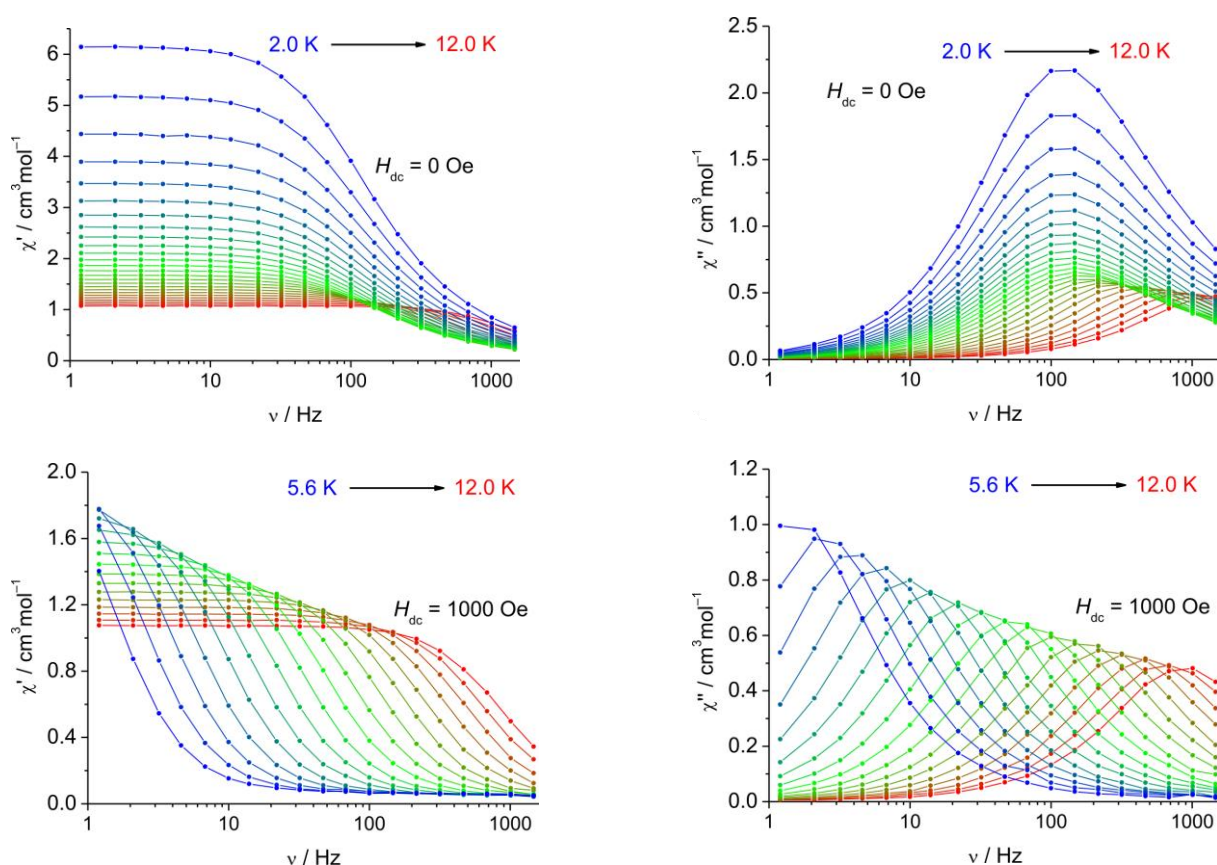


Figure 3-46 Variable-frequency variable-temperature in-phase (χ_M') and out-of-phase (χ_M'') ac magnetic susceptibility measurements for **12b** at zero applied dc field (top) and under $H_{dc} = 1000$ Oe (bottom).

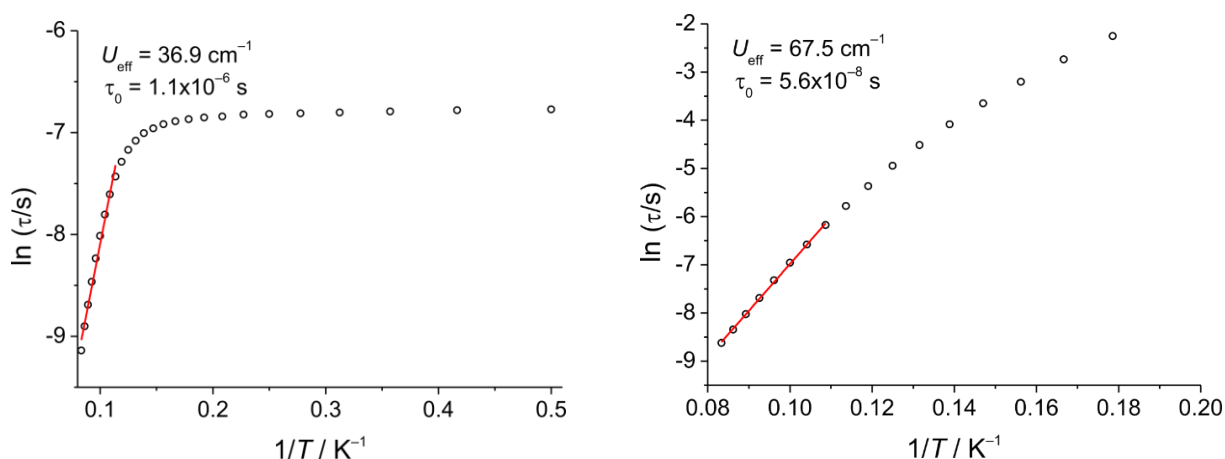


Figure 3-47 Arrhenius plot of **12b** at zero applied dc field (left) and under $H_{dc} = 1000$ Oe (right) and Orbach fits for the high-temperature data.

The Arrhenius plot yielded a small effective energy barrier $U_{eff} = 36.9 \text{ cm}^{-1}$ (0 Oe) with a relaxation time of $\tau_0 = 1.1 \cdot 10^{-6} \text{ s}$ (**Figure 3-47**). Interestingly, the U_{eff} value calculated from the applied dc field data is with 67.5 cm^{-1} almost double as high and comparable to the fit that additionally considered a QT and Raman process yielding $U_{eff} = 66.5 \text{ cm}^{-1}$ (**Figure 3-48** and **Table 3-9**).

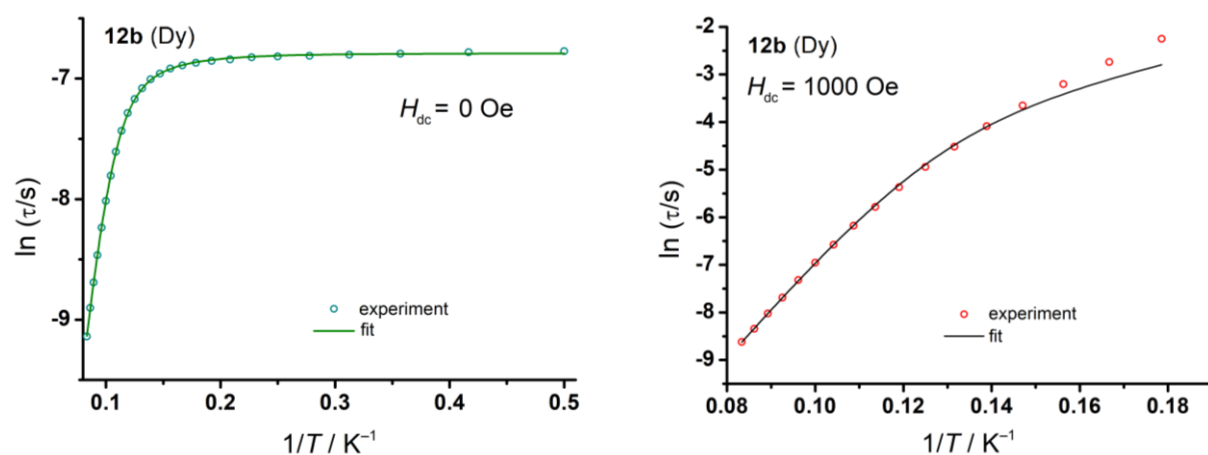


Figure 3-48 Arrhenius plot of **12b** fitted according to Eq. 3-2. (left): At zero applied dc field. (right): Under $H_{dc} = 1000$ Oe. Solid lines represent a fit to the data.

A remarkable result was obtained from the magnetization vs. field (M vs. H) measurements revealing a butterfly hysteresis for **12b**, observed between 2.0 – 3.5 K (**Figure 3-49**). Nevertheless, quantum tunneling probably prevents the retention of magnetization after removal of the applied field.

Intermolecular interactions between the magnetic metal centers possibly hamper the magnetic performance of **12b**. Therefore, to open the wings of the hysteresis at 0 Oe, those interactions need to be reduced and a magnetically dilution of the Dy(III) ions was considered to improve the magnetic performance. The diamagnetic and isomorphous lutetium compound **12e** was mixed in a 10:1 ratio with **12b** and they were crystallized to form the mixed analogue **12b@12e**.

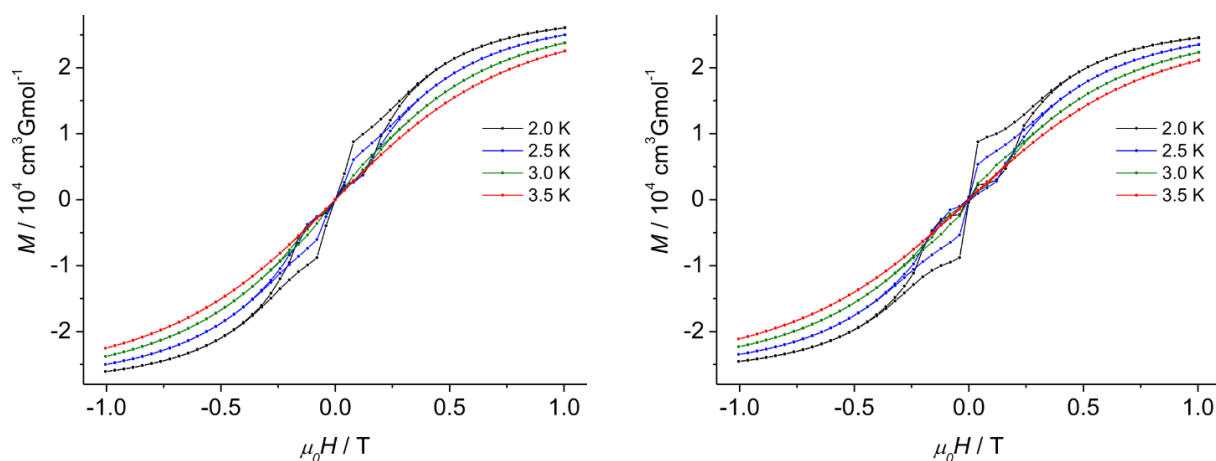


Figure 3-49 Butterfly hysteresis of the Dy(III) complex **12b** (left) and for the magnetically diluted **12b@12e** (right) between 2.0 and 3.5 K and with a sweep rate of 2.7 mTs^{-1} .

Unexpectedly, the variable-frequency variable-temperature ac magnetic susceptibility data under zero applied dc field **12b@12e** still shows a temperature independent process until 4.4 K is reached (**Figure 3-50**, top). Under an applied dc field of $H_{dc} = 1000$ Oe, no significant difference can be found compared to the applied dc field measurement for pure **12b** (**Figure 3-46** and **Figure 3-50**, bottom).

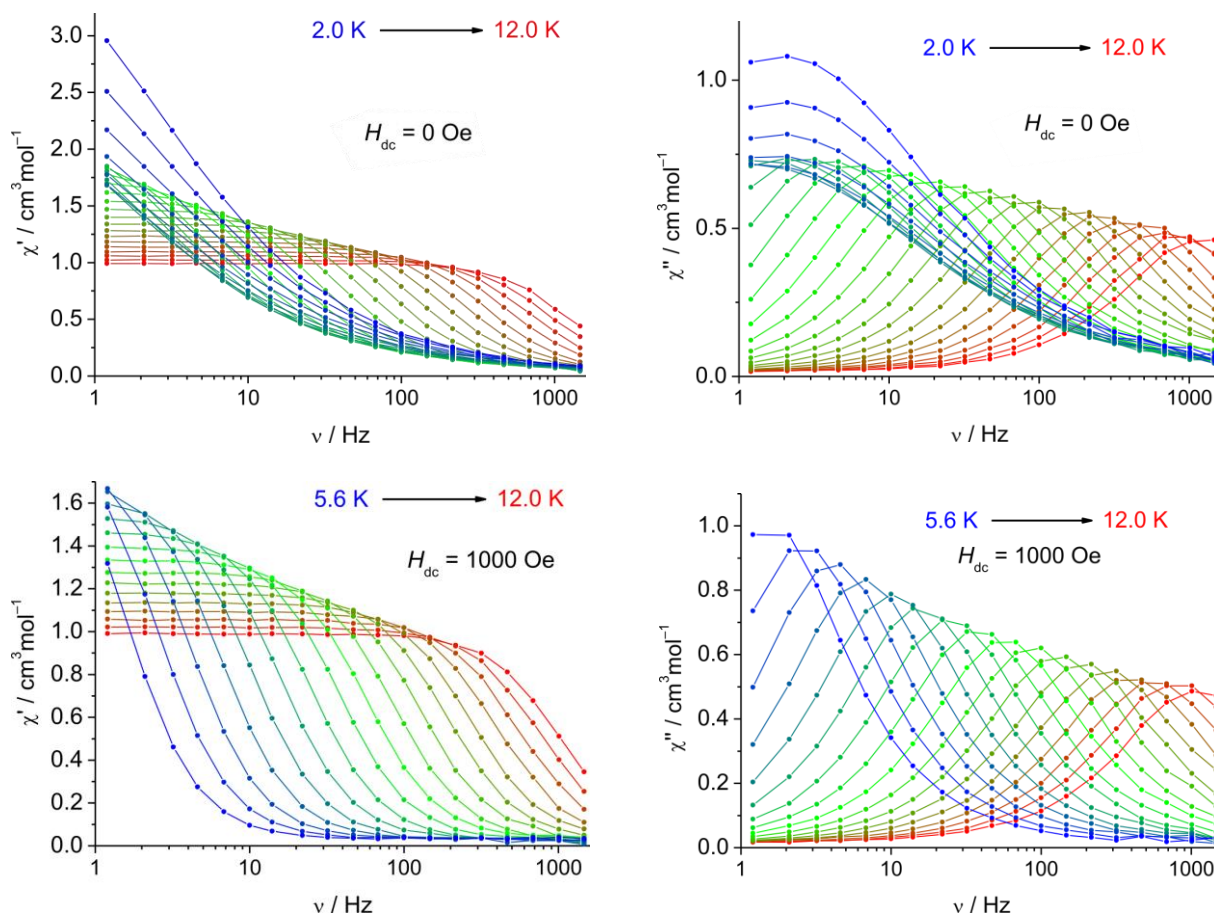


Figure 3-50 Variable-frequency variable-temperature in-phase (χ_M') and out-of-phase (χ_M'') ac magnetic susceptibility measurements for **12b@12e** at zero applied dc field (top) and under $H_{dc} = 1000$ Oe (bottom).

From the subsequently obtained Arrhenius plots, the thermal relaxation barriers (Orbach) were calculated to achieve similar values of $U_{eff} = 59.0$ cm^{-1} (0 Oe) and 66.5 cm^{-1} (1000 Oe) (**Figure 3-51**). Additionally, a fit according to **Eq. 3-2** yielded the slightly higher value of 74.3 cm^{-1} (1000 Oe) (**Figure 3-52** and **Table 3-9**). Interestingly, even though the barrier's height at zero field has doubled as a result of the magnetic dilution, almost the same result was achieved upon applying a dc field for the pure dysprosium compound **12b** ($U_{eff} = 67.5$ cm^{-1}). Additionally, a fit according to **Eq. 3-2** yielded a comparable result with $U_{eff} = 73.9$ cm^{-1} .

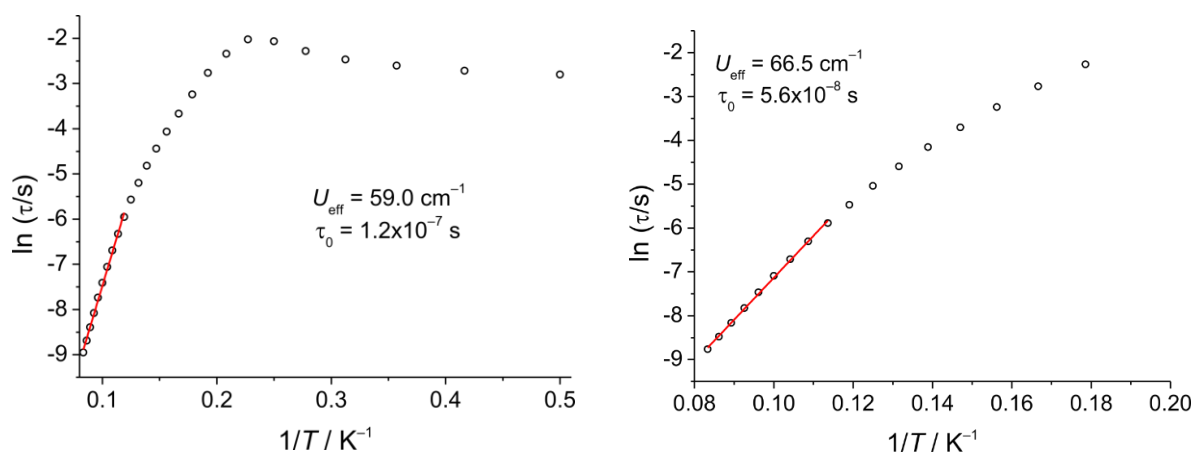


Figure 3-51 Arrhenius plot of **12b@12e** at zero applied dc field (left) and under $H_{dc} = 1000$ Oe (right).

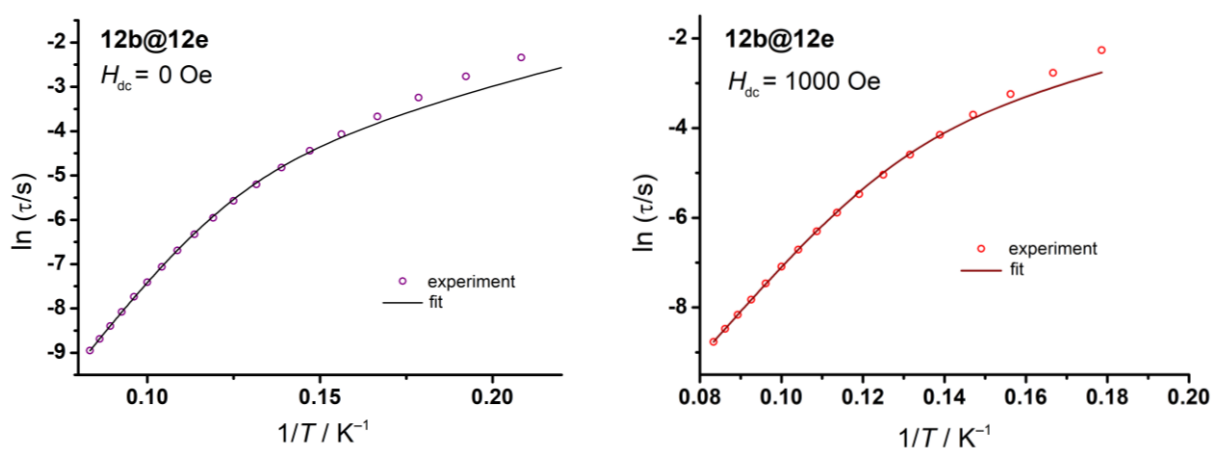


Figure 3-52 Arrhenius plot of **12b@12e** fitted according to Eq. 3-2. (left) at zero applied dc field; (right) under $H_{dc} = 1000$ Oe. Solid lines represent a fit to the data.

Table 3-9 Selected magnetic data for compounds **12a,b,d** and **12b@12c** at zero and applied dc fields of $H_{dc} = 1000$ Oe.

compound	12a	12b	12b	12b@12c	12b@12c	12d
H_{dc} (Oe)	1000	0	1000	0	1000	1000
$U_{eff,Orbach}$ (cm ⁻¹)	121	36.9	67.5	59.0	66.50	20.5
$U_{eff,fullfit}$ (cm ⁻¹)	235	66.5	73.9	71.0	74.3	34.5
$\tau_{0,Orbach}$ (s)	$1.1 \cdot 10^{-7}$	$1.1 \cdot 10^{-6}$	$5.6 \cdot 10^{-8}$	$1.2 \cdot 10^{-7}$	$5.6 \cdot 10^{-8}$	$1.05 \cdot 10^{-7}$
$\tau_{0,fullfit}$ (s)	$1.9 \cdot 10^{-9}$	$1.2 \cdot 10^{-7}$	$2.7 \cdot 10^{-8}$	$2.9 \cdot 10^{-8}$	$2.3 \cdot 10^{-8}$	$7.3 \cdot 10^{-9}$
C (s ⁻¹ K ⁻ⁿ)	0.17	0.065	0.012	0.016	$2.3 \cdot 10^{-8}$	5.2
n	3.0	4.0	4.2	4.4	$6.6 \cdot 10^{-3}$	4.4
τ_{QTM} (s)	—	$1.1 \cdot 10^{-3}$	—	—	—	—

Since the dilution did not have a significant impact on the energy barrier to spin reversal, it was concluded that further dilution attempts would not improve the magnetic performance of **12b**. Nevertheless, the butterfly-shaped hysteresis slightly improved. The wings are broader and close at a higher absolute coercive field value with an increase of 30 Oe.

Furthermore, the orientation of the main magnetic axes of the ground-state in **12b** was calculated. The axis is found nearby the *N,N'*-chelating nitrogen atoms and lies perpendicular to the chloride ions. For the oblate shaped Dy(III), a linear coordination environment is preferred. Therefore, this finding suggests that the chloride increases the amount of transverse anisotropy and that a removal in subsequent synthetic approaches may improve the magnetic performance of **12b**.

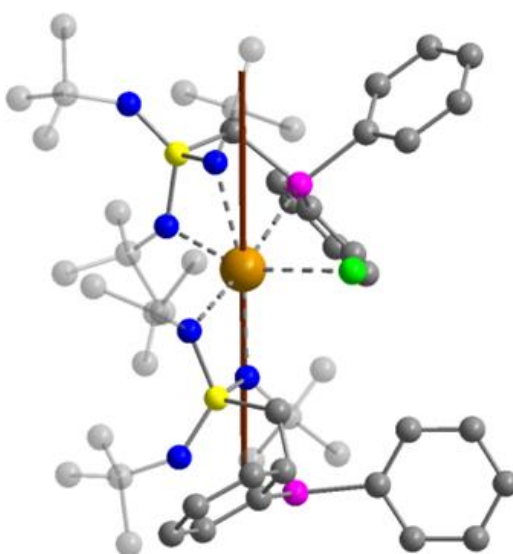


Figure 3-53 Main magnetic axes of the ground state for the dysprosium compound **12b** (brown line). Hydrogen atoms are omitted for clarity. Dysprosium (orange), chlorine (green), sulfur (yellow), phosphorus (pink), nitrogen (blue) and carbon atoms (grey).

3.3.2.3. Conclusion on f-block metal SMMs containing the triimido sulfonate $[\text{Ph}_2\text{PCH}_2\text{S}(\text{NtBu})_3]^-$

In the last chapter, the synthesis of the first triimido sulfonate $[\text{Ph}_2\text{PCH}_2\text{S}(\text{NtBu})_3]^-$ based f-element complexes **12a-e** (Ln = **a**: Tb, **b**: Dy, **c**: Ho, **d**: Er, **e**: Lu) were presented. They were further characterized by single-crystal X-ray diffraction and magnetic studies. Additionally, for the paramagnetic lutetium compound, NMR-investigations were performed confirming the formation of **12e**. The terbium and erbium compounds showed magnetic relaxation under applied dc fields and energy barriers to spin reversal of $U_{\text{eff}} = 235$ and 34.5 cm^{-1} , respectively. Furthermore, the dysprosium complex showed slow relaxation of the magnetization with $U_{\text{eff}} = 74.3 \text{ cm}^{-1}$ under zero applied dc field and a remarkable butterfly hysteresis up to 3.5 K, hence it can be classified as true single molecule magnet.

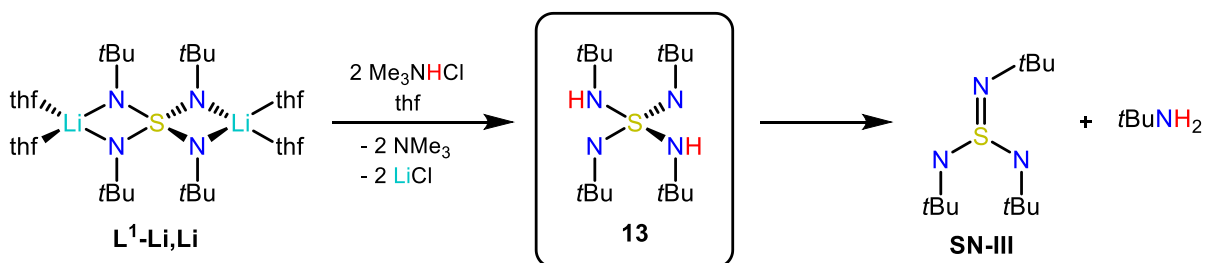
3.4. Tetraimido sulfuric acid $\text{H}_2\text{S}(\text{NtBu})_4$ – a valence isoelectronic analogue to H_2SO_4

3.4.1. Synthesis and characterization

During the last chapters, it was demonstrated that synthetic challenges for the utilization of the lithiated tetraimido sulfate $[(\text{thf})_4\text{Li}_2(\text{NtBu})_4\text{S}]$ (**L¹-Li, Li**) in metal exchange reactions mainly arise from lithium halide co-complexation and elimination. Furthermore, it was shown that protonated ligand species of the imido family offer a fruitful opportunity for various subsequent reactions (chapters 3.2.2.2 and 3.2.3.2). In order to open new synthetic routes, the protonated and valence isoelectronic imido analogue $\text{H}_2\text{S}(\text{NtBu})_4$ (**13**) to sulfuric acid H_2SO_4 was synthesized. Besides all the synthetic possibilities this compound offers, it is a unique molecule, which enables the analysis of the imido ($-\text{NtBu}$) alongside the amido ($-\text{N}(\text{H})\text{tBu}$) bond within one compound.

In a publication from 1998, Stalke *et al.* proposed the synthesis of the corresponding compound that was subsequently deprotonated using $\text{Ba}\{\text{N}(\text{SiMe}_3)_2\}_2$.^[36] However, the authors did not succeed in the isolation or any other analytical characterization of the protonated intermediate, at that time. More than 20 years later, this mission has been accomplished.^[1]

In order to synthesize $\text{H}_2\text{S}(\text{NtBu})_4$ (**13**), the lithiated tetraimido sulfate $[(\text{thf})_4\text{Li}_2(\text{NtBu})_4\text{S}]$ (**L¹-Li, Li**) was gently protonated with two equiv. of Me_3NHCl in thf at room temperature (**Scheme 3-9**). After a short reaction time of two minutes, the solvent was removed under reduced pressure. The residue was extracted with *n*-pentane and the suspension was filtered to remove LiCl . To further remove unreacted starting material or soluble LiCl -thf adducts, the extract was washed with acetonitrile. After concentrating the solvent to a minimum amount, the mixture was stored at -34°C . Crystallization started within minutes, yielding crystals of **13** that were dried under reduced pressure for isolation.



Scheme 3-9 Synthesis of the tetraimido sulfuric acid $\text{H}_2\text{S}(\text{NtBu})_4$ (**13**). Protonation of the lithiated precursor $[(\text{thf})_4\text{Li}_2(\text{NtBu})_4\text{S}]$ (**L¹-Li, Li**) with 2 equiv. of Me_3NHCl led to the isolation of crystalline **13** in 73% yield. Upon elevated temperatures or in solution **13** starts to decompose to form $\text{S}(\text{NtBu})_3$ (**SN-III**) and tBuNH_2 .

Besides Me_3NHCl as protonating agent, the synthesis of **13** was also successful with the primary amine $t\text{BuNH}_2\text{Cl}$. Due to the decomposition of **13**, a reliable prediction of isolated yields is not possible, but both syntheses revealed comparable results within the uncertainties that are inherent for the isolation. For more synthetic details see chapter 5.3.24.

As suggested, it turned out that $\text{H}_2\text{S}(\text{N}t\text{Bu})_4$ (**13**) is unstable in solution and in the solid-state, even at low temperatures. This circumstance clarifies why a short reaction time is beneficial for the synthesis and explains why reproducibility with comparable yields is only possible within a broad range. Nevertheless, the compound appears to be storable at temperatures below -34°C for several months without significant decomposition. Instead, higher temperatures generate increasing impurities of $\text{S}(\text{N}t\text{Bu})_3$ (**SN-III**), the analogue to SO_3 .^[33,250,251] Similar solubilities make fractional crystallization impossible, and attempted high-vacuum sublimation only resulted in the isolation of **SN-III**. The second decomposition product is *tert*-butylamine (**Figure 3-54**). The ratio of **13** and **SN-III** can be determined via ^1H -NMR spectroscopy and integration of the corresponding signals, which are sufficiently different in their chemical shift. **Figure 3-54** shows the ^1H -NMR spectrum of a crystalline compound composition of **13** with the impurity **SN-III** in C_6D_6 .

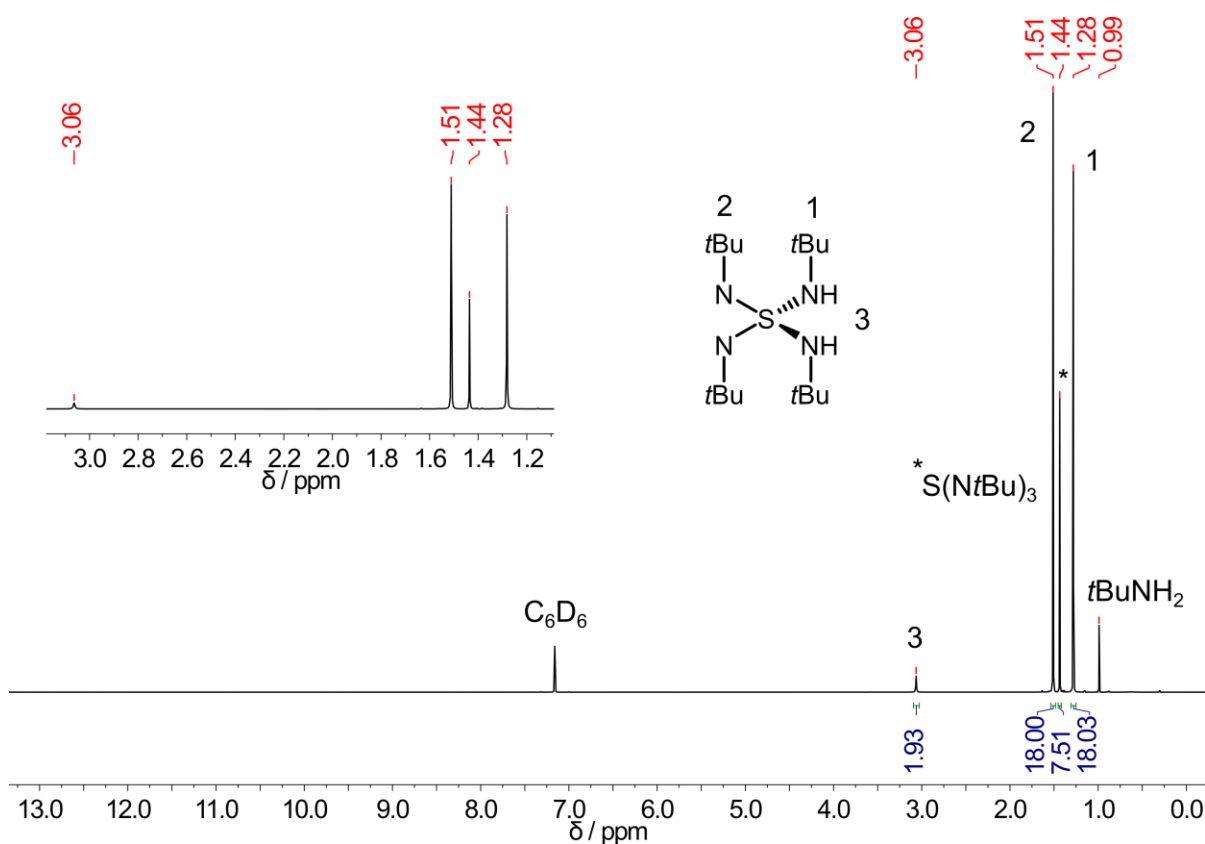


Figure 3-54 ^1H -NMR of **13** at 283 K in C_6D_6 . δ [ppm] = 1.28 (s, 18H, 2 $\text{HNC}(\text{CH}_3)_3$), 1.51 (s, 18H, 2 $\text{NC}(\text{CH}_3)_3$), 3.06 (s, 2H, 2 $\text{HNC}(\text{CH}_3)_3$). The signals for the two decomposition products can be found at $\delta = 1.44$ ppm (**SN-III**) and $\delta = 0.99$ ppm ($t\text{BuNH}_2$).

The signal of the two equivalent nitrogen bound protons of **13** can be found at $\delta = 3.06$ ppm and the $^{15}\text{N}/^1\text{H}$ HSQC (chapter 6, **Figure 6-39**) and the $^{15}\text{N}/^1\text{H}$ HMBC (chapter 6, **Figure 6-40**) correlation spectra revealed that the $\text{N}(\text{H})\text{tBu}$ have the same nitrogen environment as the *tert*-butyl groups resonating at $\delta = 1.28$ ppm. The proton-free NtBu groups at $\delta = 1.51$ ppm, in contrast, do not show any NH interference. Additionally, the ^{15}N -NMR chemical shifts of the nitrogen atoms in **13** (-253.2 ppm for NtBu and -257.4 ppm for $\text{N}(\text{H})\text{tBu}$) are different to those of $\text{S}(\text{NtBu})_3$ (**SN-III**) ($\delta = -253.2$ ppm). Since **13** decomposes in solution, both side products **SN-III** ($\delta = 1.44$ ppm) and tBuNH_2 ($\delta = 0.99$ ppm) can be found in the ^1H -NMR spectrum of $\text{H}_2\text{S}(\text{NtBu})_4$ (**13**).

The significant amount of tBuNH_2 in the ^1H -NMR spectrum, that was measured right after the freshly isolated sample (including **13** and **SN-III**) was dissolved in C_6D_6 , indicates that the imido sulfuric acid starts to decompose right after dissolving. However, a full exclusion of tBuNH_2 contaminations at the surface of the crystalline compound is not possible. Moreover, it is both possible that tBuNH_2 arises from decomposition of **13** or that contaminations can be attributed to unremoved side product from the actual reaction. Though, to verify the assumption that the imido sulfuric acid **13** decomposes to form **SN-III** and tBuNH_2 , an NMR sample has been analyzed over several hours. In case of decomposition, the corresponding signals of **13** should ultimately vanish and the signals for both decomposition products should grow in relation to **13**. The time-resolved NMR experiment is depicted in **Figure 3-55**.

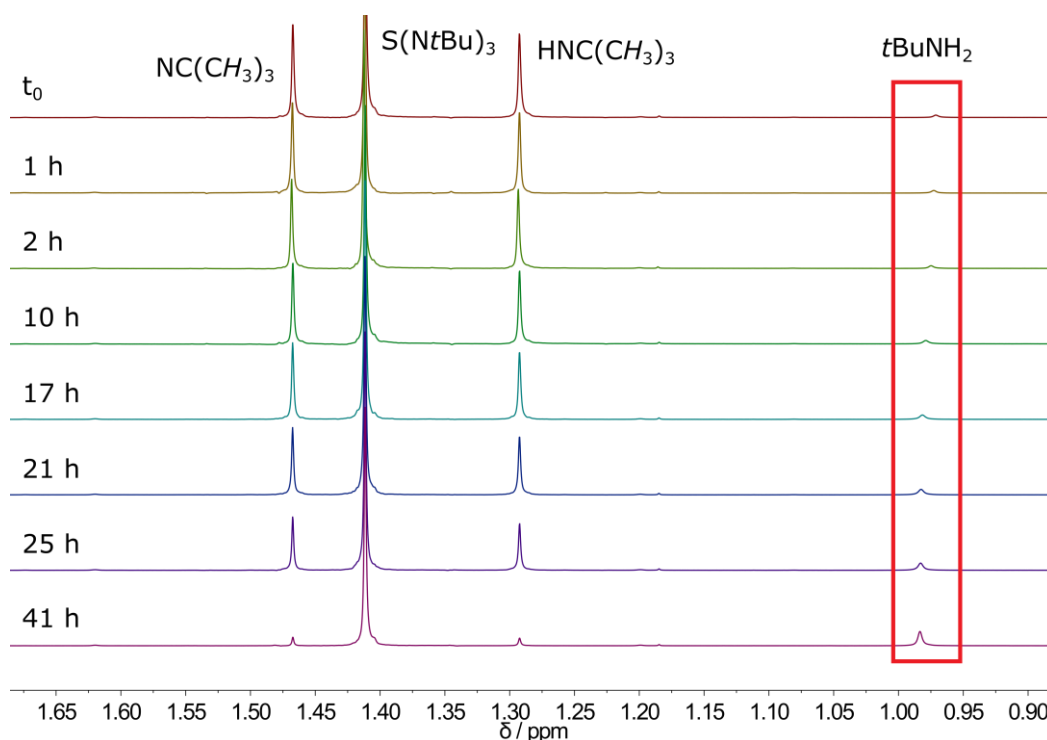


Figure 3-55 Time-resolved ^1H -NMR spectra of **13** at 283 K in toluene- d_8 . Shown are the two signals for the tBu groups of **13**, together with the two decomposition products $\text{S}(\text{NtBu})_3$ (**SN-III**) and tBuNH_2 .

Even though it was not possible to find a correlation between the decomposition and the time that elapsed during the measurement, this analysis clearly displayed that the NMR signals of **13** almost disappeared after around two days, relatively to the increasing signals of both $S(NtBu)_3$ (**SN-III**) and $tBuNH_2$.

Attempts to optimize the synthesis of **13** in terms of isolated yields and reduced impurities ultimately revealed that the crucial key is the reduction of the reaction time to an absolute minimum. Temperature-dependent optimization attempts indicated that it is reasonable to perform the reaction under room temperature, since the reaction time is drastically lowered upon reducing the temperature. However, due to a lack of comparability, an optimum temperature prediction remained unsuccessful.

Despite all the preparative obstacles it was possible to select crystals of pure **13** suitable for single crystal X-ray diffraction analysis. **13** crystallizes in the monoclinic space group $C2/c$ with half a molecule in the asymmetric unit (**Figure 3-56**).

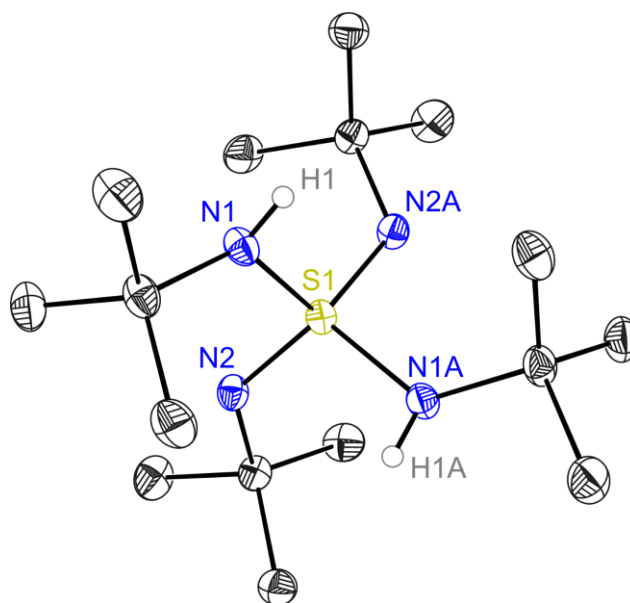


Figure 3-56 Crystal structure of $H_2S(NtBu)_4$ (**13**). Anisotropic displacement parameters are depicted at the 50% probability level. Hydrogen atoms of the tBu groups are omitted for clarity. Selected bond lengths [Å] and angles [°]: S1–N1 1.6530(9), S1–N2 1.5240(10), N1–S1–N1A 112.56(7), N1–S1–N2 100.36(5), N2–S1–N2A 128.53(7), N1–S1–N2A 107.59(5).

The central sulfur(VI) atom adopts a distorted tetrahedral geometry, created by two (H) $NtBu$ amido and two $NtBu$ imido groups. Since no indication of any N(H)/N hydrogen atom disorder was found, it would be more appropriate to emphasize the existence of two different S–N bonds (imido and amido) with two fixed hydrogen positions in a formula like $(tBuN)_2S(HNtBu)_2$ instead of $H_2S(NtBu)_4$.

Nevertheless, the latter was chosen to underline the valence isoelectronic relation to sulfuric acid H_2SO_4 . The two different S–N bond types have a pronounced difference in bond length of 1.6230(9) Å (S1–N1(H)) and 1.5240(10) Å (S1–N2) and correspond well to $\text{S}(\text{NtBu})_3$ (**SN-III**)^[50,51], $\text{S}(\text{NtBu})_2$ (**SN-I**)^[50,51] and $\text{CH}_2\{\text{S}(\text{NtBu})_2(\text{NHtBu})\}_2$ ^[51,52] on the basis of X-ray data and in the gas phase^[53,54]. One could assume double bond character for the shorter imido bond, but it is rather electrostatic interaction than a pronounced double bond character.^[51] The strong, far from ideal, distorted tetrahedral geometry of the imido acid is further described by the five different N–S–N angles. They range from 100.36(5)° for the two chemically different nitrogen atoms (HN1–S1–N2) to 128.53(7)° that spans between the two crystallographically identical proton-free imido nitrogen atoms (N2–S1–N2A).

In order to investigate the S–N bonding situation in terms of double or single bond character, and to distinguish between the imido NtBu and the amido (H)NtBu bond, a more sophisticated model is required. Therefore, high-resolution X-ray data were collected. A multipole refinement, according to the Hansen and Coppens formalism^[252] and a subsequent Quantum Theory of Atoms in Molecules (QTAIM)-based topological analysis revealed the characteristic parameters.^[253] The measurements, data processing and model refinement were done by Dr. Annika Münch.

An important characteristic to define the nature of a bond is the bond critical point (BCP). A BCP is a saddle point and local minimum in the electron density along the bond path (BP), which is the path between two atoms that possesses the maximum electron density. Herein, the position of the BCP shifted towards the electropositive atom mirrors the polarization of a bond.

The electron density $\rho(r_{\text{BCP}})$ (ED), the Laplacian $\nabla^2\rho(r_{\text{BCP}})$ (second derivative of $\rho(r_{\text{BCP}})$) and the ellipticity ε at the BCP further reveal the bonding situation. Low densities and a positive value for Laplacian are indicative for closed shell interactions, which display ionic or coordinative bonds, and negative values are associated with shared interactions and hence covalent bonds. The discussed values are summarized in **Table 3-3** and in good agreement with previously reported compounds.^[50,51]

For both S–N bond types, the BCP is shifted towards the sulfur atom indicative for an electron depletion at the sulfur and a polar character of the S–N bonds (**Figure 3-57**). This observation is illustrated by the BCP-S and BCP-N distances with $d_{\text{BCP-S1}} = 0.805(3)$ Å and $d_{\text{BCP-N1}} = 0.843(2)$ Å for the amido S–N(H) and $d_{\text{BCP-S1}} = 0.740(2)$ Å and $d_{\text{BCP-N1}} = 0.789(2)$ Å for the imido bond. The comparative analysis shows that the difference in BCP distances is slightly less pronounced for the amido relatively to the imido bond, which indicates lower polarization. Considering the estimated values for $\rho(r_{\text{BCP}})$ and $\nabla^2\rho(r_{\text{BCP}})$, further confirm the covalency of the S–N bond, that has been established earlier.^[51]

Table 3-10 Topological characteristics of $\text{H}_2\text{S}(\text{NtBu})_4$ (**13**), $\text{S}(\text{NtBu})_3$ ^[50,51] and $\text{CH}_2\{\text{S}(\text{NtBu})_2(\text{NHtBu})\}_2$.^[51,52] Depicted are the electron density $\rho(r_{\text{BCP}})$, the Laplacian values $\nabla^2\rho(r_{\text{BCP}})$, the distance of the BCP to the sulfur and nitrogen atoms $d_{\text{BCP-S/N}}$ and the ellipticity at BCP ε .

compound	bond	$\rho(r_{\text{BCP}})$ [$\text{e}\text{\AA}^{-3}$]	$\nabla^2\rho(r_{\text{BCP}})$ [$\text{e}\text{\AA}^{-5}$]	$d_{\text{BCP-S}}$ [\AA]	$d_{\text{BCP-N}}$ [\AA]	ε
$\text{H}_2\text{S}(\text{NtBu})_4$ (13)	S1–N1(H)	1.808(6)	–14.8(3)	0.805(3)	0.843(2)	0.43
	S1–N2	2.173(4)	–21.2(3)	0.740(2)	0.789(3)	0.32
$\text{S}(\text{NtBu})_3$ (SN-III)	S1–N1	2.27(3)	–10.56(8)	0.738	0.775	0.22
$\text{CH}_2\{\text{S}(\text{NtBu})_2(\text{NHtBu})\}_2$	S1–N1(H)	1.89(2)	–13.41(7)	0.780	0.870	0.11
	S1–N2	2.31(3)	–16.60(9)	0.718	0.812	0.10
	S1–N3	3.37(3)	–16.44(9)	0.718	0.802	0.06

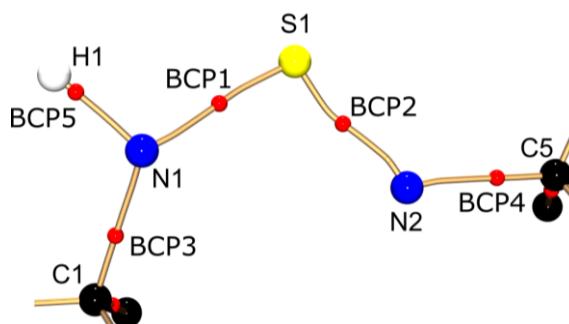


Figure 3-57 Molecular graph of the central part of **13**. Bond paths are coloured in bronze and BCPs are depicted as red spheres. Distances between the BCP and the sulfur, respectively the nitrogen atoms for the amido S–N(H) bond: $d_{\text{BCP-S1}} = 0.805(3) \text{ \AA}$; $d_{\text{BCP-N1}} = 0.843(2) \text{ \AA}$; and for the imido S–N bond: $d_{\text{BCP-S1}} = 0.740(2) \text{ \AA}$; $d_{\text{BCP-N1}} = 0.789(2) \text{ \AA}$.

Interestingly, the ellipticities of the S–N bonds (0.43 for S–N(H); 0.32 for S–N) are unusually high when assuming only single bonds in $\text{H}_2\text{S}(\text{NtBu})_4$ (**13**). In comparison, for unpolar C–C bonds, those values are attributed to double bonds where the π -density is accumulated above and underneath the cylindrical σ -bond. In **13**, to compensate the positive charge at the central sulfur, the lone-pairs located at the nitrogen atoms rise up into the bonding region causing the deformation of the bond.^[254]

The analysis of the Laplacian in the non-bonding regions of the nitrogen atoms nicely supports the assumption that the S–N imido bond is, by that explanation, not a double bond, since valence shell charge concentration (VSCC) in non-bonding regions are indicative for lone pairs (LP). For the negatively charged imido nitrogen, VSCC analysis reveals two LPs that are shifted towards the sulfur atom, which underlines the explanation for the unusually high ellipticity values (**Figure 3-58**). Furthermore, only one LP is located in the apical position of the amido S–N(H) nitrogen. Full information on the data processing and the topological analysis can be found in the PhD thesis of

Annika Münch^[255] or in the publication (1).^[1] It is known from the discussion in the previous chapters that the sum of all S–N bonds for all compounds fall in the range between 6.343(2) Å^[106] to 6.405(3) Å.^[32] The same is found for the metal free and protonated tetraimido sulfuric acid H₂S(NtBu)₄ (**13**) with 6.354(1) Å for the regular X-ray analysis and 6.351(1) Å for the high-resolution data. The SN₄ moiety flexibly responds to the electronic requirements that are induced by the coordinated metal, or in the case of **13** the bounded protons. The position of the sulfur within the more or less static SN₄ cage is flexible and adaptive to the electrostatic variations around the ligand.

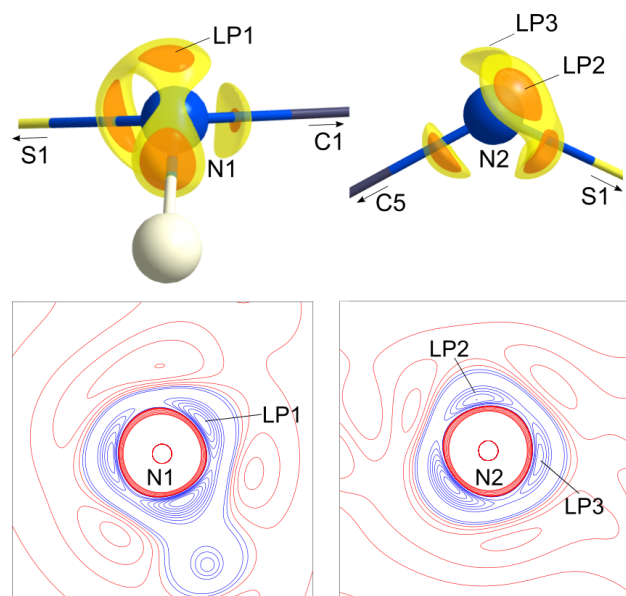


Figure 3-58 $\nabla^2\rho(r)$ at isolevel of $-52 \text{ e}\text{\AA}^{-5}$ (orange) and $-35 \text{ e}\text{\AA}^{-5}$ (yellow) at N1 and N2 in **13** and contour plots of charge concentrations in the H1–N1–LP1 and LP2–N2–LP3 plane. Contours are drawn at $\pm(1, 3, 20, 25, 30, 35, 40, 45, 50, 55, 70, 100, 115, 135) \text{ e}\text{\AA}^{-5}$, blue contours show negative values, red values show positive values

All analyses made in this chapter support the concept that the S–N bond is a strongly polarized single bond with significant electrostatic contribution, rather than a double bond with valence expansion and d-orbital participation.^[51]

3.4.2. Conclusion on tetraimido sulfuric acid H₂S(NtBu)₄ – a valence isoelectronic analogue to H₂SO₄

In the last chapter, the synthesis of the valence isoelectronic imido analogue H₂S(NtBu)₄ (**13**) to sulfuric acid H₂SO₄ was presented. Even though **13** was found to decompose in solution and in the solid state at elevated temperatures, it was possible to isolate and characterize this unique molecule by NMR spectroscopy and crystal structure analysis. Additionally performed high resolution charge density investigations revealed strongly polarized S^{δ+}–N^{δ-} bonds with virtually no indication for double bond character.

4. Summary and Outlook

The scope of this thesis was to open a new chapter in S–N chemistry by establishing polyimido sulfur(VI) ligands in the field of molecular magnetism and to introduce f-block metal chemistry to the selected systems: (1) The symmetric tetraimido sulfate $[S(NtBu)_4]^{2-}$ (L^1) to investigate exchange coupled systems, and (2) the triimido sulfonate $[Ph_2PCH_2S(NtBu)_3]^-$ (L^2) that provides additional phosphorus donation to investigate the influence of soft donor atoms on the magnetic properties (**Figure 4-1**).

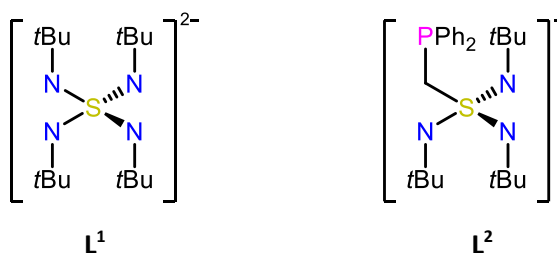


Figure 4-1 Depicted are the two S(VI) centered polyimido ligands that were used within this work. (left): The tetraimido sulfate $[S(NtBu)_4]^{2-}$ (L^1). (right): The triimido sulfonate $[Ph_2PCH_2S(NtBu)_3]^-$ (L^2).

The first results are based on L^1 and the isolation of two new bimetallic compounds, the asymmetric manganese complex $[Cl_2Mn(NtBu)_2S(tBuN)_2Mn\{ClLi(thf)_3\}_2]$ (**1**) and the symmetric cobalt complex $[(acac)Co(NtBu)_2S(tBuN)_2Co(acac)]$ (**2**) (**Figure 4-2**). The magnetic investigations revealed that both compounds exhibit an antiferromagnetic coupling of $J = -1.00$ and -6.08 cm^{-1} , respectively, which has proven the $[S(NtBu)_4]^{2-}$ ligand to be a promising candidate to mediate magnetic communication. In order to optimize its properties, further ligand tuning is required. In this context, the use of SN radical ligands seems to be promising, since they could induce a ferromagnetic coupling between the paramagnetic metal centers. In principal, a radical system should be possible for $[S(NtBu)_4]^{2-}$ as well. Furthermore, L^1 facilitates a step by step lithium exchange starting from $[(thf)_4Li_2(NtBu)_4S]$ ($L^1\text{-Li,Li}$), to synthesize (hetero)binuclear metal complexes, demonstrated by the isolation and XRD analysis of $[(acac)Co(NtBu)_2S(tBuN)_2Li(thf)_2]$ (**3**).

For the first time, f-block element complexes in a series from gadolinium to erbium, based on the tetraimido sulfate $[S(NtBu)_4]^{2-}$, were presented and characterized by crystallographic and magnetic investigations (**Figure 4-2**). Within this series, the binuclear dimeric dysprosium complex $[\{(thf)_2Li(NtBu)_2S(tBuN)_2DyCl_2\}_2 \cdot ClLi(thf)_2]$ (**10c**) was found to behave as a true single molecule magnet, with a slow magnetic relaxation between 2 – 13 K in the absence of an external applied dc field. The energy barrier to spin reversal was determined to $U_{eff} = 64.9(1)\text{ cm}^{-1}$. Also, the monomeric terbium and dysprosium species $[\{(thf)_2Li(NtBu)_2S(tBuN)_2LnCl_2(thf)_2\}]$ (**11b,c**) exhibit slow relaxation of the magnetization under applied dc fields. Therefore, these compounds can be classified as field induced

SMMs with energy barriers to spin-relaxation of $U_{\text{eff}} = 42.8(6)$ and $11.1(1) \text{ cm}^{-1}$, respectively. Since both ligand scaffolds **10** and **11** do not display a highly axial ligand field, further attempts to optimize the geometries and to benefit from the acute N,N' bite angles are worth pursuing.

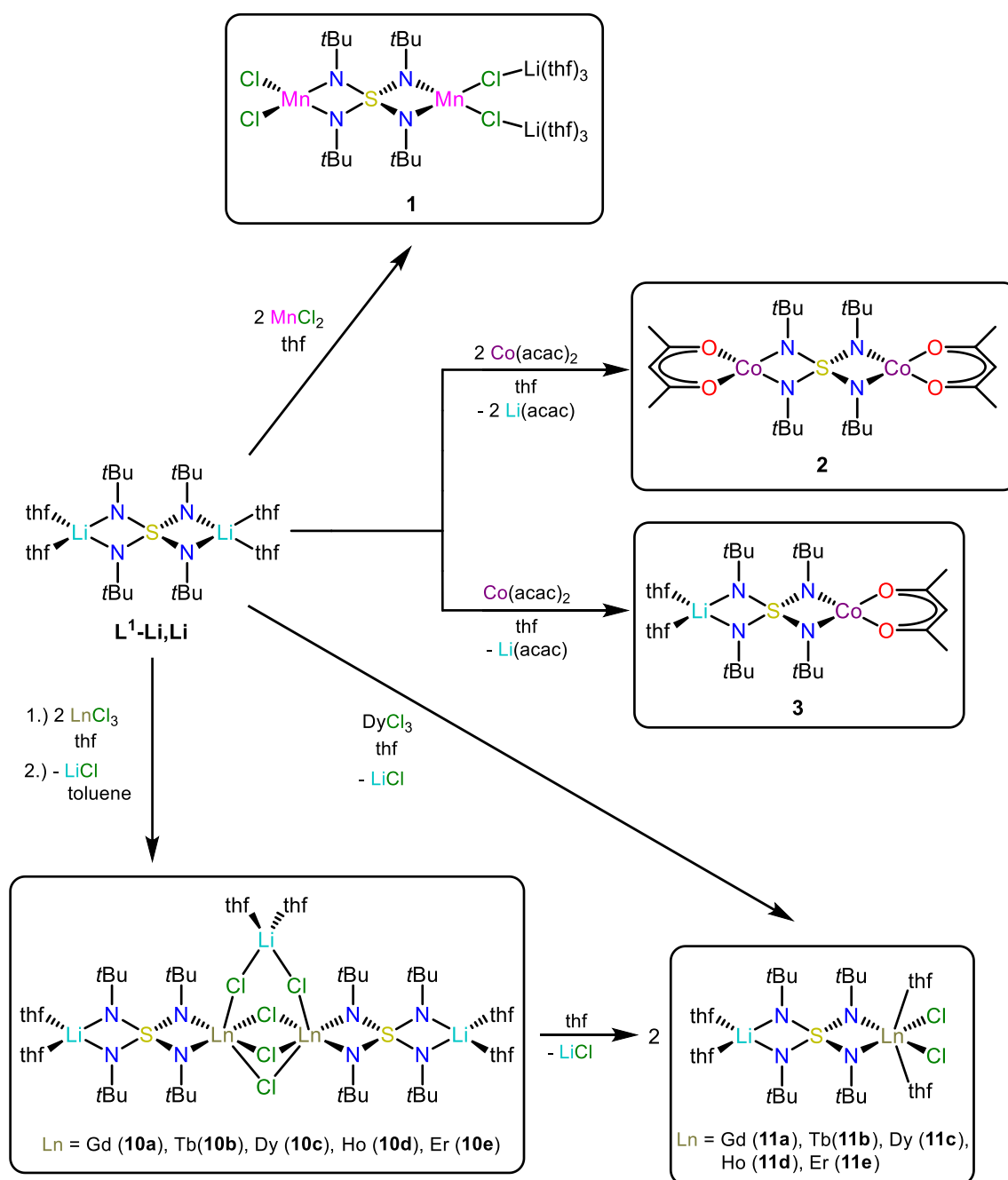


Figure 4-2 Synthetic routes for various tetraimido sulfate $[\text{S}(\text{NtBu})_4]^{2-}$ (L^1) based compounds starting from the lithiated precursor $[(\text{thf})_4\text{Li}_2(\text{NtBu})_4\text{S}]$ ($\text{L}^1\text{-Li, Li}$). Combination with 2 equiv. of MnCl_2 resulted in the isolation of the LiCl co-coordinated binuclear manganese compound $[\text{Cl}_2\text{Mn}(\text{NtBu})_2\text{S}(\text{tBuN})_2\text{Mn}\{\text{CLi}(\text{thf})_3\}_2]$ (**1**). A metal exchange reaction with one or two equiv. $\text{Co}(\text{acac})_2$ yielded the hetero bimetallic $[(\text{acac})\text{Co}(\text{NtBu})_2\text{S}(\text{tBuN})_2\text{Li}(\text{thf})_2]$ (**3**) and the homo bimetallic $[(\text{acac})\text{Co}(\text{NtBu})_2\text{S}(\text{tBuN})_2\text{Co}(\text{acac})]$ (**2**). Furthermore, the synthesis of the lanthanide complexes $[\{\text{Cl}_2\text{Ln}(\text{NtBu})_2\text{S}(\text{tBuN})_2\text{Li}(\text{thf})_2\}\{\text{CLi}(\text{thf})_2\}]$ (**10a-e**) and $[(\text{thf})_2\text{Li}(\text{NtBu})_2\text{S}(\text{tBuN})_2\text{LnCl}_2(\text{thf})_2]$ (**11a-e**), in the series from gadolinium to erbium utilizing lanthanide(III) chlorides, are depicted.

For **10c**, LiCl elimination together with a substitution of the two axial chloro atoms for larger non-coordinating ligands might be effective to enhance magnetic performance. Lower coordinated dysprosium and terbium ions in higher axial LFs would probably help to tune the magnetic properties of the triply positive and oblate shaped lanthanide ions.

To further address the benefits that arise from distorted geometries in transition metal complexes, the trigonal planar Fe(II) and Co(II) compounds were synthesized (**Figure 4-3**). The complexes containing the $[S(NtBu)_4]^{2-}$ (L^1) ligand are accessible through a metal exchange reaction with the appropriate $M\{N(SiMe_3)_2\}_2$, while the $[Ph_2PCH_2S(NtBu)_3]^-$ (L^2) based compounds exploits the basicity of the hexamethyldisilazide metal sources through deprotonation of $[Ph_2PCH_2S(NtBu)_2NHtBu]$ (**4**). The cobalt species **7** and **9** showed slow magnetic relaxation under applied dc fields. The very acute N–M–N bite angles lead to a considerable deviation from idealized trigonal planar geometry, which seems to be favorable due to the high anisotropies that were found for those compounds ($D = +43$ and -80 cm $^{-1}$).

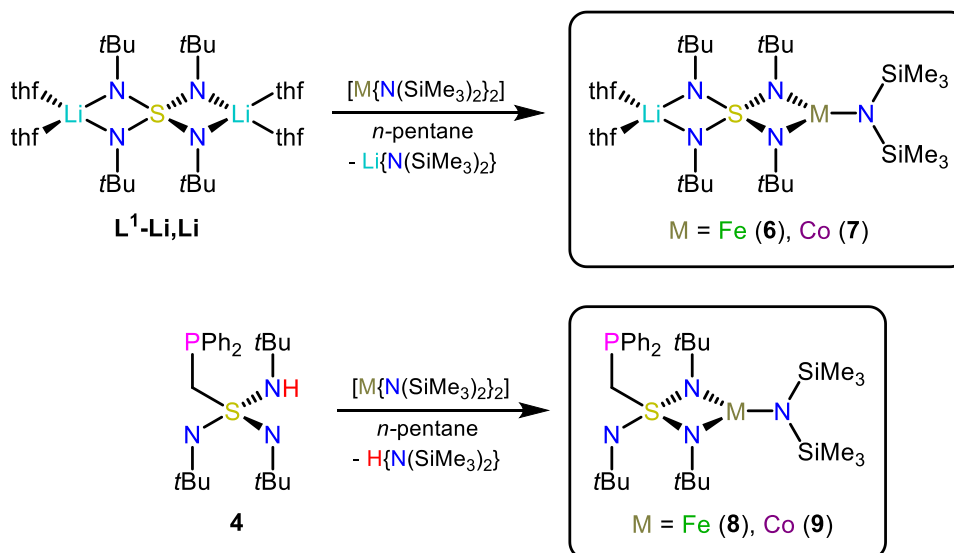


Figure 4-3 Synthesis of the $[S(NtBu)_4]^{2-}$ (L^1) and $[Ph_2PCH_2S(NtBu)_3]^-$ (L^2) based metal complexes $[(thf)_2Li\{NtBu\}_4S]M\{N(SiMe_3)_2\}_2$, with $M = Fe$ (**6**), Co (**7**) and $[M\{N(SiMe_3)_2\}_2\{Ph_2PCH_2S(NtBu)_3\}]$, with $M = Fe$ (**8**) and Co (**9**). **6** and **7** are accessible through a metal exchange reaction of the lithiated precursor $[(thf)_4Li_2(NtBu)_4S]$ ($L^1\text{-Li, Li}$) with one equiv. of the appropriate $M\{N(SiMe_3)_2\}_2$ in n -pentane, while **8** and **9** can be obtained through a deprotonation of $[Ph_2PCH_2S(NtBu)_2NHtBu]$ (**4**).

Theoretical calculations further revealed an appreciable influence of phosphine substituent to the magnetic performance. Due to the large distance between the metal and phosphorus atom, the direct interaction might be small. Nevertheless, the position of the metal relatively to the N,N,N plane seems to be crucial for the magnetic performance, which is influenced by the phosphorus atom. $[Ph_2PCH_2S(NtBu)_2NHtBu]$ (**4**) was further deprotonated by $K\{N(SiMe_3)_2\}$ to form the potassium compound $[K(thf)_3\{Ph_2PCH_2S(NtBu)_3\}]$ (**5**). In order to prevent lithium halide co-complexation in metal exchange reaction, **5** was targeted as a ligand precursor to subsequent complexation reactions. This

ultimately resulted in the synthesis of the first triimido sulfonate $[\text{Ph}_2\text{PCH}_2\text{S}(\text{NtBu})_3]^-$ (L^2) based f-element complexes **12a-e** ($\text{Ln} = \text{a: Tb, b: Dy, c: Ho, d: Er, e: Lu}$) (**Figure 4-4**).

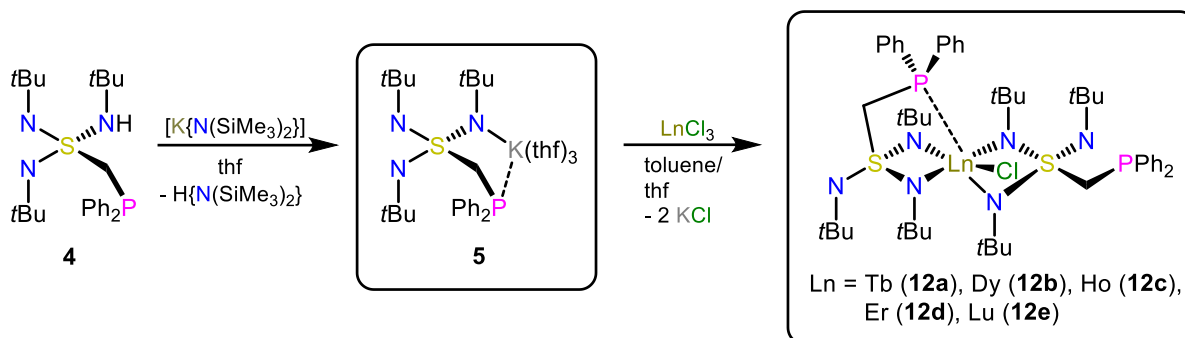


Figure 4-4 Synthesis of the potassium complex $[\text{K}(\text{thf})_3\{\text{Ph}_2\text{PCH}_2\text{S}(\text{NtBu})_3\}]$ (**5**) by deprotonation of $[\text{Ph}_2\text{PCH}_2\text{S}(\text{NtBu})_2\text{NHtBu}]$ (**4**) with 1 equiv. of $\text{K}\{\text{N}(\text{SiMe}_3)_2\}$ in thf and the subsequent isolation of the lanthanide complexes $[\text{LnCl}\{\text{Ph}_2\text{PCH}_2\text{S}(\text{NtBu})_3\}_2]$ **12a-e** ($\text{Ln} = \text{a: Tb, b: Dy, c: Ho, d: Er, e: Lu}$) from a reaction with the appropriate lanthanide(III) chlorides in a mixture of toluene and thf.

Within this series, the dysprosium complex showed slow relaxation of the magnetization under the absence of an applied dc field and a butterfly hysteresis up to 3.5 K, and can therefore be classified as a true single molecule magnet (**Figure 4-5**). Furthermore, the terbium and erbium compounds showed magnetic relaxation under applied dc fields and energy barriers to spin reversal of $U_{\text{eff}} = 235$ and 34.5 cm^{-1} . To further tune the magnetic performances of **12**, strategies towards halide abstraction can be followed. Within the field of f-element cyclopentadienide complexes, the use of $[\text{Et}_3\text{Si}(\text{H})\text{SiEt}_3][\text{B}(\text{C}_6\text{F}_5)_4]$ or $\text{CH}_2=\text{CHCH}_2\text{MgCl}$ followed by $[\text{HNEt}_3][\text{BPh}_4]$ are well established pathways for the exchange of halides against larger, non-coordinating ligands. This seems promising in order to optimize the SMM properties of **12a** and **12b**.

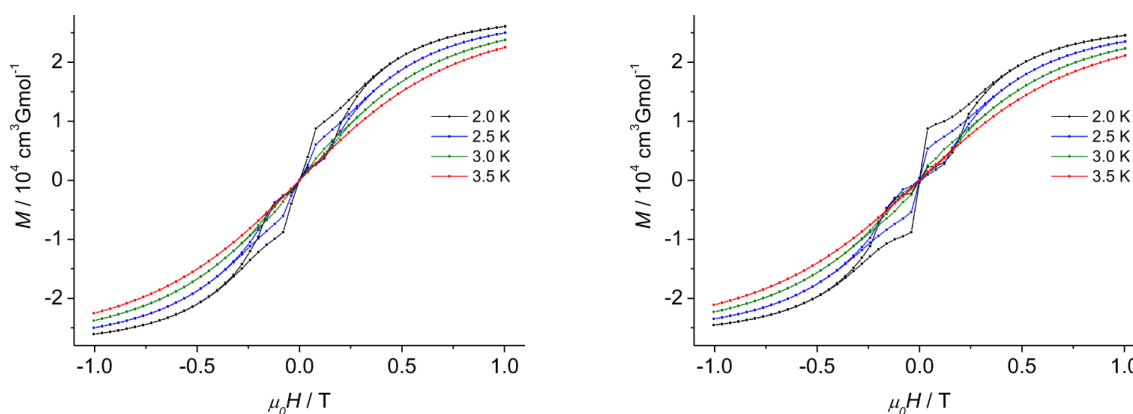


Figure 4-5 Butterfly hysteresis of the Dy(III) complex **12b** (left) and for the magnetically diluted **12b@12e** (right) between 2.0 to 3.5 K.

Finally, the synthesis of the valence isoelectronic imido analogue $\text{H}_2\text{S}(\text{NtBu})_4$ (**13**) to sulfuric acid H_2SO_4 was presented. **13** was found to decompose in solution and in the solid state at elevated temperatures. Nevertheless, it was possible to isolate and characterize this unique molecule by NMR spectroscopy and crystal structure analysis. Additionally, high resolution charge density investigations revealed strongly polarized $\text{S}^{\delta+}-\text{N}^{\delta-}$ bonds with virtually no indication for double bond character. The utilization of **5** as starting material for metal exchange reactions showed the beneficial properties of a potassium precursor, since it prevented alkali metal halide co-complexation. Hence, the protonated species **13** opens the opportunity of a subsequent deprotonation and a LiCl contamination-free synthesis.

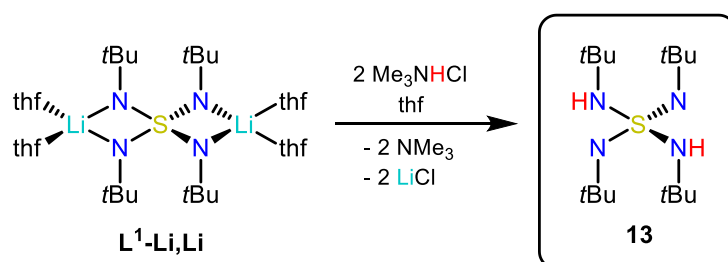


Figure 4-6 Synthesis of the valence isoelectronic tetraimido sulfuric acid $\text{H}_2\text{S}(\text{NtBu})_4$ (**13**) through protonation of $[(\text{thf})_4\text{Li}_2(\text{NtBu})_4\text{S}]$ ($\text{L}^1\text{-Li, Li}$) with 2 equiv. of Me_3NHCl in thf.

Altogether, the SN ligand platform seem to be a promising alternative to the intensively studied ligand systems commonly used towards the design of single-molecule magnets. The polar $\text{S}^{\delta+}-\text{N}^{\delta-}$ bonds can easily adapt to the electronic and geometric requirements of various metals, offering a wide range of possible coordination complexes. Within this work, several d-element SMMs were obtained and, for the first time, f-element SMMs based on the polyimido sulfur(VI) ligands L^1 and L^2 were synthesized. Furthermore, the valence isoelectronic imido analogue $\text{H}_2\text{S}(\text{NtBu})_4$ (**13**) to sulfuric acid was isolated and deeply analyzed, which could be utilized as a precursor in subsequent deprotonation reactions, under the exclusion of potential alkali metal halide co-complexation.

5. Experimental Section

5.1. General procedures

All reactions were performed under the strict exclusion of air and moisture using modified *Schlenk* techniques in a dry and purified nitrogen or argon atmosphere or in an argon glovebox (*LABmaster eco* by *MBRAUN*).^[256–258] Glass ware has been dried in an oven at 130°C for at least 1 d prior to use and has been assembled while still being hot. Filtration was done using dried *Whatman* fiberglass filters (GF/B, 25 mm), which were attached with Teflon[®] tape to cannulas, or as filter for modified syringes. Solvents were dried using standard laboratory procedures (*n*-pentane from sodium/potassium alloy; C₆D₆ and thf from potassium; *n*-hexane, toluene from sodium; thf-*d*₈ from LiAlH₄). Freshly distilled and degassed (via “pump-freeze”) solvents were stored over activated molecular sieves (3 Å), prior to use. Commercially available starting materials were used without further purification. Other starting materials were synthesized according to the given literature procedures.

5.2. Analytical methods

5.2.1. NMR spectroscopy

The NMR spectra were measured at room temperature, except stated differently, on either a *BRUKER Avance III 300* or an *Avance III HD 500*. The measurements were performed with 5 – 10% solutions of deuterated solvents. Chemical shifts δ are given in ppm, referenced to the residual proton signal of the deuterated solvent as internal standard.^[238,259] The coupling constant *J* is reported in Hz and the abbreviations for multiplicity are used as follows: s = singlet, d = doublet, t = triplet, m = multiplet, br = broad.^[238] Tetramethylsilane was used as an external standard for ¹H and ¹³C, orthophosphoric acid for ³¹P spectra, respectively. A correct signal assignment for 2D correlation spectra was ensured by using common techniques (COSY, HSQC and HMBC).^[260,261] Data processing was performed using *MestReNova 14.2.0* by *Mestrelab Research*.

5.2.2. Mass spectrometry

LIFDI-MS spectra were collected on a *Jeol AccuTOF* spectrometer at the Central Analytical Department of the *Institute of Organic and Biomolecular Chemistry, Georg-August-University* Göttingen. The isotope pattern is given as mass to charge ratio *m/z* for the molecule or fragment ions and are correlated to the isotopes with the highest natural abundance (e.g. ¹H, ¹²C, ¹⁴N, ¹⁶O, ³¹P, ³²S).

5.2.3. Elemental analysis

Elemental analyses (C, H, N, S) were performed on an Elementar *vario EL III* at the *Analytical Laboratory* of the *Institute of Inorganic Chemistry*, Georg-August-University Göttingen. Deviations between the measured and the calculated elemental composition are due to the loss of lattice solvent molecules or minor impurities.

5.2.4. Mössbauer spectroscopy

Mössbauer spectra were collected from Serhiy Demeshko with a ^{57}Co source in a rhodium matrix using an alternating constant acceleration *Wissel* Mössbauer spectrometer that operated in the transmission mode, equipped with a *Janis* closed-cycle helium cryostat. Isomer shifts are given relative to iron metal at ambient temperature. Simulation of the experimental data was performed with the *Mfit* program using *Lorentzian* line doublets. The program was developed by E. Bill, *Max-Planck Institute for Chemical Energy Conversion*, Mülheim an der Ruhr.

5.2.5. Magnetic measurements

The magnetic measurements and data processing presented in this thesis were done by Dr. C. Legendre^[2,4,5], Dr. S. Demeshko^[4,5], Prof. Dr. S. Demir^[3] and F. Benner^[3]. More details can be found in the underlying publications (2) – (5).^[2–5]

Magnetic susceptibility data were collected using a Quantum-Design *MPMS-XL-5* SQUID magnetometer (equipped with a 5 T magnet) or a Quantum Design *MPMS-3* SQUID magnetometer, respectively. DC susceptibility data measurements for compounds **10a-e** and **11b-e** were performed at temperatures ranging from 2 to 300 K, using applied fields of 1 T. All other compounds were measured from 2 to 210 K in a magnetic field of 0.5 T.

The samples were prepared in an argon glove-box. The crystalline material was crushed, placed in a gel capsule and covered with a few drops of a low-viscosity inert oil. Therefore, either perfluoropolyether Fomblin YL VAC 25/6 (liquefies above 215 K) or Eicosane (liquefies above 310 K; used for compounds **10a-e** and **11b-e**) was added.

The use of oil covers the samples which prevents magnetic torqueing and the loss of solvent molecules. Furthermore, it provides good thermal contact between the sample and the bath. The capsule was

placed in a non-magnetic sample holder, the tubes were sealed air-tight, transferred and finally inserted in the SQUID magnetometer for the measurements.

The raw data files were corrected for the diamagnetic contribution with experimentally obtained susceptibility values for the gel bucket with $\chi_g = -5.70 \cdot 10^{-7} \text{ emu} / (\text{g} \cdot \text{Oe})$ and for the oil with $\chi_g = -3.51 \cdot 10^{-7} \text{ emu} / (\text{g} \cdot \text{Oe})$ according to $M_{\text{dia}} = \chi_g \cdot m \cdot H$. The molar susceptibility data were corrected for the diamagnetic contribution according to $\chi_{M,\text{dia}} (\text{sample}) = -0.5 \cdot M \cdot 10^{-6} \text{ cm}^3 \text{ mol}^{-1}$. Temperature-independent paramagnetism (TIP) was included according to $\chi_{\text{calc}} = \chi + \text{TIP}$.^[127]

The dc magnetic susceptibility data for compounds **1** and **2** were fitted according to the spin Hamiltonian $\hat{H} = -2JS_1S_2$ by using the *Julx-v16/Jul-2s* program.^[262]

The $\chi_M T$ and VTVH data for the other transition metal complexes were fitted according to the spin Hamiltonian displayed in

Eq. 5-1 taking Zeeman splitting and zero-field splitting into account.

Eq. 5-1:

$$\hat{H} = \mu_B (S_x g_x B_x + S_y g_y B_y + S_z g_z B_z) + D \left[\hat{S}_z^2 - \frac{1}{3} S(S+1) + \frac{E}{D} (\hat{S}_x^2 - \hat{S}_y^2) \right]$$

The Cole-Cole plots were analyzed with the CC-Fit program.^[263] The temperature dependence of the extracted values of the relaxation times for the main relaxation process was used to construct Arrhenius plots and to determine the value of the effective energy barrier to spin reversal U_{eff} .

Eq. 5-2:

$$\frac{1}{\tau_{\text{obs}}} = \tau_0^{-1} \exp \left(-U_{\text{eff}} / k_B T \right)$$

Here, τ_{obs} is the observed relaxation time, τ_0 the relaxation rate for the Orbach process and k_B the Boltzmann constant.

The full fits were made according to the following equation:

Eq. 5-3:

$$\frac{1}{\tau_{\text{obs}}} = AH^4 T + \tau_0^{-1} \exp \left(-U_{\text{eff}} / k_B T \right) + \tau_{\text{QTM}}^{-1} + CT^n$$

Here, the first term is from the direct process, the second the Orbach relaxation, the third term models the QTM and the fourth is for the Raman process. A, C and n are constants, H is an applied magnetic field and τ_{QTM} the relaxation rate for QTM.

The plots were worked-up and visualized using the OriginPro 8.5 software.^[264]

The orientation of the main magnet axes presented in here were calculated by Dr. C. Legendre and Prof. Dr. S. Demir using the program Magellan.^[265]

5.2.6. Computational calculations

The calculations were performed by Dr. Christina Legendre. A detailed information can be found in the publication (4).^[4]

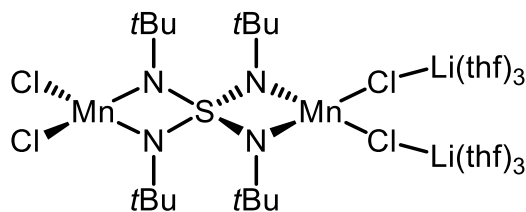
CASSCF/NEVPT2 multi-configurational calculations are based on the molecular geometry obtained from the experimental single crystal XRD analysis and were used to calculate the electronic energy levels. Correlated calculations were carried out using Complete Active Space Self Consistent Field (*CASSCF*)^[266] in combination with N-Electron Valence Perturbation Theory to second order (*NEVPT2*)^[267] as implemented in the ORCA package.^[268,269] Nonrelativistic *CASSCF* energy levels and wave functions have been computed averaging over the electron densities of all considered states.

Spin-orbit coupling (*SOC*) was considered using a mean field spin-orbit coupling operator. Mixing of non-relativistic configuration interaction (*CI*) eigenfunctions and splitting of the corresponding eigenvalues were considered by Quasi Degenerate Perturbation Theory (*QDPT*). *Ab initio* ligand field theory (*AILFT*) calculations were based on the wave functions obtained from the *CASSCF-NEVPT2* calculations by using the *actorbs dorbs* command in the input file.^[270]

The Douglas-Kroll-Hess triple- ζ DKH-def2-TZVP basis-set was used and coordinates were obtained from experimental X-ray data. Before the calculations, the coordinate system was chosen so that it matches with the molecular d-orbitals using the Avogadro software.^[271]

Since the *NEVPT-2* calculations gave more realistic results than pure *CASSCF* calculations, the presented results in the work are relying on the results obtained after the application of the *NEVPT-2* perturbation. The values of the *D* and *g*-tensors, the populations of the 3d orbitals and the Kramers' doublets (*KDs*) energy levels are reported from the *NEVPT-2* calculations. The energy levels are reported from *AILFT* calculations.

5.3. Synthesis and characterization

5.3.1. $[\text{Cl}_2\text{Mn}(\text{N}t\text{Bu})_2\text{S}(t\text{BuN})_2\text{Mn}\{\text{ClLi}(\text{thf})_3\}_2]$ (**1**)

A mixture of $[(\text{thf})_4\text{Li}_2(\text{N}t\text{Bu})_4\text{S}]$ (500.0 mg, 0.8080 mmol) and MnCl_2 (203.4 mg, 1.616 mmol) were dissolved in THF (20 mL) at room temperature. After stirring for 1 d the reaction mixture was filtered and reduced in volume. Storing at -34°C yielded orange crystals suitable for X-ray analysis after 3 d. The solvent was removed and the product was washed with *n*-pentane (2 x 2 mL). To gain more of the compound the mother liquor was concentrated, *n*-pentane (0.5 mL) was added and it was crystallized and worked up in the same manner.

Empirical formula: $\text{C}_{40}\text{H}_{84}\text{Cl}_4\text{Li}_2\text{Mn}_2\text{N}_4\text{O}_6\text{S}$

Molecular weight: 1014.75 g/mol

Yield: 547.4 mg, 0.5394 mmol, 67%

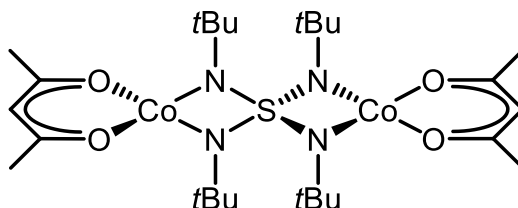
Elemental analysis for $\text{C}_{40}\text{H}_{84}\text{Cl}_4\text{Li}_2\text{Mn}_2\text{N}_4\text{O}_6\text{S}$ (found (calc.) [%]): C 42.19 (47.35), H 7.86 (8.34), N 7.20 (5.52), S 4.56 (3.16).

The low C and high N and S values are due to loss of coordinating thf molecules. Doing the measurement directly after washing with *n*-pentane yields better fitting values.

Elemental analysis for $\text{C}_{40}\text{H}_{84}\text{Cl}_4\text{Li}_2\text{Mn}_2\text{N}_4\text{O}_6\text{S}$ (found (calc.) [%]): C 45.55 (47.35), H 7.75 (8.34), N 6.42 (5.52), S 4.09 (3.16).

Nevertheless, the crystalline material slowly loses mass over a period of several hours leading to a more powdery sample indicating thf to evaporate over time. This also effects the solubility of the whole compound. Performing the measurement after drying under reduced pressure leads to a compound with approximately two thf molecules coordinating.

Elemental analysis for $\text{C}_{24}\text{H}_{52}\text{Cl}_4\text{Li}_2\text{Mn}_2\text{N}_4\text{O}_2\text{S}$ (found (calc.) [%]): C 39.77 (39.69), H 6.61 (7.22), N 7.74 (7.71), S 5.09 (4.41).

5.3.2. [(acac)Co(NtBu)₂S(tBuN)₂Co(acac)] (2)

A mixture of [(thf)₄Li₂(NtBu)₄S] (500.0 mg, 0.8080 mmol) and Co(acac)₂ (415.6 mg, 1.616 mmol) were dissolved in THF (15 mL) at room temperature. After stirring for 1 d the reaction mixture was filtered and the solvent was removed under reduced pressure. The residue was dissolved in *n*-pentane (5 mL) and the solution was filtered again. Storing at −34°C yielded red crystals suitable for X-ray analysis after 3 d. To gain more of the compound the mother liquor was concentrated and stored at −34°C.

Empirical formula: C₂₆ H₅₀ Co₂ N₄ O₄ S

Molecular weight: 632.64 g/mol

Yield: 415.6 mg, 0.6569 mmol, 81%

¹H-NMR (500.13 MHz, 298 K, C₆D₆): δ [ppm] = −33.02 (s br, 36H, 4 NC(CH₃)₃), 23.52 (s br, 12H, 4 acac-CH₃), 72.35 (s br, 2H, 2 acac-CH).

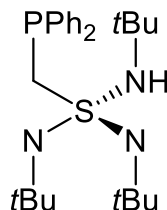
¹³C{¹H}-NMR (125.76 MHz, 298 K, C₆D₆): δ [ppm] = 353.21 (s), 372.75 (s), 653.88 (s), 710.94 (s), 1172.73 (s).

¹H-NMR (500.13 MHz, 343 K, C₆D₆): δ [ppm] = −27.77 (s br, 36H, 4 NC(CH₃)₃), 20.45 (s br, 12H, 4 acac-CH₃), 60.12 (s br, 2H, 2 acac-CH).

¹³C{¹H}-NMR (125.76 MHz, 343 K, C₆D₆): δ [ppm] = 320.65 (s, NC(CH₃)₃), 339.08 (s, acac-CH), 580.34 (s), 645.12 (s), 1032.82 (s, acac-CH₃).

LIFDI-MS: m/z: 632.2 [M]⁺.

Elemental analysis for C₂₆H₅₀Co₂N₄O₄S (found (calc.) [%]): C 49.36 (49.36), H 8.28 (7.97), N 8.70 (8.86), S 4.87 (5.07).

5.3.3. $\text{Ph}_2\text{PCH}_2\text{S}(\text{NtBu})_2\text{NHtBu}$ (**4**)

A mixture of the lithium precursor $[(\text{tmeda})\text{Li}\{(\text{NtBu})_3\text{S}(\text{CH}_2\text{PPh}_2)\}]$ (3.000 g, 5.284 mmol) and tBuNH_3Cl (579 mg, 5.28 mmol) were suspended in *n*-pentane (25 mL) and stirred for 1 d at room temperature. Subsequently LiCl was filtered off and the solution was concentrated under reduced pressure. Crystallization started within hours at -34°C yielding colorless crystals. The solvent was removed and the product was dried under reduced pressure.

Empirical formula: $\text{C}_{25} \text{H}_{40} \text{N}_3 \text{P S}$

Molecular weight: 445.65 g/mol

Yield: 2.040 g, 4.577 mol, 87%

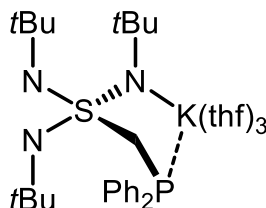
^1H -NMR (500.13 MHz, 298 K, C_6D_6): δ [ppm] = 1.29 (s, 9H, $\text{HNC}(\text{CH}_3)_3$), 1.47 (s, 18H, 2 $\text{NC}(\text{CH}_3)_3$), 3.86 (s, 2H, PCH_2), 4.05 (d, $^4J_{\text{HP}} = 5$ Hz, $\text{HN}(\text{CH}_3)_3$), 7.03 – 7.07 (m, 2H, *p*-Ph-*H*), 7.09 – 7.12 (m, 4H, *m*-Ph-*H*), 7.61 – 7.65 (m, 4H, *o*-Ph-*H*).

$^{13}\text{C}\{^1\text{H}\}$ -NMR (125.76 MHz, 298 K, C_6D_6): δ [ppm] = 30.39 (s, $\text{HNC}(\text{CH}_3)_3$), 33.47 (s, $\text{NC}(\text{CH}_3)_3$), 53.30 (s, $\text{NC}(\text{CH}_3)_3$), 54.54 (s, $\text{HNC}(\text{CH}_3)_3$), 65.20 (d, $^1J_{\text{CP}} = 30.2$ Hz, PCH_2), 128.64 (d, $^1J_{\text{CP}} = 6.7$ Hz, *m*-Ph-C), 128.74 (s, *p*-Ph-C), 133.56 (d, $^2J_{\text{CP}} = 19.2$ Hz, *o*-Ph-C), 140.07 (d, $^2J_{\text{CP}} = 14.3$ Hz, *ipso*-Ph-C).

^{15}N -NMR (50.70 MHz, 298 K, C_6D_6): δ [ppm] = -249.4 (s, $\text{NC}(\text{CH}_3)_3$), -269.4 (s, $\text{HNC}(\text{CH}_3)_3$).

$^{31}\text{P}\{^1\text{H}\}$ -NMR (202.46 MHz, 298 K, C_6D_6): δ [ppm] = -16.98 (s).

Elemental analysis for $\text{C}_{25}\text{H}_{40}\text{N}_3\text{PS}$ (found (calc.) [%]): C 67.00 (67.38), H 9.14 (9.05), N 9.54 (9.43), S 7.94 (7.19).

5.3.4. $[K(thf)_3\{Ph_2PCH_2S(NtBu)_3\}]$ (5)

A solution of $K\{N(SiMe_3)_2\}$ (1.119 g, 5.610 mmol) in thf (15 mL) was added to a solution of $Ph_2PCH_2S(NtBu)_2NHtBu$ (2.500 g, 5.610 mmol) in thf (10 mL) at room temperature. After stirring for 1 d the solvent was removed under reduced pressure. The residue was dissolved in a mixture of *n*-pentane/thf (15 mL / 3 mL) and filtered. Crystallization started within minutes after storing at -34°C yielding colorless crystals suitable for X-ray analysis. The product was isolated, washed with *n*-pentane (2 x 2 mL) and dried under reduced pressure.

Empirical formula: $C_{37}H_{63}K N_3O_3PS$ (with thf); $C_{25}H_{39}KN_3PS$ (without thf)

Molecular weight: 700.06 g/mol (with thf); 483.74 g/mol (without thf)

Yield: 2.384 g, 3.406 mmol, 61% (with thf); 4.928 mmol, 88% (without thf)

$^1\text{H-NMR}$ (500.13 MHz, 298 K, C_6D_6): δ [ppm] = 1.65 (s, 27H, 3 $NC(CH_3)_3$), 3.94 (d, $^2J_{HP} = 5.0$ Hz, 2H, PCH_2), 7.07 – 7.09 (m, 2H, 2 *p*-Ph-*H*), 7.15 – 7.18 (m, 4H, 2 *m*-Ph-*H*), 7.84 – 7.87 (s, 2H, *o*-Ph-*H*).

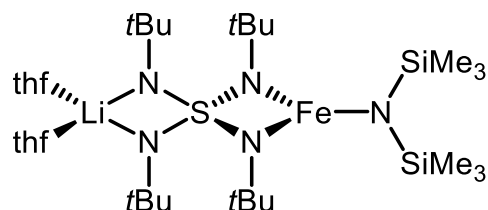
$^{13}\text{C}\{^1\text{H}\}$ -NMR (125.76 MHz, 298 K, C_6D_6): δ [ppm] = 34.00 (s, $NC(CH_3)_3$), 52.73 (s, $NC(CH_3)_3$), 66.11 (d, $^1J_{CP} = 21.1$ Hz, PCH_2), 128.22 (s, *p*-Ph-C), 128.37 (d, $^3J_{CP} = 6.3$ Hz, *m*-Ph-C), 133.74 (d, $^2J_{CP} = 17.4$ Hz, *o*-Ph-C), 142.28 (d, $^1J_{CP} = 9.4$ Hz, *ipso*-Ph-C).

$^{15}\text{N-NMR}$ (50.70 MHz, 298 K, C_6D_6): δ [ppm] = -253.33 (s).

$^{31}\text{P}\{^1\text{H}\}$ -NMR (202.46 MHz, 298 K, C_6D_6): δ [ppm] = -18.14 (s).

Elemental analysis for $C_{25}H_{39}KN_3PS$ (found (calc.) [%]): C 61.73 (62.07), H 7.84 (8.13), N 8.85 (8.69), S 7.44 (6.63).

Performing the NMR experiment after washing with *n*-pentane yielded a compound with coordinating thf that slowly evaporated over a period of days, while drying under reduced pressure led to a thf free complex.

5.3.5. $[(\text{thf})_2\text{Li}\{(\text{N}t\text{Bu})_4\text{S}\}\text{Fe}\{\text{N}(\text{SiMe}_3)_2\}]$ (6)

A mixture of $[(\text{thf})_4\text{Li}_2(\text{N}t\text{Bu})_4\text{S}]$ (250.0 mg, 0.4040 mmol) and $\text{Fe}\{\text{N}(\text{SiMe}_3)_2\}_2$ (152.2 mg, 0.4040 mmol) were dissolved in *n*-pentane (15 mL) at room temperature. After stirring for 1 d the reaction mixture was filtered and the filtrate was concentrated (9 mL) under reduced pressure. Crystallization started within minutes after storing at -34°C yielding yellow crystals (266.8 mg) suitable for X-ray analysis. For further purification, the target compound was recrystallized and could be isolated after filtering and drying under reduced pressure.

Empirical formula: $\text{C}_{30}\text{H}_{70}\text{FeLiN}_5\text{O}_2\text{Si}_2$

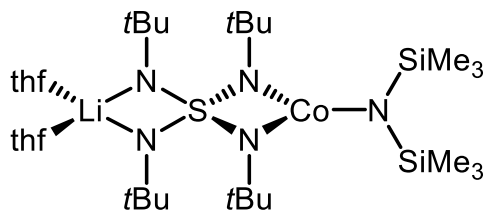
Molecular weight: 683.94 g/mol

Yield: 218.1 mg, 0.3189 mmol, 79%

^1H -NMR (500.13 MHz, 298 K, C_6D_6): δ [ppm] = -9.54 (s br, 18H, 6 CH_3), -4.05 (s br, 18H, 6 CH_3), 1.60 (s br, 18H, 6 CH_3), 4.39 (s, 8H, thf-*H*), 8.98 (s, 8H, thf-*H*).

^7Li -NMR (194.37 MHz, 298 K, C_6D_6): δ [ppm] = 88.77 (s).

Elemental analysis for $\text{C}_{30}\text{H}_{70}\text{FeLiN}_5\text{O}_2\text{Si}_2$ (found (calc.) [%]): C 52.60 (52.68), H 10.54 (10.32), N 10.36 (10.24), S 5.71 (4.69).

5.3.6. [(thf)₂Li{(NtBu)₄S}Co{N(SiMe₃)₂}] (7)

A mixture of [(thf)₄Li₂(NtBu)₄S] (250.0 mg, 0.4040 mmol) and Co{N(SiMe₃)₃}₂ (153.4 mg, 0.4040 mmol) were dissolved in *n*-pentane (15 mL) at room temperature. After stirring for 1 d, *n*-pentane (7 mL) was added and the reaction mixture was filtered. Crystallization started within minutes after storing at −34°C yielding purple crystals (261.5 mg) suitable for X-ray analysis. For further purification, the target compound was recrystallized and could be isolated after filtering and drying under reduced pressure.

Empirical formula: C₃₀ H₇₀ Co Li N₅ O₂ S Si₂

Molecular weight: 687.03 g/mol

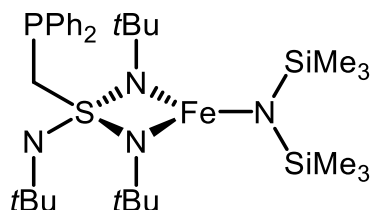
Yield: 216.2 mg, 0.3147 mmol, 78%

¹H-NMR (500.13 MHz, 298 K, C₆D₆): δ [ppm] = −19.98 (s br, 18H, 6 CH₃), −13.36 (s br, 18H, 6 CH₃), −1.80 (s br, 18H, 6 CH₃), 6.84 (s, 8H, thf-*H*), 13.52 (s, 8H, thf-*H*).

⁷Li-NMR (194.37 MHz, 298 K, C₆D₆): δ [ppm] = 6.42 (s).

¹³C{¹H}-NMR (125.76 MHz, 298 K, C₆D₆): δ [ppm] = 24.87 (s, CH₃), 32.55 (s, thf-C), 58.54 (s, NC(CH₃)₃), 79.73 (s, thf-C), 318.05 (s, CH₃), 605.26 (s, CH₃), 973.52 (s, NC(CH₃)₃).

Elemental analysis for C₃₀H₇₀CoLiN₅O₂SSi₂ (found (calc.) [%]): C 53.00 (52.45), H 10.47 (10.27), N 10.58 (10.19), S 6.48 (4.67).

5.3.7. $[\text{Fe}\{\text{N}(\text{SiMe}_3)_2\}\{\text{Ph}_2\text{PCH}_2\text{S}(\text{N}t\text{Bu})_3\}]$ (**8**)

A mixture of $\text{Ph}_2\text{PCH}_2\text{S}(\text{N}t\text{Bu})_2\text{NH}t\text{Bu}$ (250.0 mg, 0.5610 mmol) and $\text{Fe}\{\text{N}(\text{SiMe}_3)_3\}_2$ (211.3 mg, 0.5610 mmol) were dissolved in *n*-pentane (5 mL) at room temperature. After stirring for 1 d the reaction mixture was filtered and reduced in volume. Storing at -34°C yielded orange crystals suitable for X-ray analysis after 2 d. The solvent was removed and the product was dried under reduced pressure.

Empirical formula: $\text{C}_{31}\text{H}_{57}\text{FeN}_4\text{PSSi}_2$

Molecular weight: 660.87 g/mol

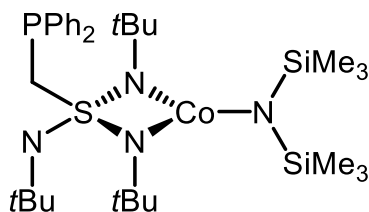
Yield: 329.1 mg, 0.4980 mmol, 89%

^1H -NMR (500.13 MHz, 298 K, C_6D_6): δ [ppm] = -7.07 (s br, 18H, 6 CH_3), 2.87 - 6.43 (m, 24H), 6.98 (s, 4H, Ph-*H*), 11.41 (s br, 9H, 3 CH_3), 93.68 (s, 2H).

^1H -NMR (500.13 MHz, 323 K, C_6D_6): δ [ppm] = -5.92 (s br, 18H, 6 CH_3), 3.72 - 6.29 (m, 24H), 10.50 (s br, 9H, 3 CH_3), 84.00 (s, 2H).

$^{31}\text{P}\{^1\text{H}\}$ -NMR (202.46 MHz, 298 K, C_6D_6): No signal could be detected.

Elemental analysis for $\text{C}_{31}\text{H}_{57}\text{FeN}_4\text{PSSi}_2$ (found (calc.) [%]): C 56.44 (56.34), H 8.91 (8.69), N 8.47 (8.48), S 5.07 (4.85).

5.3.8. $[\text{Co}\{\text{N}(\text{SiMe}_3)_2\}\{\text{Ph}_2\text{PCH}_2\text{S}(\text{N}t\text{Bu})_3\}]$ (9)

A mixture of $\text{Ph}_2\text{PCH}_2\text{S}(\text{N}t\text{Bu})_2\text{NH}t\text{Bu}$ (250.0 mg, 0.5610 mmol) and $\text{Fe}\{\text{N}(\text{SiMe}_3)_3\}_2$ (213.0 mg, 0.5610 mmol) were dissolved in *n*-pentane (5 mL) at room temperature. After stirring for 1 d the reaction mixture was filtered and reduced in volume. Storing at -34°C yielded green crystals suitable for X-ray analysis after 2 d. The solvent was removed and the product was dried under reduced pressure.

Empirical formula: $\text{C}_{31}\text{H}_{57}\text{CoN}_4\text{PSSi}_2$

Molecular weight: 663.96 g/mol

Yield: 341.8 mg, 0.5148 mmol, 92%

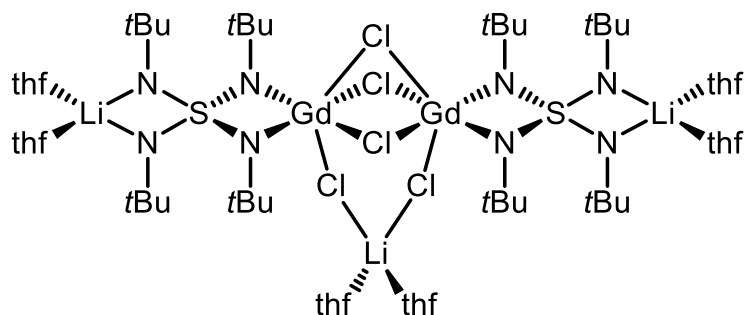
^1H -NMR (500.13 MHz, 298 K, C_6D_6): δ [ppm] = -19.12 (s br, 18H, 6 CH_3), -12.50 (s br, 9H, 3 CH_3), -9.90 (s br, 9H, 3 CH_3), 5.59 (s br, 9H, 3 CH_3), 7.72 (s, 2H), 8.24 (s, 4H, Ph-*H*), 9.76 (s br, 4H, Ph-*H*), 144.15 (s, 2H).

^1H -NMR (500.13 MHz, 323 K, C_6D_6): δ [ppm] = -15.61 (s br, 18H, 6 CH_3), -10.13 (s br, 18H, 6 CH_3), 5.52 (s br, 9H, 3 CH_3), 8.10 (s, 2H), 8.77 (s, 4H, Ph-*H*), 11.54 (s br, 4H, Ph-*H*), 125.96 (s, 2H).

$^{13}\text{C}\{^1\text{H}\}$ -NMR (125.76 MHz, 298 K, C_6D_6): δ [ppm] = 46.49 (s), 124.02 (s), 131.79 (s), 133.33 (s), 144.87 (s), 180.69 (s), 475.12 (s), 514.69 (s), 622.50 (s), 830.15 (s).

$^{31}\text{P}\{^1\text{H}\}$ -NMR (202.46 MHz, 298 K, C_6D_6): δ [ppm] = 540.01 (s).

Elemental analysis for $\text{C}_{31}\text{H}_{57}\text{CoN}_4\text{PSSi}_2$ (found (calc.) [%]): C 56.03 (56.08), H 8.91 (8.65), N 8.40 (8.44), S 5.02 (4.86).

5.3.9. $[\{\text{Cl}_2\text{Gd}(\text{NtBu})_2\text{S}(\text{NtBu})_2\text{Li}(\text{thf})_2\}_2 \cdot \{\text{CLi}(\text{thf})_2\}]$ (**10a**)

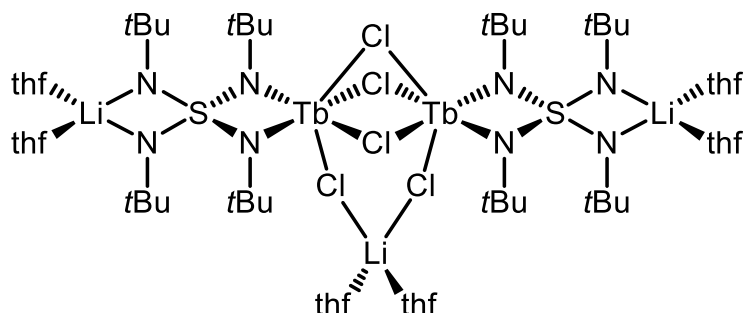
A mixture of $[(\text{thf})_4\text{Li}_2(\text{NtBu})_4\text{S}]$ (500.0 mg, 0.8080 mmol) and GdCl_3 (213.0 mg, 0.8080 mmol) were dissolved in thf (20 mL) at room temperature. After stirring for 1 h the reaction mixture was concentrated (7 mL), filtered and subsequently the solvent was removed under reduced pressure. The residue was dissolved in toluene (5 mL) and the solution was filtered. Crystallization started after 30 min at room temperature. For further crystallization, the mixture was stored at -34°C yielding colorless crystals suitable for X-ray analysis after 2 d. The solvent was removed and the product was washed with *n*-pentane (2 x 2 mL).

Empirical formula: $\text{C}_{56} \text{H}_{120} \text{Cl}_5 \text{Gd}_2 \text{Li}_3 \text{N}_8 \text{O}_6 \text{S}_2 (\text{C}_7 \text{H}_8)$

Molecular weight: 1670.46 g/mol

Yield: 266.9 mg, 0.1598 mmol, 40%

Elemental analysis for $\text{C}_{56}\text{H}_{120}\text{Cl}_5\text{Gd}_2\text{Li}_3\text{N}_8\text{O}_6\text{S}_2(\text{C}_7\text{H}_8)$ (found (calc.) [%]): C 42.91 (45.30), H 6.92 (7.72), N 6.51 (6.71), S 4.47 (3.84).

5.3.10. $[\{\text{Cl}_2\text{Tb}(\text{N}^t\text{Bu})_2\text{S}(\text{N}^t\text{Bu})_2\text{Li}(\text{thf})_2\}_2 \cdot \{\text{ClLi}(\text{thf})_2\}]$ (**10b**)

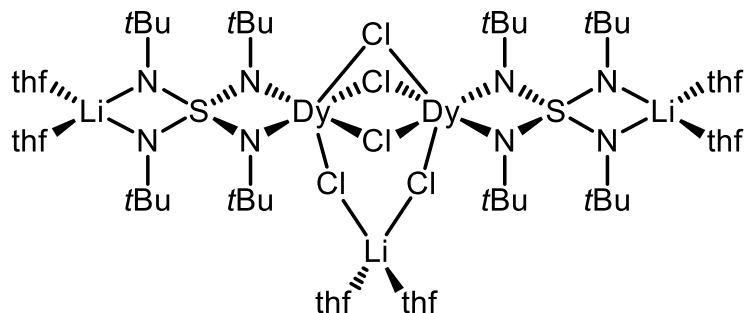
A mixture of $[(\text{thf})_4\text{Li}_2(\text{N}^t\text{Bu})_4\text{S}]$ (500.0 mg, 0.8080 mmol) and TbCl_3 (214.3 mg, 0.8080 mmol) were dissolved in thf (20 mL) at room temperature. After stirring for 1 d the reaction mixture was concentrated (7 mL), filtered and subsequently the solvent was removed under reduced pressure. The residue was dissolved in toluene (5 mL) and the solution was filtered. Crystallization started within minutes at room temperature. For further crystallization, the mixture was stored at -34°C yielding colorless crystals suitable for X-ray analysis after 2 d. The solvent was removed and the product was washed with *n*-pentane (2 x 2 mL).

Empirical formula: $\text{C}_{56} \text{H}_{120} \text{Cl}_5 \text{Tb}_2 \text{Li}_3 \text{N}_8 \text{O}_6 \text{S}_2$ ($\text{C}_7 \text{H}_8$)

Molecular weight: 1673.81 g/mol

Yield: 304.6 mg, 0.1820 mmol, 45%

Elemental analysis for $\text{C}_{56}\text{H}_{120}\text{Cl}_5\text{Tb}_2\text{Li}_3\text{N}_8\text{O}_6\text{S}_2(\text{C}_7 \text{H}_8)$ (found (calc.) [%]): C 43.64 (45.21), H 7.87 (7.71), N 6.88 (6.69), S 4.80 (3.83).

5.3.11. $[\{\text{Cl}_2\text{Dy}(\text{NtBu})_2\text{S}(\text{NtBu})_2\text{Li}(\text{thf})_2\}_2 \cdot \{\text{ClLi}(\text{thf})_2\}]$ (**10c**)

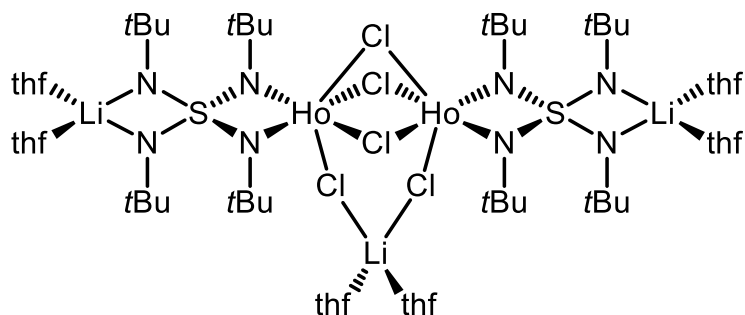
A mixture of $[(\text{thf})_4\text{Li}_2(\text{NtBu})_4\text{S}]$ (500.0 mg, 0.8080 mmol) and DyCl_3 (217.2 mg, 0.8080 mmol) were dissolved in thf (20 mL) at room temperature. After stirring for 1 d the reaction mixture was concentrated (7 mL), filtered and subsequently the solvent was removed under reduced pressure. The residue was dissolved in toluene (5 mL) and the solution was filtered. Crystallization started within minutes at room temperature. For further crystallization, the mixture was stored at -34°C yielding colorless crystals suitable for X-ray analysis after 2 d. The solvent was removed and the product was washed with *n*-pentane (2 x 2 mL).

Empirical formula: $\text{C}_{56} \text{H}_{120} \text{Cl}_5 \text{Dy}_2 \text{Li}_3 \text{N}_8 \text{O}_6 \text{S}_2$ ($\text{C}_7 \text{H}_8$)

Molecular weight: 1680.96 g/mol

Yield: 281.5 mg, 0.1675 mmol, 41%

Elemental analysis for $\text{C}_{56}\text{H}_{120}\text{Cl}_5\text{Dy}_2\text{Li}_3\text{N}_8\text{O}_6\text{S}_2(\text{C}_7 \text{H}_8)$ (found (calc.) [%]): C 42.63 (45.02), H 7.62 (7.68), N 6.61 (6.67), S 4.14 (3.81).

5.3.12. $[\{\text{Cl}_2\text{Ho}(\text{NtBu})_2\text{S}(\text{NtBu})_2\text{Li}(\text{thf})_2\}_2 \cdot \{\text{ClLi}(\text{thf})_2\}]$ (**10d**)

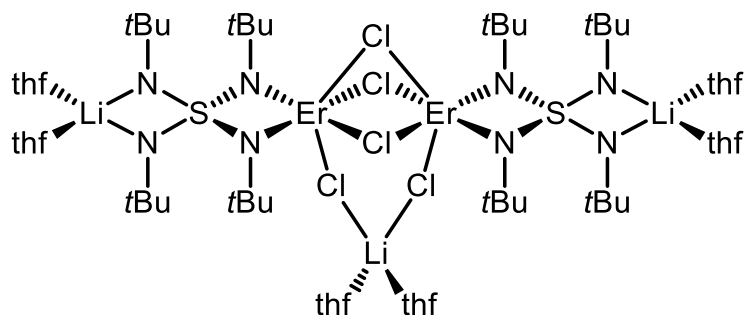
A mixture of $[(\text{thf})_4\text{Li}_2(\text{NtBu})_4\text{S}]$ (500.0 mg, 0.8080 mmol) and HoCl_3 (219.2 mg, 0.8080 mmol) were dissolved in thf (20 mL) at room temperature. After stirring for 1 d the reaction mixture was concentrated (7 mL), filtered and subsequently the solvent was removed under reduced pressure. The residue was dissolved in toluene (5 mL) and the solution was filtered. Crystallization started after 30 min at room temperature. For further crystallization, the mixture was stored at -34°C yielding colorless crystals suitable for X-ray analysis after 2 d. The solvent was removed and the product was washed with *n*-pentane (2 x 2 mL).

Empirical formula: $\text{C}_{56} \text{H}_{120} \text{Cl}_5 \text{HO}_2 \text{Li}_3 \text{N}_8 \text{O}_6 \text{S}_2 (\text{C}_7 \text{H}_8)$

Molecular weight: 1685.82 g/mol

Yield: 137.1 mg, 0.08133 mmol, 20%

Elemental analysis for $\text{C}_{56}\text{H}_{120}\text{Cl}_5\text{HO}_2\text{Li}_3\text{N}_8\text{O}_6\text{S}_2(\text{C}_7 \text{H}_8)$ (found (calc.) [%]): C 41.27 (44.89), H 7.06 (7.65), N 6.71 (6.65), S, 3.92 (3.80).

5.3.13. $[\{\text{Cl}_2\text{Er}(\text{N}t\text{Bu})_2\text{S}(\text{N}t\text{Bu})_2\text{Li}(\text{thf})_2\}_2 \cdot \{\text{ClLi}(\text{thf})_2\}]$ (**10e**)

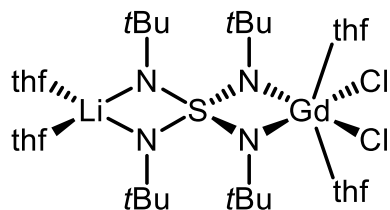
A mixture of $[(\text{thf})_4\text{Li}_2(\text{N}t\text{Bu})_4\text{S}]$ (500.0 mg, 0.8080 mmol) and ErCl_3 (221.1 mg, 0.8080 mmol) were dissolved in thf (20 mL) at room temperature. After stirring for 1 d the reaction mixture was concentrated (7 mL), filtered and subsequently the solvent was removed under reduced pressure. The residue was dissolved in toluene (5 mL) and the solution was filtered. Crystallization started after 3 h at room temperature. For further crystallization, the mixture was stored at -34°C yielding colorless crystals suitable for X-ray analysis after 2 d. The solvent was removed and the product was washed with *n*-pentane (2 x 2 mL).

Empirical formula: $\text{C}_{56} \text{H}_{120} \text{Cl}_5 \text{Er}_2 \text{Li}_3 \text{N}_8 \text{O}_6 \text{S}_2 (\text{C}_7 \text{H}_8)$

Molecular weight: 1690.48 g/mol

Yield: 113.8 mg, 0.06732 mmol, 17%

Elemental analysis for $\text{C}_{56}\text{H}_{120}\text{Cl}_5\text{Er}_2\text{Li}_3\text{N}_8\text{O}_6\text{S}_2(\text{C}_7\text{H}_8)$ (found (calc.) [%]): C 42.67 (44.76), H 7.60 (7.63), N 7.14 (6.63), S, 5.08 (3.79).

5.3.14. $[\{(\text{thf})_2\text{Cl}_2\text{Gd}(\text{N}t\text{Bu})_2\text{S}(\text{N}t\text{Bu})_2\text{Li}(\text{thf})_2\}_2] \text{ (11a)}$ 

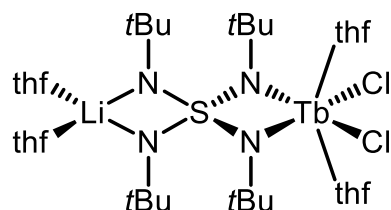
$[\{\text{Cl}_2\text{Gd}(\text{N}t\text{Bu})_2\text{S}(\text{N}t\text{Bu})_2\text{Li}(\text{thf})_2\}_2 \cdot \{\text{ClLi}(\text{thf})_2\}]$ (150.0 mg, 89.80 μmol) was dissolved in thf (3 mL) and filtered. Crystallization started within hours at room temperature whereupon the mixture was stored at -34°C to improve the yield. The target compound was isolated and washed with *n*-pentane (2 x 1 mL) yielding colorless crystals suitable for X-ray analysis.

Empirical formula: $\text{C}_{32} \text{H}_{68} \text{Cl}_2 \text{Gd} \text{Li} \text{N}_4 \text{O}_4 \text{S}$

Molecular weight: 840.07 g/mol

Yield: 98.3 mg, 0.117 mmol, 65%

Elemental analysis for $\text{C}_{32}\text{H}_{68}\text{Cl}_2\text{GdLiN}_4\text{O}_4\text{S}$ (found (calc.) [%]): C 45.82 (45.75), H 8.59 (8.16), N 6.54 (6.67), S 4.01 (3.82).

5.3.15. $[\{(thf)_2Cl_2Tb(NtBu)_2S(NtBu)_2Li(thf)_2\}_2]$ (**11b**)

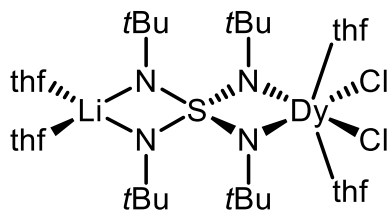
$[\{Cl_2Tb(NtBu)_2S(NtBu)_2Li(thf)_2\}_2 \cdot \{ClLi(thf)_2\}]$ (150.0 mg, 89.62 μ mol) was dissolved in thf (2 mL) and filtered. Crystallization started within hours at room temperature whereupon the mixture was stored at -34°C to improve the yield. The target compound was isolated and washed with *n*-pentane (2 x 1 mL) yielding colorless crystals suitable for X-ray analysis.

Empirical formula: $C_{32}H_{68}Cl_2TbLiN_4O_4S$

Molecular weight: 841.75 g/mol

Yield: 99.6 mg, 0.118 mmol, 66%

Elemental analysis for $C_{32}H_{68}Cl_2TbLiN_4O_4S$ (found (calc.) [%]): C 45.98 (45.66), H 8.66 (8.14), N 6.50 (6.66), S 4.34 (3.81).

5.3.16. $[(\text{thf})_2\text{Cl}_2\text{Dy}(\text{NtBu})_2\text{S}(\text{NtBu})_2\text{Li}(\text{thf})_2]_2$ (**11c**)

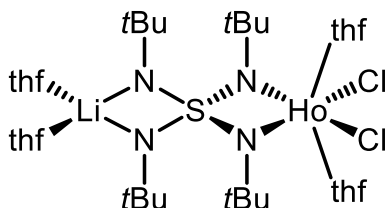
$[(\text{Cl}_2\text{Dy}(\text{NtBu})_2\text{S}(\text{NtBu})_2\text{Li}(\text{thf})_2)]_2 \cdot \{\text{ClLi}(\text{thf})_2\}$ (150.0 mg, 89.23 μmol) was dissolved in thf (3 mL) and filtered. Crystallization started within hours at room temperature whereupon the mixture was stored at -34°C to improve the yield. The target compound was isolated and washed with *n*-pentane (2 x 1 mL) yielding colorless crystals suitable for X-ray analysis.

Empirical formula: $\text{C}_{32} \text{H}_{68} \text{Cl}_2 \text{Dy Li N}_4 \text{O}_4 \text{S}$

Molecular weight: 845.32 g/mol

Yield: 105.2 mg, 0.06222 mmol, 70%

Elemental analysis for $\text{C}_{32}\text{H}_{68}\text{Cl}_2\text{DyLiN}_4\text{O}_4\text{S}$ (found (calc.) [%]): C 46.58 (45.47), H 8.71 (8.11), N 6.44 (6.63), S 4.77 (3.79).

5.3.17. $[\{(thf)_2Cl_2Ho(NtBu)_2S(NtBu)_2Li(thf)_2\}_2] \text{ (11d)}$ 

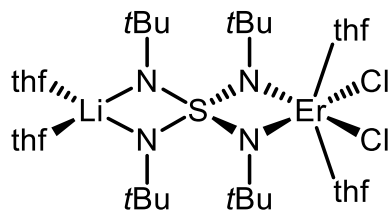
$[\{Cl_2Ho(NtBu)_2S(NtBu)_2Li(thf)_2\}_2 \cdot \{ClLi(thf)_2\}]$ (150.0 mg, 88.98 μ mol) was dissolved in thf (3 mL) and filtered. Crystallization started within hours at room temperature whereupon the mixture was stored at -34°C to improve the yield. The target compound was isolated and washed with *n*-pentane (2 x 1 mL) yielding pale orange crystals suitable for X-ray analysis.

Empirical formula: $C_{32}H_{68}Cl_2HoLiN_4O_4S$

Molecular weight: 847.75 g/mol

Yield: 115.5 mg, 0.06812 mmol, 77%

Elemental analysis for $C_{32}H_{68}Cl_2HoLiN_4O_4S$ (found (calc.) [%]): C 45.89 (45.34), H 8.50 (8.09), N 6.38 (6.61), S 3.90 (3.78).

5.3.18. $[\{(\text{thf})_2\text{Cl}_2\text{Er}(\text{N}t\text{Bu})_2\text{S}(\text{N}t\text{Bu})_2\text{Li}(\text{thf})_2\}_2] \text{ (11e)}$ 

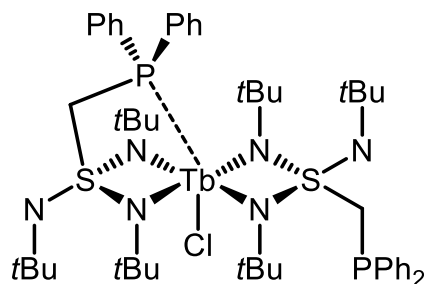
$[\{\text{Cl}_2\text{Er}(\text{N}t\text{Bu})_2\text{S}(\text{N}t\text{Bu})_2\text{Li}(\text{thf})_2\}_2 \cdot \{\text{ClLi}(\text{thf})_2\}]$ (100.0 mg, 59.15 μmol) was dissolved in thf (2 mL) and filtered. Crystallization started within hours at room temperature whereupon the mixture was stored at -34°C to improve the yield. The target compound was isolated and washed with *n*-pentane (2 x 1 mL) yielding pale pink crystals suitable for X-ray analysis.

Empirical formula: $\text{C}_{32} \text{H}_{68} \text{Cl}_2 \text{Er Li N}_4 \text{O}_4 \text{S}$

Molecular weight: 850.08 g/mol

Yield: 74.6 mg, 0.0439 mmol, 74%

Elemental analysis for $\text{C}_{32}\text{H}_{68}\text{Cl}_2\text{ErLiN}_4\text{O}_4\text{S}$ (found (calc.) [%]): C 45.55 (45.21), H 8.61 (8.06), N 6.35 (6.59), S 4.13 (3.77).

5.3.19. [ClTb{Ph₂PCH₂S(NtBu)₃}₂] (12a)

The potassium precursor [K{Ph₂PCH₂S(NtBu)₃}] (500.0 mg, 1.034 mmol) and TbCl₃ (137.1 mg, 0.517 mmol) were suspended in toluene (40 mL), thf (0.8 mL) was added and the mixture was stirred for 1 d at room temperature. Subsequently, KCl was filtered off and the solvent was removed under reduced pressure. The residue was extracted with thf, filtered and the solvent was removed in vacuo again. To obtain the target compound as crystalline material the raw product was dissolved in thf (2.5 mL) and layered with *n*-pentane (12.5 mL). Crystallization started within hours up to several days at room temperature yielding pale yellow crystals that were isolated and washed with *n*-pentane (2 x 1 mL).

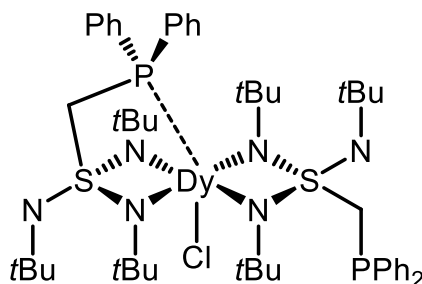
Empirical formula: C₅₀ H₇₈ Cl N₆ P₂ S₂ Tb (C_{2.12} H_{4.47} O_{0.38})

Molecular weight: 1119.71 g/mol

Yield: 240.4 mg, 0.2147 mmol, 42%

LIFDI-MS: m/z: 1047.3 [M-Cl]⁺.

Elemental analysis for C₅₀H₇₈ClN₆P₂S₂Tb(C_{2.12}H_{4.47}O_{0.38}) (found (calc.) [%]): C 55.78 (55.91), H 7.37 (7.42), N 7.50 (7.51), S 5.82 (5.73).

5.3.20. $[\text{ClDy}\{\text{Ph}_2\text{PCH}_2\text{S}(\text{NtBu})_3\}_2]$ (**12b**)

The potassium precursor $[\text{K}\{\text{Ph}_2\text{PCH}_2\text{S}(\text{NtBu})_3\}]$ (500.0 mg, 1.034 mmol) and DyCl_3 (139.0 mg, 0.517 mmol) were suspended in toluene (40 mL), thf (0.8 mL) was added and the mixture was stirred for 1 d at room temperature. Subsequently, KCl was filtered off and the solvent was removed under reduced pressure. The residue was extracted with thf, filtered and the solvent was removed in vacuo again. To receive the target compound as crystalline material the raw product was dissolved in thf (2.5 mL) and layered with *n*-pentane (12.5 mL). Crystallization started within hours up to several days at room temperature yielding pale yellow crystals that were isolated and washed with *n*-pentane (2 x 1 mL).

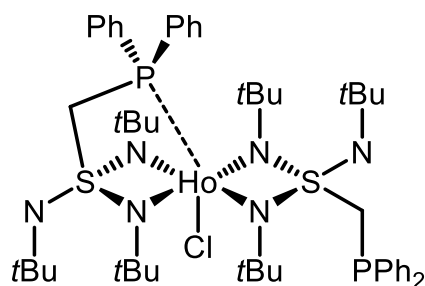
Empirical formula: $\text{C}_{50} \text{H}_{78} \text{Cl} \text{N}_6 \text{P}_2 \text{S}_2 \text{Dy} (\text{C}_{2.25} \text{H}_{4.99} \text{O}_{0.25})$

Molecular weight: 1123.29 g/mol

Yield: 285.3 mg, 0.2540 mmol, 49%

LIFDI-MS: m/z : 1052.4 $[\text{M}-\text{Cl}]^+$.

Elemental analysis for $\text{C}_{50}\text{H}_{78}\text{ClN}_6\text{P}_2\text{S}_2\text{Dy}(\text{C}_{2.25}\text{H}_{4.99}\text{O}_{0.25})$ (found (calc.) [%]): C 55.80 (55.87), H 7.21 (7.45), N 7.57 (7.48), S 5.92 (5.71).

5.3.21. $[\text{ClHo}\{\text{Ph}_2\text{PCH}_2\text{S}(\text{NtBu})_3\}_2]$ (**12c**)

The potassium precursor $[\text{K}\{\text{Ph}_2\text{PCH}_2\text{S}(\text{NtBu})_3\}]$ (500.0 mg, 1.034 mmol) and HoCl_3 (140.3 mg, 0.517 mmol) were suspended in toluene (40 mL), thf (0.8 mL) was added and the mixture was stirred for 1 d at room temperature. Subsequently, KCl was filtered off and the solvent was removed under reduced pressure. The residue was extracted with thf, filtered and the solvent was removed in vacuo again. To receive the target compound as crystalline material the raw product was dissolved in thf (2.5 mL) and layered with *n*-pentane (12.5 mL). Crystallization started within hours up to several days at room temperature yielding pale orange crystals that were isolated and washed with *n*-pentane (2 x 1 mL).

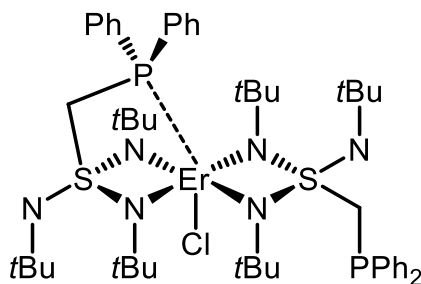
Empirical formula: $\text{C}_{50} \text{H}_{78} \text{Cl} \text{N}_6 \text{P}_2 \text{S}_2 \text{Ho} (\text{C}_{2.14} \text{H}_{4.56} \text{O}_{0.36})$

Molecular weight: 1125.73 g/mol

Yield: 298.6 mg, 0.2653 mmol, 51%

LIFDI-MS: m/z : 1053.3 $[\text{M}-\text{Cl}]^+$.

Elemental analysis for $\text{C}_{50}\text{H}_{78}\text{ClN}_6\text{P}_2\text{S}_2\text{Ho}(\text{C}_{2.14}\text{H}_{4.56}\text{O}_{0.36})$ (found (calc.) [%]): C 54.75 (55.63), H 7.30 (7.39), N 7.36 (7.47), S 5.91 (5.70).

5.3.22. $[\text{ClEr}\{\text{Ph}_2\text{PCH}_2\text{S}(\text{N}^t\text{Bu})_3\}_2]$ (**12d**)

The potassium precursor $[\text{K}\{\text{Ph}_2\text{PCH}_2\text{S}(\text{N}^t\text{Bu})_3\}]$ (500.0 mg, 1.034 mmol) and ErCl_3 (141.5 mg, 0.517 mmol) were suspended in toluene (40 mL), thf (0.8 mL) was added and the mixture was stirred for 1 d at room temperature. Subsequently, KCl was filtered off and the solvent was removed under reduced pressure. The residue was extracted with thf, filtered and the solvent was removed in vacuo again. To receive the target compound as crystalline material the raw product was dissolved in thf (2.5 mL) and layered with *n*-pentane (12.5 mL). Crystallization started within hours up to several days at room temperature yielding pale pink crystals that were isolated and washed with *n*-pentane (2 x 1 mL).

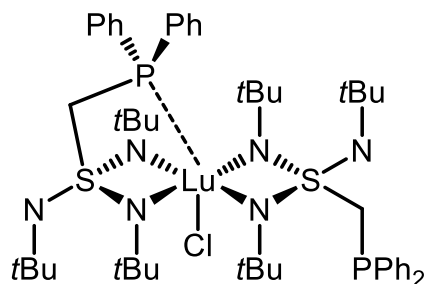
Empirical formula: $\text{C}_{50} \text{H}_{78} \text{Cl} \text{N}_6 \text{P}_2 \text{S}_2 \text{Er} (\text{C}_{2.09} \text{H}_{4.38} \text{O}_{0.41})$

Molecular weight: 1128.07 g/mol

Yield: 259.8 mg, 0.2303 mmol, 45%

LIFDI-MS: m/z : 1056.3 $[\text{M}-\text{Cl}]^+$.

Elemental analysis for $\text{C}_{50}\text{H}_{78}\text{ClN}_6\text{P}_2\text{S}_2\text{Er}(\text{C}_{2.09}\text{H}_{4.38}\text{O}_{0.41})$ (found (calc.) [%]): C 54.53 (55.46), H 7.20 (7.36), N 7.33 (7.45), S 5.70 (5.68).

5.3.23. $[\text{ClLu}\{\text{Ph}_2\text{PCH}_2\text{S}(\text{NtBu})_3\}_2]$ (**12e**)

The potassium precursor $[\text{K}\{\text{Ph}_2\text{PCH}_2\text{S}(\text{NtBu})_3\}]$ (500.0 mg, 1.034 mmol) and LuCl_3 (145.4 mg, 0.517 mmol) were suspended in toluene (40 mL), thf (0.8 mL) was added and the mixture was stirred for 1 d at room temperature. Subsequently, KCl was filtered off and the solvent was removed under reduced pressure. The residue was extracted with thf, filtered and the solvent was removed in vacuo again. To receive the target compound as crystalline material the raw product was dissolved in thf (2.5 mL) and layered with *n*-pentane (12.5 mL). Crystallization started within hours up to several days at room temperature yielding colorless crystals that were isolated and washed with *n*-pentane (2 x 1 mL).

Empirical formula: $\text{C}_{50} \text{H}_{78} \text{Cl} \text{N}_6 \text{P}_2 \text{S}_2 \text{Lu} (\text{C}_{2.27} \text{H}_{5.08} \text{O}_{0.23})$

Molecular weight: 1135.77 g/mol

Yield: 175.3 mg, 0.1543 mmol, 30%

^1H -NMR (500.13 MHz, 298 K, C_6D_6): δ [ppm] = 1.50 (s, 18H, 2 $\text{NC}(\text{CH}_3)_3$), 1.65 (s, 36H, 4 $\text{Lu-NC}(\text{CH}_3)_3$), 4.77 – 5.06 (m, 4H, 2 PCH_2), 6.96 – 7.13 (m, 12H, *m,p*-Ph-H), 7.63 (s, 4H, *o*-Ph-H), 7.99 (s, 4H, *o*-Ph-H).

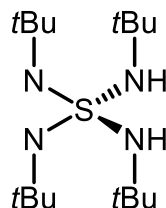
$^{13}\text{C}\{^1\text{H}\}$ -NMR (125.76 MHz, 298 K, C_6D_6): δ [ppm] = 33.42 (s, $\text{NC}(\text{CH}_3)_3$), 34.24 (s, $\text{Lu-NC}(\text{CH}_3)_3$), 54.24 (s, $\text{Lu-NC}(\text{CH}_3)_3$), 55.18 (s, $\text{NC}(\text{CH}_3)_3$), 64.79 (s br, PCH_2), 128.69 – 128.77 (m, *m,m,p*-Ph-C), 129.53 (s, *p*-Ph-C), 133.03 (d, $^2J_{\text{CP}} = 16.6$ Hz, *o*-Ph-C), 135.27 (d, $^2J_{\text{CP}} = 18.6$ Hz, *o*-Ph-C), 138.77 (s, *ipso*-Ph-C).

^{15}N -NMR (50.70 MHz, 298 K, C_6D_6): δ [ppm] = -216.5 (s, $\text{Lu-NC}(\text{CH}_3)_3$), -218.7 (s, $\text{Lu-NC}(\text{CH}_3)_3$), -255.2 (s, $\text{NC}(\text{CH}_3)_3$).

$^{31}\text{P}\{^1\text{H}\}$ -NMR (202.46 MHz, 298 K, C_6D_6): δ [ppm] = -24.59 (s).

LIFDI-MS: m/z : 1063.6 $[\text{M-Cl}]^+$.

Elemental analysis for $\text{C}_{50}\text{H}_{78}\text{ClN}_6\text{P}_2\text{S}_2\text{Lu}(\text{C}_{2.27}\text{H}_{5.08}\text{O}_{0.23})$ (found (calc.) [%]): C 55.03 (55.28), H 7.12 (7.37), N 7.48 (7.40), S 6.12 (5.65).

5.3.24. $\text{H}_2\text{S}(\text{NtBu})_4$ (**13**)*Method A:*

A mixture of $[(\text{thf})_4\text{Li}_2(\text{NtBu})_4\text{S}]$ (100.0 mg, 0.1616 mmol) and Me_3NHCl (34.0 mg, 0.356 mmol) were dissolved in thf (2 mL) at room temperature. After stirring for 5 min the solvent was removed under reduced pressure. The residue was dissolved in *n*-pentane (1 mL) and the solution was filtered to remove LiCl. The filtrate was concentrated again, washed with MeCN (0.2 mL) and stored at -34°C . Crystallization started within minutes yielding colorless crystals suitable for X-ray analysis. The product was isolated and dried under reduced pressure.

Since the target compound is not stable at room temperature, it is always contaminated with its decomposition product $\text{S}(\text{NtBu})_3$. The ratio of those can be determined by NMR, but due to the decomposition the amount of product and the overall isolated substance can differ a lot..

Method B:

A mixture of $[(\text{thf})_4\text{Li}_2(\text{NtBu})_4\text{S}]$ (100.0 mg, 0.1616 mmol) and $t\text{BuNH}_3\text{Cl}$ (39.0 mg, 0.356 mmol) were dissolved in thf (2 mL) at room temperature. After stirring for 2 min the solvent was removed under reduced pressure. The residue was dissolved in *n*-pentane (1 mL) and the solution was filtered to remove LiCl. The filtrate was concentrated again, washed with MeCN (0.2 mL) and stored at -34°C . Crystallization started within minutes yielding colorless crystals suitable for X-ray analysis. The product was isolated and dried under reduced pressure.

Empirical formula: $\text{C}_{16} \text{H}_{38} \text{N}_4 \text{S}$

Molecular weight: 318.57 g/mol

Yield (A): 44.1 mg (35.5 mg product), 0.111 mmol, 69%

Yield (B): 51.4 mg (37.7 mg product), 0.118 mmol, 73%

^1H -NMR (500.13 MHz, 283 K, C_6D_6): δ [ppm] = 1.28 (s, 18H, 2 $\text{HNC}(\text{CH}_3)_3$), 1.51 (s, 18H, 2 $\text{NC}(\text{CH}_3)_3$), 3.06 (s, 2H, 2 $\text{HNC}(\text{CH}_3)_3$).

$^{13}\text{C}\{^1\text{H}\}$ -NMR (125.76 MHz, 283 K, C_6D_6): δ [ppm] = 30.06 (s, $\text{HNC}(\text{CH}_3)_3$), 32.96 (s, $\text{NC}(\text{CH}_3)_3$), 52.95 (s, $\text{NC}(\text{CH}_3)_3$), 53.81 (s, $\text{HNC}(\text{CH}_3)_3$).

^{15}N -NMR (50.70 MHz, 283 K, C_6D_6): δ [ppm] = -257.41 ($\text{NC}(\text{CH}_3)_3$), -253.19 ($\text{HNC}(\text{CH}_3)_3$).

5.4. Crystallographic section

5.4.1. Crystal selection and handling

Air- and moisture-sensitive crystal for single-crystal X-ray diffraction analysis were either preselected from a *Schlenk* flask under an argon gas flow, followed by a quick transfer into perfluorinated polyether oil on a microscope slide, or under an argon atmosphere in a glovebox. Under air, the crystals were immediately shock-cooled with a nitrogen gas flow using the *X-TEMP2* device.^[272–274] Suitable crystals were selected using a microscope equipped with a polarizer. The selected crystals were then mounted to the tip of a *MiTeGen*[®]*MicroMount*, fixed to a goniometer head and shock-cooled to 100(2) K by the corresponding crystal cooling device.^[275]

5.4.2. Data collection and processing

Data collection was performed either on a *BRUKER Smart APEX* diffractometer with an *Incoatec I μ S-Mo-Microsource* ($\lambda = 0.71073 \text{ \AA}$), a *BRUKER TXS* rotating-Mo-anode ($\lambda = 0.71073 \text{ \AA}$) or a *BRUKER Smart APEX* with an *Incoatec I μ S-Ag-Microsource* ($\lambda = 0.56086 \text{ \AA}$).^[276] All diffractometers were equipped with an *Oxford Cryosystems* crystal cooling device, an *APEX II CCD* detector and either *Incoatec Quazar* or *Helios* mirror optics, mounted on a D8-goniometer.

All diffractometers were controlled by the *APEX2* program suite.^[277] Prior to each experiment, a quick measurement (*matrix-scan*) was recorded to check the crystal quality, cell parameters and to determine the required exposure time. Measurements were conducted in a ω -scan mode with a step width of 0.5° . Determination and refinement of the unit cell was done with the *APEX2*^[277] or *APEX3*^[278] program suite. All data were integrated with *SAINT*^[279] and a semi-empirical absorption correction was applied with *SADABS*^[280] or in the case of non-merohedral twinning with *TWINABS*.^[281] Additional, if required for the data, a 3λ correction was performed.^[282] Data statistics and preliminary space group determination as well as file setup for structure solution and refinement was carried out with *XPREF*.^[283]

5.4.3. Structure solution and refinement

All structures have been solved by direct methods using *SHELXT* within *SHELXTL*.^[284] Structure solution was performed on F_o^2 , which are directly proportional to the measured intensities, via *SHELXL* within *SHELXTL* using the *ShelXle GUI*.^[285] If not stated differently, all C-bonded hydrogen atoms were refined isotropically on calculated positions using a riding model. The positions were geometrically optimized and the U_{iso} were constrained to 1.2 U_{eq} of the pivot atom or 1.5 U_{eq} of the methyl carbon atom. All refinements were performed to minimize the function $M(p_i, k)$ shown in **Eq. 5-4** using the weights w_H defined in **Eq. 5-5**, with the structural parameters p_i and the scale factor k .

Eq. 5-4:

$$M(p_i, k) = \sum_H w [k|F_{obs}(H)|^2 - |F_{calc}(H)|^2]^2 = \min$$

Eq. 5-5:

$$w_H^{-1} = \sigma_H^2 F_{obs}^2 + (g1 \cdot P)^2 + g2 \cdot P \quad \text{with } P = \frac{F_{obs}^2 + 2F_{calc}^2}{3}$$

The results of the refinements were verified by comparison of the calculated and the observed structure factors. Commonly used criteria are the residuals $R1$ shown in **Eq. 5-6** and $wR2$ shown in **Eq. 5-7** with $wR2$ being more significant since the model is refined against F^2 .

Eq. 5-6:

$$R1 = \frac{\sum ||F_{obs}| - |F_{calc}||}{\sum ||F_{obs}||}$$

Eq. 5-7:

$$wR2 = \sqrt{\frac{\sum w(F_{obs}^2 - F_{calc}^2)^2}{\sum w(F_{obs}^2)^2}}$$

Furthermore, the goodness of fit (GoF , S), a figure of merit showing the relation between deviation of F_{calc} from F_{obs} and the over-determination of refined parameters is calculated with **Eq. 5-8**, with the number of reflections n and the number of parameters p .

Eq. 5-8:

$$S = \sqrt{\frac{\sum w(F_{obs}^2 - F_{calc}^2)^2}{n-p}}$$

Residual densities from the different Fourier analyses should be small. These residuals are usually found in the bonding regions due to the model restrictions. Higher residuals for heavy scatterers are acceptable as they arise mainly from absorption effects and Fourier truncation errors due to the limited recorded resolution range. The highest peak and deepest hole from difference Fourier analysis are listed in the crystallographic tables. The quality of the model is depicted by the size, ellipticity and orientation of the ADPs. These ADPs should be equal in size with little ellipticity and oriented perpendicular to the bonds. All graphics were generated and plotted with the *xp*^[286] program with the anisotropic displacement parameters at the 50 % probability level unless stated differently.

5.4.4. Treatment of disorder

Structures containing disordered fragments were refined using constraints and restraints. Constraints, such as the site occupation factor and AFIX instruction, have been used. Furthermore, distance restraints like *SADI* and *SAME* and anisotropic displacement parameter (ADP) restraints like *SIMU*, *DELU* and *RIGU* were employed.^[287] Those restraints are treated as additional experimental observations, which increases the data to refine against. Therefore, the minimization function changes according to **Eq. 5-9**.

Eq. 5-9:

$$M = \sum w(F_{\text{obs}}^2 - F_{\text{calc}}^2)^2 + \sum w_r(R_{\text{target}} - R_{\text{calc}})^2$$

5.5. Determined structures

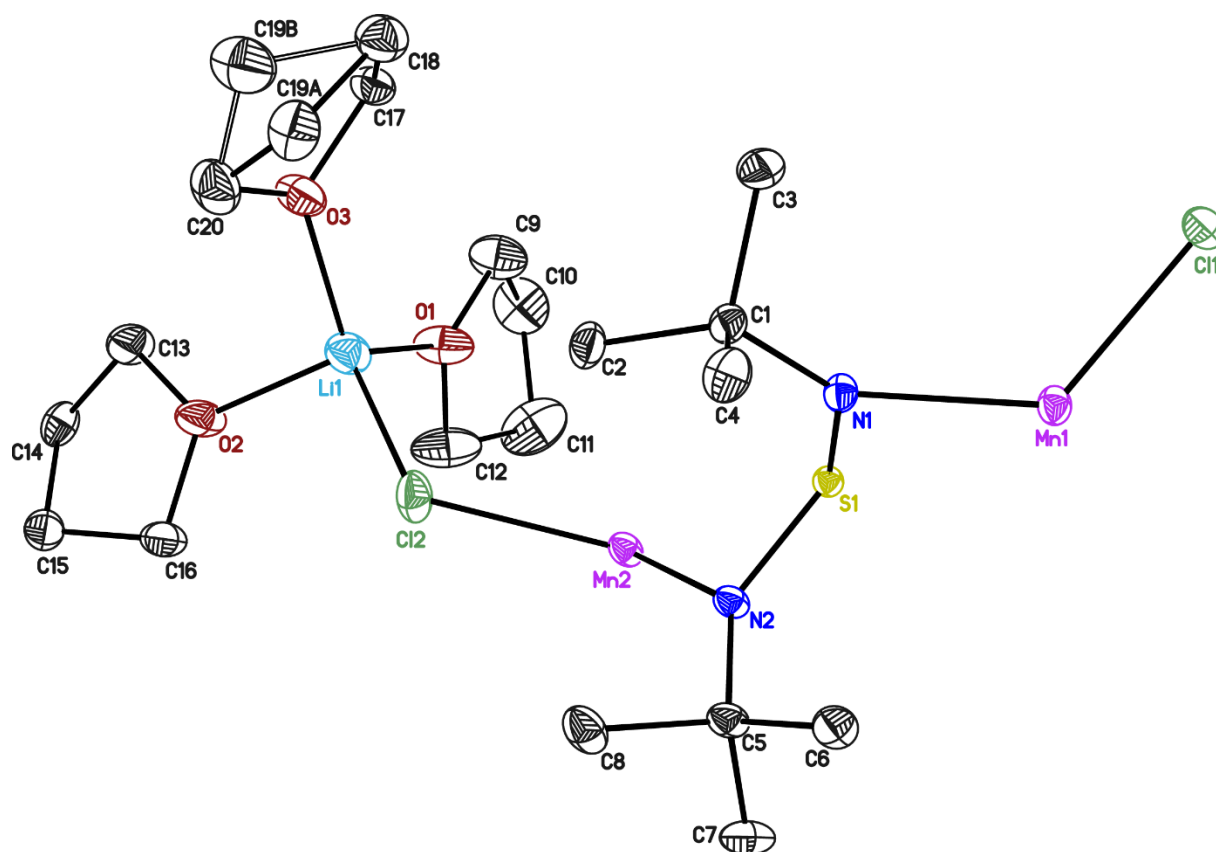
5.5.1. $[\text{Cl}_2\text{Mn}(\text{N}t\text{Bu})_2\text{S}(t\text{BuN})_2\text{Mn}\{\text{ClLi}(\text{thf})_3\}_2]$ (**1**)

Figure 5-1. Asymmetric unit of **1**. Anisotropic displacement parameters are depicted on a probability level of 50%. Hydrogen atoms are omitted for clarity. The disordered C19 was refined on two positions. The occupancy of the main positions for C19A was refined to 0.814(5). For the refinement distance restraints and restraints for the anisotropic displacement parameters were used.

Table 5-1. Crystal data of **1**.

CCDC no.	2038409	Z	4
Empirical formula	$\text{C}_{40}\text{H}_{84}\text{Cl}_4\text{Li}_2\text{Mn}_2\text{N}_4\text{O}_6\text{S}$	$\rho_{\text{calc}} [\text{g}/\text{cm}^3]$	1.273
Formula weight [g/mol]	1014.73	$\mu [\text{mm}^{-1}]$	0.761
Temperature [K]	100(2)	F(000)	2160
Wavelength [Å]	0.71073	θ range [°]	1.766 to 27.521
Crystal system	Monoclinic	Reflections collected	40671
Space group	C2/c	Independent reflections	6070
a [Å]	21.477(3)	R(int)	0.0268
b [Å]	14.586(2)	Crystal dimensions [mm]	0.202 x 0.178 x 0.109
c [Å]	19.278(2)	Restraints / parameter	297 / 287
α [°]	90	GoF	1.058
β [°]	118.75(2)	R1 / wR2 ($I > 2\sigma(I)$)	0.0230 / 0.0590
γ [°]	90	R1 / wR2 (all data)	0.0261 / 0.0611
Volume [Å ³]	5294.6(15)	max. diff peak / hole [$\text{e} \text{ Å}^{-3}$]	0.403 / -0.285

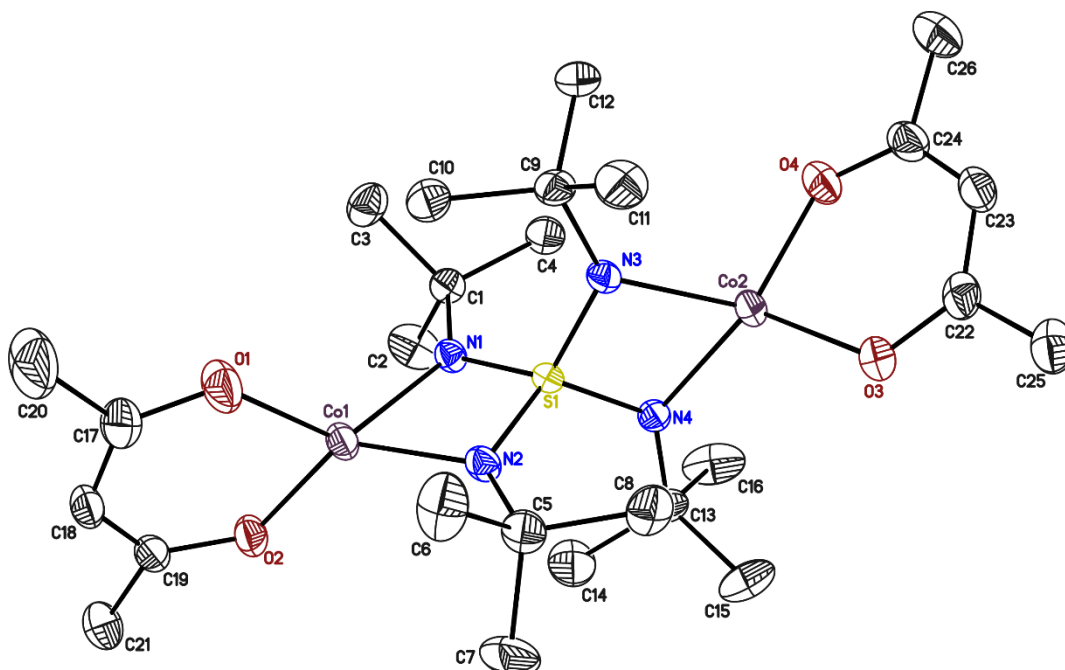
5.5.2. $[(\text{acac})\text{Co}(\text{NtBu})_2\text{S}(\text{tBuN})_2\text{Co}(\text{acac})]$ (**2a**)

Figure 5-2. Asymmetric unit of **2a**. The anisotropic displacement parameters are depicted at the 50% probability level. The hydrogen atoms are omitted for clarity.

Table 5-2. Crystal data of **2a**.

CCDC no.	2038411	Z	4
Empirical formula	$\text{C}_{26}\text{H}_{50}\text{Co}_2\text{N}_4\text{O}_4\text{S}$	ρ_{calc} [g/cm^3]	1.301
Formula weight [g/mol]	632.62	μ [mm^{-1}]	0.588
Temperature [K]	100(2)	F(000)	1344
Wavelength [\AA]	0.56086	θ range [$^\circ$]	1.515 to 21.750
Crystal system	Monoclinic	Reflections collected	64128
Space group	$P2_1/n$	Independent reflections	7777
a [\AA]	12.655(2)	R(int)	0.0448
b [\AA]	19.653(3)	Crystal dimensions [mm]	0.252 x 0.179 x 0.102
c [\AA]	13.043(2)	Restraints / parameter	0 / 350
α [$^\circ$]	90	GoF	1.025
β [$^\circ$]	95.45(2)	R1 / wR2 ($I > 2\sigma(I)$)	0.0301 / 0.0714
γ [$^\circ$]	90	R1 / wR2 (all data)	0.0434 / 0.0784
Volume [\AA^3]	3229.2(9)	max. diff peak / hole [e \AA^{-3}]	0.831 / -0.369

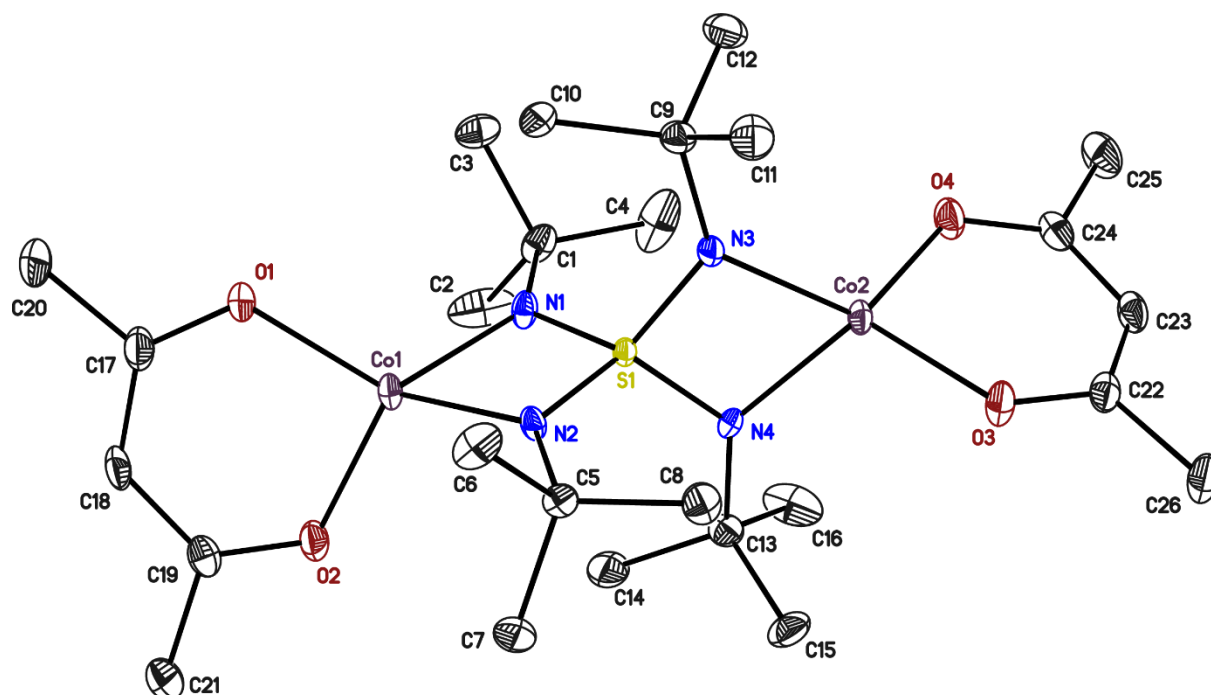
5.5.3. [(acac)Co(NtBu)₂S(tBuN)₂Co(acac)] (2b)

Figure S-3. Asymmetric unit of **2b**. The anisotropic displacement parameters are depicted at the 50% probability level. The hydrogen atoms are omitted for clarity.

Table S-3. Crystal data of **2b**.

CCDC no.	2038410	Z	4
Empirical formula	C ₂₆ H ₅₀ Co ₂ N ₄ O ₄ S	ρ_{calc} [g/cm ³]	1.295
Formula weight [g/mol]	632.62	μ [mm ⁻¹]	0.585
Temperature [K]	80(2)	F(000)	1344
Wavelength [Å]	0.56086	θ range [°]	1.606 to 22.302
Crystal system	Orthorhombic	Reflections collected	65890
Space group	Pna2 ₁	Independent reflections	8387
a [Å]	20.053(3)	R(int)	0.0387
b [Å]	11.548(2)	Crystal dimensions [mm]	0.455 x 0.292 x 0.258
c [Å]	14.017(2)	Restraints / parameter	1 / 350
α [°]	90	GoF	1.018
β [°]	90	R1 / wR2 (I > 2 σ (I))	0.0218 / 0.0471
γ [°]	90	R1 / wR2 (all data)	0.0253 / 0.0483
Volume [Å ³]	3245.9(9)	max. diff peak / hole [e Å ⁻³]	0.252 / -0.219

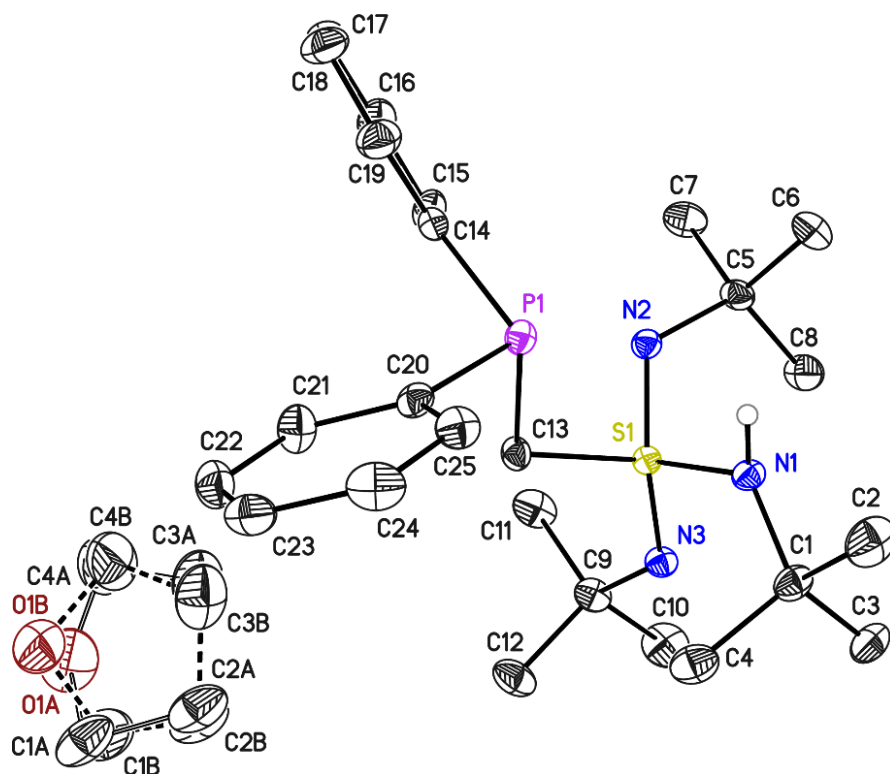
5.5.5. $\text{Ph}_2\text{PCH}_2\text{S}(\text{NtBu})_2\text{NHtBu}$ (**4**)

Figure S-5 Asymmetric unit of **4**. Anisotropic displacement parameters are depicted on a probability level of 50%. Hydrogen atoms bond to carbon atoms are omitted for clarity. The THF molecule was disordered about an inversion centre in two crystallographic independent positions. The occupancy of the main positions refined to 0.302(7). For the refinement distance restraints and restraints and constraints for the anisotropic displacement parameters were used. The hydrogen atom bond to N1 was refined freely with a distance restraint.

Table S-5 Crystal data of **4**.

CCDC no.	2068811	Z	4
Empirical formula	$\text{C}_{54}\text{H}_{88}\text{N}_6\text{OP}_2\text{S}_2\text{C}_{25}\text{H}_{40}\text{N}_3\text{PS}$ $\cdot x \text{ 0.5 C}_4\text{H}_8\text{O}$	Crystal dimensions [mm]	0.307 x 0.162 x 0.154
Formula weight [g/mol]	963.36481.68	μ [mm^{-1}]	0.105
Temperature [K]	100(2)	F(000)	1048
Wavelength [\AA]	0.56086	θ range [$^\circ$]	1.694 to 20.579
Crystal system	Monoclinic	Reflections collected	42662
Space group	$P2_1/n$	Independent reflections	5834
a [\AA]	a = 9.042(2)	R(int)	0.0428
b [\AA]	b = 37.946(6)	ρ_{calc} [g/cm^3]	1.128
c [\AA]	c = 9.357(2)	Restraints / parameter	237 / 358
α [$^\circ$]	90	GoF	1.0073
β [$^\circ$]	117.91(2)	R1 / wR2 ($I > 2\sigma(I)$)	0.0373 / 0.0813
γ [$^\circ$]	90	R1 / wR2 (all data)	0.0457 / 0.0852
Volume [\AA^3]	2837.0(11)	max. diff peak / hole [e \AA^{-3}]	0.390 / -0.321

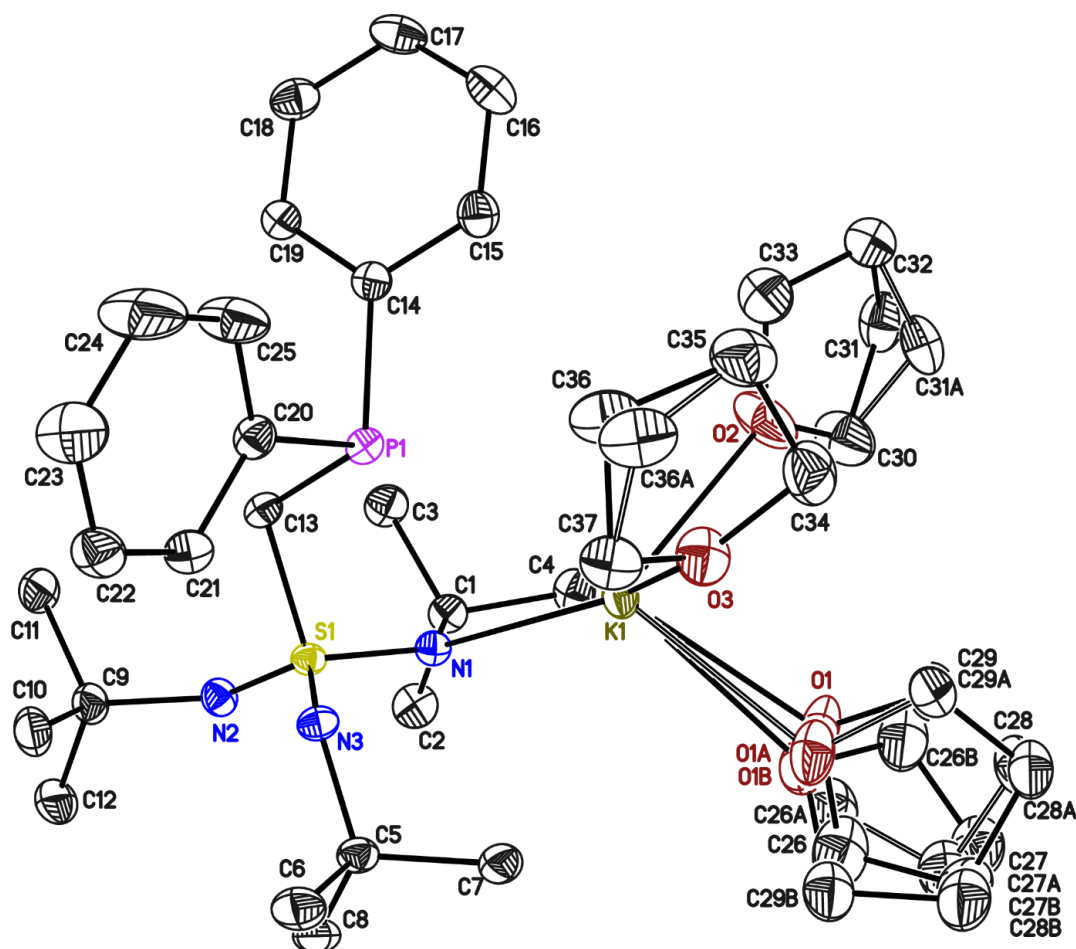
5.5.6. $[K(thf)_3\{Ph_2PCH_2S(NtBu)_3\}]$ (5)

Figure 5-6. Asymmetric unit of **5**. Anisotropic displacement parameters are depicted on a probability level of 50%. Hydrogen atoms are omitted for clarity. The disordered C31/A was refined on two positions. The occupancy of the main positions for C31 refined to 0.723(12). The disordered C36/A was refined on two positions. The occupancy of the main positions for C36 was refined to 0.80(2). The thf molecule with O1 was refined on three positions with the occupancies of the main position for 0.670(3), 0.240(3) and 0.089(2). For the refinement of the disordered parts distance restraints and restraints for the anisotropic displacement parameters were used.

Table 5-6. Crystal data of **5**.

CCDC no.	2104539	Z	4
Empirical formula	$C_{37}H_{63}KN_3O_3PS$	ρ_{calc} [g/cm ³]	1.161
Formula weight [g/mol]	700.03	μ [mm ⁻¹]	0.141
Temperature [K]	100(2)	F(000)	1520
Wavelength [Å]	0.56086	θ range [°]	1.367 to 20.276
Crystal system	Monoclinic	Reflections collected	135236
Space group	$P2_1/n$	Independent reflections	7900
a [Å]	12.652(2)	R(int)	0.0558
b [Å]	23.512(3)	Crystal dimensions [mm]	0.294 x 0.184 x 0.140
c [Å]	13.643(2)	Restraints / parameter	917 / 537
α [°]	90	GoF	1.037
β [°]	99.32(2)	R1 / wR2 ($I > 2\sigma(I)$)	0.0345 / 0.0801
γ [°]	90	R1 / wR2 (all data)	0.0472 / 0.0872
Volume [Å ³]	4004.9(10)	max. diff peak / hole [e Å ⁻³]	0.347 / -0.323

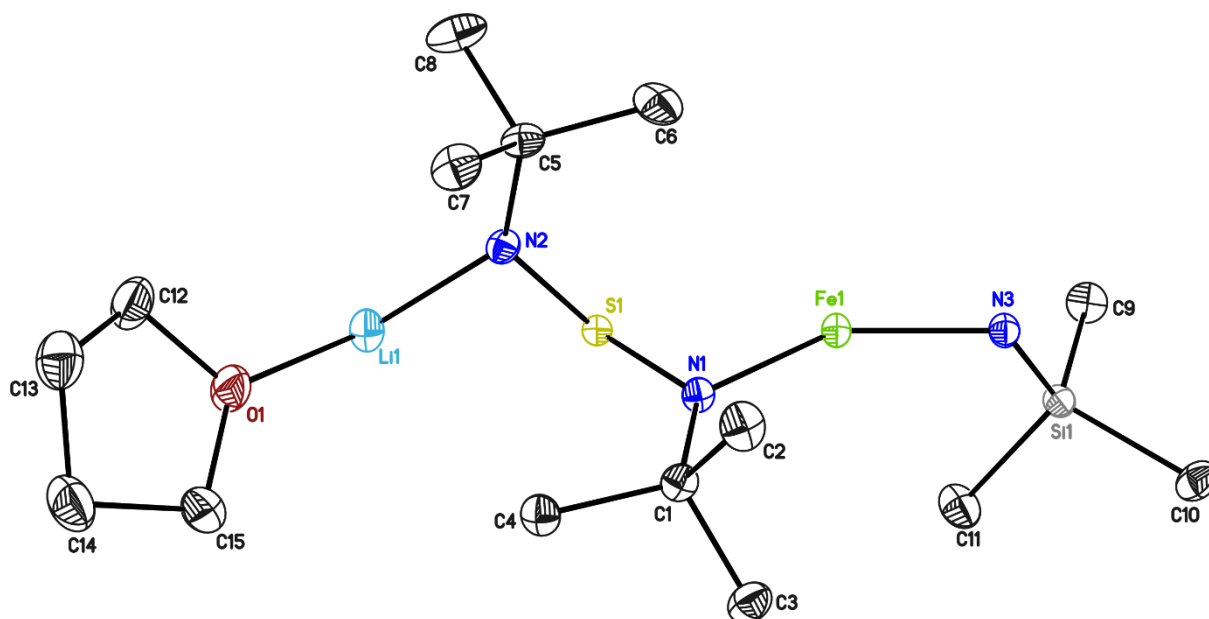
5.5.7. [(thf)₂Li{(NtBu)₄S}Fe{N(SiMe₃)₂}] (6)

Figure S-7. Asymmetric unit of **6**. The anisotropic displacement parameters are depicted at the 50% probability level. The hydrogen atoms are omitted for clarity.

Table S-7. Crystal data of **6**.

CCDC no.	2068811	Z	4
Empirical formula	C ₃₀ H ₇₀ FeLiN ₅ O ₂ SSi ₂	ρ_{calc} [g/cm ³]	1.141
Formula weight [g/mol]	683.94	μ [mm ⁻¹]	0.275
Temperature [K]	100(2)	F(000)	1496
Wavelength [Å]	0.56086	θ range [°]	1.535 to 20.817
Crystal system	Monoclinic	Reflections collected	28551
Space group	C2/c	Independent reflections	4234
a [Å]	15.535(2)	R(int)	0.0460
b [Å]	15.411(2)	Crystal dimensions [mm]	0.338 x 0.270 x 0.190
c [Å]	18.112(3)	Restraints / parameter	0 / 201
α [°]	90	GoF	1.039
β [°]	113.30(2)	R1 / wR2 ($I > 2\sigma(I)$)	0.0297 / 0.0693
γ [°]	90	R1 / wR2 (all data)	0.0405 / 0.0735
Volume [Å ³]	3982.6(11)	max. diff peak / hole [e Å ⁻³]	0.314 / -0.285

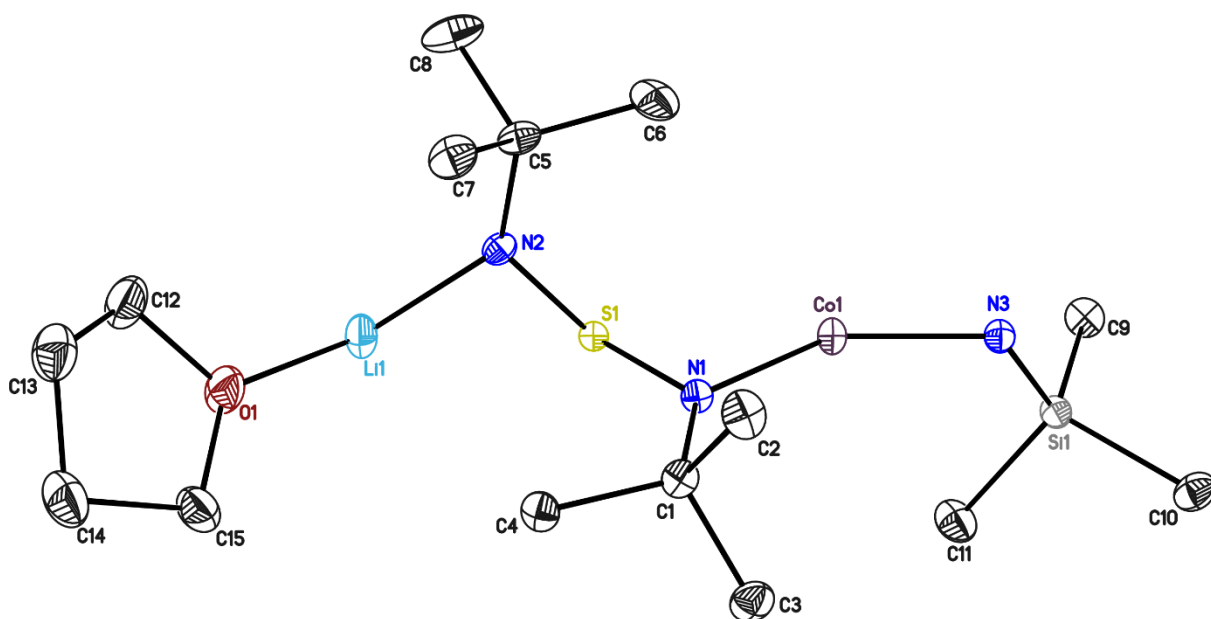
5.5.8. [(thf)₂Li{(NtBu)₄S}Co{N(SiMe₃)₂}] (7)

Figure 5-8. Asymmetric unit of **7**. The anisotropic displacement parameters are depicted at the 50% probability level. The hydrogen atoms are omitted for clarity.

Table 5-8. Crystal data of **7**.

CCDC no.	2068813	Z	4
Empirical formula	C ₃₀ H ₇₀ CoLiN ₅ O ₂ SSi ₂	ρ_{calc} [g/cm ³]	1.150
Formula weight [g/mol]	687.02	μ [mm ⁻¹]	0.304
Temperature [K]	100(2)	F(000)	1500
Wavelength [Å]	0.56086	θ range [°]	1.538 to 20.066
Crystal system	Monoclinic	Reflections collected	35851
Space group	C2/c	Independent reflections	3798
a [Å]	15.534(2)	R(int)	0.0696
b [Å]	15.343(2)	Crystal dimensions [mm]	0.259 x 0.109 x 0.082
c [Å]	18.113(3)	Restraints / parameter	0 / 201
α [°]	90	GoF	1.038
β [°]	113.24(2)	R1 / wR2 (I > 2 σ (I))	0.0327 / 0.0686
γ [°]	90	R1 / wR2 (all data)	0.0482 / 0.0744
Volume [Å ³]	3966.7(11)	max. diff peak / hole [e Å ⁻³]	0.314 / -0.317

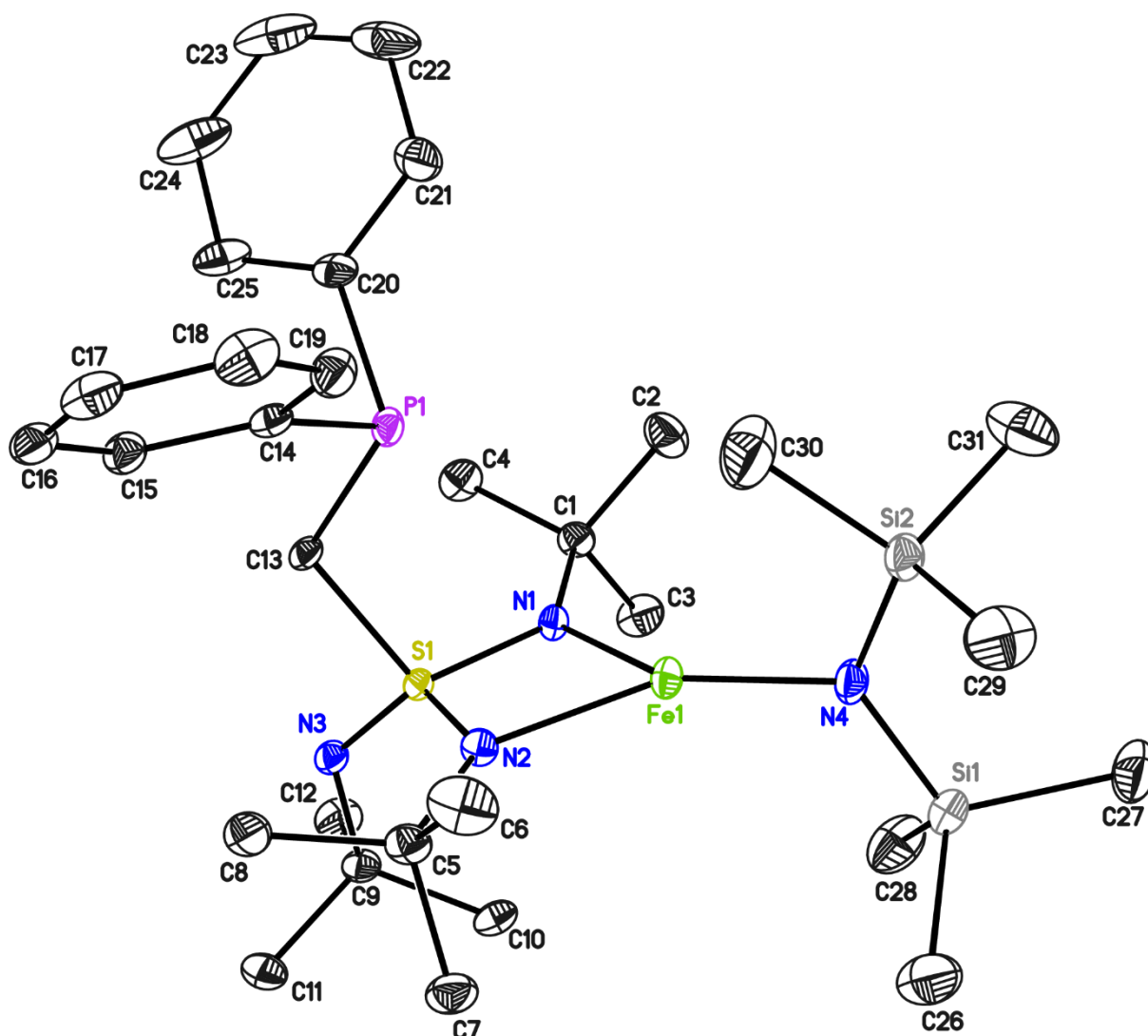
5.5.9. $[\text{Fe}\{\text{N}(\text{SiMe}_3)_2\}\{\text{Ph}_2\text{PCH}_2\text{S}(\text{NtBu})_3\}]$ (**8**)

Figure S-9. Asymmetric unit of **8**. The anisotropic displacement parameters are depicted at the 50% probability level. The hydrogen atoms are omitted for clarity.

Table S-9. Crystal data of **8**.

CCDC no.	2068814	Z	4
Empirical formula	$\text{C}_{31}\text{H}_{57}\text{FeN}_4\text{PSSi}_2$	$\rho_{\text{calc}} [\text{g}/\text{cm}^3]$	1.159
Formula weight $[\text{g}/\text{mol}]$	660.86	$\mu [\text{mm}^{-1}]$	0.306
Temperature $[\text{K}]$	100(2)	$F(000)$	1424
Wavelength $[\text{\AA}]$	0.56086	θ range $^\circ$	1.506 to 20.563
Crystal system	Monoclinic	Reflections collected	56945
Space group	$P2_1/c$	Independent reflections	7774
a $[\text{\AA}]$	10.736(2)	$R(\text{int})$	0.0642
b $[\text{\AA}]$	31.052(3)	Crystal dimensions $[\text{mm}]$	0.191 x 0.137 x 0.098
c $[\text{\AA}]$	11.938(2)	Restraints / parameter	0 / 376
α $^\circ$	90	GoF	1.028
β $^\circ$	107.92(2)	$R1 / wR2$ ($I > 2\sigma(I)$)	0.0364 / 0.0737
γ $^\circ$	90	$R1 / wR2$ (all data)	0.0546 / 0.0796
Volume $[\text{\AA}^3]$	3786.7(11)	max. diff peak / hole $[\text{e} \text{\AA}^{-3}]$	0.347 / -0.344

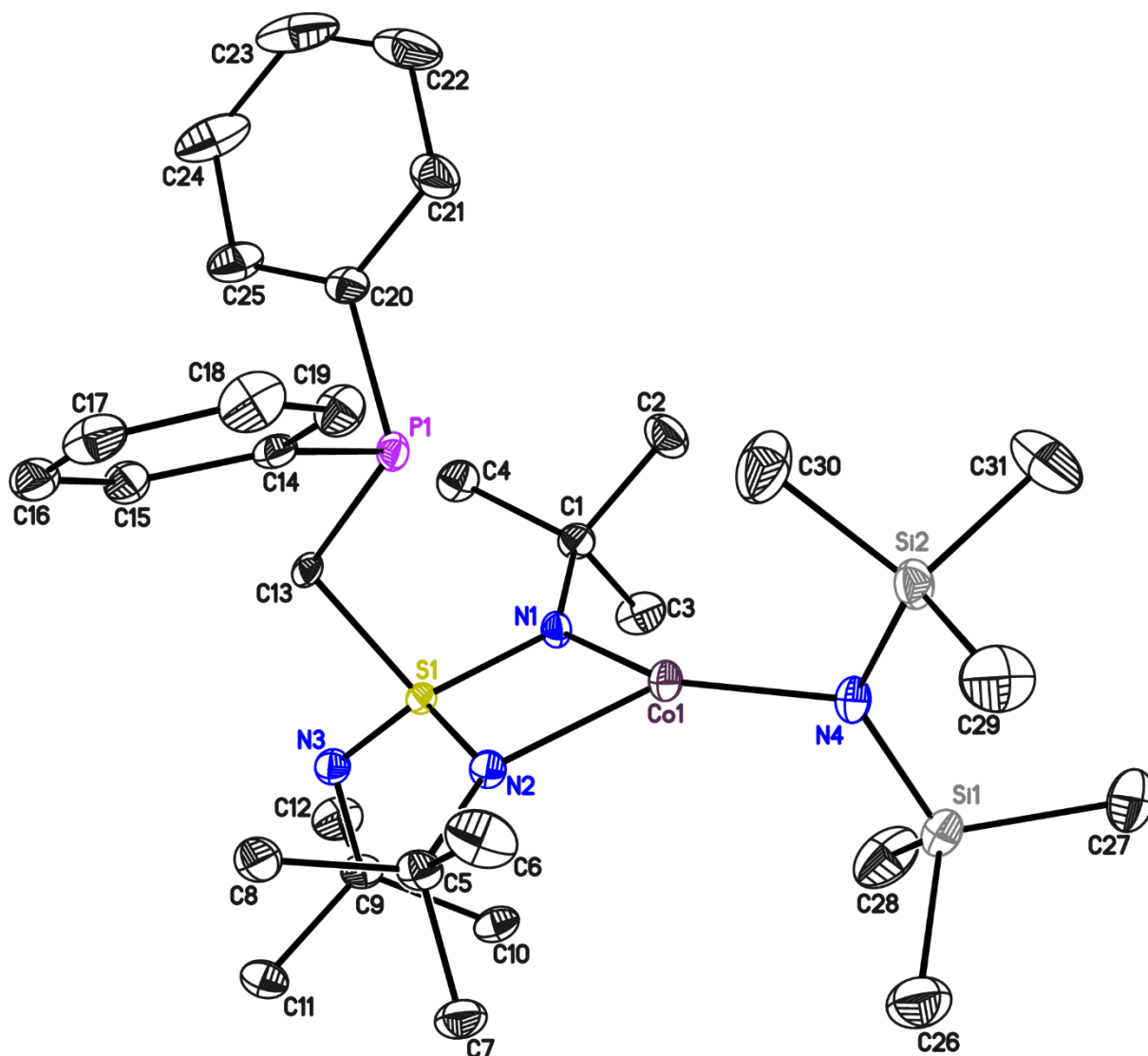
5.5.10. $[\text{Co}\{\text{N}(\text{SiMe}_3)_2\}\{\text{Ph}_2\text{PCH}_2\text{S}(\text{NtBu})_3\}]$ (9)

Figure 5-10. Asymmetric unit of **9**. The anisotropic displacement parameters are depicted at the 50% probability level. The hydrogen atoms are omitted for clarity.

Table 5-10. Crystal data of **9**.

CCDC no.	2068815	Z	4
Empirical formula	$\text{C}_{31}\text{H}_{57}\text{CoN}_4\text{PSSi}_2$	$\rho_{\text{calc}} [\text{g}/\text{cm}^3]$	1.171
Formula weight $[\text{g}/\text{mol}]$	663.94	$\mu [\text{mm}^{-1}]$	0.337
Temperature $[\text{K}]$	100(2)	$F(000)$	1428
Wavelength $[\text{\AA}]$	0.56086	θ range $[\circ]$	1.514 to 21.387
Crystal system	Monoclinic	Reflections collected	164140
Space group	$P2_1/c$	Independent reflections	8646
a $[\text{\AA}]$	10.737(2)	$R(\text{int})$	0.0463
b $[\text{\AA}]$	31.049(3)	Crystal dimensions $[\text{mm}]$	0.234 x 0.175 x 0.108
c $[\text{\AA}]$	11.858(2)	Restraints / parameter	0 / 376
α $[\circ]$	90	GoF	1.101
β $[\circ]$	107.77(2)	$R1 / wR2$ ($I > 2\sigma(I)$)	0.0337 / 0.0724
γ $[\circ]$	90	$R1 / wR2$ (all data)	0.0415 / 0.0754
Volume $[\text{\AA}^3]$	3764.5(11)	max. diff peak / hole $[\text{e } \text{\AA}^{-3}]$	0.796 / -0.321

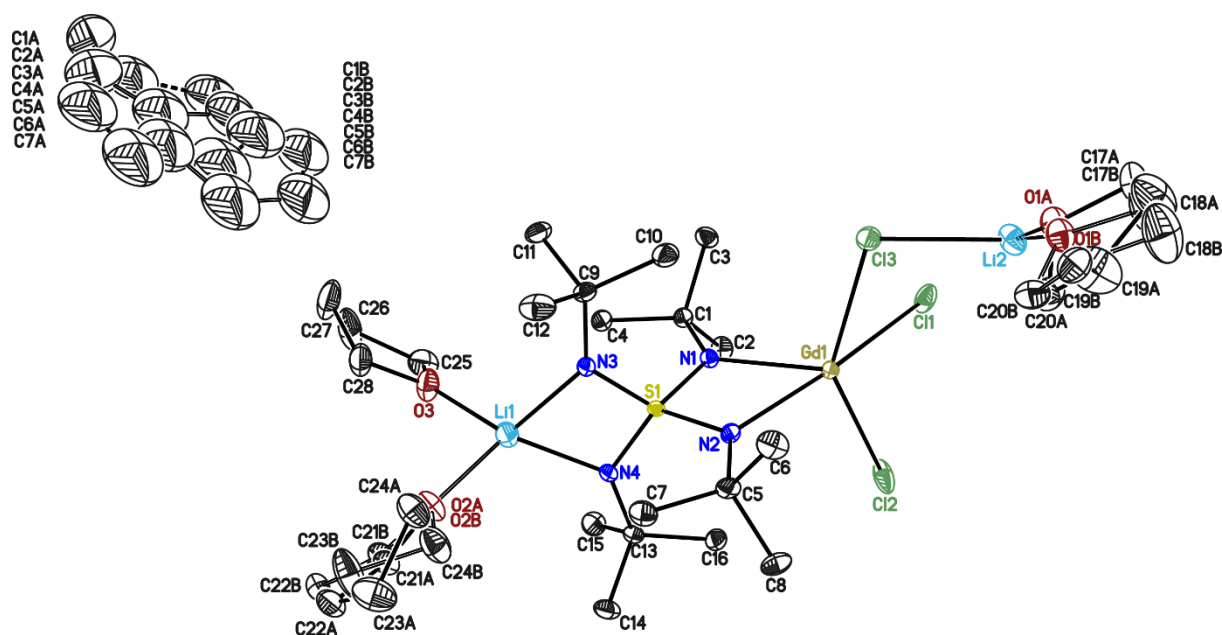
5.5.11. $[\{\text{Cl}_2\text{Gd}(\text{NtBu})_2\text{S}(\text{NtBu})_2\text{Li}(\text{thf})_2\}_2 \cdot \{\text{ClLi}(\text{thf})_2\}]$ (**10a**)

Figure 5-11. Asymmetric unit of **10a**. Anisotropic displacement parameters are depicted on a probability level of 50%. Hydrogen atoms are omitted for clarity. The disordered thf molecules were refined on two positions. The occupancy of the main positions for the thf molecule with O1B was refined to 0.543(14) and for the thf molecule with O2A was refined to 0.623(13). The disordered toluene was refined on four positions, of which two each are related by a 2-fold axis. The occupancy of the main positions was refined to 0.309(5). For the refinement, distance restraints and restraints for the anisotropic displacement parameters were used.

Table 5-11. Crystal data of **10a**.

CCDC no.	2069109	Z	4
Empirical formula	$\text{C}_{63}\text{H}_{128}\text{Cl}_5\text{Gd}_2\text{Li}_3\text{N}_8\text{O}_6\text{S}_2$	ρ_{calc} [g/cm^3]	1.389
Formula weight [g/mol]	1670.42	μ [mm^{-1}]	1.023
Temperature [K]	100(2)	$F(000)$	3456
Wavelength [\AA]	0.56086	θ range [$^\circ$]	1.705 to 22.031
Crystal system	Monoclinic	Reflections collected	121073
Space group	C2/c	Independent reflections	9970
a [\AA]	27.193(3)	$R(\text{int})$	0.0299
b [\AA]	18.003(2)	Crystal dimensions [mm]	0.230 x 0.211 x 0.154
c [\AA]	19.262(2)	Restraints / parameter	1067 / 581
α [$^\circ$]	90	GoF	1.085
β [$^\circ$]	122.08(2)	$R1$ / $wR2$ ($I > 2\sigma(I)$)	0.0169 / 0.0370
γ [$^\circ$]	90	$R1$ / $wR2$ (all data)	0.0230 / 0.0407
Volume [\AA^3]	7990(2)	max. diff peak / hole [e \AA^{-3}]	0.941 / -0.489

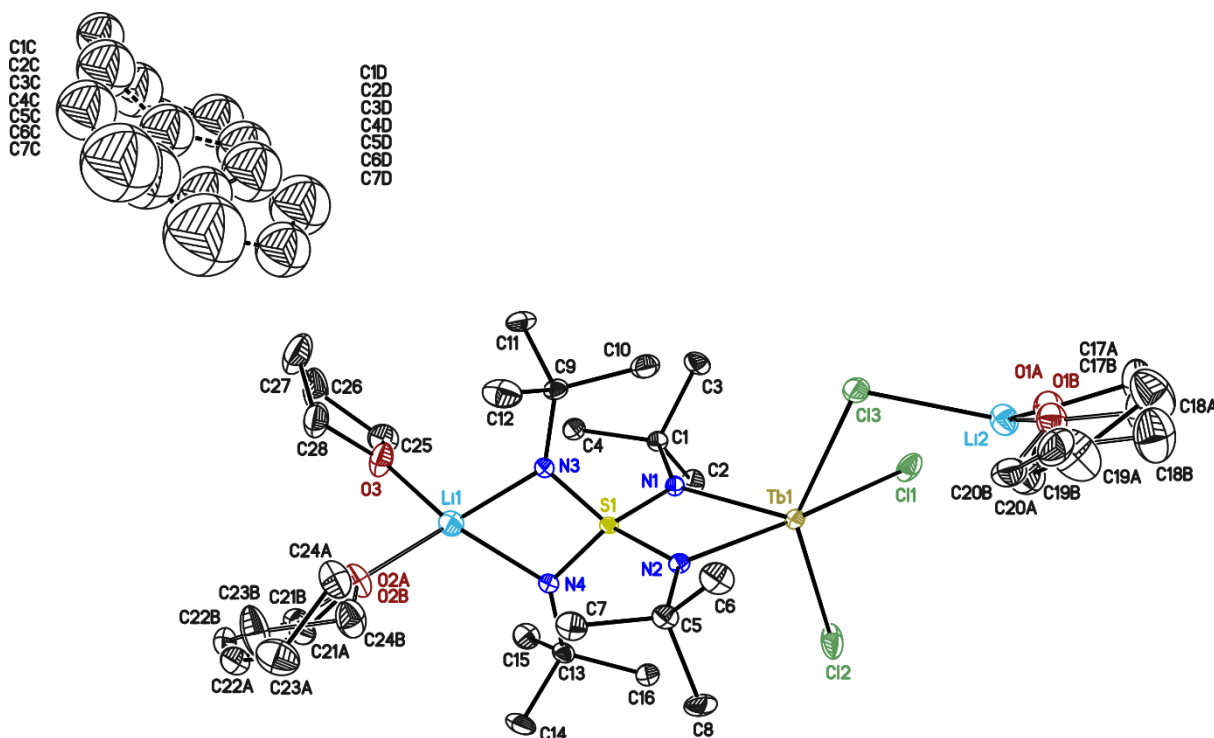
5.5.12. $[\{\text{Cl}_2\text{Tb}(\text{NtBu})_2\text{S}(\text{NtBu})_2\text{Li}(\text{thf})_2\}_2 \cdot \{\text{ClLi}(\text{thf})_2\}]$ (**10b**)

Figure 5-12. Asymmetric unit of **10b**. Anisotropic displacement parameters are depicted on a probability level of 50%. Hydrogen atoms are omitted for clarity. The disordered thf molecules were refined on two positions. The occupancy of the main positions for the thf molecule with O1A was refined to 0.51(2) and for the thf molecule with O2A to 0.603(19). The disordered toluene was refined on four positions, of which two each are related by a 2-fold axis. The occupancy of the main positions was refined to 0.250(7). All carbon atoms of the toluene were refined isotropically. For the refinement, distance restraints and restraints for the anisotropic displacement parameters were used.

Table 5-12. Crystal data of **10b**.

CCDC no.	2069110	Z	4
Empirical formula	$\text{C}_{63}\text{H}_{128}\text{Cl}_5\text{Tb}_2\text{Li}_3\text{N}_8\text{O}_6\text{S}_2$	ρ_{calc} [g/cm^3]	1.396
Formula weight [g/mol]	1673.76	μ [mm^{-1}]	1.081
Temperature [K]	100(2)	F(000)	3464
Wavelength [\AA]	0.56086	θ range [$^\circ$]	1.729 to 21.397
Crystal system	Monoclinic	Reflections collected	70797
Space group	C2/c	Independent reflections	9172
a [\AA]	27.151(3)	R(int)	0.0621
b [\AA]	18.004(2)	Crystal dimensions [mm]	0.196 x 0.148 x 0.146
c [\AA]	19.231(2)	Restraints / parameter	656 / 481
α [$^\circ$]	90	GoF	1.017
β [$^\circ$]	122.08(2)	R1 / wR2 ($I > 2\sigma(I)$)	0.0265 / 0.0553
γ [$^\circ$]	90	R1 / wR2 (all data)	0.0416 / 0.0609
Volume [\AA^3]	7965(2)	max. diff peak / hole [e \AA^{-3}]	0.721 / -0.609

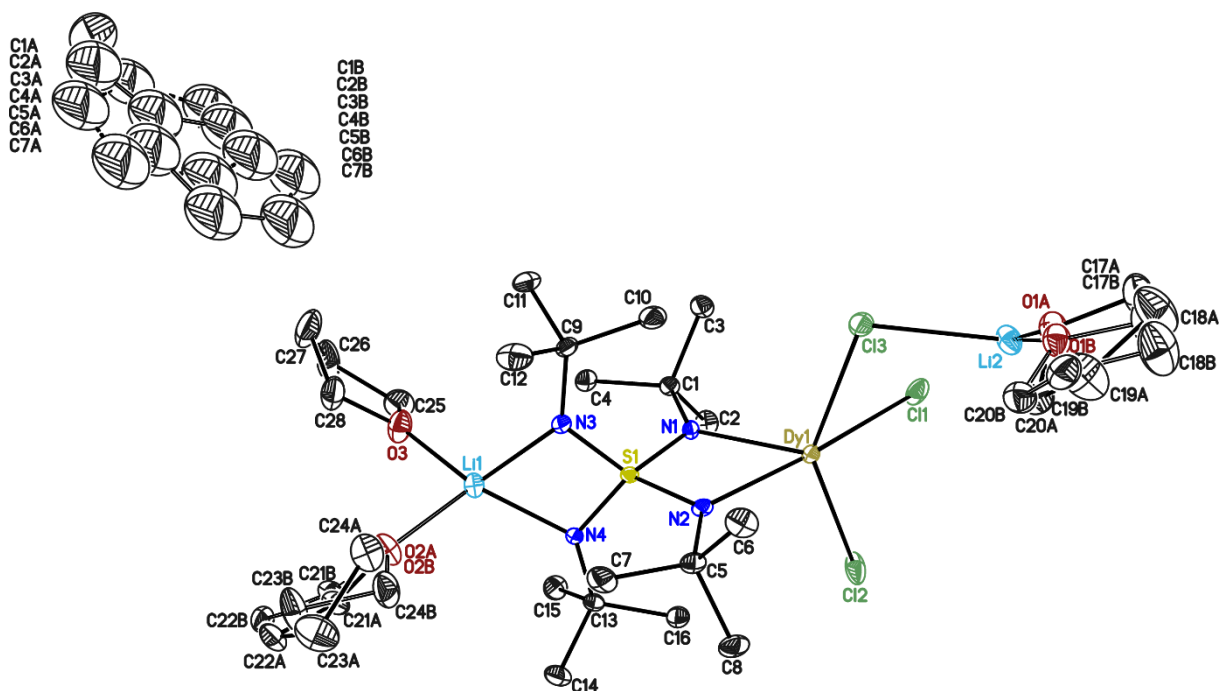
5.5.13. $[\{\text{Cl}_2\text{Dy}(\text{NtBu})_2\text{S}(\text{NtBu})_2\text{Li}(\text{thf})_2\}_2 \cdot \{\text{CLi}(\text{thf})_2\}]$ (**10c**)

Figure 5-13. Asymmetric unit of **10c**. Anisotropic displacement parameters are depicted on a probability level of 50%. Hydrogen atoms are omitted for clarity. The disordered thf molecules were refined on two positions. The occupancy of the main positions for the thf molecule with O1A was refined to 0.51(2) and for the thf molecule with O2A to 0.636(17). The disordered toluene was refined on four positions, of which two each are related by a 2-fold axis. The occupancy of the main positions was refined to 0.322(6). For the refinement distance restraints and restraints for the anisotropic displacement parameters were used.

Table 5-13. Crystal data of **10c**.

CCDC no.	2069111	Z	4
Empirical formula	$\text{C}_{63}\text{H}_{128}\text{Cl}_5\text{Dy}_2\text{Li}_3\text{N}_8\text{O}_6\text{S}_2$	$\rho_{\text{calc}} [\text{g}/\text{cm}^3]$	1.405
Formula weight $[\text{g}/\text{mol}]$	1680.92	$\mu [\text{mm}^{-1}]$	1.142
Temperature $[\text{K}]$	100(2)	$F(000)$	3472
Wavelength $[\text{\AA}]$	0.56086	θ range $^\circ$	1.727 to 22.016
Crystal system	Monoclinic	Reflections collected	107564
Space group	C2/c	Independent reflections	9922
a $[\text{\AA}]$	27.079(3)	$R(\text{int})$	0.0722
b $[\text{\AA}]$	17.966(2)	Crystal dimensions $[\text{mm}]$	0.144 x 0.134 x 0.084
c $[\text{\AA}]$	19.243(2)	Restraints / parameter	1079 / 581
α $^\circ$	90	GoF	1.030
β $^\circ$	121.90(2)	$R1 / wR2$ ($I > 2\sigma(I)$)	0.0256 / 0.0511
γ $^\circ$	90	$R1 / wR2$ (all data)	0.0416 / 0.0571
Volume $[\text{\AA}^3]$	7948(2)	max. diff peak / hole $[\text{e} \text{\AA}^{-3}]$	0.769 / -0.746

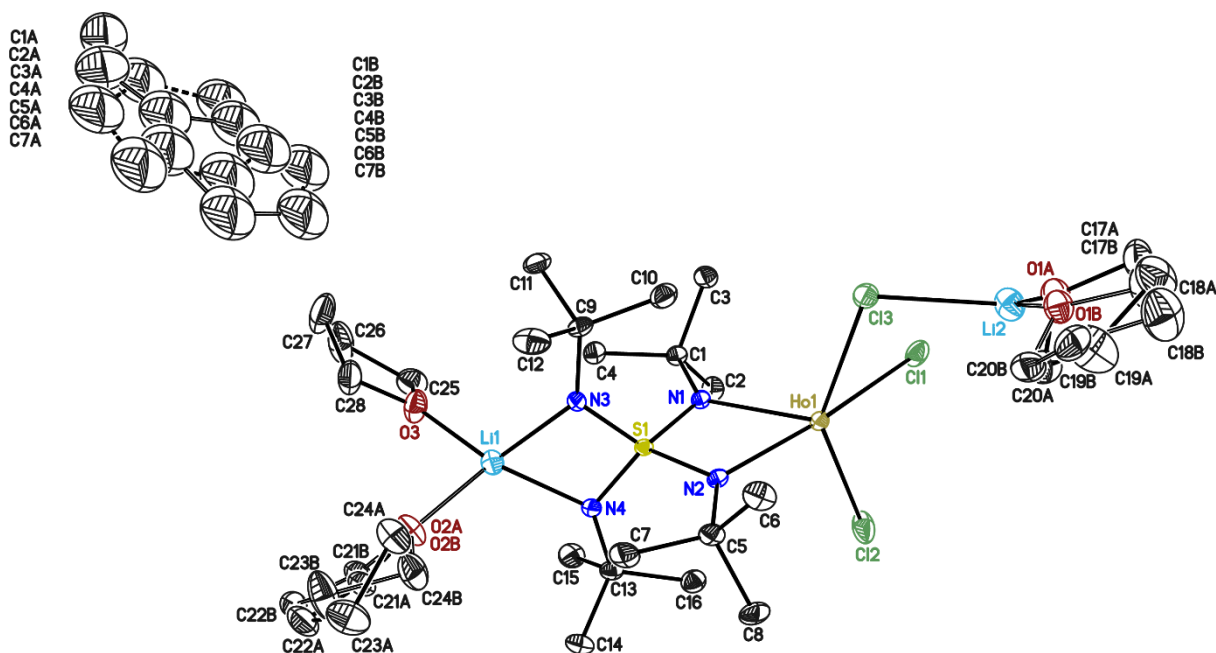
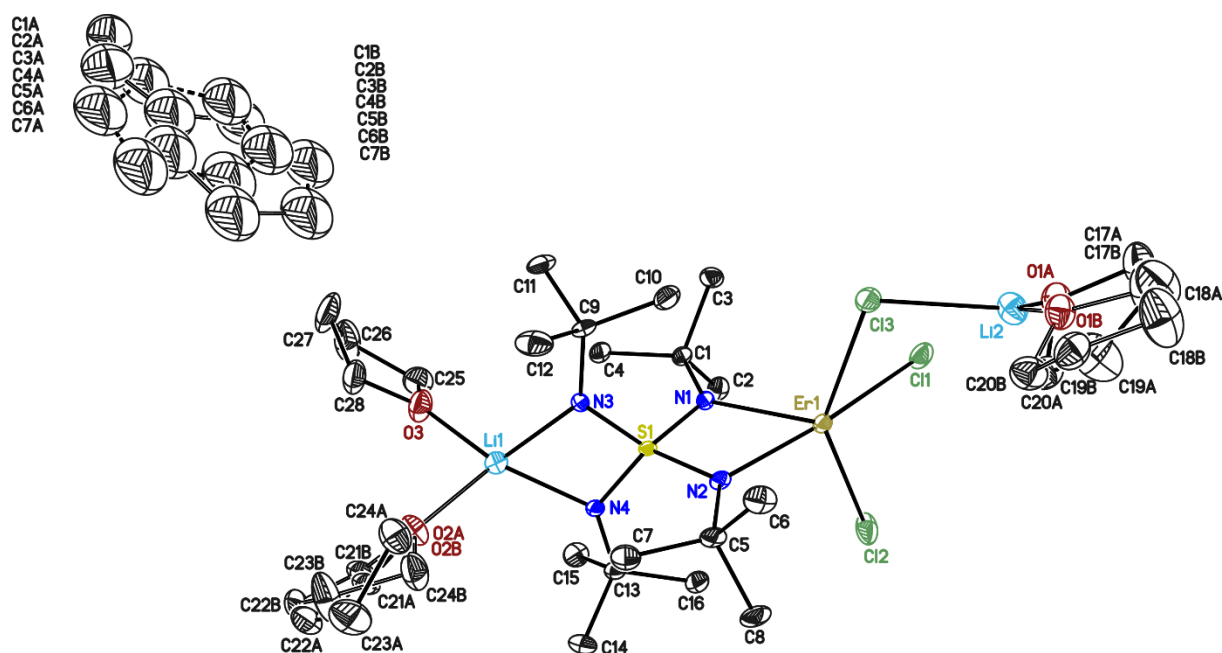
5.5.14. $[\{\text{Cl}_2\text{Ho}(\text{NtBu})_2\text{S}(\text{NtBu})_2\text{Li}(\text{thf})_2\}_2 \cdot \{\text{CLi}(\text{thf})_2\}]$ (**10d**)

Figure 5-14. Asymmetric unit of **10d**. Anisotropic displacement parameters are depicted on a probability level of 50%. Hydrogen atoms are omitted for clarity. The disordered thf molecules were refined on two positions. The occupancy of the main positions for the thf molecule with O1A was refined to 0.471(19) and for the thf molecule with O2A to 0.640(16). The disordered toluene was refined on four positions, of which two each are related by a 2-fold axis. The occupancy of the main positions was refined to 0.331(6). For the refinement distance restraints and restraints for the anisotropic displacement parameters were used.

Table 5-14. Crystal data of **10d**.

CCDC no.	2069112	Z	4
Empirical formula	$\text{C}_{63}\text{H}_{128}\text{Cl}_5\text{Ho}_2\text{Li}_3\text{N}_8\text{O}_6\text{S}_2$	$\rho_{\text{calc}} [\text{g}/\text{cm}^3]$	1.411
Formula weight $[\text{g}/\text{mol}]$	1685.78	$\mu [\text{mm}^{-1}]$	1.200
Temperature $[\text{K}]$	100(2)	$F(000)$	3480
Wavelength $[\text{\AA}]$	0.56086	θ range $[\circ]$	1.709 to 21.419
Crystal system	Monoclinic	Reflections collected	116183
Space group	C2/c	Independent reflections	9147
a $[\text{\AA}]$	26.992(3)	$R(\text{int})$	0.0464
b $[\text{\AA}]$	17.963(2)	Crystal dimensions $[\text{mm}]$	0.195 x 0.126 x 0.111
c $[\text{\AA}]$	19.258(2)	Restraints / parameter	1079 / 581
α $[\circ]$	90	GoF	1.067
β $[\circ]$	121.82(2)	$R1 / wR2$ ($I > 2\sigma(I)$)	0.0210 / 0.0452
γ $[\circ]$	90	$R1 / wR2$ (all data)	0.0334 / 0.0505
Volume $[\text{\AA}^3]$	7934(2)	max. diff peak / hole $[\text{e} \text{\AA}^{-3}]$	0.971 / -0.781

5.5.15. $[\{\text{Cl}_2\text{Er}(\text{NtBu})_2\text{S}(\text{NtBu})_2\text{Li}(\text{thf})_2\}_2 \cdot \{\text{ClLi}(\text{thf})_2\}]$ (**10e**)

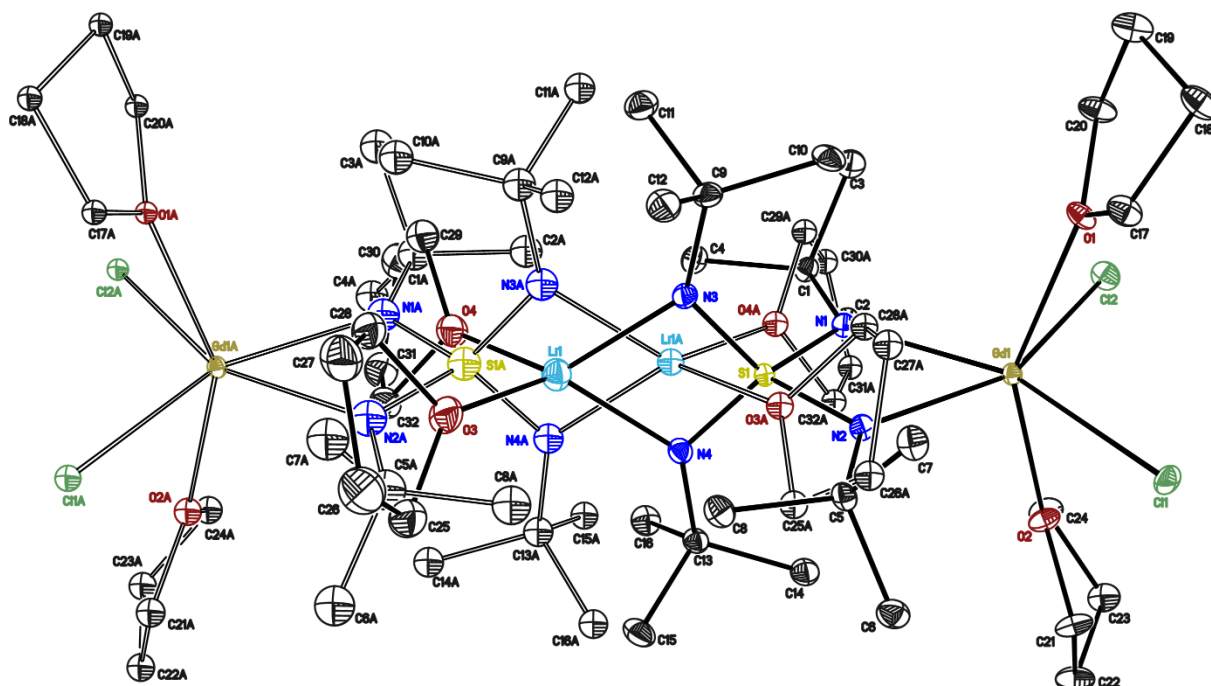
5.5.16. $[(\text{thf})_2\text{Cl}_2\text{Gd}(\text{NtBu})_2\text{S}(\text{NtBu})_2\text{Li}(\text{thf})_2]_2$ (**11a**)

Figure 5-16. Asymmetric unit of **11a**. Anisotropic displacement parameters are depicted on a probability level of 50%. Hydrogen atoms are omitted for clarity. The whole molecule is disordered and was refined on two positions. The occupancy of the main positions was refined to 0.9628(5). For the refinement, distance restraints and restraints for the anisotropic displacement parameters were used. The structure was refined as an inversion twin.

Table 5-16. Crystal data of **11a**.

CCDC no.	2069114	Z	4
Empirical formula	$\text{C}_{32}\text{H}_{68}\text{Cl}_2\text{GdLiN}_4\text{O}_4\text{S}$	$\rho_{\text{calc}} [\text{g}/\text{cm}^3]$	1.410
Formula weight $[\text{g}/\text{mol}]$	840.05	$\mu [\text{mm}^{-1}]$	1.018
Temperature $[\text{K}]$	100(2)	$F(000)$	1748
Wavelength $[\text{\AA}]$	0.56086	θ range $[\circ]$	1.565 to 22.657
Crystal system	Orthorhombic	Reflections collected	172173
Space group	$\text{Pca}2_1$	Independent reflections	10704
a $[\text{\AA}]$	16.939(2)	$R(\text{int})$	0.0956
b $[\text{\AA}]$	12.911(2)	Crystal dimensions $[\text{mm}]$	0.190 x 0.097 x 0.097
c $[\text{\AA}]$	18.093(3)	Restraints / parameter	3946 / 600
α $[\circ]$	90	GoF	1.029
β $[\circ]$	90	$R1 / wR2$ ($I > 2\sigma(I)$)	0.0242 / 0.0472
γ $[\circ]$	90	$R1 / wR2$ (all data)	0.0365 / 0.0509
Volume $[\text{\AA}^3]$	3956.9(10)	max. diff peak / hole $[\text{e } \text{\AA}^{-3}]$	0.600 / -0.673

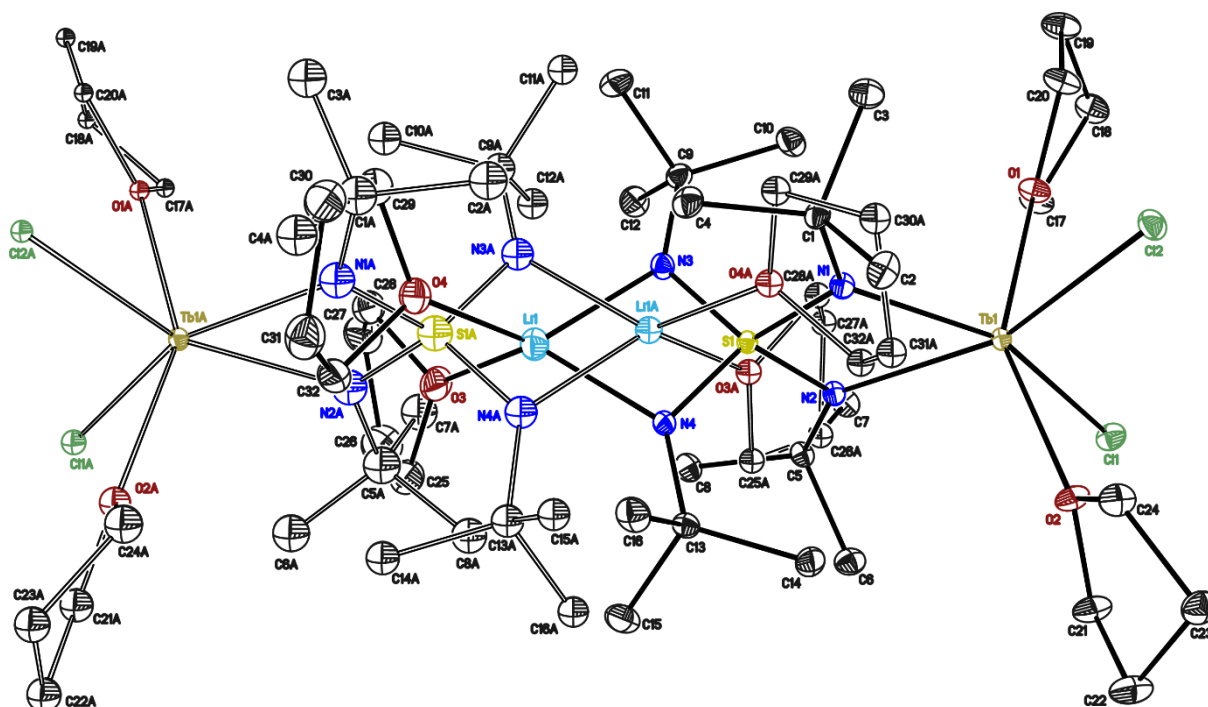
5.5.17. $\{[(\text{thf})_2\text{Cl}_2\text{Tb}(\text{NtBu})_2\text{S}(\text{NtBu})_2\text{Li}(\text{thf})_2]_2\}$ (**11b**)

Figure 5-17. Asymmetric unit of **11b**. Anisotropic displacement parameters are depicted on a probability level of 50%. Hydrogen atoms are omitted for clarity. The whole molecule is disordered and was refined on two positions. The occupancy of the main positions was refined to 0.9877(4). For the refinement, distance restraints and restraints for the anisotropic displacement parameters were used. The structure was refined as an inversion twin.

Table 5-17. Crystal data of **11b**.

CCDC no.	2069115	Z	4
Empirical formula	$\text{C}_{32}\text{H}_{68}\text{Cl}_2\text{TbLiN}_4\text{O}_4\text{S}$	ρ_{calc} [g/cm^3]	1.417
Formula weight [g/mol]	841.72	μ [mm^{-1}]	1.077
Temperature [K]	100(2)	$F(000)$	1752
Wavelength [\AA]	0.56086	θ range [$^\circ$]	1.902 to 27.890
Crystal system	Orthorhombic	Reflections collected	99654
Space group	$\text{Pca}2_1$	Independent reflections	19090
a [\AA]	16.900(2)	$R(\text{int})$	0.0630
b [\AA]	12.910(2)	Crystal dimensions [mm]	0.132 x 0.120 x 0.102
c [\AA]	18.088(3)	Restraints / parameter	3948 / 600
α [$^\circ$]	90	GoF	1.011
β [$^\circ$]	90	$R1 / wR2$ ($I > 2\sigma(I)$)	0.0282 / 0.0488
γ [$^\circ$]	90	$R1 / wR2$ (all data)	0.0473 / 0.0529
Volume [\AA^3]	3946.4(10)	max. diff peak / hole [e \AA^{-3}]	0.510 / -0.659

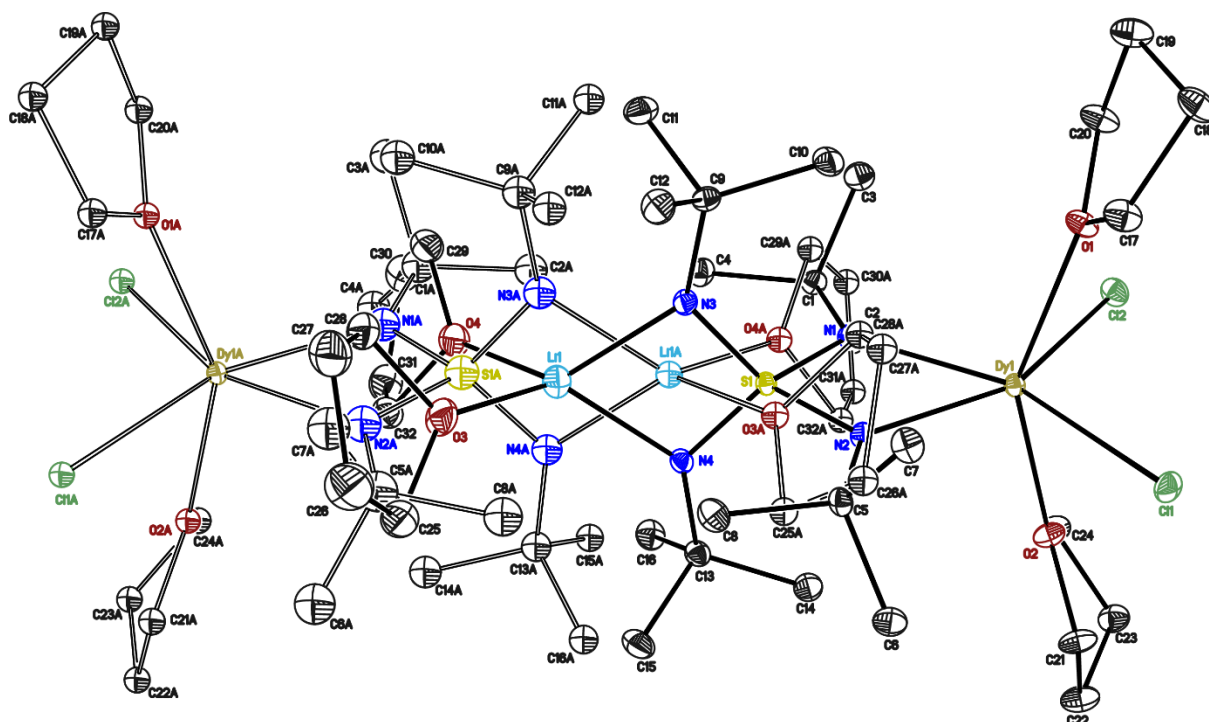
5.5.18. $[(\text{thf})_2\text{Cl}_2\text{Dy}(\text{NtBu})_2\text{S}(\text{NtBu})_2\text{Li}(\text{thf})_2]_2$ (**11c**)

Figure 5-18. Asymmetric unit of **11c**. Anisotropic displacement parameters are depicted on a probability level of 50%. Hydrogen atoms are omitted for clarity. The whole molecule is disordered and was refined on two positions. The occupancy of the main positions was refined to 0.9730(4). For the refinement, distance restraints and restraints for the anisotropic displacement parameters were used. The structure was refined as an inversion twin.

Table 5-18. Crystal data of **11c**.

CCDC no.	2069116	Z	4
Empirical formula	$\text{C}_{32}\text{H}_{68}\text{Cl}_2\text{DyLi}_4\text{O}_4\text{S}$	$\rho_{\text{calc}} [\text{g}/\text{cm}^3]$	1.410
Formula weight $[\text{g}/\text{mol}]$	845.30	$\mu [\text{mm}^{-1}]$	1.125
Temperature $[\text{K}]$	100(2)	$F(000)$	1756
Wavelength $[\text{\AA}]$	0.56086	θ range $[\circ]$	1.563 to 23.612
Crystal system	Orthorhombic	Reflections collected	289767
Space group	Pca_2_1	Independent reflections	12081
a $[\text{\AA}]$	16.967(7)	$R(\text{int})$	0.0637
b $[\text{\AA}]$	12.925(6)	Crystal dimensions $[\text{mm}]$	0.204 x 0.125 x 0.079
c $[\text{\AA}]$	18.161(8)	Restraints / parameter	3922 / 600
α $[\circ]$	90	GoF	1.072
β $[\circ]$	90	$R1 / wR2$ ($I > 2\sigma(I)$)	0.0191 / 0.0400
γ $[\circ]$	90	$R1 / wR2$ (all data)	0.0275 / 0.0426
Volume $[\text{\AA}^3]$	3983(3)	max. diff peak / hole $[\text{e } \text{\AA}^{-3}]$	0.626 / -0.525

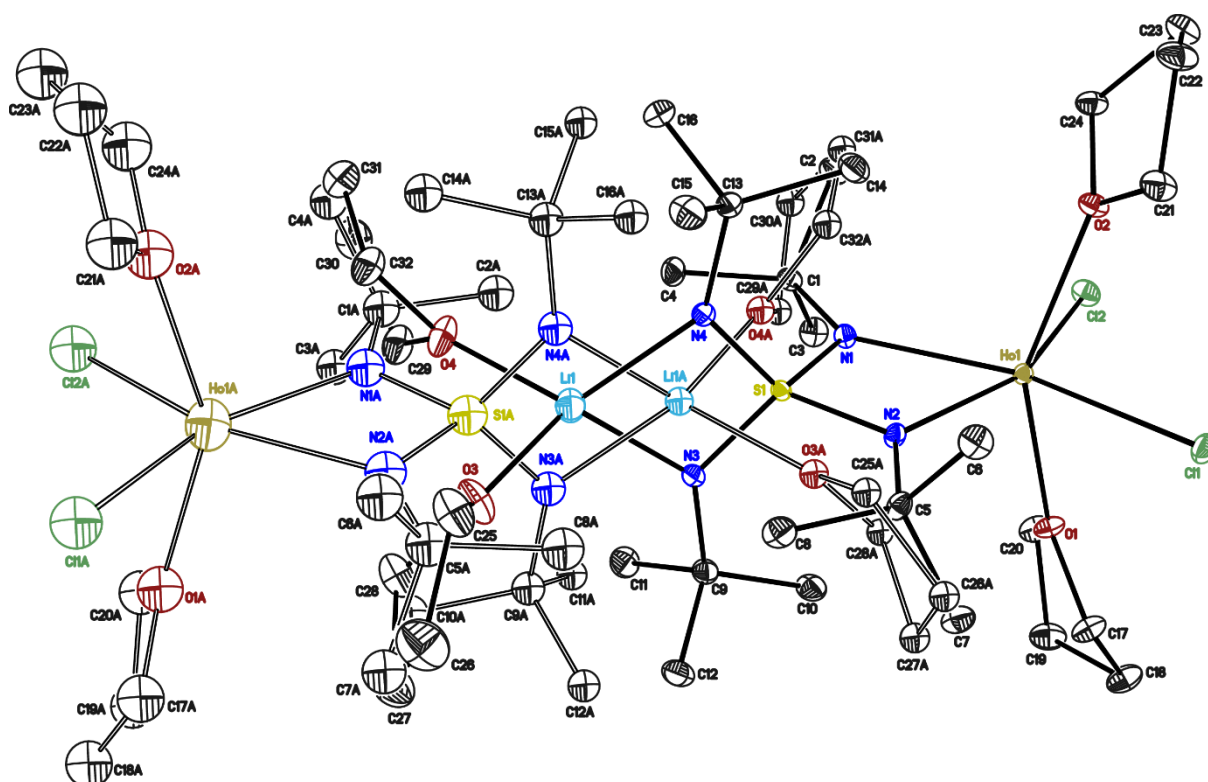
5.5.19. $\{[(\text{thf})_2\text{Cl}_2\text{Ho}(\text{NtBu})_2\text{S}(\text{NtBu})_2\text{Li}(\text{thf})_2]_2\}$ (**11d**)

Figure 5-19. Asymmetric unit of **11d**. Anisotropic displacement parameters are depicted on a probability level of 50%. Hydrogen atoms are omitted for clarity. The whole molecule is disordered and was refined on two positions. The occupancy of the main positions was refined to 0.9267(7). For the refinement, distance restraints and restraints for the anisotropic displacement parameters were used. The structure was refined as an inversion twin.

Table 5-19. Crystal data of **11d**.

CCDC no.	2069117	Z	4
Empirical formula	$\text{C}_{32}\text{H}_{68}\text{Cl}_2\text{HoLiN}_4\text{O}_4\text{S}$	$\rho_{\text{calc}} [\text{g}/\text{cm}^3]$	1.434
Formula weight $[\text{g}/\text{mol}]$	847.73	$\mu [\text{mm}^{-1}]$	1.197
Temperature $[\text{K}]$	100(2)	$F(000)$	1760
Wavelength $[\text{\AA}]$	0.56086	θ range $^\circ$	1.570 to 27.864
Crystal system	Orthorhombic	Reflections collected	133552
Space group	$\text{Pca}2_1$	Independent reflections	19027
a $[\text{\AA}]$	16.887(2)	$R(\text{int})$	0.0587
b $[\text{\AA}]$	12.873(2)	Crystal dimensions $[\text{mm}]$	0.229 x 0.185 x 0.170
c $[\text{\AA}]$	18.069(3)	Restraints / parameter	3927 / 606
α $^\circ$	90	GoF	1.045
β $^\circ$	90	$R1 / wR2$ ($I > 2\sigma(I)$)	0.0251 / 0.0559
γ $^\circ$	90	$R1 / wR2$ (all data)	0.0341 / 0.0598
Volume $[\text{\AA}^3]$	3928.0(10)	max. diff peak / hole $[\text{e } \text{\AA}^{-3}]$	1.466 / -1.079

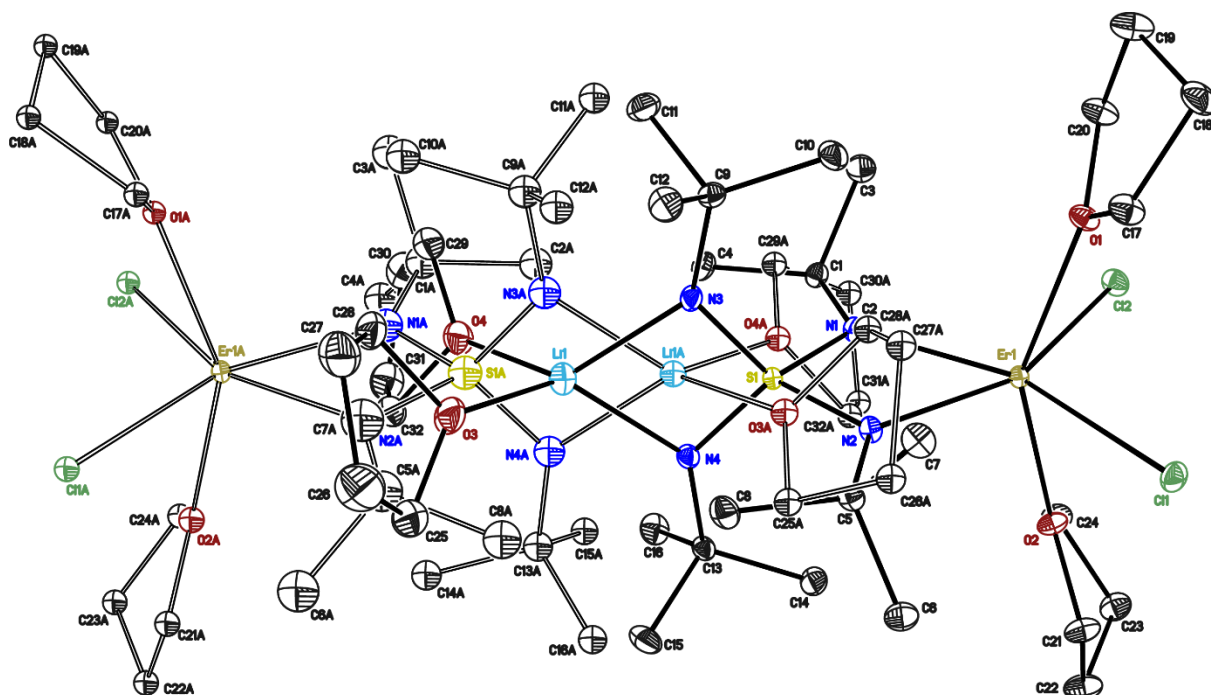
5.5.20. $[(\text{thf})_2\text{Cl}_2\text{Er}(\text{NtBu})_2\text{S}(\text{NtBu})_2\text{Li}(\text{thf})_2]_2$ (**11e**)

Figure 5-20. Asymmetric unit of **11e**. Anisotropic displacement parameters are depicted on a probability level of 50%. Hydrogen atoms are omitted for clarity. The whole molecule is disordered and was refined on two positions. The occupancy of the main positions was refined to 0.9879(3). For the refinement distance restraints and restraints for the anisotropic displacement parameters were used. The structure was refined as an inversion twin.

Table 5-20. Crystal data of **11e**.

CCDC no.	2069118	Z	4
Empirical formula	$\text{C}_{32}\text{H}_{68}\text{Cl}_2\text{ErLi}_4\text{O}_4\text{S}$	$\rho_{\text{calc}} [\text{g}/\text{cm}^3]$	1.439
Formula weight $[\text{g}/\text{mol}]$	850.06	$\mu [\text{mm}^{-1}]$	1.270
Temperature $[\text{K}]$	100(2)	$F(000)$	1764
Wavelength $[\text{\AA}]$	0.56086	θ range $[\circ]$	1.779 to 27.923
Crystal system	Orthorhombic	Reflections collected	198994
Space group	$\text{Pca}2_1$	Independent reflections	19082
$a [\text{\AA}]$	16.883(2)	$R(\text{int})$	0.0507
$b [\text{\AA}]$	12.859(2)	Crystal dimensions $[\text{mm}]$	0.228 x 0.176 x 0.157
$c [\text{\AA}]$	18.070(3)	Restraints / parameter	3929 / 599
$\alpha [^\circ]$	90	GoF	1.018
$\beta [^\circ]$	90	$R1 / wR2$ ($I > 2\sigma(I)$)	0.0185 / 0.0369
$\gamma [^\circ]$	90	$R1 / wR2$ (all data)	0.0266 / 0.0392
Volume $[\text{\AA}^3]$	3923.0(10)	max. diff peak / hole $[\text{e } \text{\AA}^{-3}]$	0.556 / -0.690

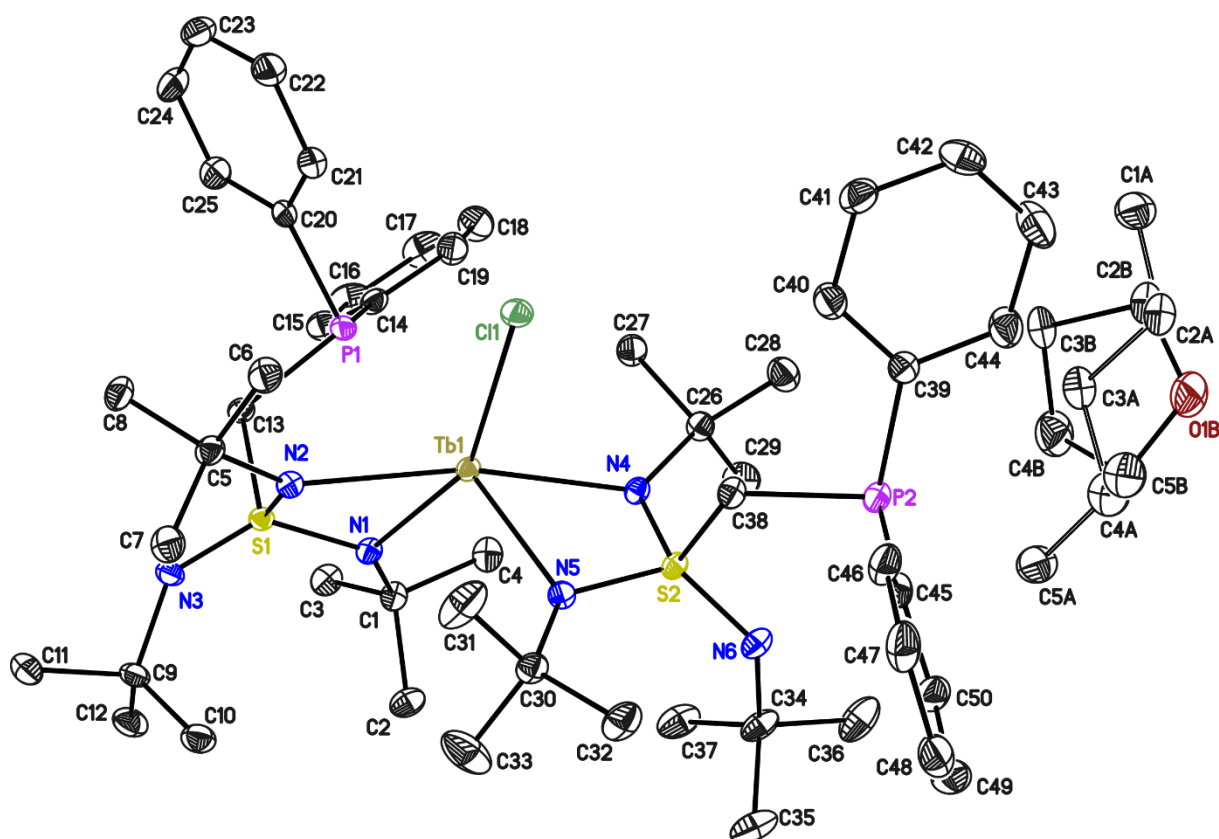
5.5.21. [CITb{Ph₂PCH₂S(NtBu)₃}₂] (12a)

Figure 5-21. Asymmetric unit of **12a**. Anisotropic displacement parameters are depicted on a probability level of 50%. Hydrogen atoms are omitted for clarity. The solvent was disordered about a two-fold axis. Additionally, it was refined as a mixture of n-pentane and thf. The occupancy of n-pentane refined to 0.117(3). For the refinement of the disordered parts distance restraints and restraints for the anisotropic displacement parameters were used. Atomic displacements of atoms very close to each other were constrained to be identical.

Table 5-21. Crystal data of **12a**.

CCDC no.	2104540	Z	8
Empirical formula	C ₅₀ H ₇₈ ClN ₆ P ₂ S ₂ Tb (C _{2.12} H _{4.47} O _{0.38})	ρ _{calc} [g/cm ³]	1.332
Formula weight [g/mol]	1119.67	μ [mm ⁻¹]	0.793
Temperature [K]	100(2)	F(000)	4674
Wavelength [Å]	0.56086	θ range [°]	1.572 to 22.621
Crystal system	Monoclinic	Reflections collected	118347
Space group	C2/c	Independent reflections	15074
a [Å]	35.479(3)	R(int)	0.0669
b [Å]	15.397(2)	Crystal dimensions [mm]	0.128 x 0.112 x 0.075
c [Å]	20.521(2)	Restraints / parameter	202 / 653
α [°]	90	GoF	1.016
β [°]	94.93(2)	R1 / wR2 (I > 2σ(I))	0.0289 / 0.0542
γ [°]	90	R1 / wR2 (all data)	0.0469 / 0.0594
Volume [Å ³]	11169(2)	max. diff peak / hole [e Å ⁻³]	0.546 / -0.568

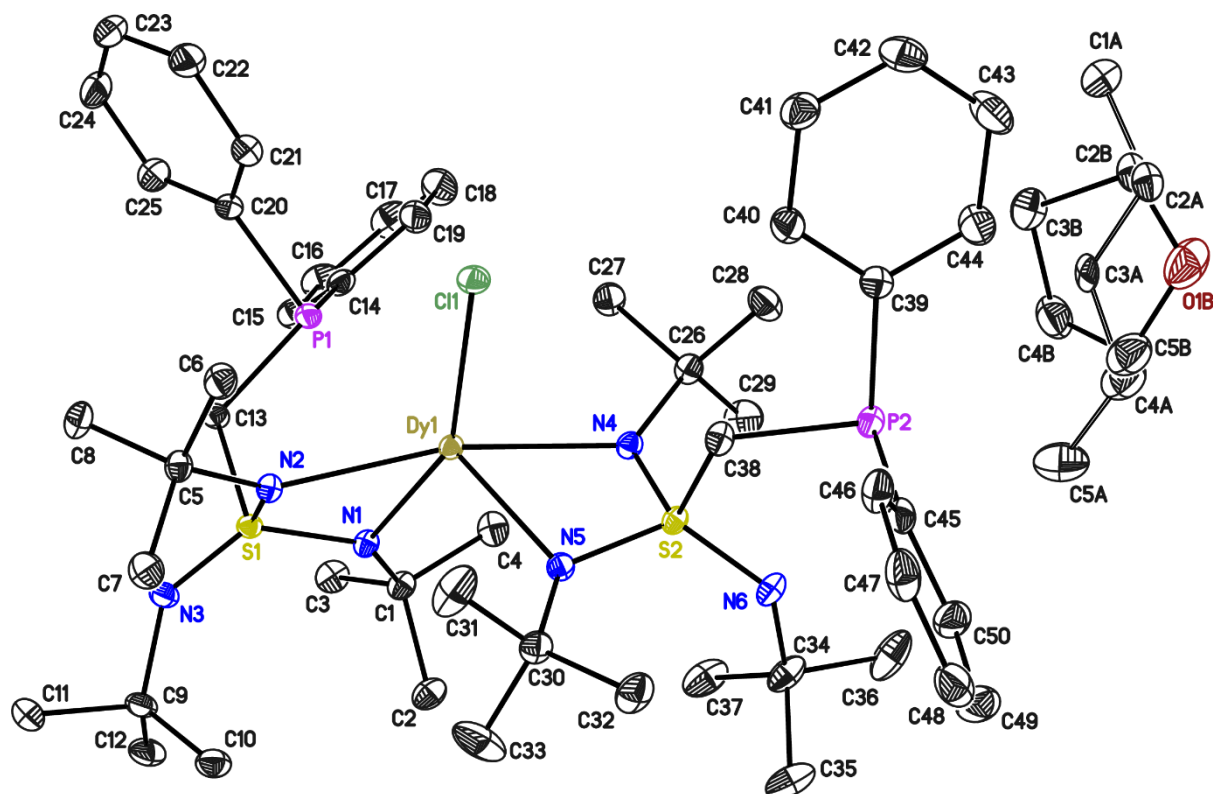
5.5.22. [ClDy(Ph₂PCH₂S(NtBu)₃)₂] (12b)

Figure 5-22. Asymmetric unit of **12b**. Anisotropic displacement parameters are depicted on a probability level of 50%. Hydrogen atoms are omitted for clarity. The solvent was disordered about a two-fold axis. Additionally, it was refined as a mixture of n-pentane and thf. The occupancy of n-pentane refined to 0.248(2). For the refinement of the disordered parts distance restraints and restraints for the anisotropic displacement parameters were used. Atomic displacements of atoms very close to each other were constrained to be identical.

Table 5-22. Crystal data of **12b**.

CCDC no.	2104541	Z	8
Empirical formula	C ₅₀ H ₇₈ ClN ₆ P ₂ S ₂ Dy (C _{2.25} H _{4.99} O _{0.25}) ₂	ρ _{calc} [g/cm ³]	1.343
Formula weight [g/mol]	1123.25	μ [mm ⁻¹]	0.839
Temperature [K]	100(2)	F(000)	4684
Wavelength [Å]	0.56086	θ range [°]	1.363 to 24.472
Crystal system	Monoclinic	Reflections collected	290042
Space group	C2/c	Independent reflections	18647
a [Å]	35.454(4)	R(int)	0.0597
b [Å]	15.335(2)	Crystal dimensions [mm]	0.183 x 0.150 x 0.124
c [Å]	20.523(3)	Restraints / parameter	208 / 658
α [°]	90	GoF	1.021
β [°]	95.29(2)	R1 / wR2 (I > 2σ(I))	0.0250 / 0.0478
γ [°]	90	R1 / wR2 (all data)	0.0394 / 0.0526
Volume [Å ³]	11111(3)	max. diff peak / hole [e Å ⁻³]	0.608 / -0.556

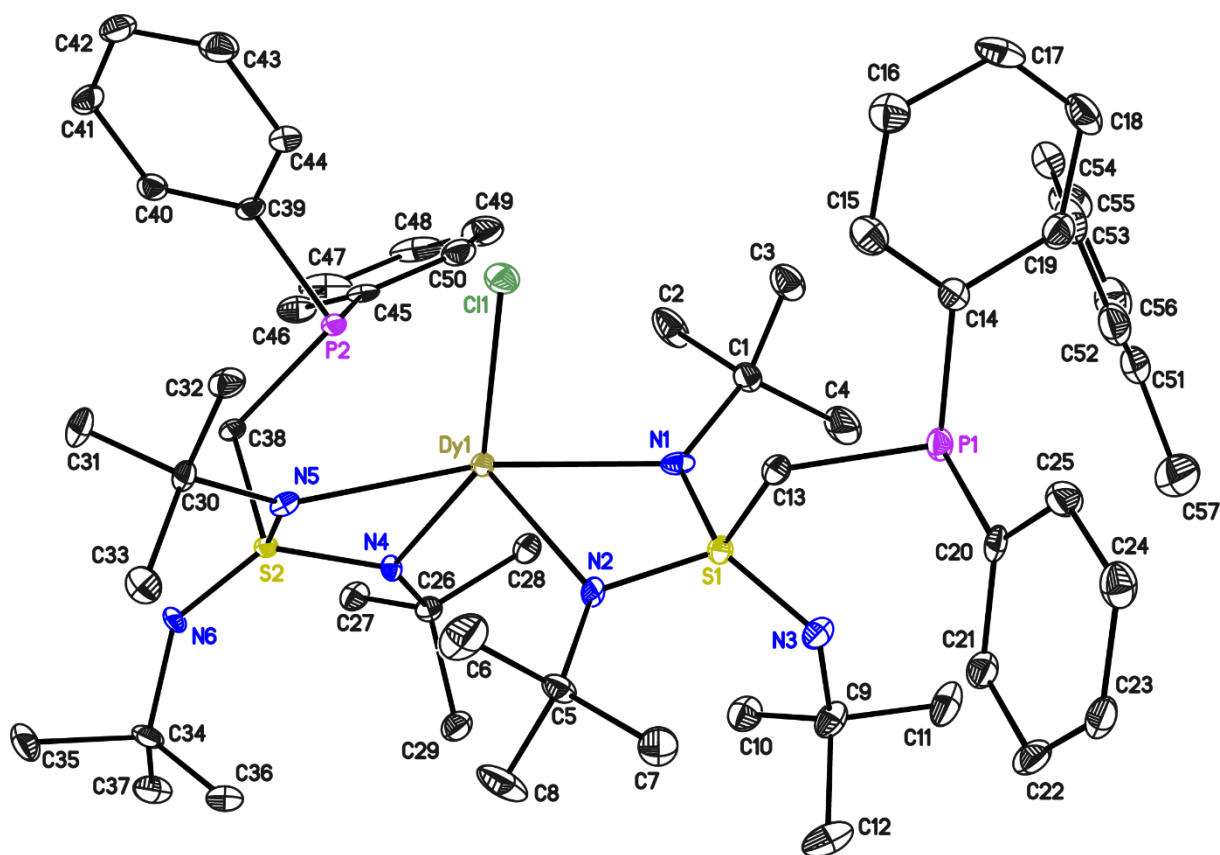
5.5.23. [ClDy{Ph₂PCH₂S(NtBu)₃}₂] (12b_tol)

Figure 5-23. Asymmetric unit of **12b_tol**. The anisotropic displacement parameters are depicted at the 50% probability level. The hydrogen atoms are omitted for clarity.

Table 5-23. Crystal data of **12b_tol**.

Structure code	JJ290	Z	2
Empirical formula	C ₅₇ H ₈₆ ClDyN ₆ P ₂ S ₂	ρ_{calc} [g/cm ³]	1.359
Formula weight [g/mol]	1179.32	μ [mm ⁻¹]	0.811
Temperature [K]	100(2)	F(000)	1230
Wavelength [Å]	0.56086	θ range [°]	1.638 to 20.597
Crystal system	Triclinic	Reflections collected	137164
Space group	P-1	Independent reflections	11829
a [Å]	10.579(2)	R(int)	0.0868
b [Å]	14.590(2)	Crystal dimensions [mm]	0.171 x 0.064 x 0.046
c [Å]	20.124(3)	Restraints / parameter	0 / 641
α [°]	109.86(2)	GoF	1.136
β [°]	98.06(2)	R1 / wR2 ($I > 2\sigma(I)$)	0.0370 / 0.0708
γ [°]	91.99(2)	R1 / wR2 (all data)	0.0491 / 0.0745
Volume [Å ³]	2881.2(9)	max. diff peak / hole [e Å ⁻³]	1.448 / -1.058

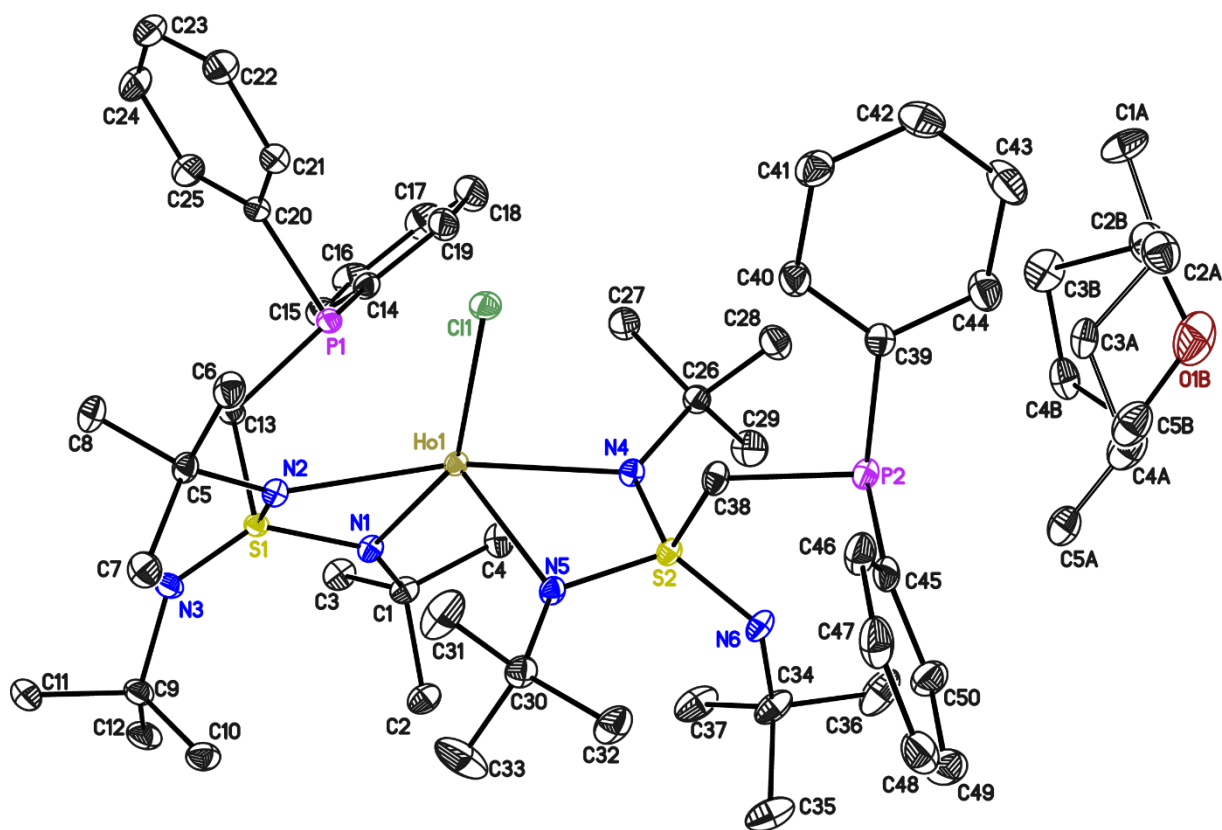
5.5.24. $[\text{ClHo}\{\text{Ph}_2\text{PCH}_2\text{S}(\text{NtBu})_3\}_2]$ (**12c**)

Figure 5-24. Asymmetric unit of **12c**. Anisotropic displacement parameters are depicted on a probability level of 50%. Hydrogen atoms are omitted for clarity. The solvent was disordered about a two-fold axis. Additionally, it was refined as a mixture of n-pentane and thf. The occupancy of n-pentane refined to 0.141(2). For the refinement of the disordered parts distance restraints and restraints for the anisotropic displacement parameters were used. Atomic displacements of atoms very close to each other were constrained to be identical.

Table 5-24. Crystal data of **12c**.

CCDC no.	2104542	Z	8
Empirical formula	$\text{C}_{50}\text{H}_{78}\text{ClN}_6\text{P}_2\text{S}_2\text{Ho}$ ($\text{C}_{2.14}\text{H}_{4.56}\text{O}_{0.36}$)	ρ_{calc} [g/cm^3]	1.343
Formula weight [g/mol]	1125.68	μ [mm^{-1}]	0.877
Temperature [K]	100(2)	F(000)	4690
Wavelength [\AA]	0.56086	θ range [$^\circ$]	1.719 to 25.627
Crystal system	Monoclinic	Reflections collected	175315
Space group	C2/c	Independent reflections	21358
a [\AA]	35.511(3)	R(int)	0.0583
b [\AA]	15.330(2)	Crystal dimensions [mm]	0.206 x 0.186 x 0.165
c [\AA]	20.538(2)	Restraints / parameter	208 / 658
α [$^\circ$]	90	GoF	1.014
β [$^\circ$]	95.09(2)	R1 / wR2 ($I > 2\sigma(I)$)	0.0252 / 0.0472
γ [$^\circ$]	90	R1 / wR2 (all data)	0.0403 / 0.0520
Volume [\AA^3]	11136(2)	max. diff peak / hole [$\text{e}/\text{\AA}^{-3}$]	0.559 / -0.659

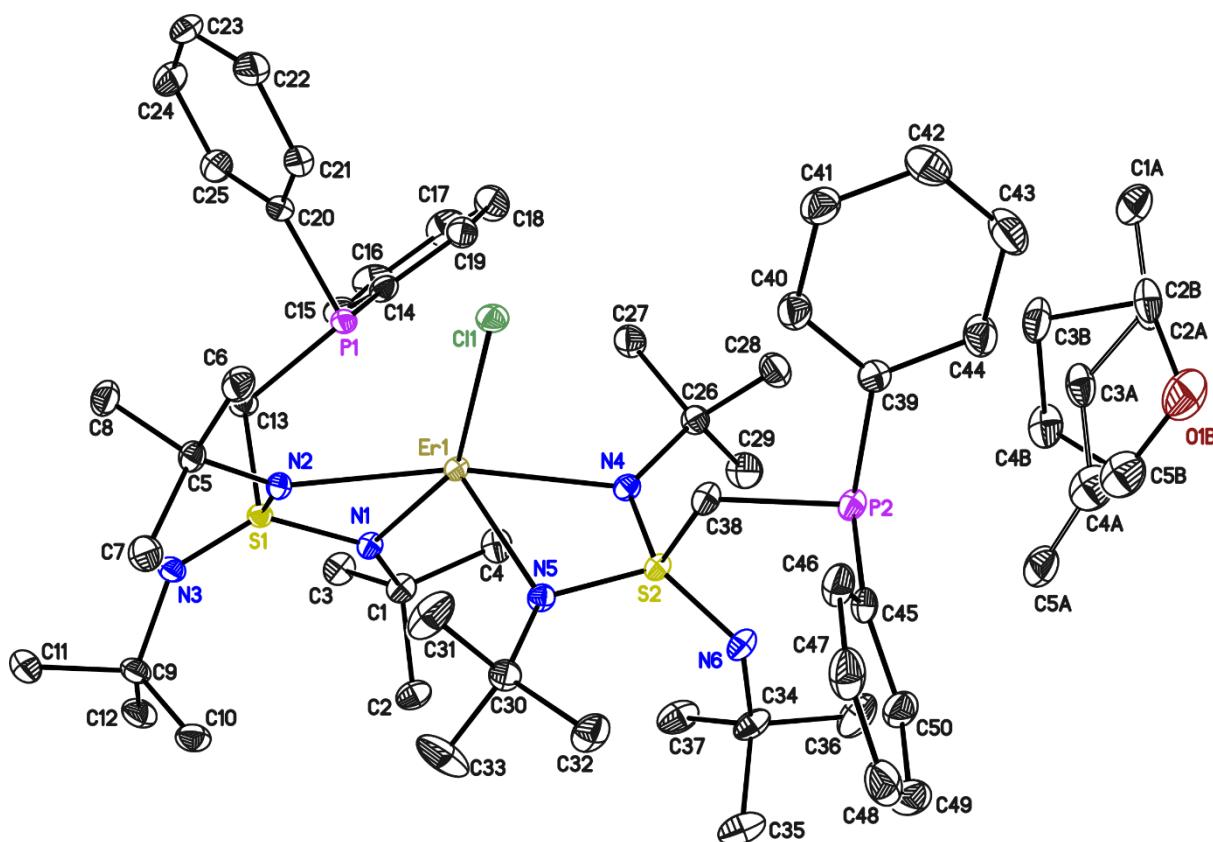
5.5.25. $[\text{ClEr}\{\text{Ph}_2\text{PCH}_2\text{S}(\text{NtBu})_3\}_2]$ (**12d**)

Figure 5-25. Asymmetric unit of **12d**. Anisotropic displacement parameters are depicted on a probability level of 50%. Hydrogen atoms are omitted for clarity. The solvent was disordered about a two-fold axis. Additionally, it was refined as a mixture of n-pentane and thf. The occupancy of n-pentane refined to 0.094(2). For the refinement of the disordered parts distance restraints and restraints for the anisotropic displacement parameters were used. Atomic displacements of atoms very close to each other were constrained to be identical.

Table 5-25. Crystal data of **12d**.

CCDC no.	2104543	Z	8
Empirical formula	$\text{C}_{50}\text{H}_{78}\text{ClN}_6\text{P}_2\text{S}_2\text{Er}$ ($\text{C}_{2.09}\text{H}_{4.38}\text{O}_{0.41}$)	ρ_{calc} [g/cm^3]	1.349
Formula weight [g/mol]	1128.01	μ [mm^{-1}]	0.930
Temperature [K]	100(2)	F(000)	4698
Wavelength [\AA]	0.56086	θ range [$^\circ$]	1.721 to 22.957
Crystal system	Monoclinic	Reflections collected	315196
Space group	C2/c	Independent reflections	15629
a [\AA]	35.495(3)	R(int)	0.0737
b [\AA]	15.308(2)	Crystal dimensions [mm]	0.175 x 0.126 x 0.102
c [\AA]	20.513(2)	Restraints / parameter	208 / 652
α [$^\circ$]	90	GoF	1.029
β [$^\circ$]	94.92(2)	R1 / wR2 ($I > 2\sigma(I)$)	0.0239 / 0.0460
γ [$^\circ$]	90	R1 / wR2 (all data)	0.0372 / 0.0501
Volume [\AA^3]	11105(2)	max. diff peak / hole [e \AA^{-3}]	0.568 / -0.645

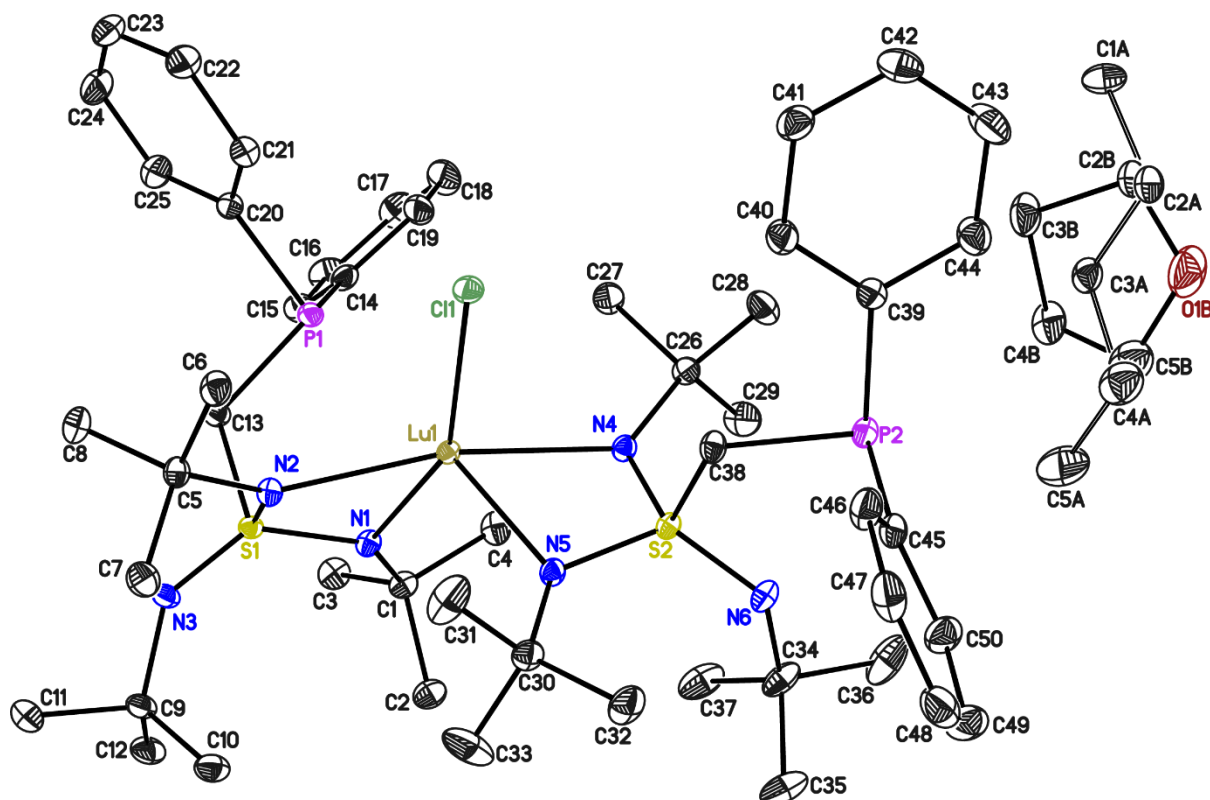
5.5.26. [ClLu{Ph₂PCH₂S(NtBu)₃}₂] (12e)

Figure 5-26. Asymmetric unit of **12e**. Anisotropic displacement parameters are depicted on a probability level of 50%. Hydrogen atoms are omitted for clarity. The solvent was disordered about a two-fold axis. Additionally, it was refined as a mixture of n-pentane and thf. The occupancy of n-pentane refined to 0.2709(19). For the refinement of the disordered parts distance restraints and restraints for the anisotropic displacement parameters were used. Atomic displacements of atoms very close to each other were constrained to be identical.

Table 5-26. Crystal data of **12e**.

CCDC no.	2104544	Z	8
Empirical formula	C ₅₀ H ₇₈ ClIn ₆ P ₂ S ₂ Lu (C _{2.27} H _{5.08} O _{0.23})	ρ_{calc} [g/cm ³]	1.357
Formula weight [g/mol]	1135.72	μ [mm ⁻¹]	1.072
Temperature [K]	100(2)	F(000)	4724
Wavelength [Å]	0.56086	θ range [°]	1.909 to 25.621
Crystal system	Monoclinic	Reflections collected	207945
Space group	C2/c	Independent reflections	21310
a [Å]	35.623(4)	R(int)	0.0549
b [Å]	15.253(2)	Crystal dimensions [mm]	0.199 x 0.162 x 0.132
c [Å]	20.560(3)	Restraints / parameter	202 / 658
α [°]	90	GoF	1.012
β [°]	95.54(2)	R1 / wR2 (I > 2 σ (I))	0.0223 / 0.0430
γ [°]	90	R1 / wR2 (all data)	0.0339 / 0.0464
Volume [Å ³]	11119(3)	max. diff peak / hole [e Å ⁻³]	0.541 / -0.553

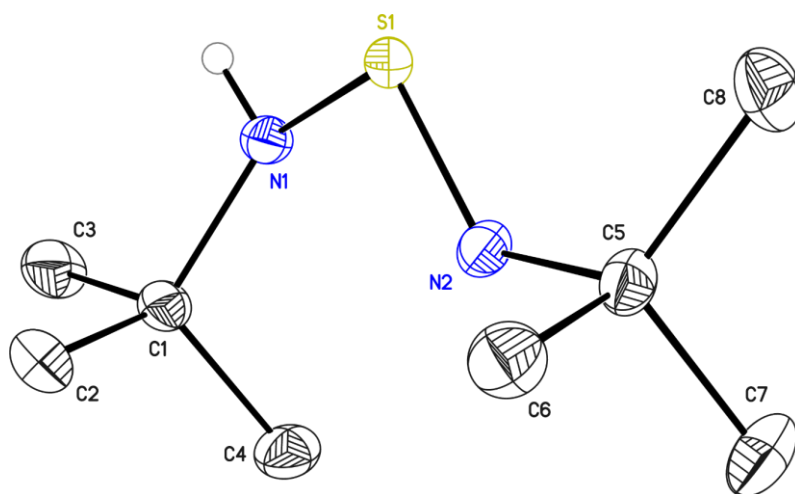
5.5.27. $\text{H}_2\text{S}(\text{NtBu})_4$ (**13**)

Figure 5-27. Asymmetric unit of **13**. The anisotropic displacement parameters are depicted at the 50% probability level. The hydrogen atoms are omitted for clarity.

Table 5-27. Crystal data of **13**.

Structure code	JJ143	Z	4
Empirical formula	$\text{C}_{16}\text{H}_{38}\text{N}_4\text{S}$	$\rho_{\text{calc}} [\text{g}/\text{cm}^3]$	1.052
Formula weight $[\text{g}/\text{mol}]$	318.56	$\mu [\text{mm}^{-1}]$	0.163
Temperature $[\text{K}]$	100(2)	$F(000)$	712
Wavelength $[\text{\AA}]$	0.71073	θ range $[\circ]$	2.663 to 29.617
Crystal system	Monoclinic	Reflections collected	16638
Space group	$\text{C2}/c$	Independent reflections	2826
a $[\text{\AA}]$	17.175(4)	$R(\text{int})$	0.0390
b $[\text{\AA}]$	8.624(2)	Crystal dimensions $[\text{mm}]$	0.132 x 0.112 x 0.101
c $[\text{\AA}]$	15.245(4)	Restraints / parameter	0 / 106
α $[\circ]$	90	GoF	1.026
β $[\circ]$	117.03(2)	$R1 / wR2$ ($I > 2\sigma(I)$)	0.0340 / 0.0852
γ $[\circ]$	90	$R1 / wR2$ (all data)	0.0445 / 0.0906
Volume $[\text{\AA}^3]$	2011.4(9)	max. diff peak / hole $[\text{e } \text{\AA}^{-3}]$	0.415 / -0.270

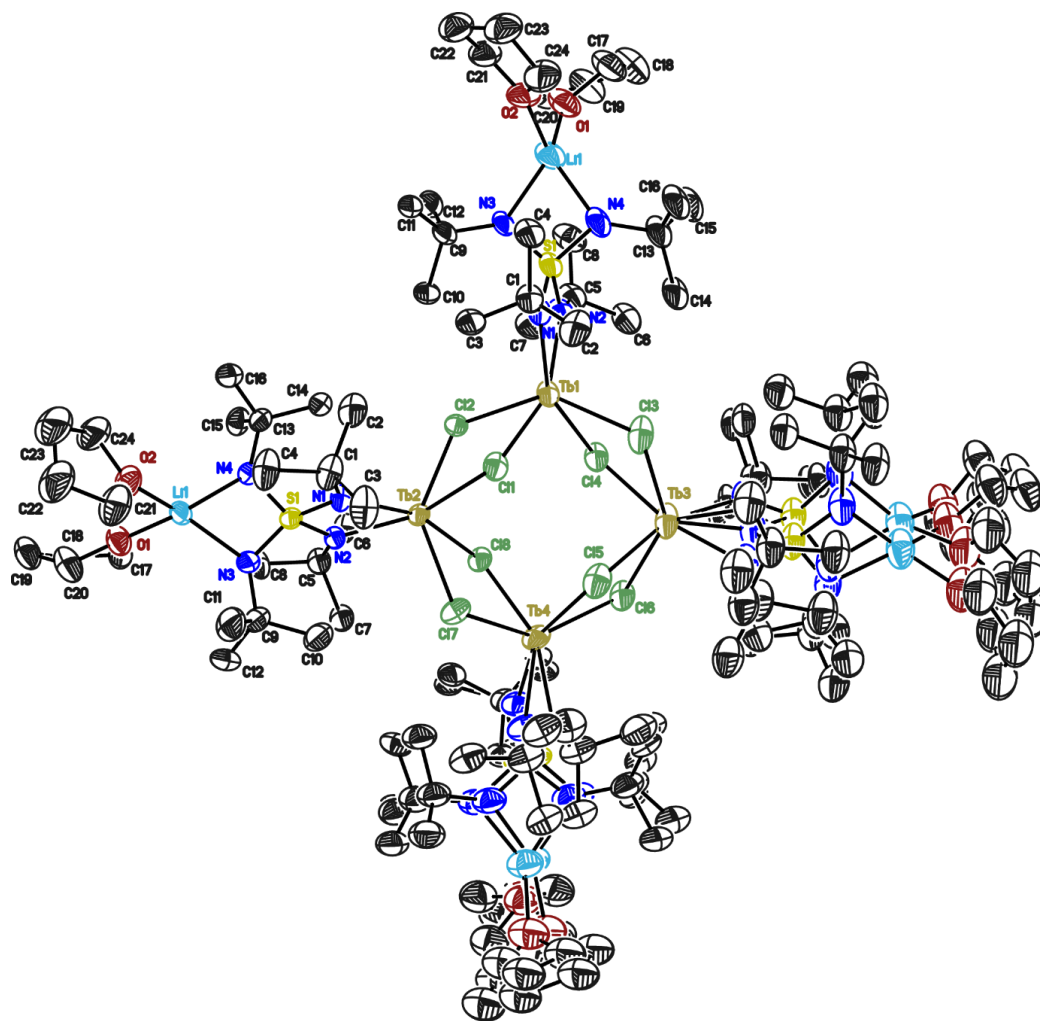
5.5.28. $[\{\text{Cl}_2\text{Tb}(\text{NtBu})_2\text{S}(\text{NtBu})_2\text{Li}(\text{thf})_2\}_4] \text{ (14)}$ 

Figure 5-28. Asymmetric unit of **14**. Anisotropic displacement parameters are depicted on a probability level of 50%. Hydrogen atoms are omitted for clarity. The ligands coordinating Tb3 and Tb4, including the coordinated lithium atom and the thf molecules, are disordered and were refined on two positions each. The occupancy of the main position for the ligand coordinating to Tb3 was refined to 0.584(5) and the one coordinating to Tb4 with 0.512(6), respectively. For the refinement, distance restraints and restraints for the anisotropic displacement parameters were used. The crystal contained solvent channels filled with disordered toluene molecules, which were treated using SQUEEZE from the PLATON software package.

Table 5-28. Crystal data of **14**.

CCDC no	2069119	Z	8
Empirical formula	$\text{C}_{96}\text{H}_{208}\text{Cl}_8\text{Li}_4\text{N}_{16}\text{O}_8\text{S}_4\text{Tb}_4$	$\rho_{\text{calc}} [\text{g}/\text{cm}^3]$	1.160
Formula weight $[\text{g}/\text{mol}]$	2790.05	$\mu [\text{mm}^{-1}]$	1.053
Temperature $[\text{K}]$	100(2)	$F(000)$	11456
Wavelength $[\text{\AA}]$	0.56086	θ range $^\circ$	1.518 to 18.206
Crystal system	Monoclinic	Reflections collected	285015
Space group	$C2/c$	Independent reflections	22853
a $[\text{\AA}]$	67.205(4)	$R(\text{int})$	0.1400
b $[\text{\AA}]$	22.803(2)	Crystal dimensions $[\text{mm}]$	0.169 x 0.152 x 0.100
c $[\text{\AA}]$	21.301(2)	Restraints / parameter	10529 / 1863
α $^\circ$	90	GoF	1.133
β $^\circ$	101.92(2)	$R1 / wR2$ ($I > 2\sigma(I)$)	0.0760 / 0.1492
γ $^\circ$	90	$R1 / wR2$ (all data)	0.1216 / 0.1760
Volume $[\text{\AA}^3]$	31939(5)	max. diff peak / hole $[\text{e } \text{\AA}^{-3}]$	2.743 / -1.501

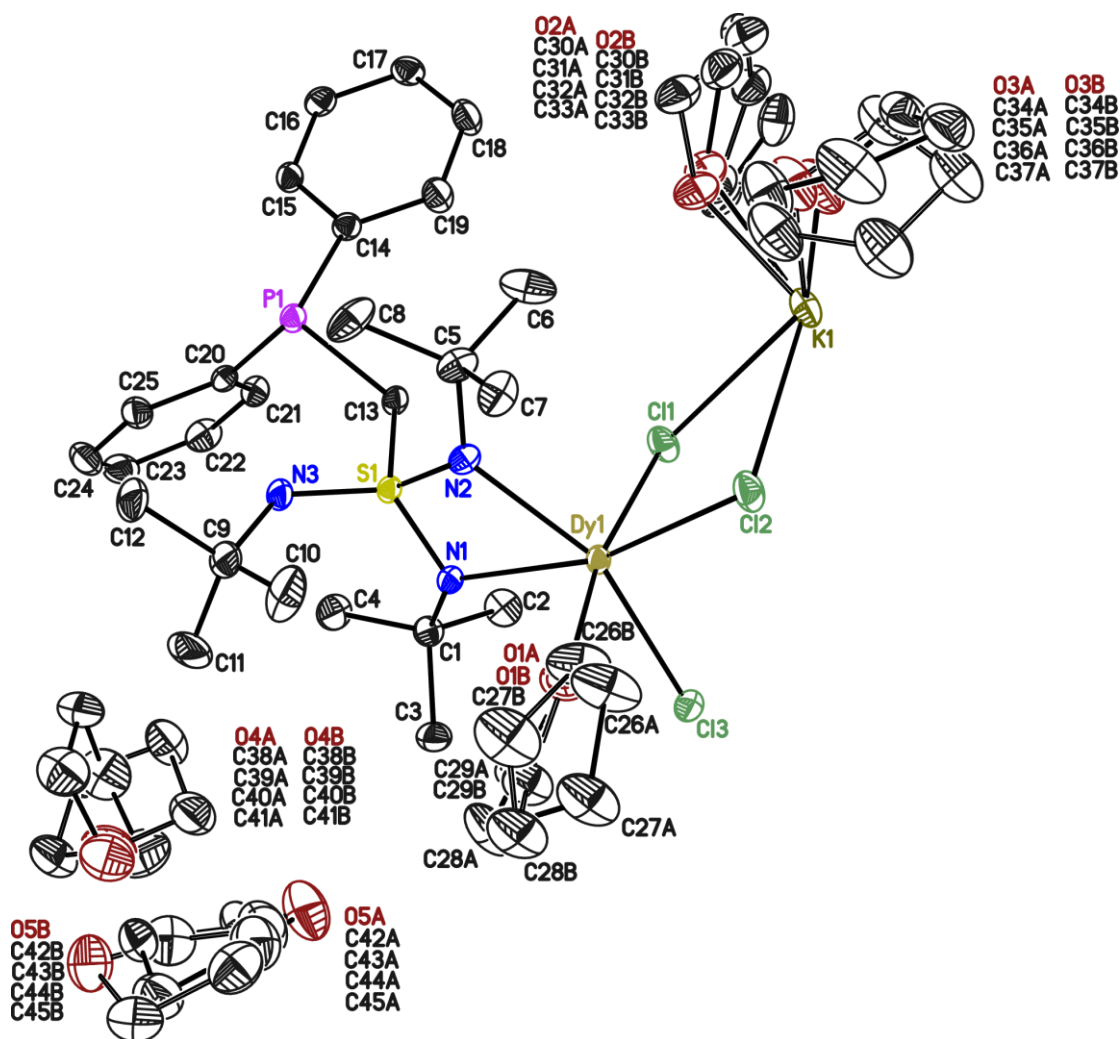
5.5.29. $[\{\text{Ph}_2\text{PCH}_2\text{S}(\text{NtBu})_3\text{Dy}(\text{thf})\text{Cl}_3\text{K}(\text{thf})_2\}_2] \text{ (15)}$ 

Figure 5-29. Asymmetric unit of **15**. The anisotropic displacement parameters are depicted at the 50% probability level. The hydrogen atoms are omitted for clarity.

Table 5-29. Crystal data of **15**.

Structure code	JJ_LM30	Z	1
Empirical formula	$\text{C}_{90}\text{H}_{158}\text{Cl}_6\text{Dy}_2\text{K}_2\text{N}_6\text{O}_{10}\text{P}_2\text{S}_2$	$\rho_{\text{calc}} [\text{g}/\text{cm}^3]$	1.400
Formula weight $[\text{g}/\text{mol}]$	2226.175	$\mu [\text{mm}^{-1}]$	0.938
Temperature $[\text{K}]$	100(2)	$F(000)$	1154
Wavelength $[\text{\AA}]$	0.56086	θ range $[\circ]$	1.565 to 21.427
Crystal system	Triclinic	Reflections collected	168694
Space group	P-1	Independent reflections	12195
$a [\text{\AA}]$	10.477(2)	$R(\text{int})$	0.0367
$b [\text{\AA}]$	12.611(2)	Crystal dimensions $[\text{mm}]$	0.295 x 0.187 x 0.133
$c [\text{\AA}]$	20.473(3)	Restraints / parameter	1906 / 780
$\alpha [^\circ]$	85.00(3)	GoF	1.065
$\beta [^\circ]$	81.126(2)	$R1 / wR2 (I > 2\sigma(I))$	0.0185 / 0.0426
$\gamma [^\circ]$	81.98(2)	$R1 / wR2 (\text{all data})$	0.0228 / 0.0445
Volume $[\text{\AA}^3]$	2640.8(8)	max. diff peak / hole $[\text{e} \text{\AA}^{-3}]$	0.514 / -0.590

6. Appendix

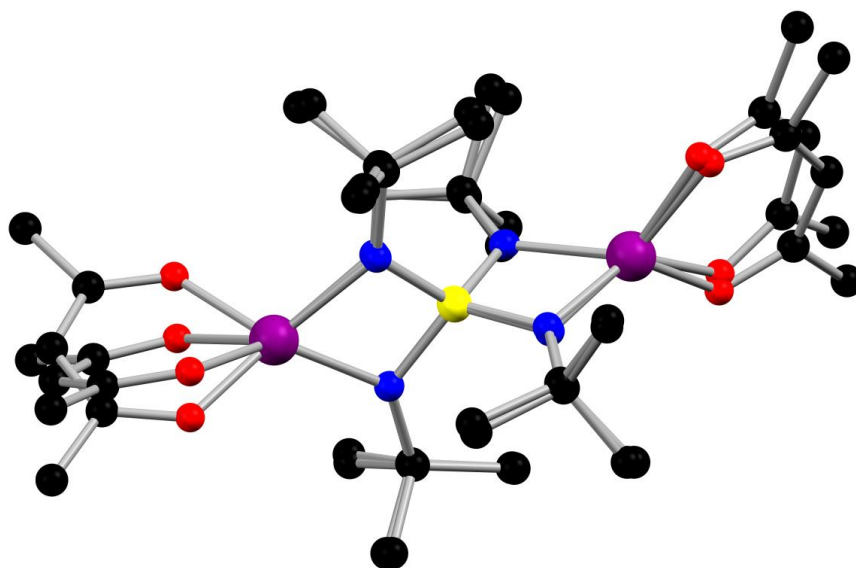


Figure 6-1 Superimposed structures **2a** and **2b**. Almost identical positions for the $[S(NtBu)_4]^{2-}$ ligand (L^1) and the two cobalt ions, but greater deviation for the acetylacetonate-Co angles. C in black, N in blue, O in red, S in yellow and Co in purple.

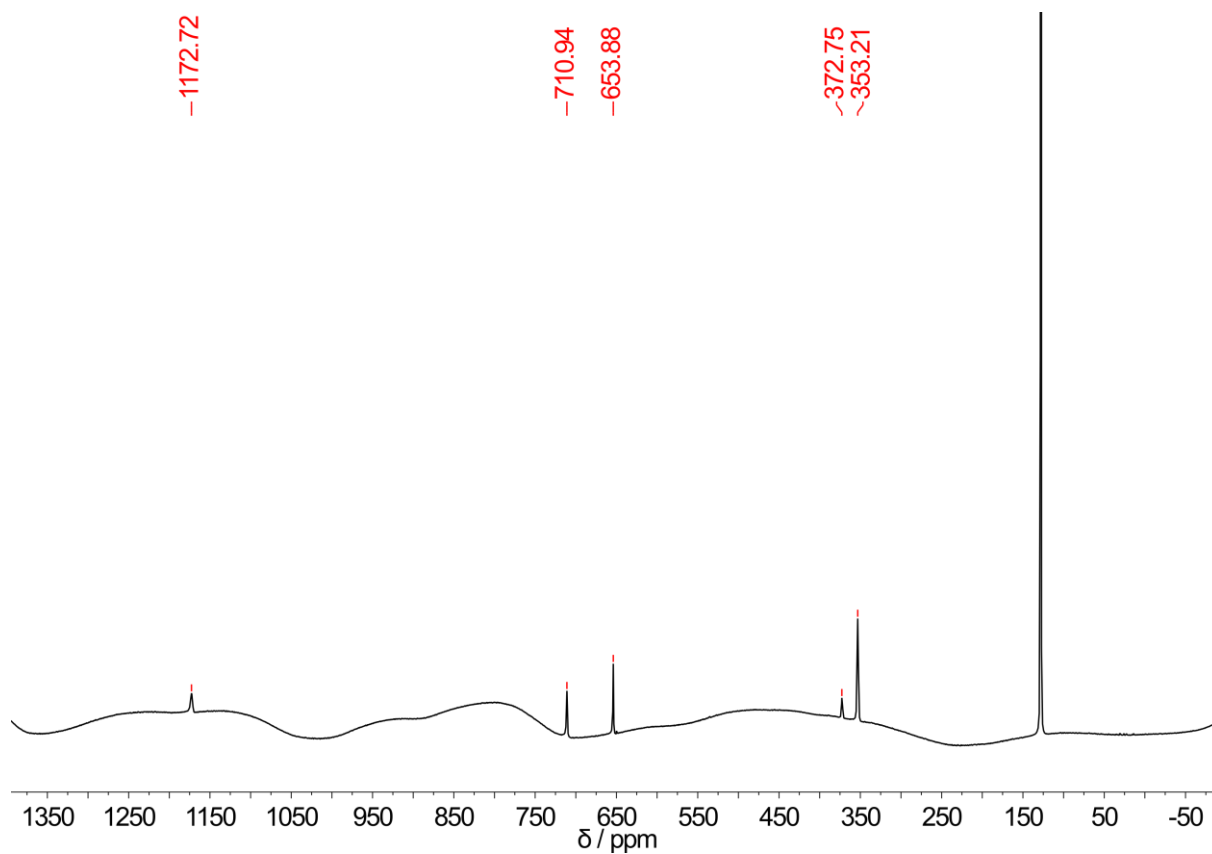


Figure 6-2 $^{13}C\{^1H\}$ -NMR of **2** at 298 K in C_6D_6 .

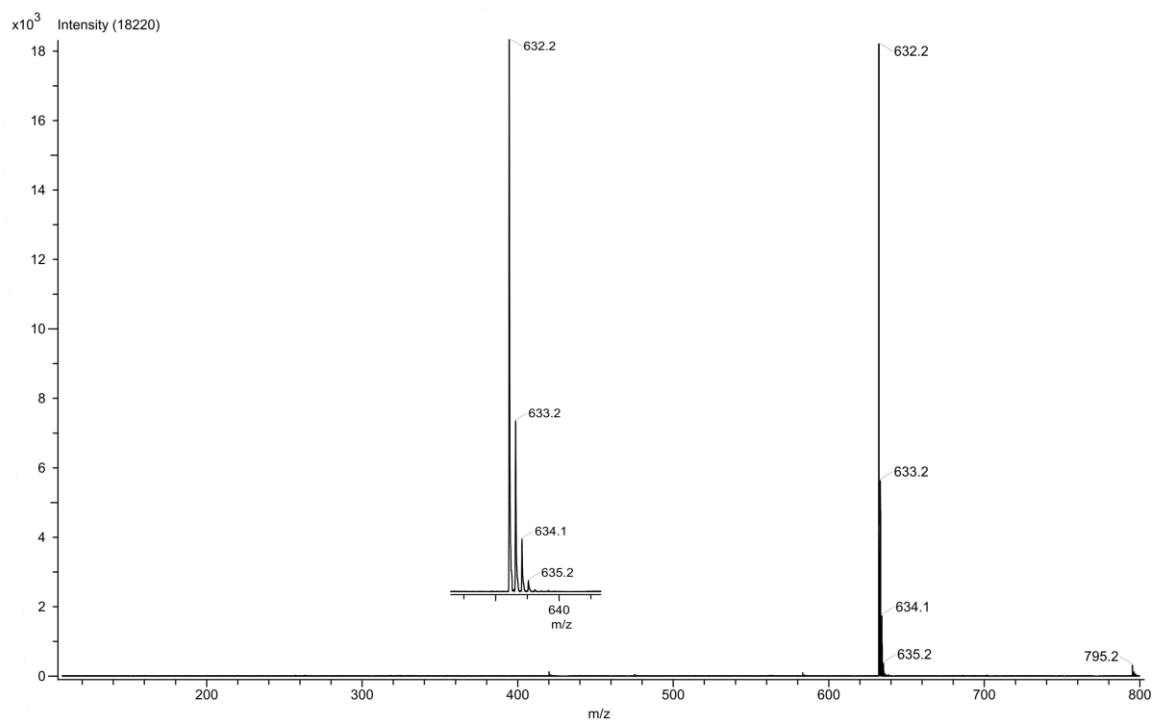


Figure 6-3 LIFDI mass spectrum of **2** from a thf solution with expected molar mass of 632.2 g/mol and isotope pattern.

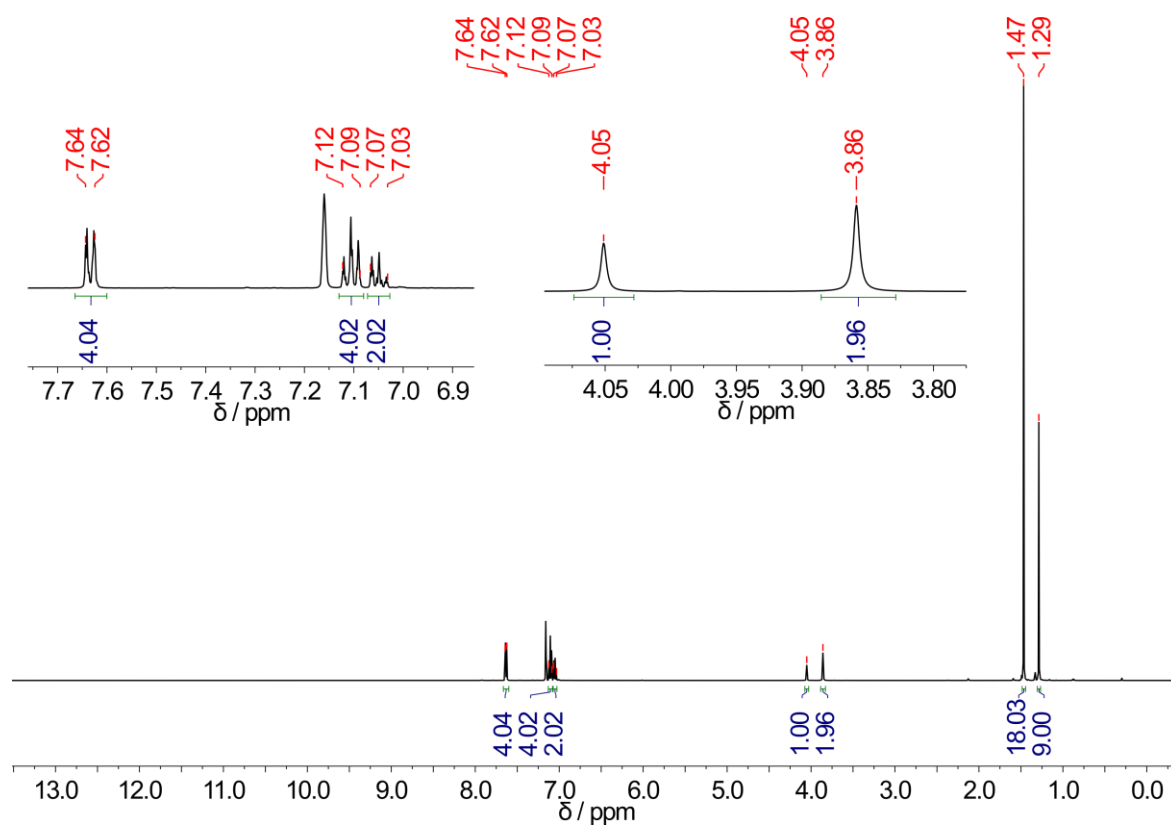


Figure 6-4 $^1\text{H}\{^{31}\text{P}\}$ -NMR of **4** at 298 K in C_6D_6

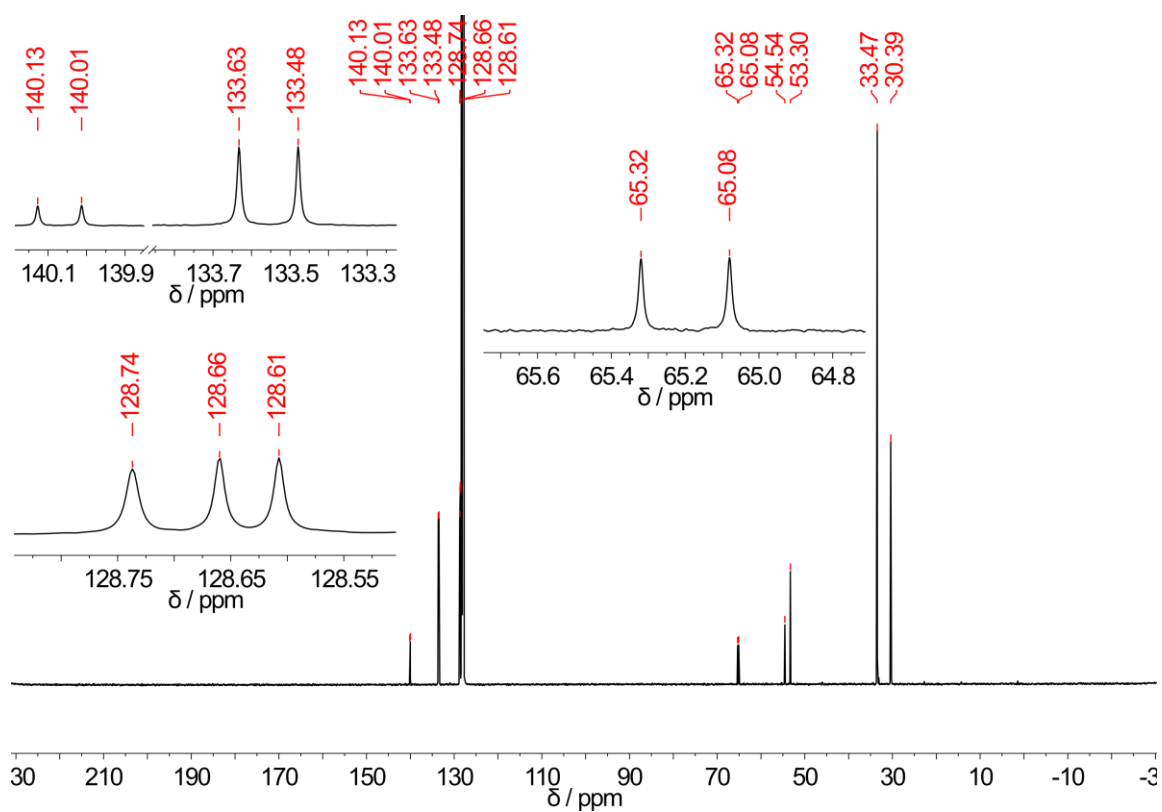


Figure 6-5 $^{13}\text{C}\{^1\text{H}\}$ -NMR of **4** at 298 K in C_6D_6 .

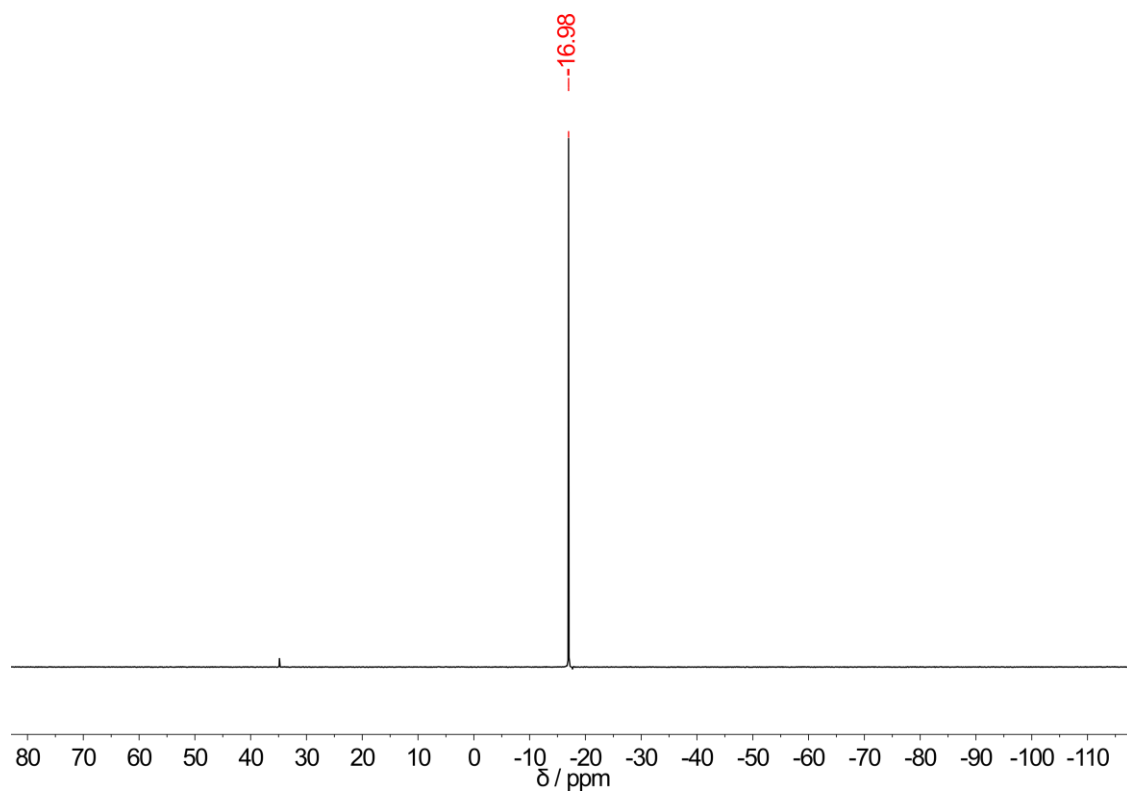


Figure 6-6 ^{31}P -NMR of **4** at 298 K in C_6D_6 .

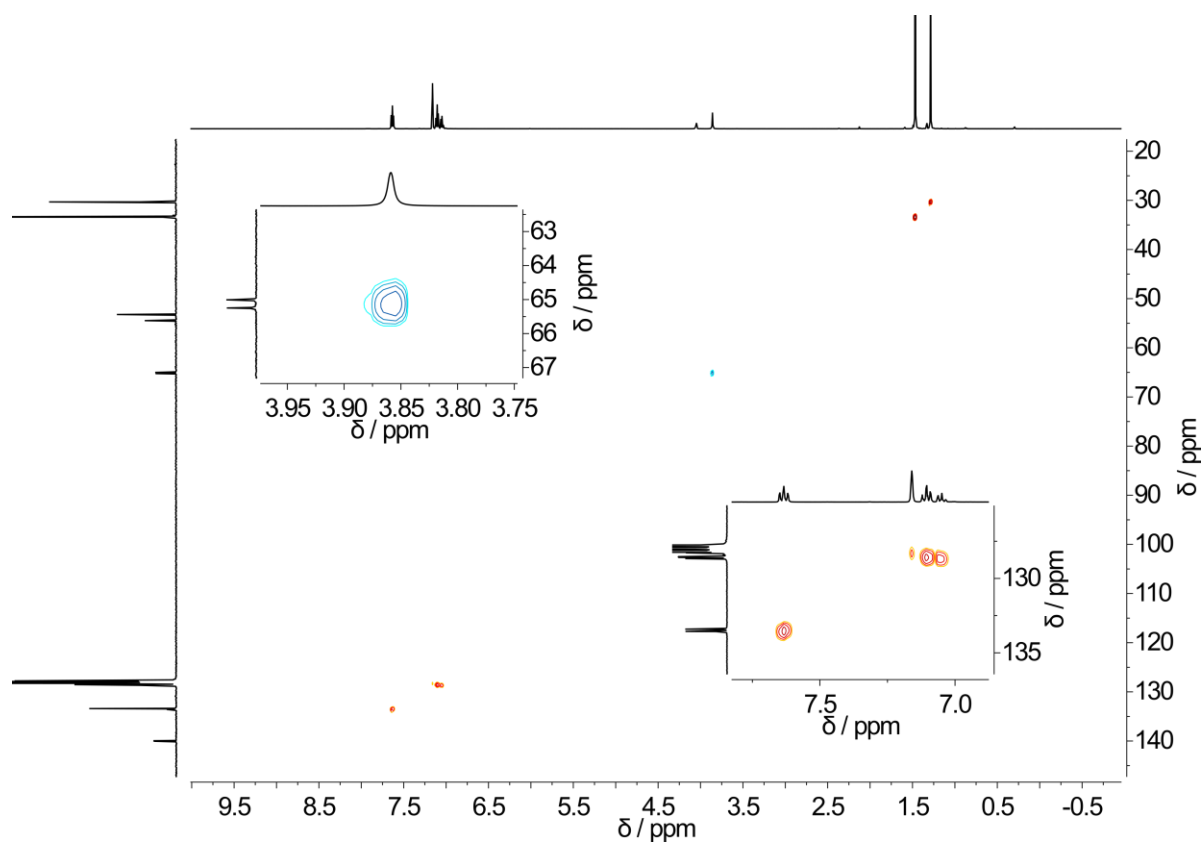


Figure 6-7 $^{13}\text{C}/^1\text{H}$ -HSQC-NMR of **4** at 298 K in C_6D_6 .

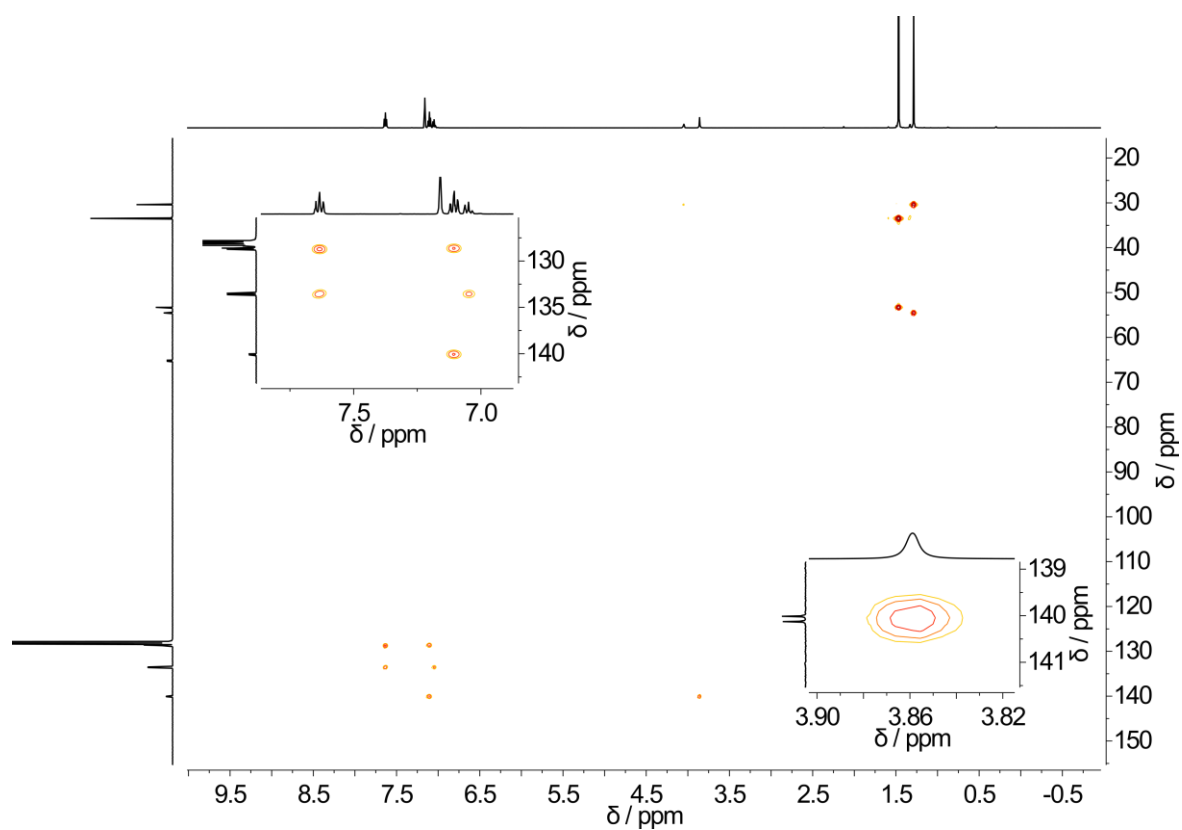


Figure 6-8 $^{13}\text{C}/^1\text{H}$ -HMBC-NMR of **4** at 298 K in C_6D_6 .

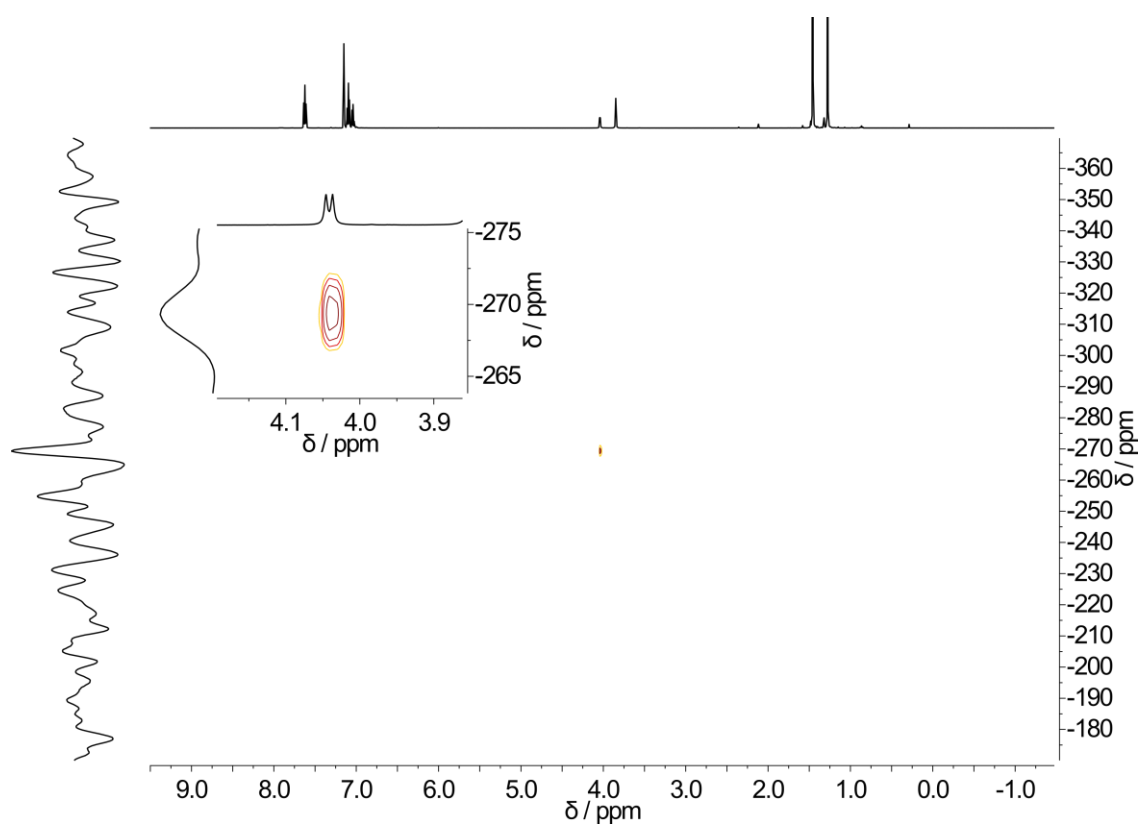


Figure 6-9 $^{15}\text{N}/^1\text{H}$ -HSQC-NMR of **4** at 298 K in C_6D_6 .

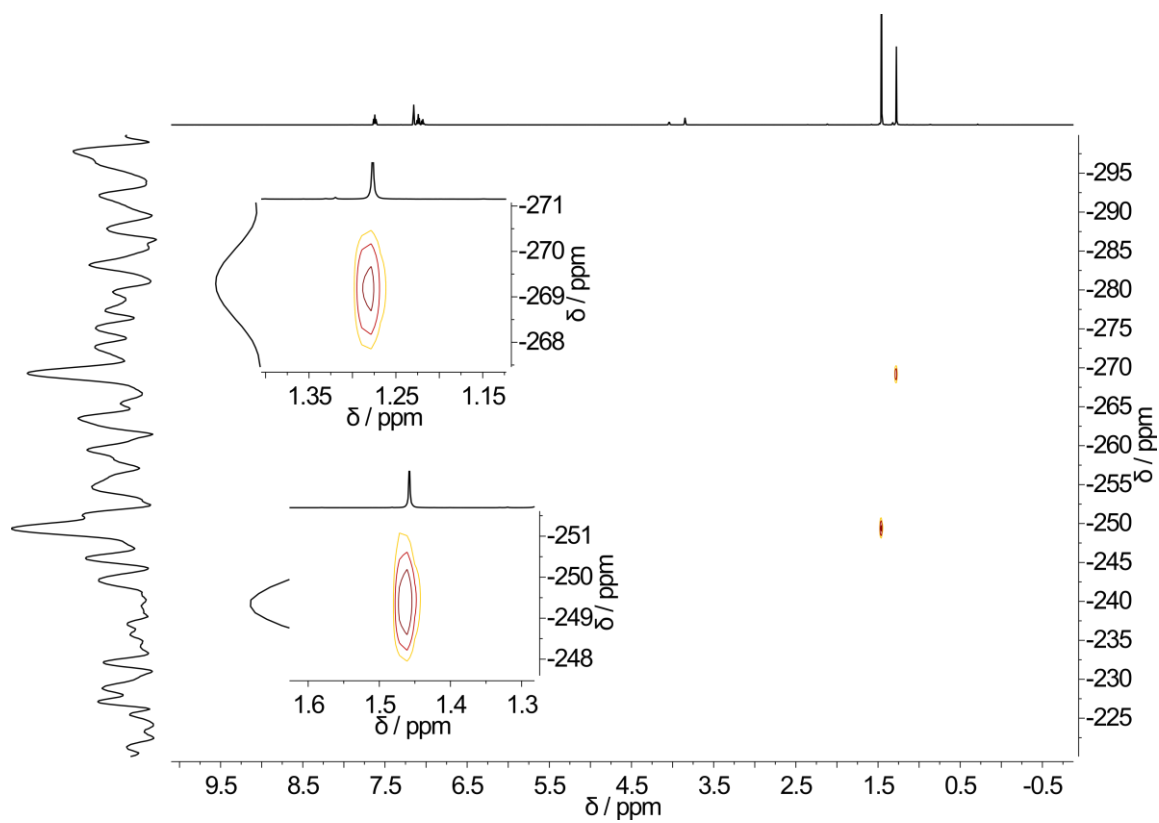


Figure 6-10 $^{15}\text{N}/^1\text{H}$ -HMBC-NMR of **4** at 298 K in C_6D_6 .

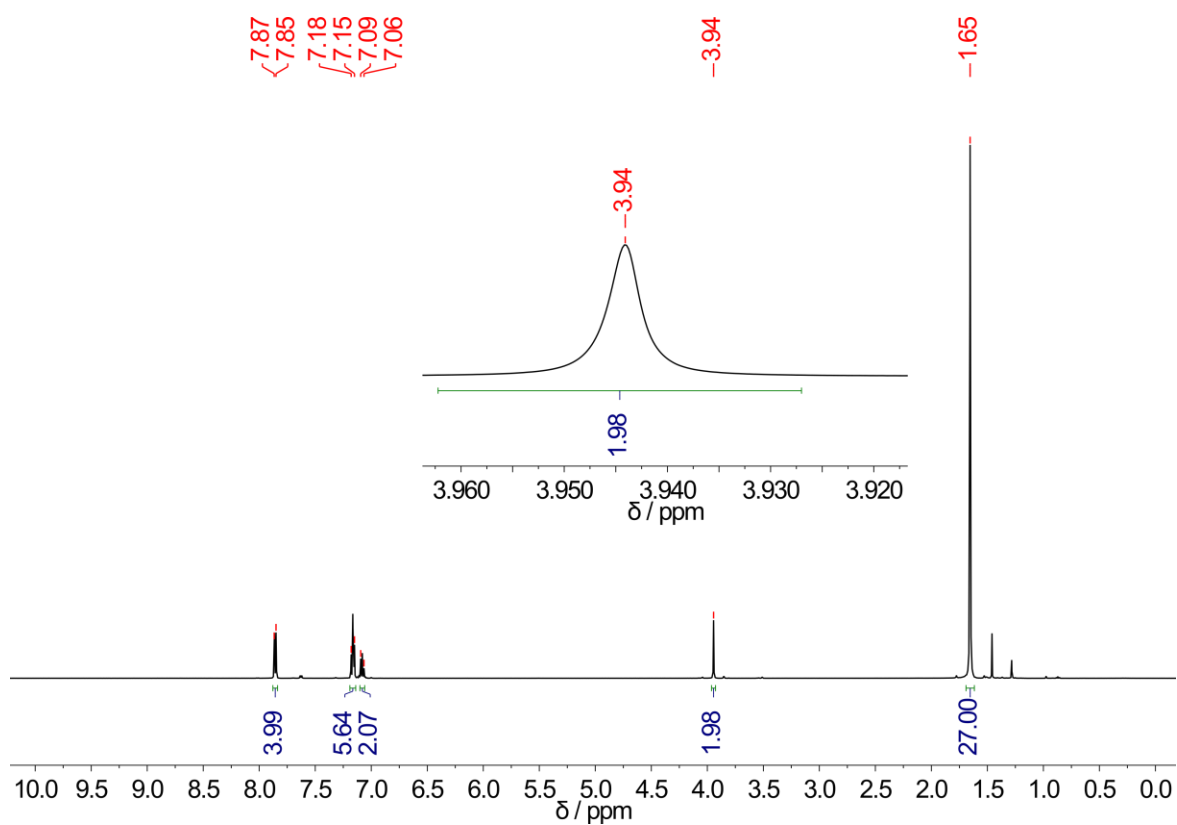


Figure 6-11 $^1\text{H}\{^{31}\text{P}\}$ -NMR of **5** at 298 K in C_6D_6 .

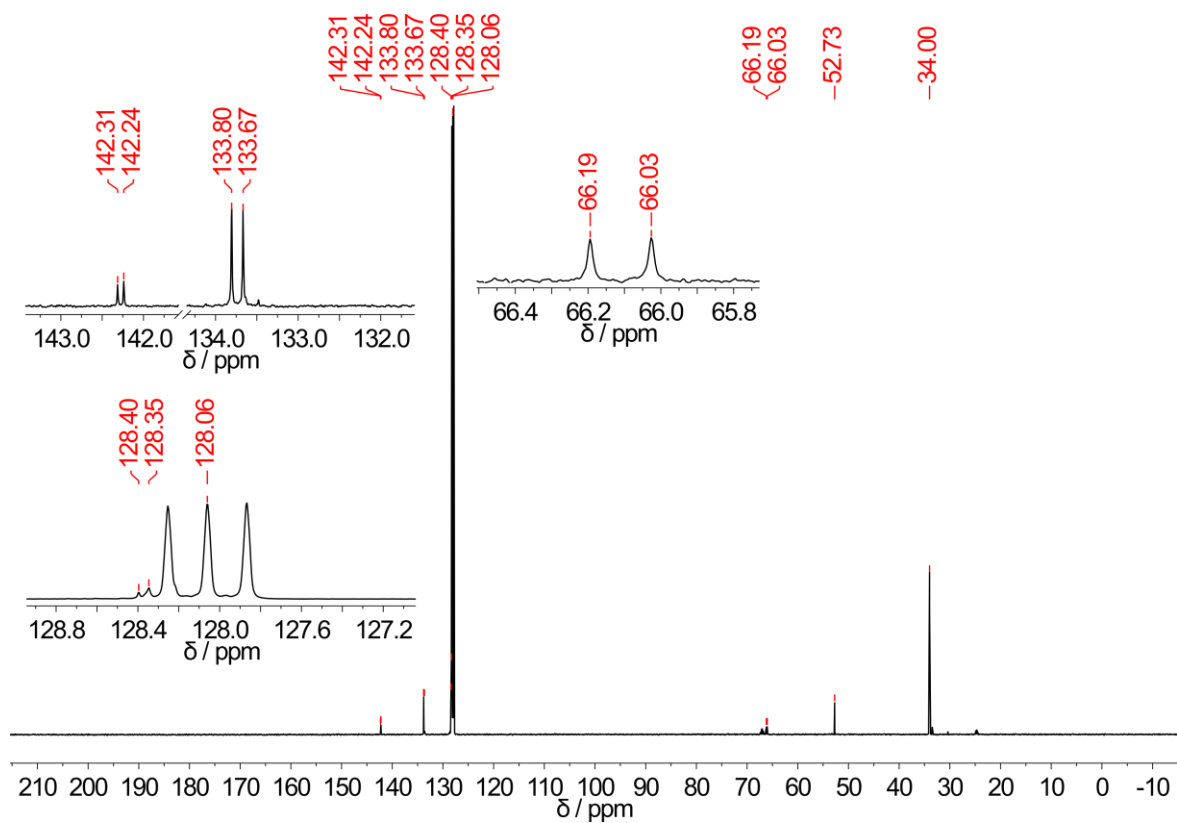


Figure 6-12 ^{13}C -NMR of **5** at 298 K in C_6D_6 .

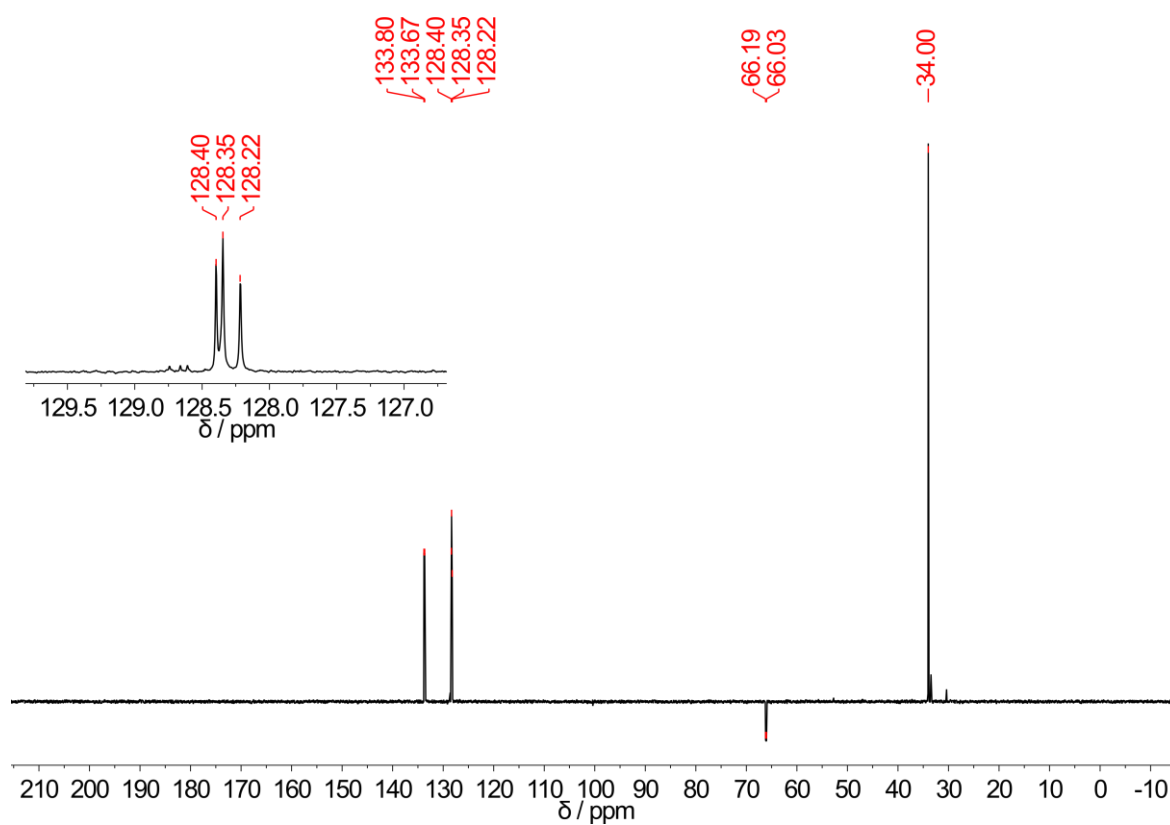


Figure 6-13 ^{13}C -DEPT-135-NMR of **5** at 298 K in C_6D_6 .

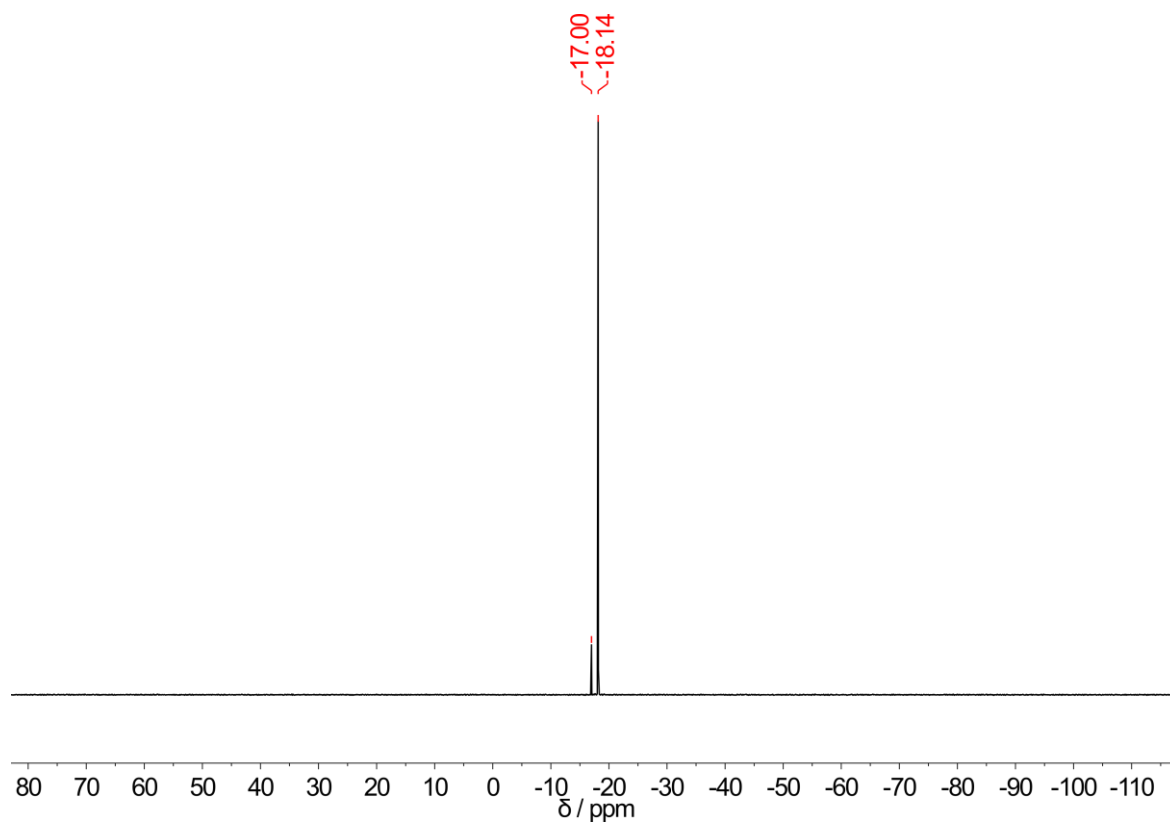


Figure 6-14 $^{31}\text{P}\{^1\text{H}\}$ -NMR of **5** at 298 K in C_6D_6 .

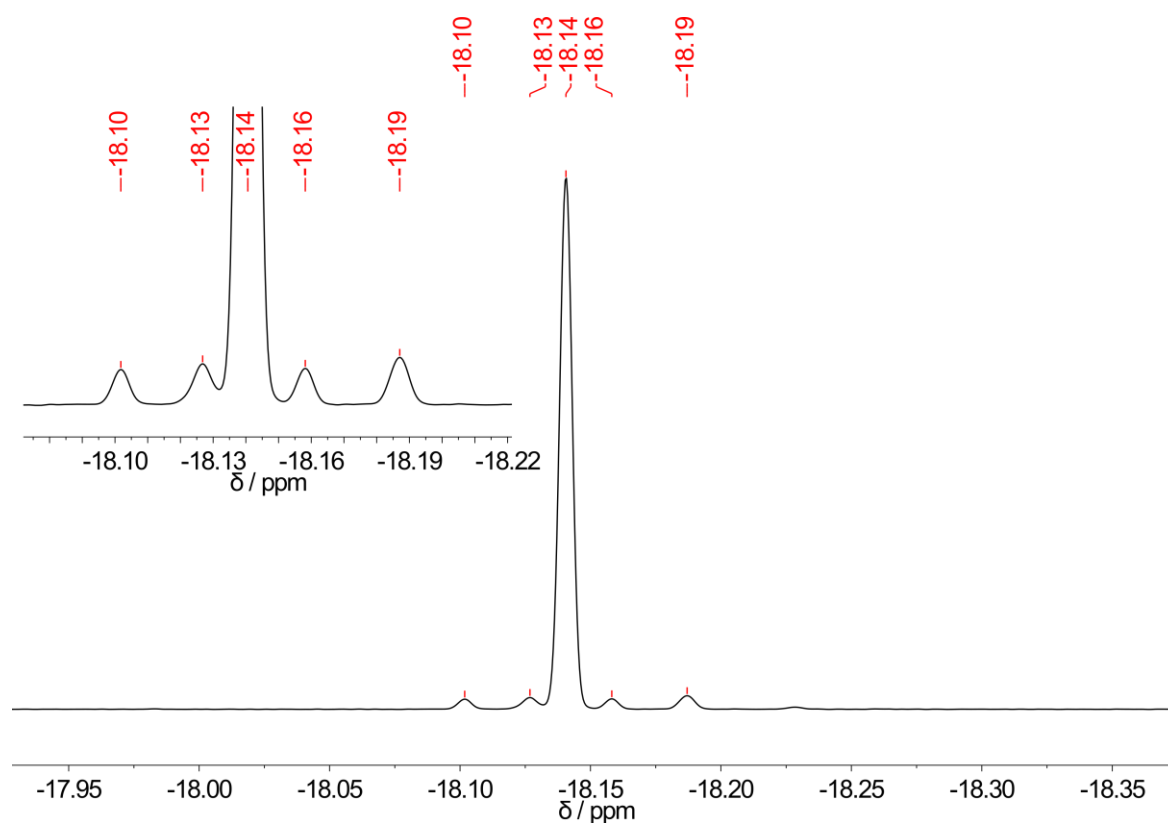


Figure 6-15 $^{31}\text{P}\{^1\text{H}\}$ -NMR of **5** at 298 K in C_6D_6 . Depicted is the ^{31}P - ^{13}C -coupling.

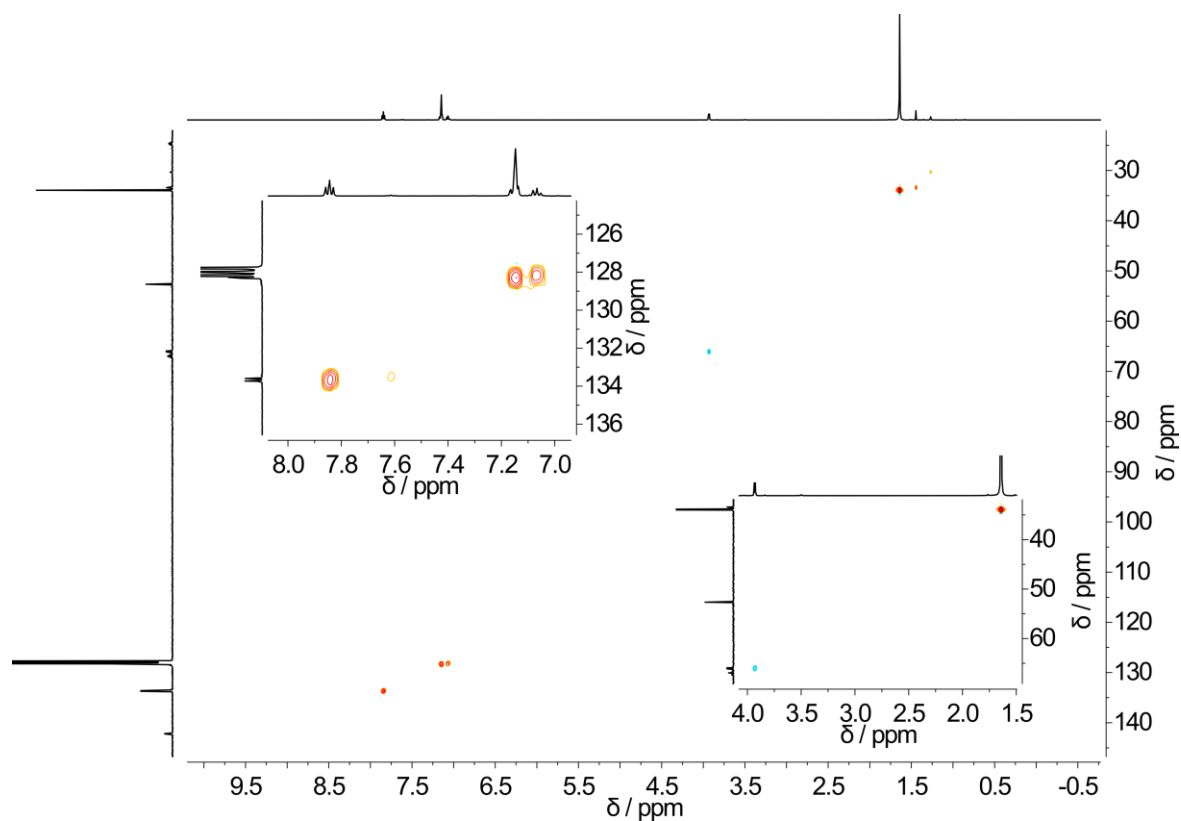


Figure 6-16 $^{13}\text{C}/^1\text{H}$ -HSQC-NMR of **5** at 298 K in C_6D_6 .

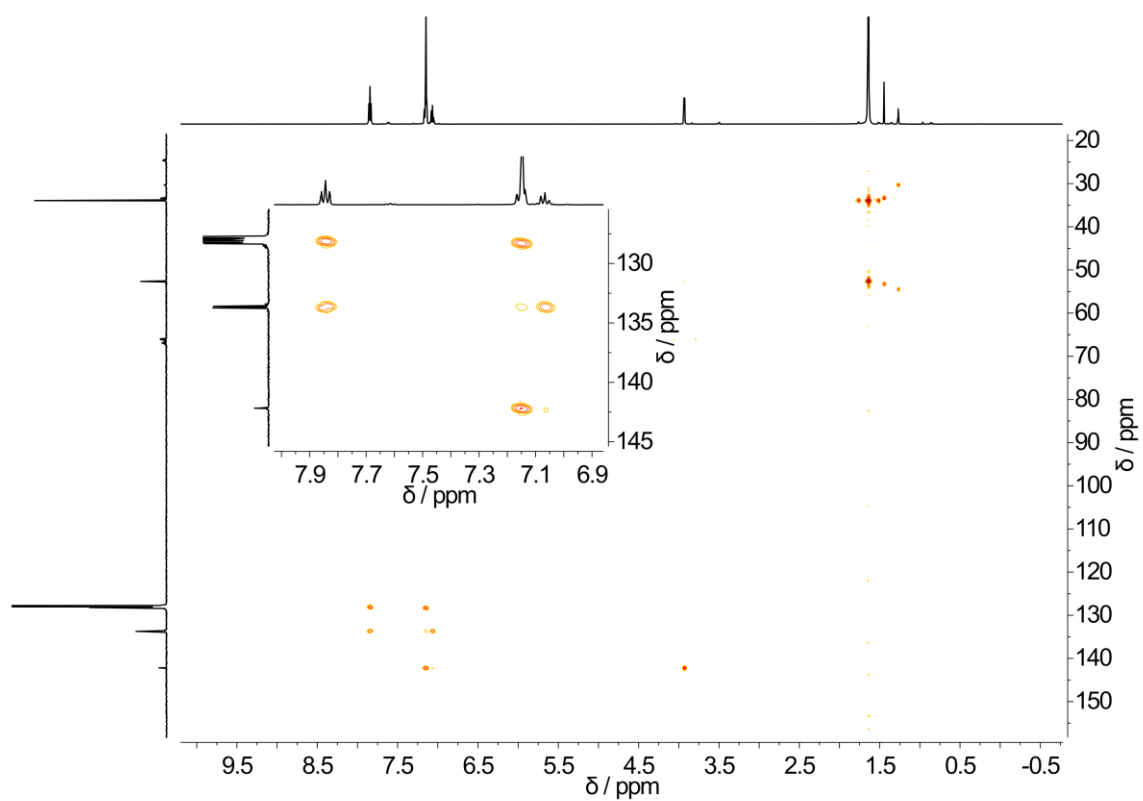


Figure 6-17 $^{13}\text{C}/^1\text{H}$ -HMBC-NMR of **5** at 298 K in C_6D_6 .

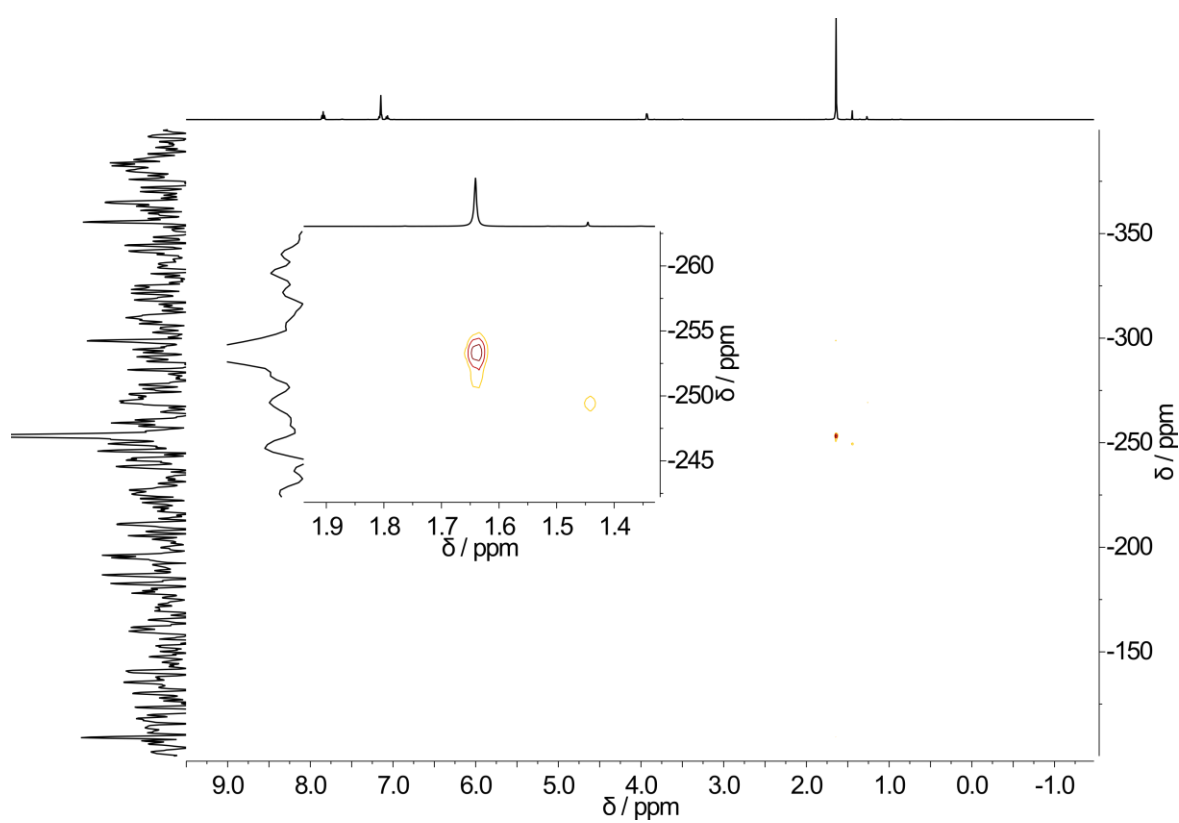


Figure 6-18 $^{15}\text{N}/^1\text{H}$ -HMBC-NMR of **5** at 298 K in C_6D_6 .

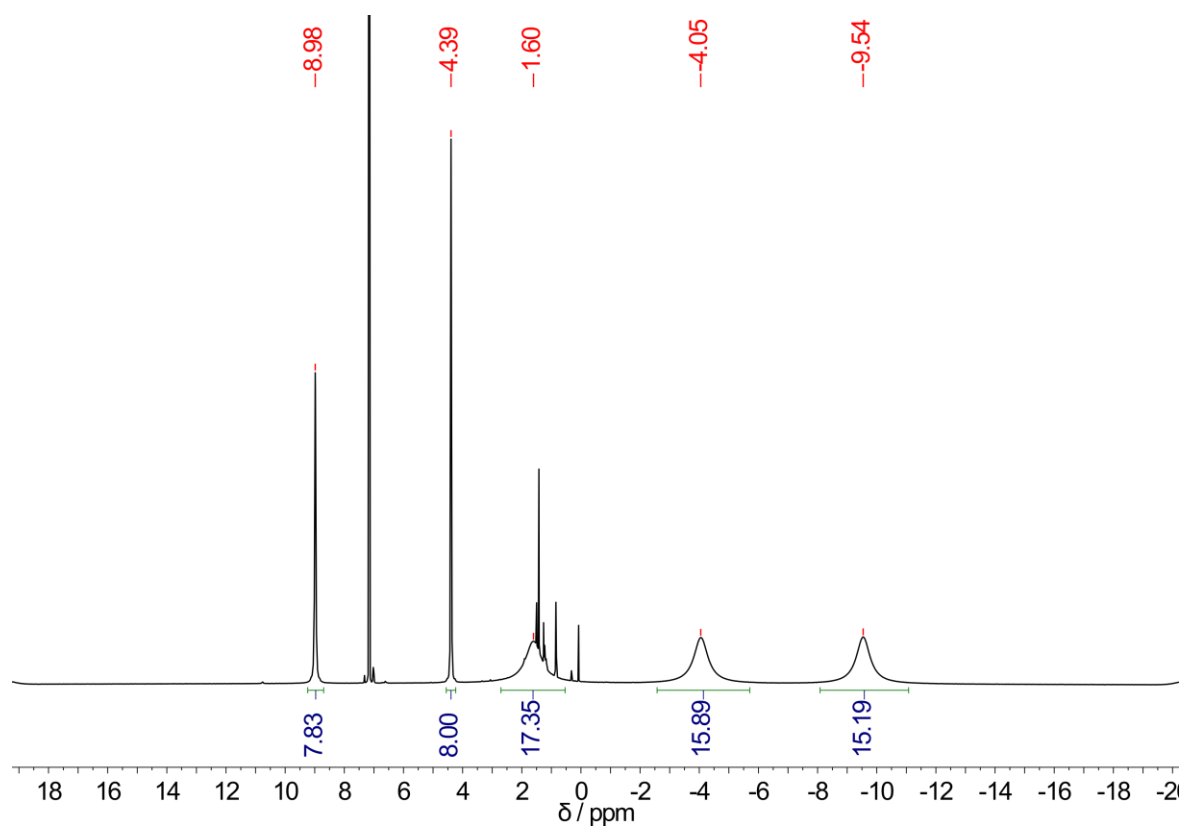


Figure 6-19 ^1H -NMR of **6** at 298 K in C_6D_6 .

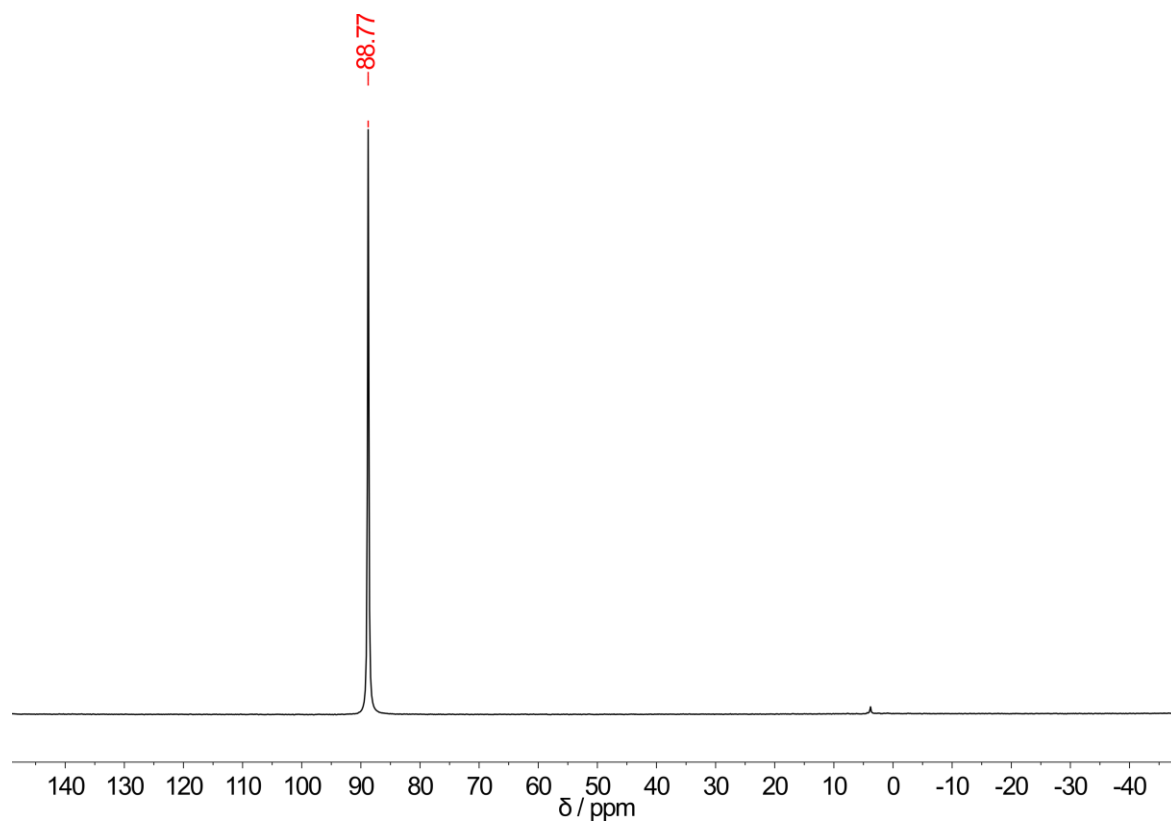


Figure 6-20 ^7Li -NMR of **6** at 298 K in C_6D_6 .

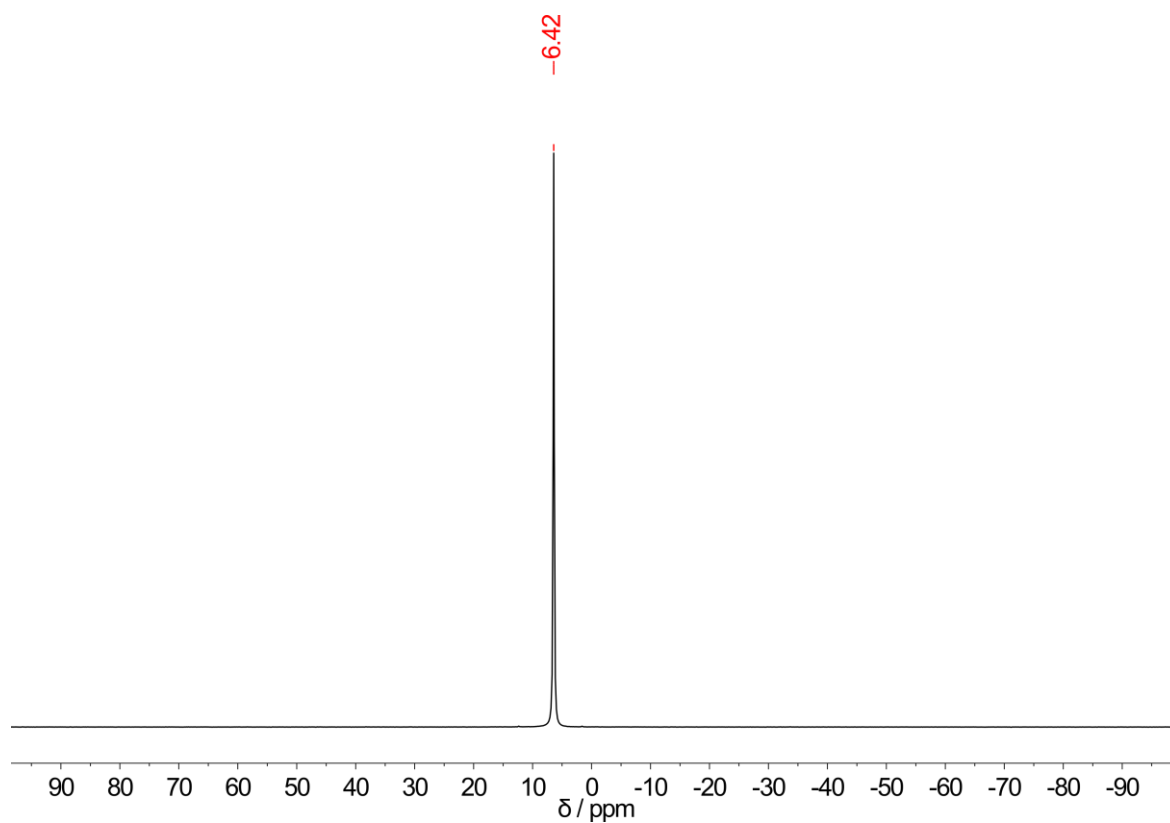


Figure 6-21 ^7Li -NMR of **7** at 298 K in C_6D_6 .

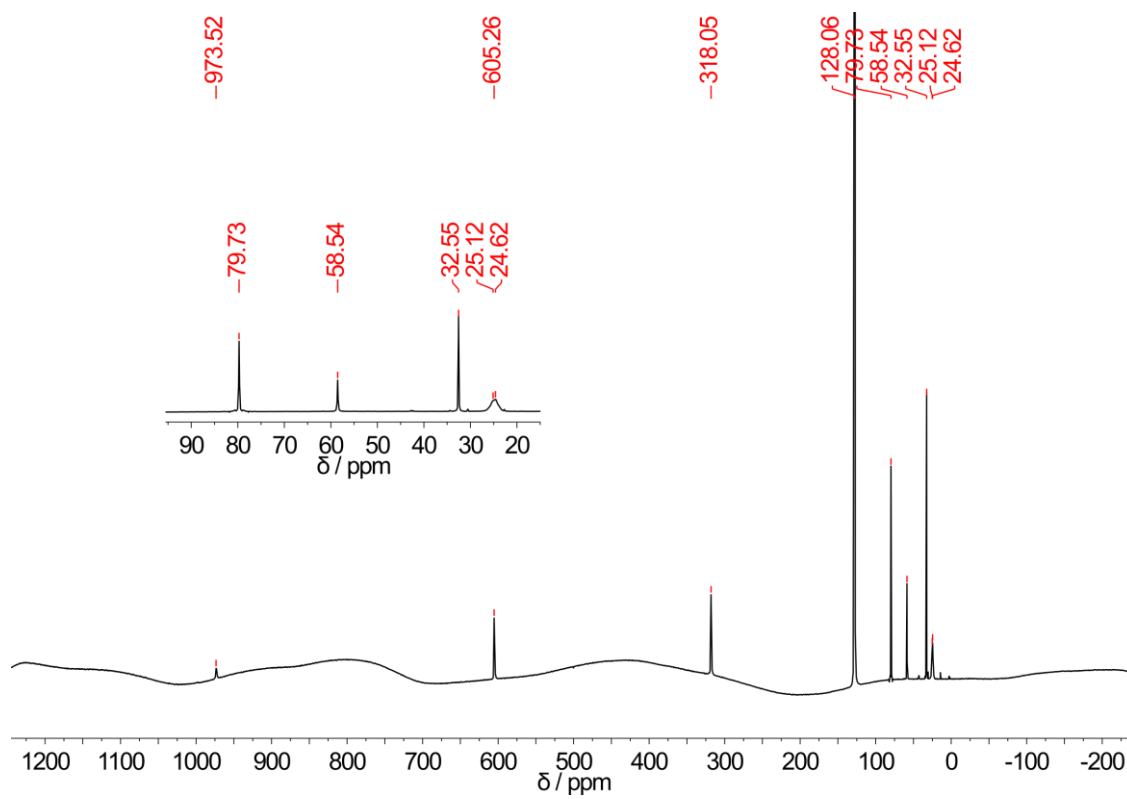


Figure 6-22 $^{31}\text{C}\{^1\text{H}\}$ -NMR of **7** at 298 K in C_6D_6 .

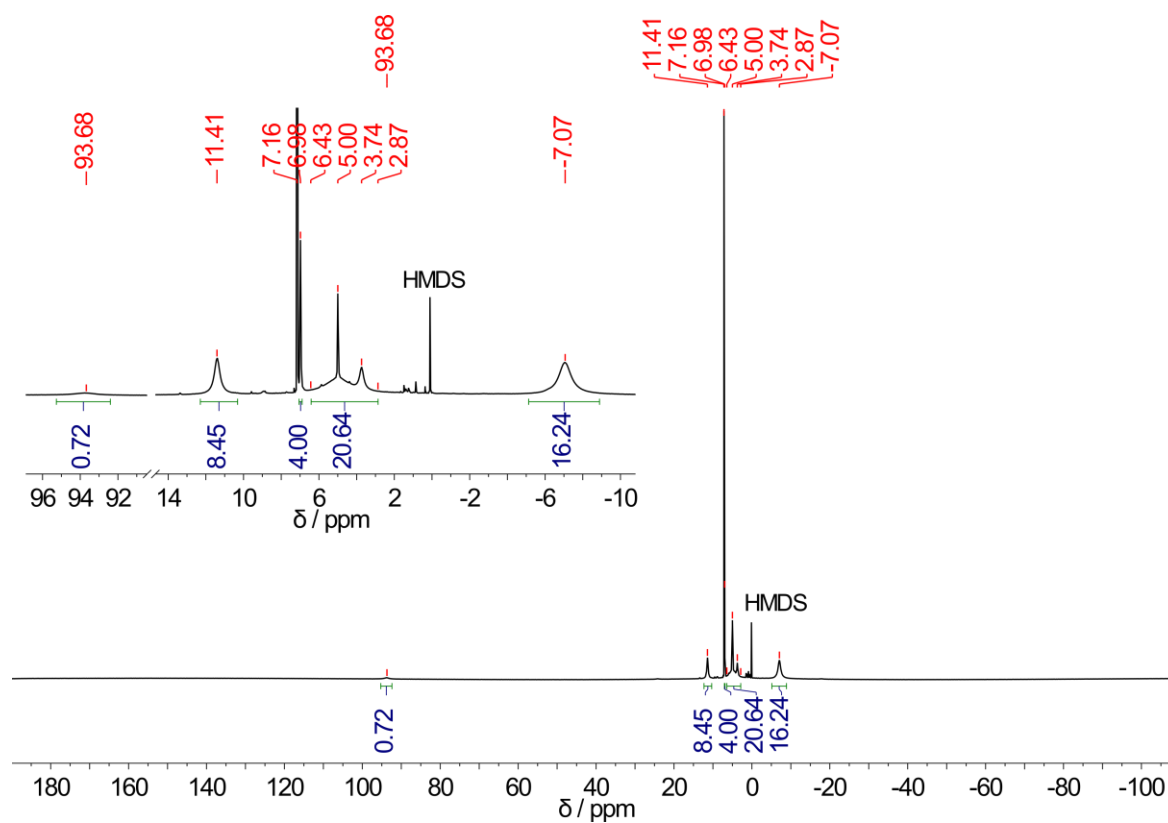


Figure 6-23 ^1H -NMR of **8** at 298 K in C_6D_6 .

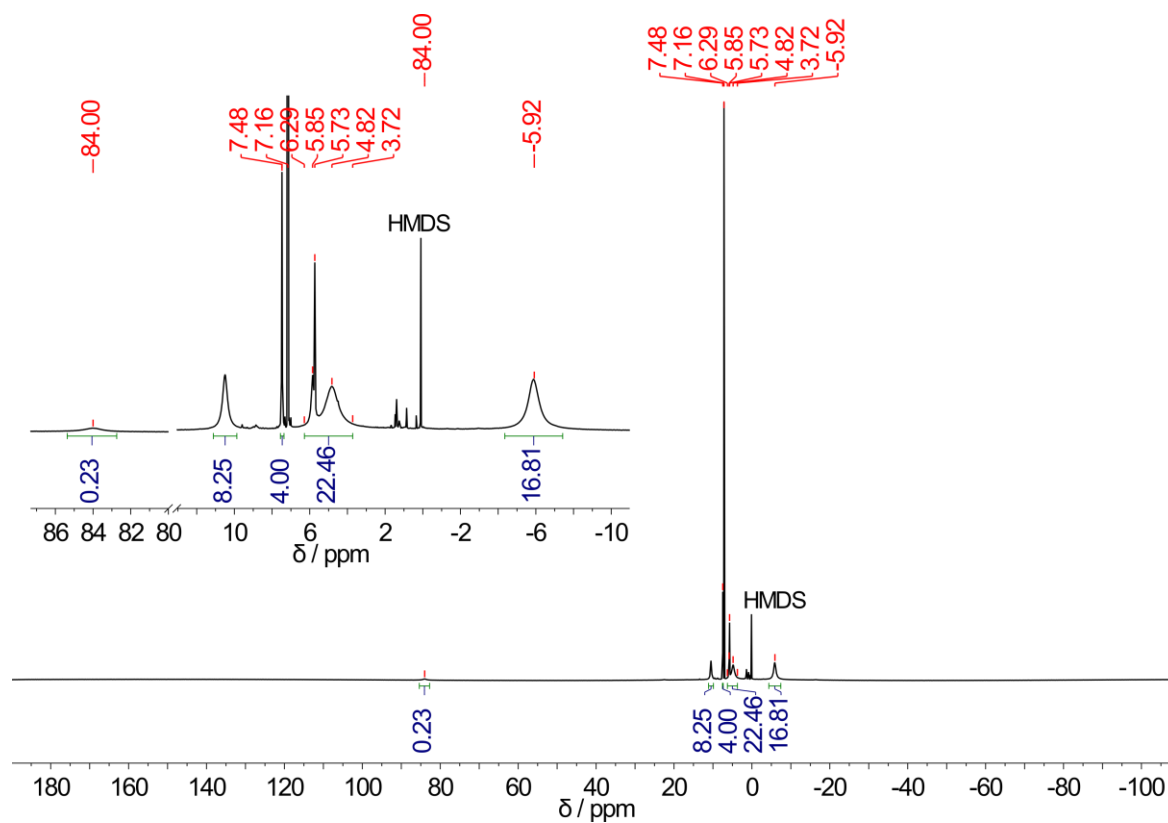


Figure 6-24 ^1H -NMR of **8** at 323 K in C_6D_6 .

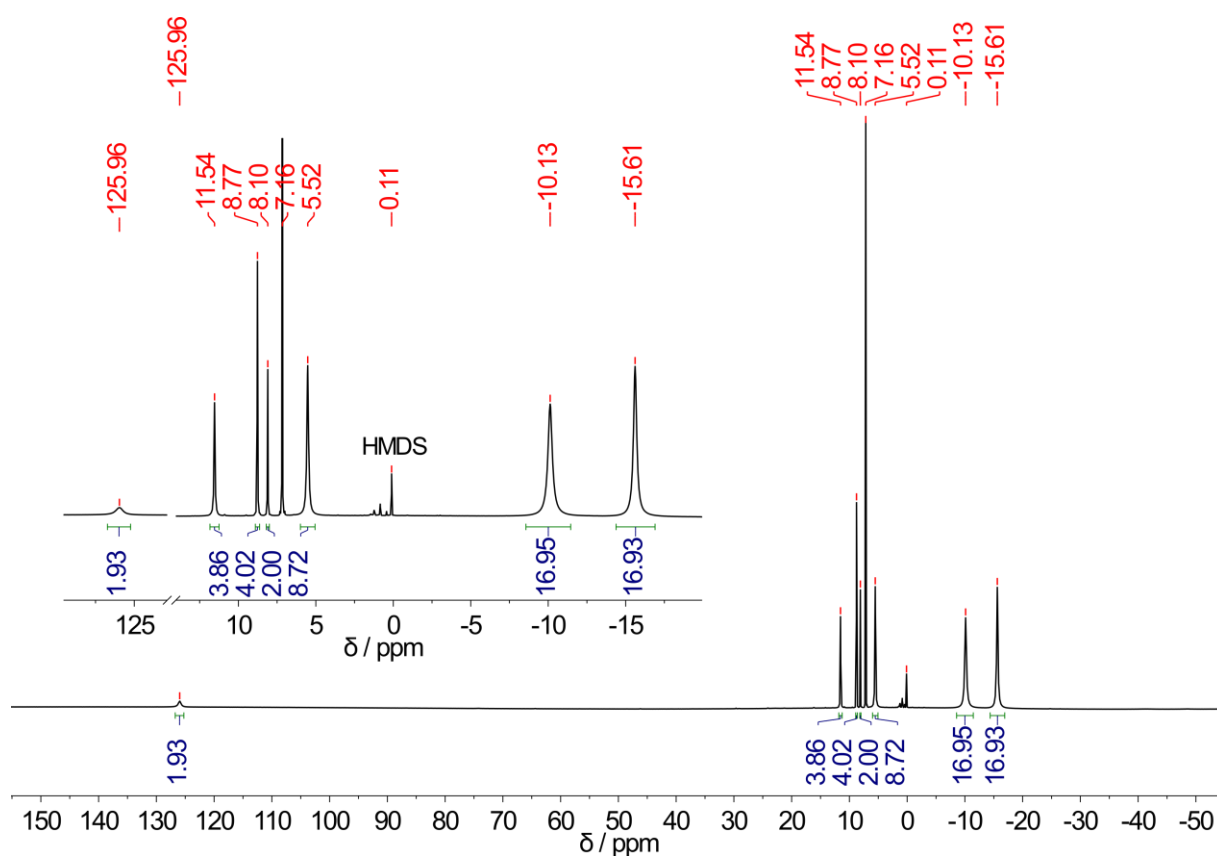


Figure 6-25 ^1H -NMR spectrum of **9** at 323 K in C_6D_6 . δ [ppm] = -15.61 (s br, 18H, 6 CH_3), -10.13 (s br, 18H, 6 CH_3), 5.52 (s br, 9H, 3 CH_3), 8.10 (s, 2H), 8.77 (s, 4H, Ph-H), 11.54 (s br, 4H, Ph-H), 125.96 (s, 2H).

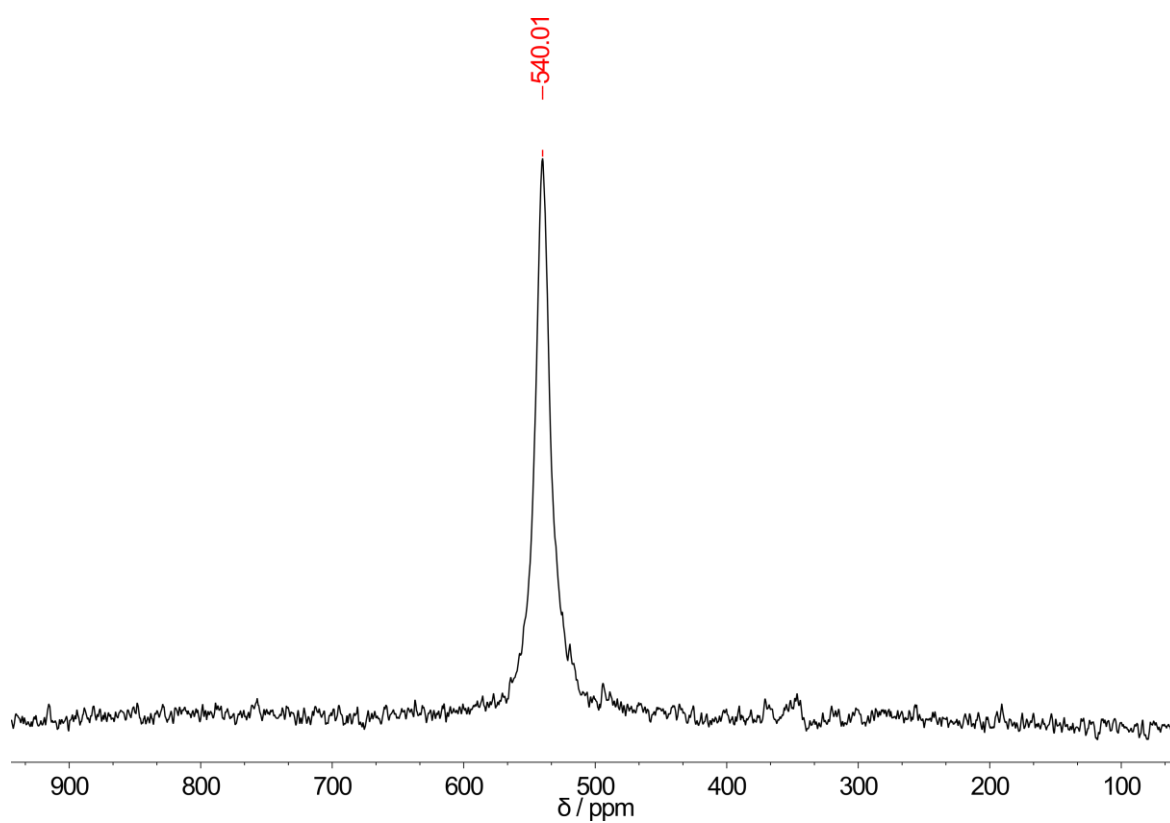


Figure 6-26 ^{31}P -NMR of **9** at 323 K in C_6D_6 .

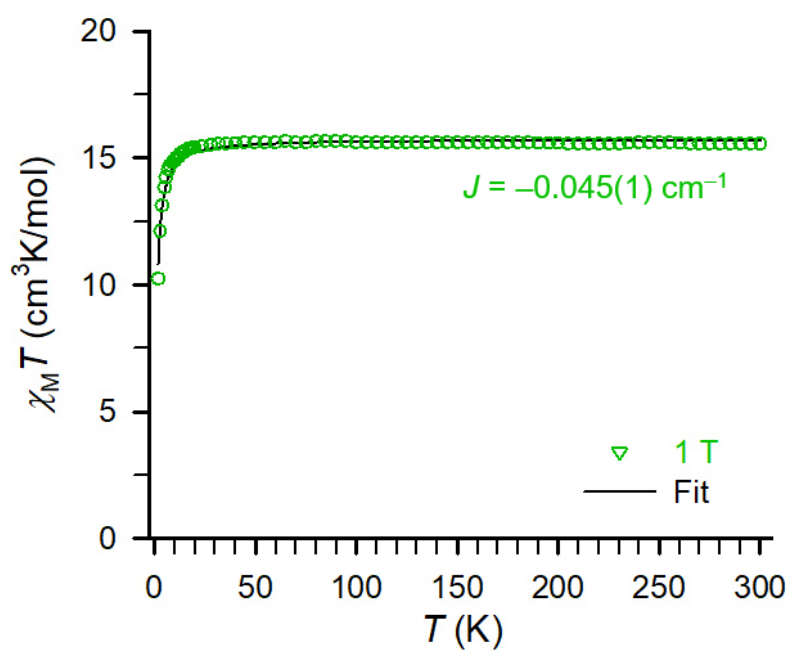


Figure 6-27 Variable-temperature dc magnetic susceptibility measurement for **10a** at 1 T applied dc field. The black line represents a fit to the data.

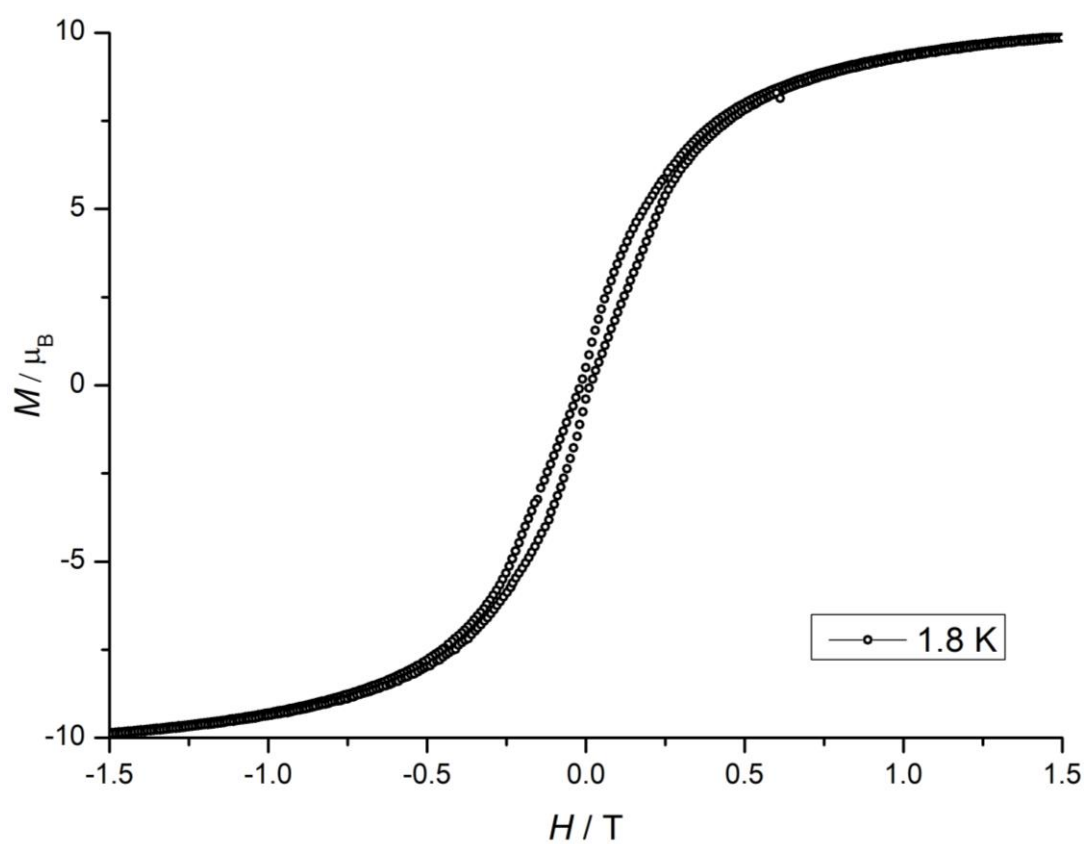


Figure 6-28 Variable field magnetization (M) for **10c** collected at 1.8 K at an average sweep rate of 0.01 T s^{-1} .

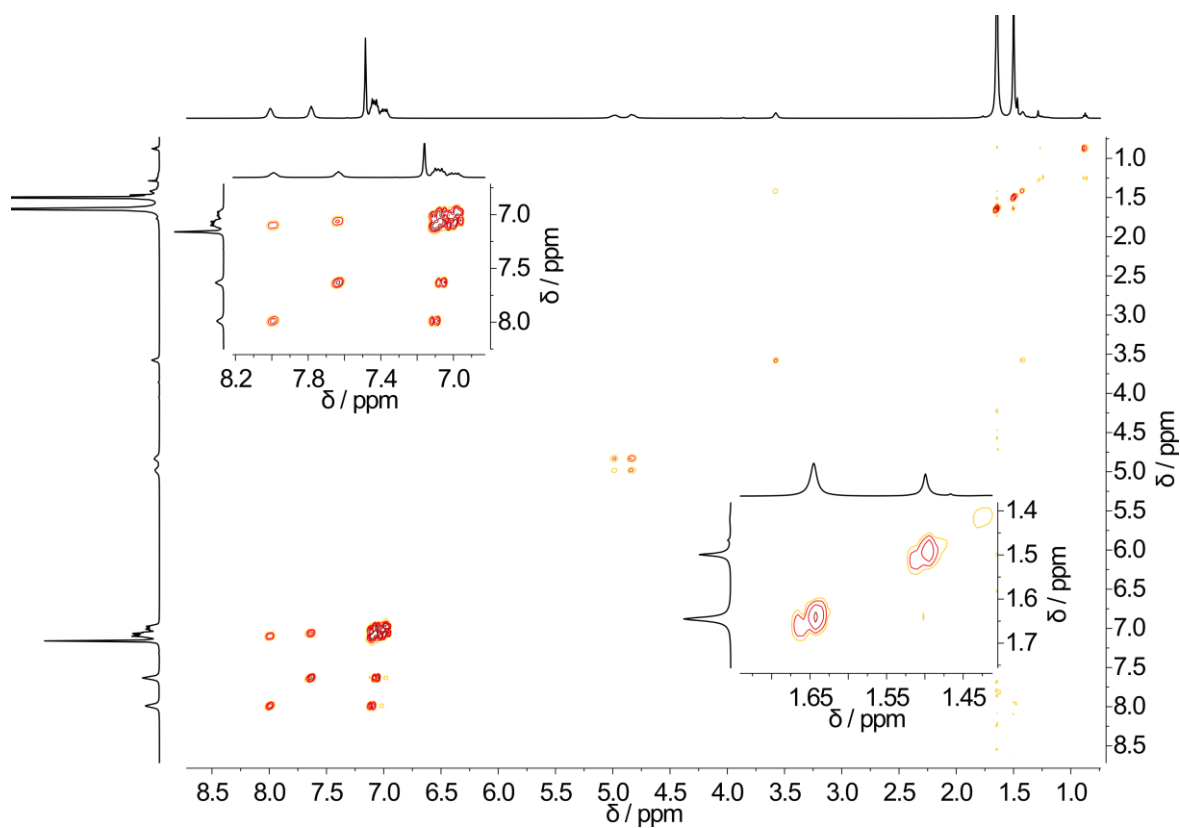


Figure 6-29 ^1H -COSY-NMR of **12e** at 298 K in C_6D_6 .

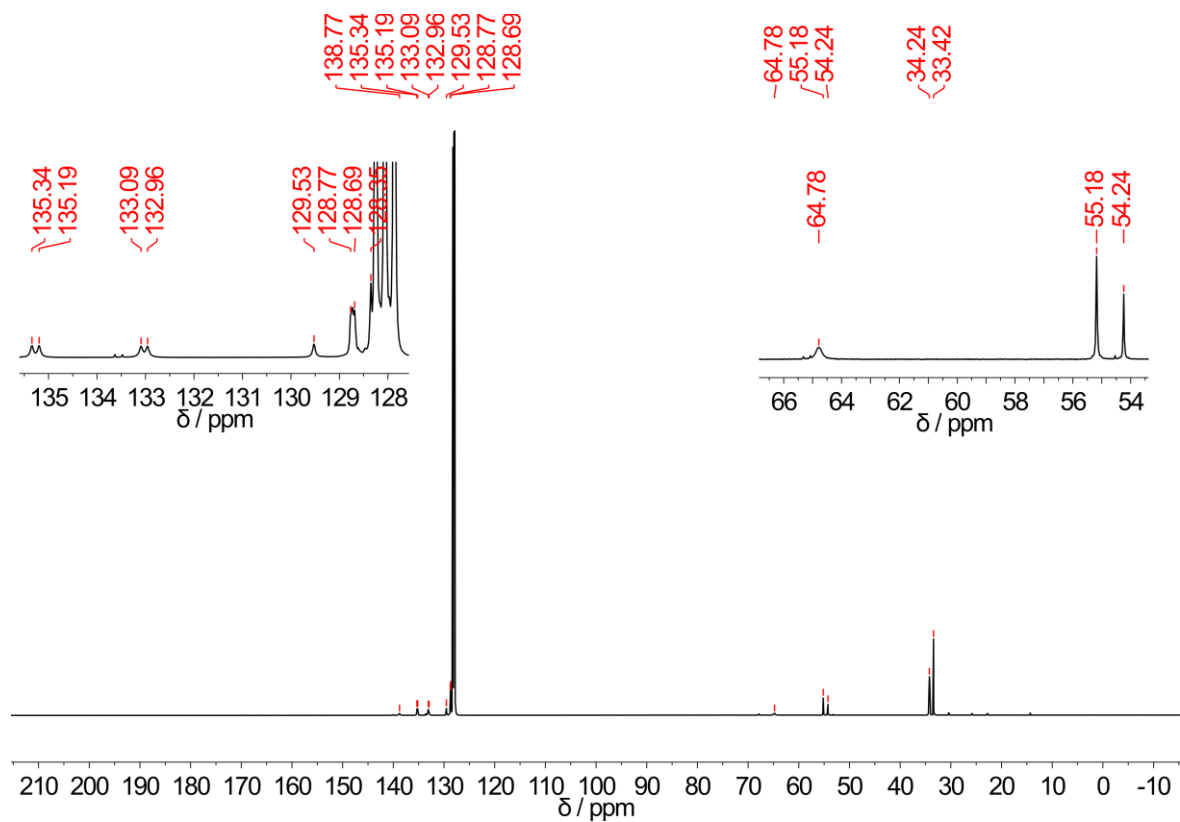


Figure 6-30 $^{13}\text{C}\{^1\text{H}\}$ -NMR of **12e** at 298 K in C_6D_6 .

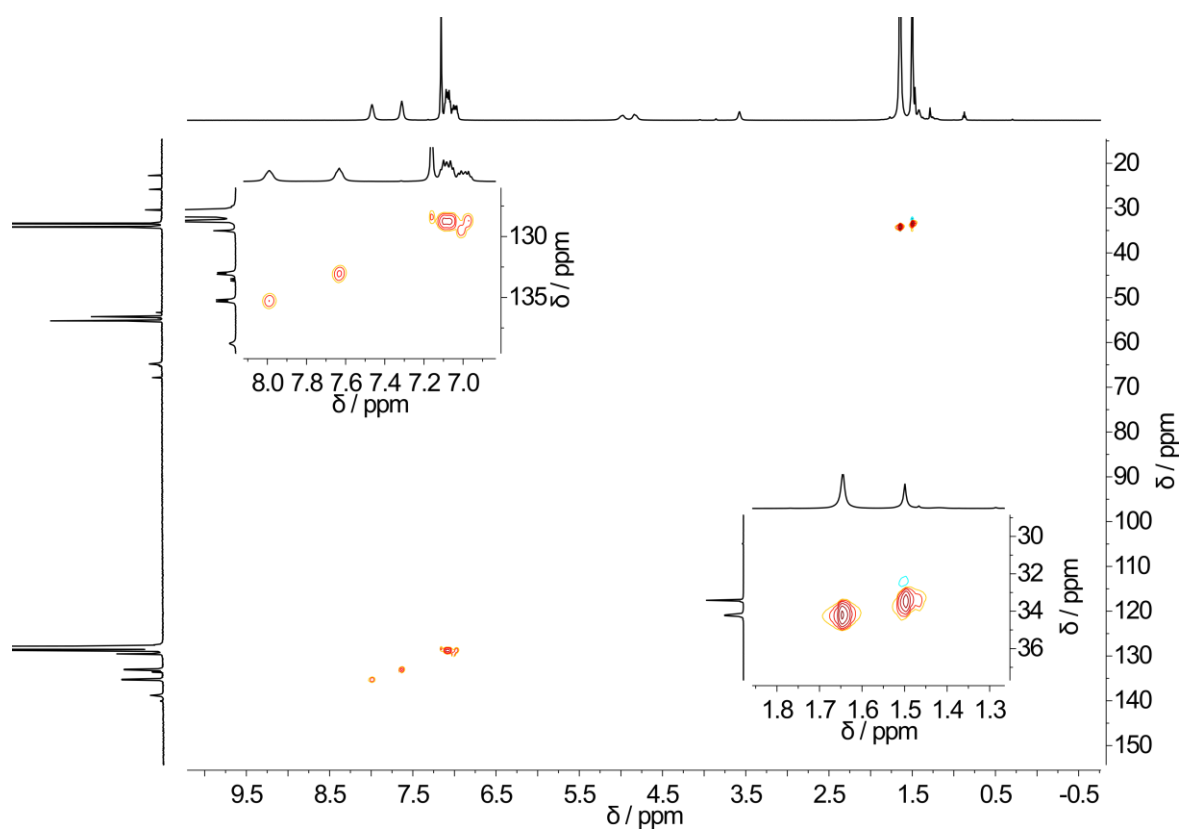


Figure 6-31 $^{13}\text{C}/^1\text{H}$ -HSQC-NMR of **12e** at 298 K in C_6D_6 .

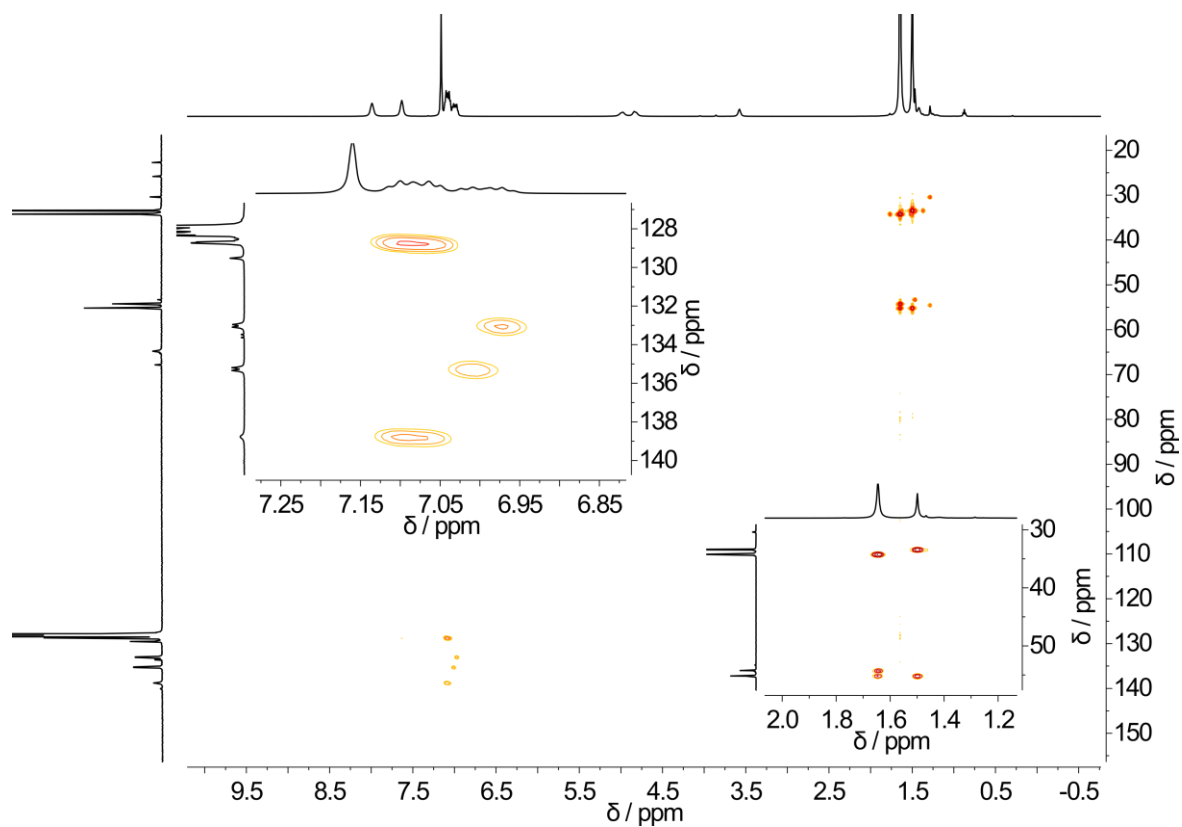


Figure 6-32 $^{13}\text{C}/^1\text{H}$ -HMBC-NMR of **12e** at 298 K in C_6D_6 .

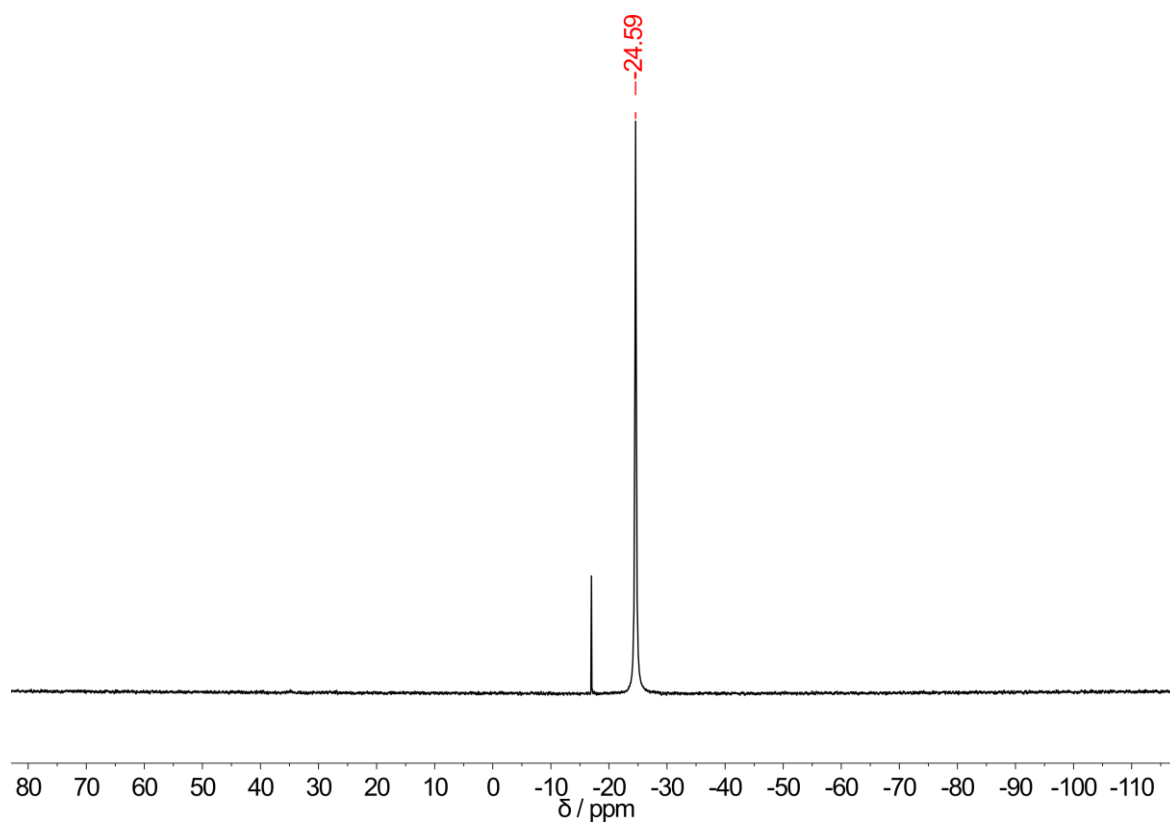


Figure 6-33 $^{31}\text{P}\{^1\text{H}\}$ -NMR of **12e** at 298 K in C_6D_6 .

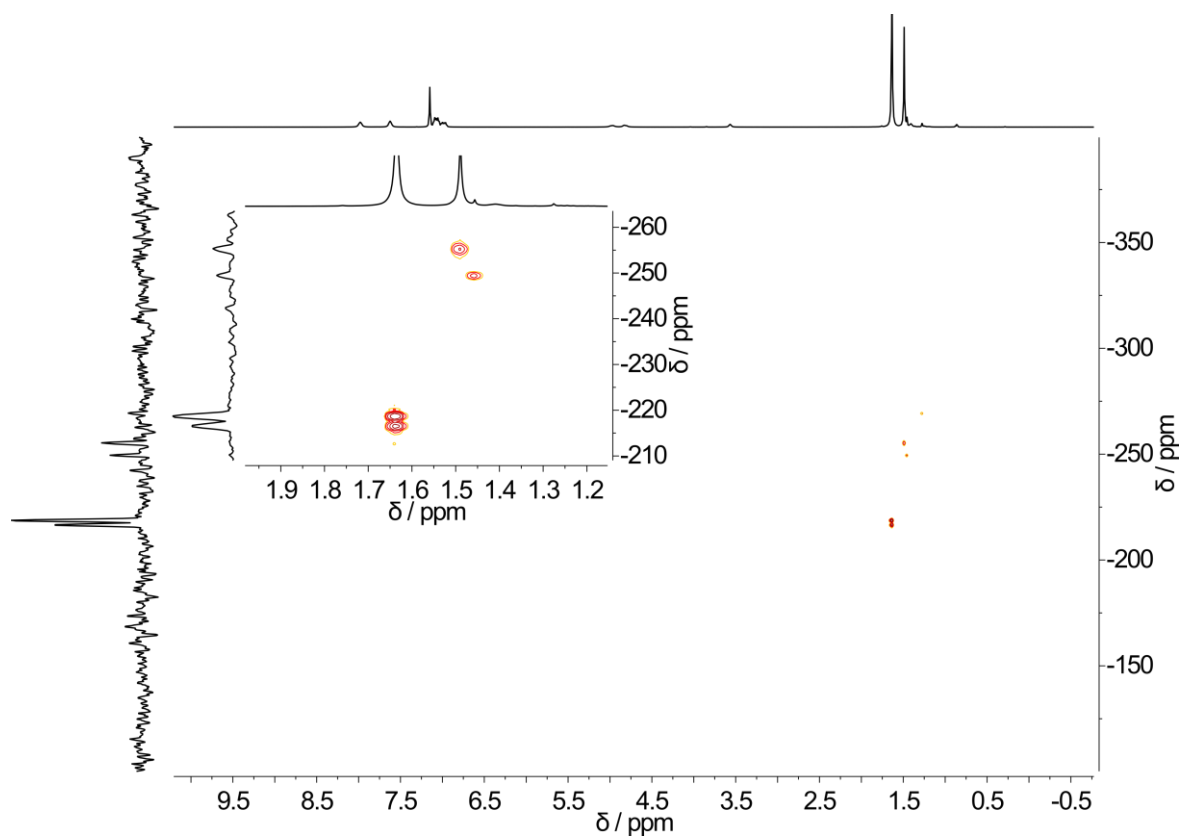


Figure 6-34 $^{15}\text{N}/^1\text{H}$ -HMBC-NMR of **12e** at 298 K in C_6D_6 .

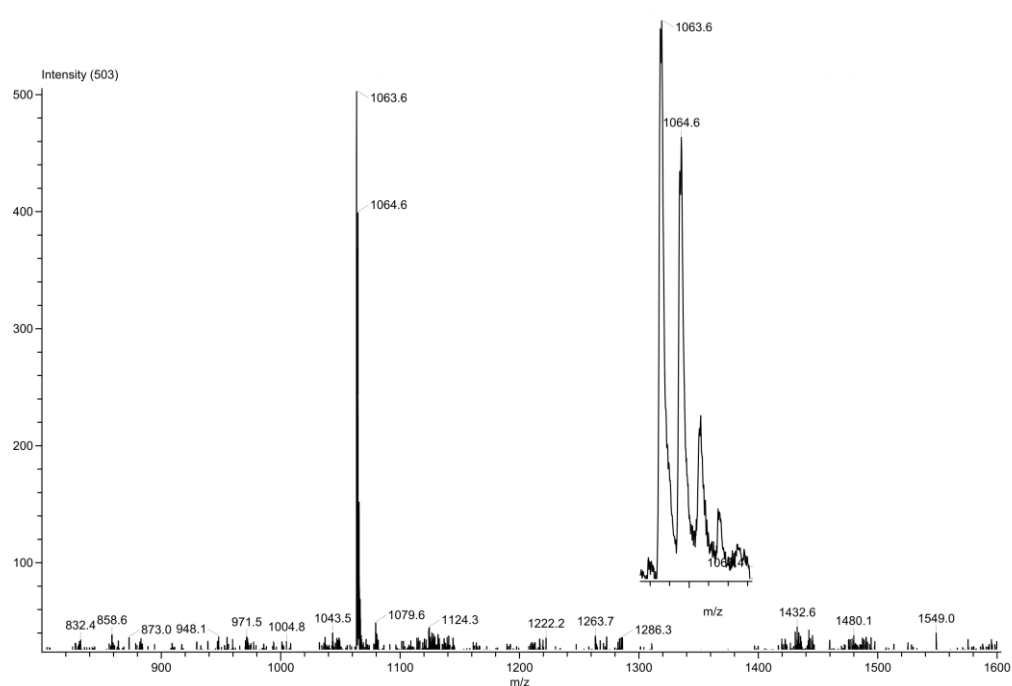


Figure 6-35 LIFDI mass spectrum of **12e** from a thf solution with expected m/z of 1063.5 $[M-Cl]^+$ and the corresponding isotope pattern.

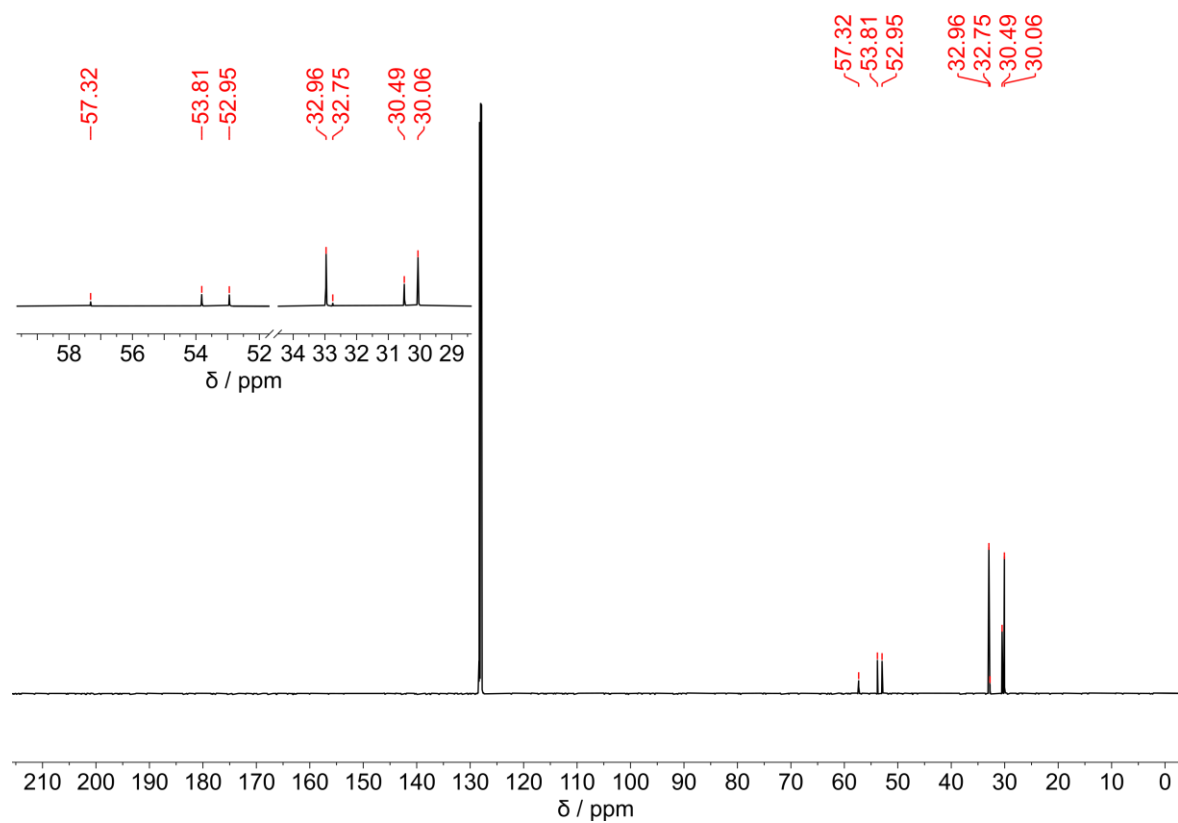


Figure 6-36 $^{13}C\{^1H\}$ -NMR of **13** at 298 K in C_6D_6 .

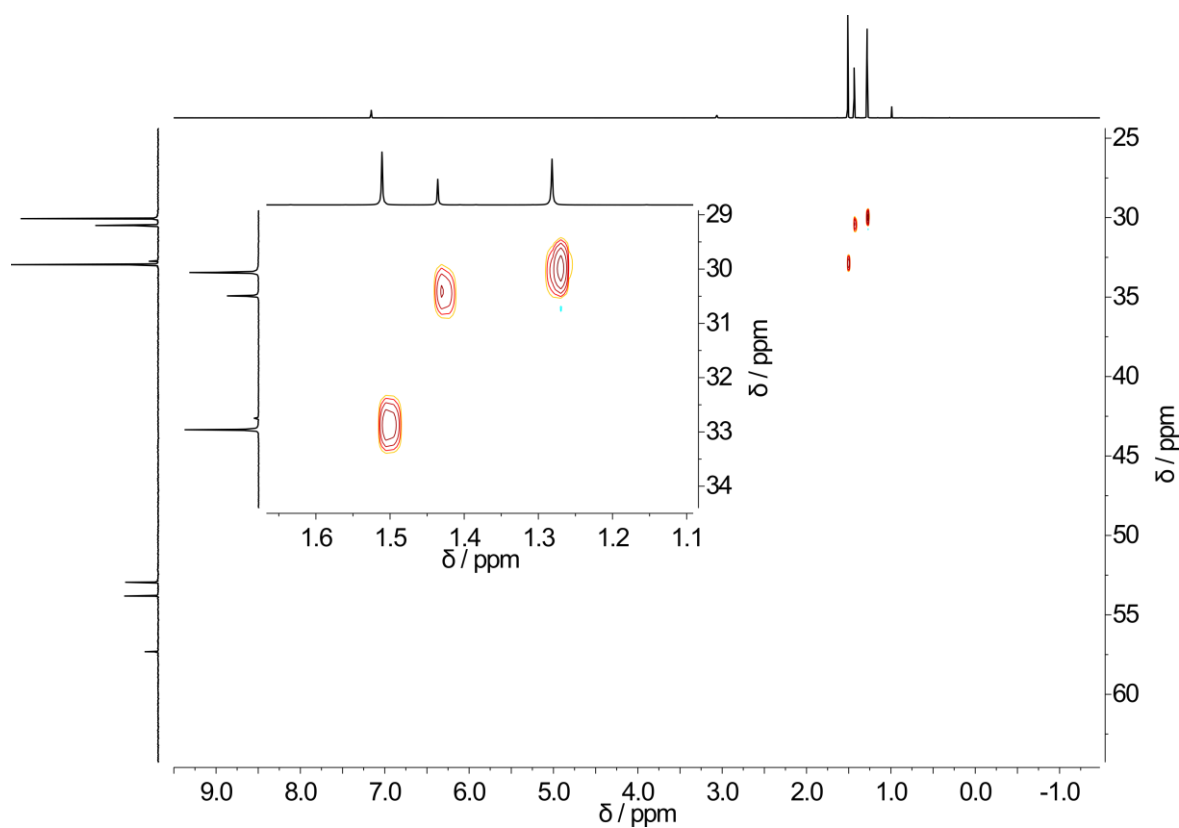


Figure 6-37 $^{13}\text{C}/^1\text{H}$ -HSQC-NMR of **13** at 298 K in C_6D_6 .

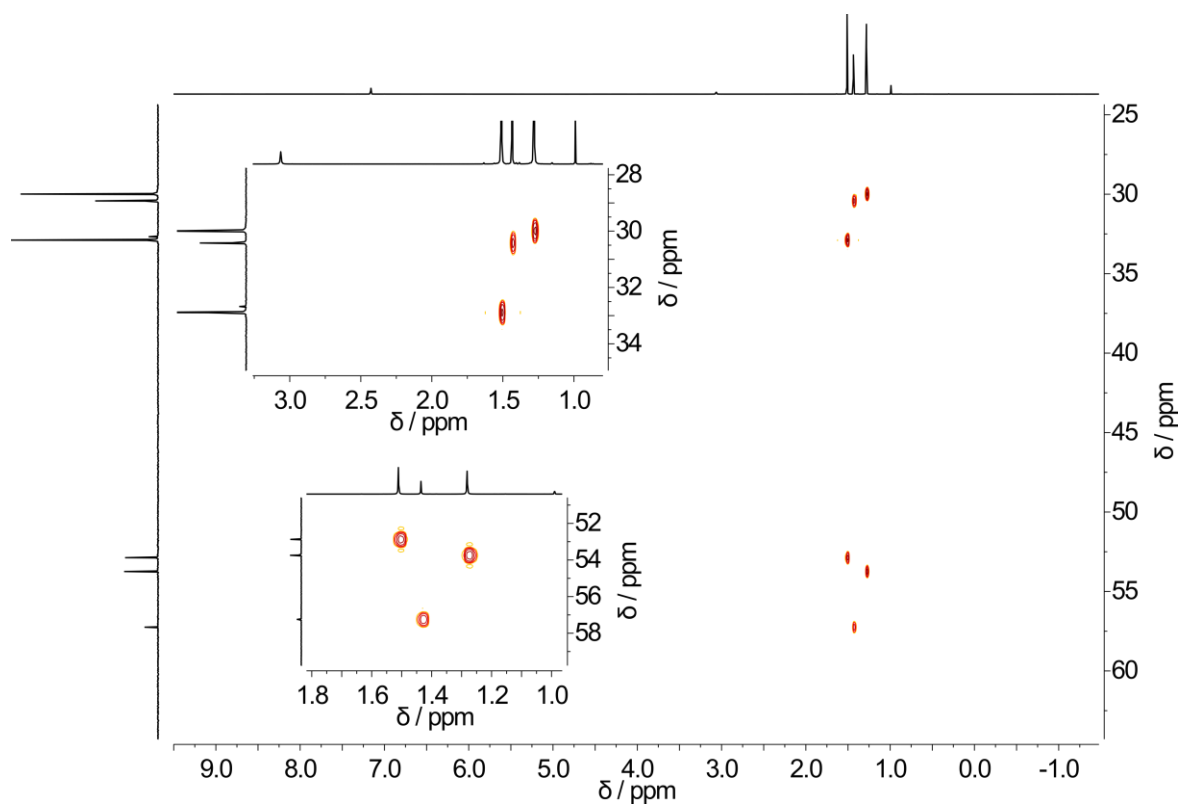


Figure 6-38 $^{13}\text{C}/^1\text{H}$ -HMBC-NMR of **13** at 298 K in C_6D_6 .

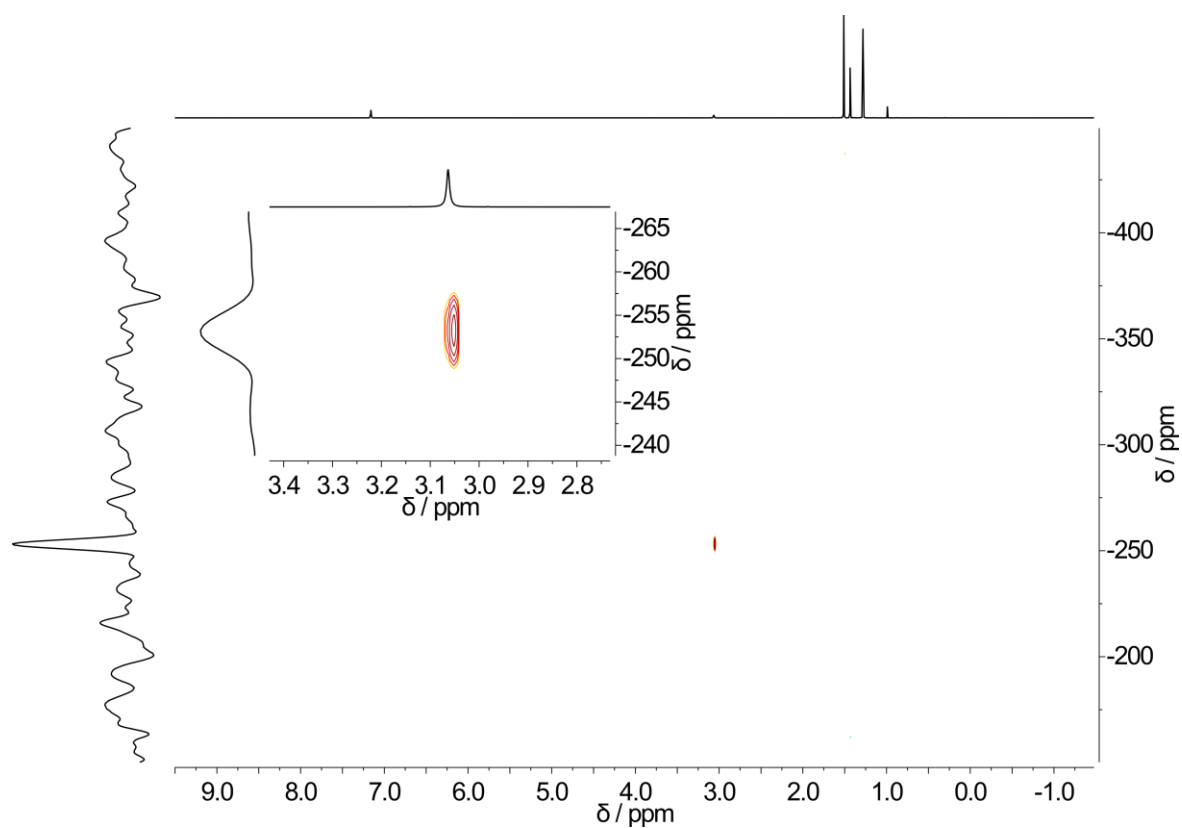


Figure 6-39 $^{15}\text{N}/^1\text{H}$ -HSQC-NMR of **13** at 298 K in C_6D_6 .

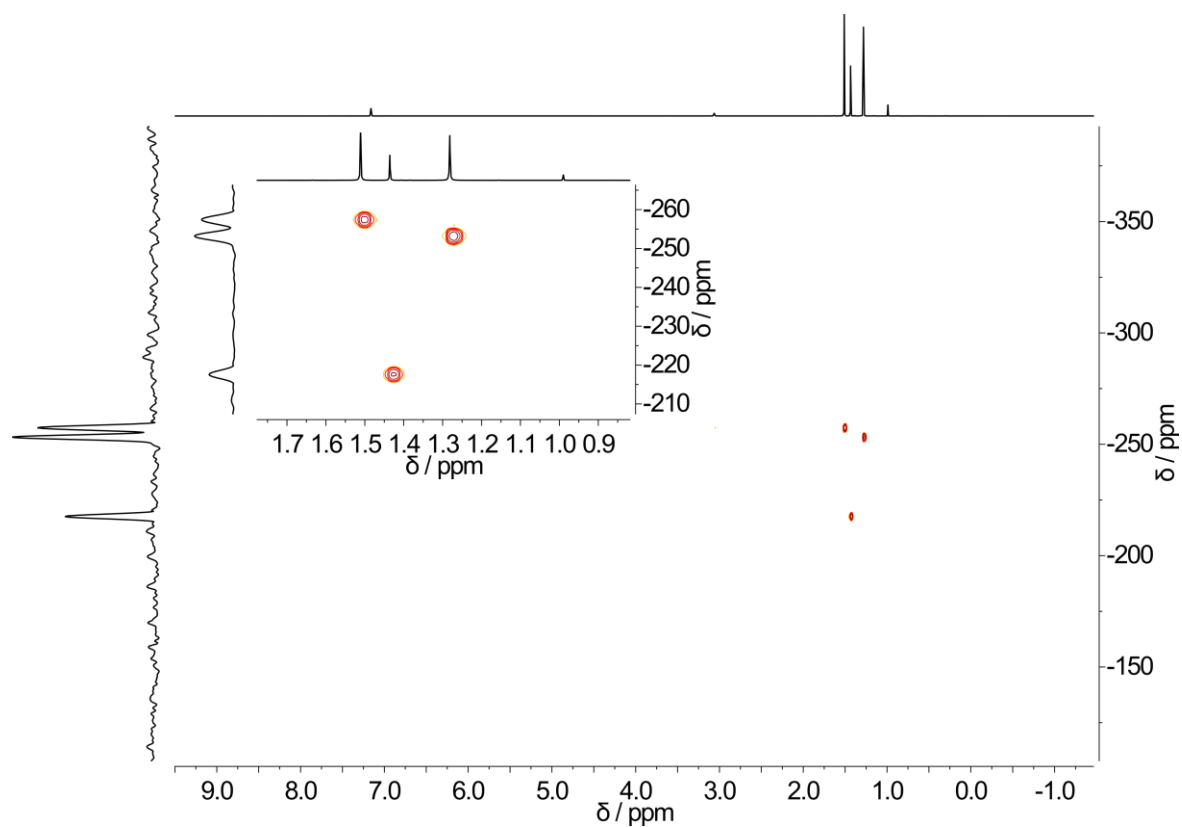


Figure 6-40 $^{15}\text{N}/^1\text{H}$ -HMBC-NMR of **13** at 298 K in C_6D_6 .

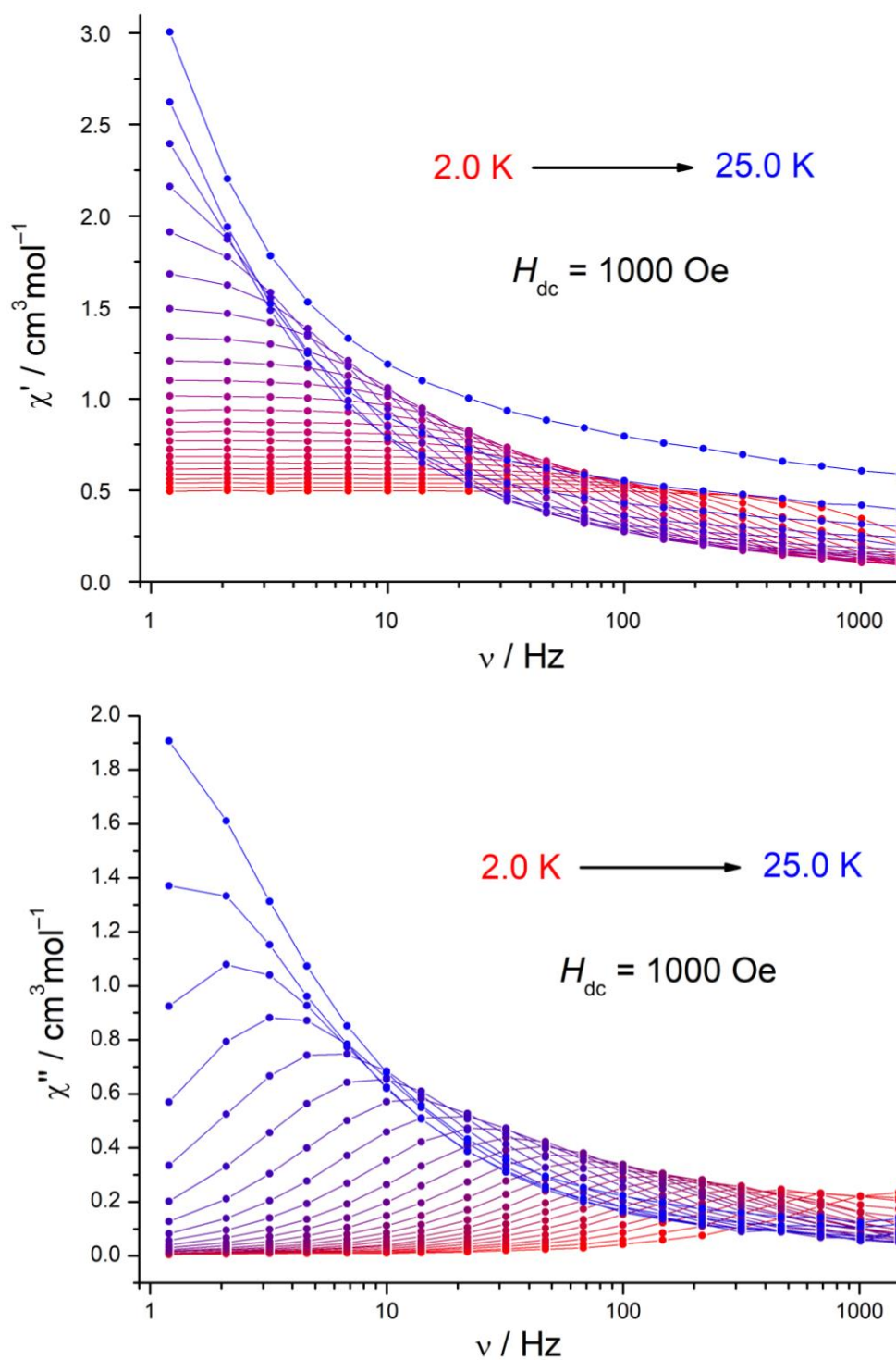


Figure 6-41 Variable-frequency variable-temperature in-phase (χ'_M) and out-of-phase (χ''_M) ac magnetic susceptibility measurements for **12a** under an applied dc field of $H_{dc} = 1000$ Oe.

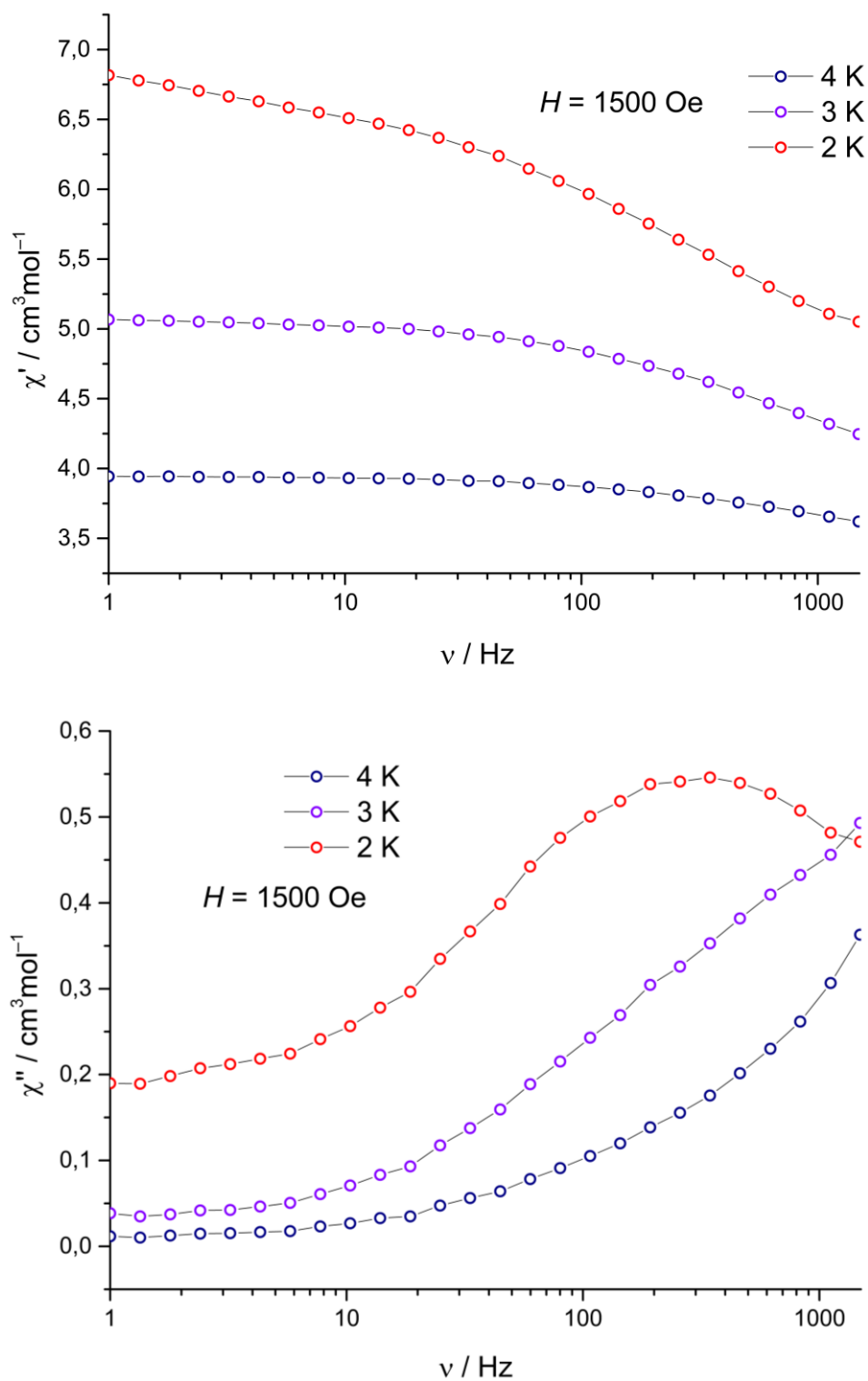


Figure 6-42 Variable-frequency variable-temperature in-phase (χ'_M) and out-of-phase (χ''_M) ac magnetic susceptibility measurements for **12c** under an applied dc field of $H_{dc} = 1500$ Oe.

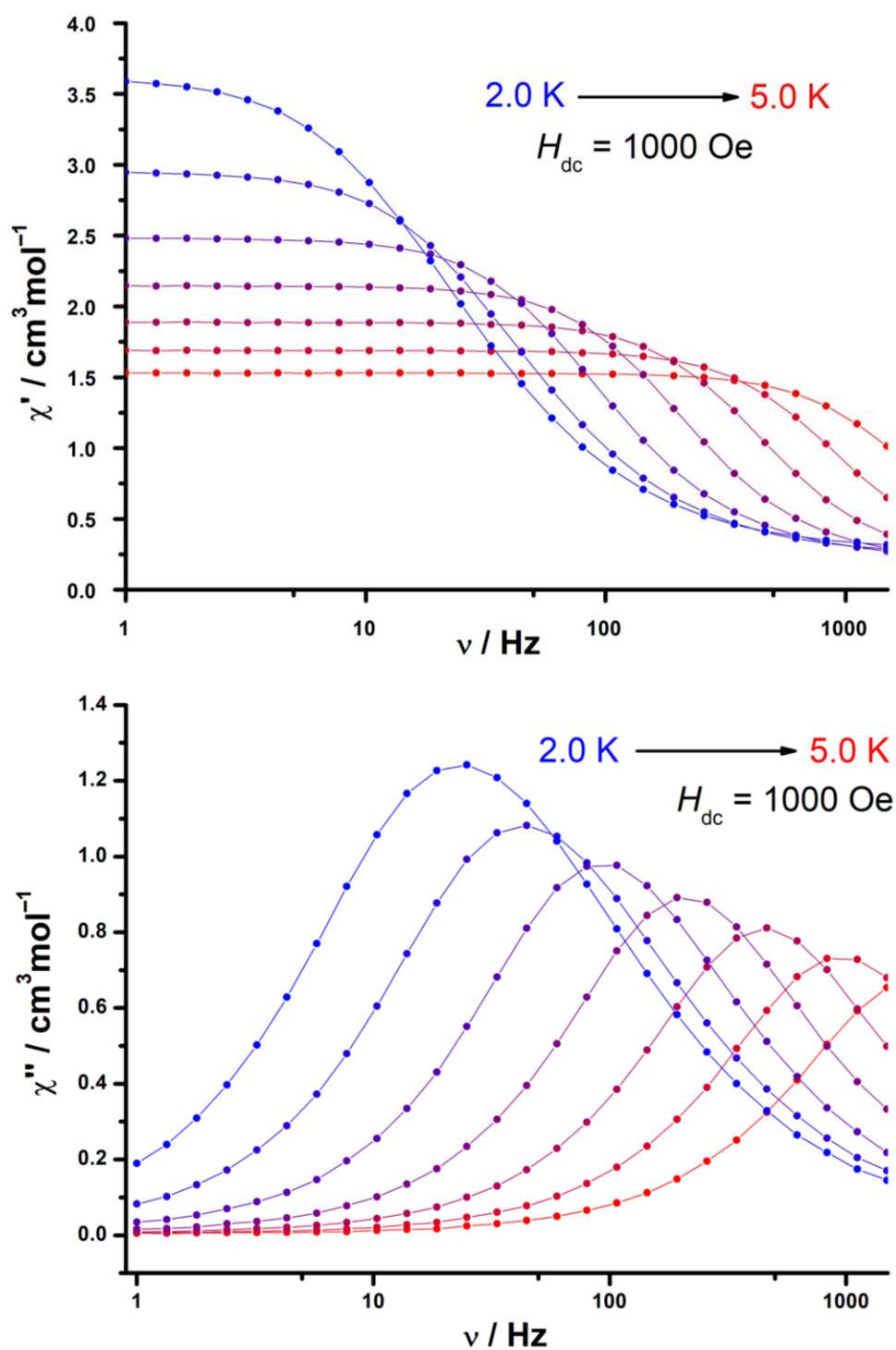


Figure 6-43 Variable-frequency variable-temperature in-phase (χ'_M) and out-of-phase (χ''_M) ac magnetic susceptibility measurements for **12d** under an applied dc field of $H_{dc} = 1000$ Oe.

7. References

- [1] J. Jung, A. Münch, R. Herbst-Irmer, D. Stalke, *Angew. Chem. Int. Ed.* **2021**, *60*, 5679; *Angew. Chem.*, **2021**, *133*, 5742.
- [2] J. Jung, C. M. Legendre, R. Herbst-Irmer, D. Stalke, *Inorganic chemistry* **2021**, *60*, 967.
- [3] J. Jung, F. Benner, R. Herbst-Irmer, S. Demir, D. Stalke, *Chem. Eur. J.* **2021**, *27*, 12310.
- [4] J. Jung, C. M. Legendre, S. Demeshko, R. Herbst-Irmer, D. Stalke, *Inorg. Chem.* **2021**, *60*, 9580.
- [5] J. Jung, C. M. Legendre, S. Demeshko, R. Herbst-Irmer, D. Stalke, *Dalton Trans.* **2021**, *50*, 17194.
- [6] M. Gregory, *J. Pharm.* **1835**, *21*, 315.
- [7] M.-J. Fordos, A. Gélis, *Compt. Rend.* **1850**, *31*, 702.
- [8] R. Schenck, *Liebigs Ann. Chem.* **1896**, *290*, 171.
- [9] M. H. M. Arnold, J. A. C. Hugill, J. M. Hutson, *J. Chem. Soc.* **1936**, 1645.
- [10] M. Goehring, *Chem. Ber.* **1947**, *80*, 110.
- [11] D. Clark, *J. Chem. Soc.* **1952**, 1615.
- [12] B. D. Sharma, J. Donohue, *Acta Cryst* **1963**, *16*, 891.
- [13] F. P. Burt, *J. Chem. Soc., Trans.* **1910**, *97*, 1171.
- [14] M. Goehring, D. Voigt, *Naturwissenschaften* **1953**, *40*, 482.
- [15] V. V. Walatka, M. M. Labes, J. H. Perlstein, *Phys. Rev. Lett.* **1973**, *31*, 1139.
- [16] C.-h. Hsu, M. M. Labes, *J. Chem. Phys.* **1974**, *61*, 4640.
- [17] R. L. Greene, G. B. Street, L. J. Suter, *Phys. Rev. Lett.* **1975**, *34*, 577.
- [18] M. M. Labes, P. Love, L. F. Nichols, *Chem. Rev.* **1979**, *79*, 1.
- [19] M. Goehring, G. Weis, *Angew. Chem.* **1956**, *68*, 678.
- [20] U. Wannagat, H. Kuckertz, *Angew. Chem. Int. Ed.* **1962**, *1*, 113; *Angew. Chem.* **1962**, *74*, 117.
- [21] D. H. Clemens, A. J. Bell, J. L. O'Brien, *Tetrahedron Lett.* **1965**, *6*, 1491.
- [22] D. H. Clemens, A. J. Bell, J. L. O'Brien, *Tetrahedron Lett.* **1965**, *6*, 1487.
- [23] O. Glemser, R. Mews, *Angew. Chem. Int. Ed.* **1980**, *19*, 883; *Angew. Chem.* **1980**, *92*, 904.
- [24] R. Mews, O. Glemser, *Inorg. Chem.* **1972**, *11*, 2521.
- [25] O. Glemser, H. Schröder, *Z. Anorg. Allg. Chem.* **1956**, *284*, 97.
- [26] O. Glemser, J. Wegener, *Angew. Chem Int. Ed.* **1970**, *9*, 309; *Angew. Chem.* **1970**, *82*, 324.
- [27] R. Appel, B. Ross, *Angew. Chem. Int. Ed.* **1968**, *7*, 546; *Angew. Chem.* **1968**, *80*, 561.
- [28] O. Glemser, S. Pohl, F.-M. Tesky, R. Mews, *Angew. Chem. Int. Ed.* **1977**, *16*, 789; *Angew. Chem.* **1977**, *89*, 829.
- [29] W. Lidy, W. Sundermeyer, W. Verbeek, *Z. Anorg. Allg. Chem.* **1974**, *406*, 228.
- [30] R. Mews, P. G. Watson, E. Lork, *Coord. Chem. Rev.* **1997**, *158*, 233.

- [31] R. Fleischer, S. Freitag, F. Pauer, D. Stalke, *Angew. Chem. Int. Ed.*, **1996**, *35*, 204; *Angew. Chem.* **1996**, *108*, 208.
- [32] R. Fleischer, A. Rothenberger, D. Stalke, *Angew. Chem. Int. Ed.* **1997**, *36*, 1105; *Angew. Chem.*, **1997**, *109*, 1140.
- [33] R. Fleischer, S. Freitag, D. Stalke, *Dalton Trans.* **1998**, 193.
- [34] R. Fleischer, D. Stalke, *Coord. Chem. Rev.* **1998**, *176*, 431.
- [35] D. Stalke, *Chem. Commun.* **2012**, *48*, 9559.
- [36] R. Fleischer, B. Walfort, A. Gbureck, P. Scholz, W. Kiefer, D. Stalke, *Chem. Eur. J.* **1998**, *4*, 2266.
- [37] D. Stalke, *Proc. Indian Acad. Sci. (Chem. Sci.)* **2000**, *112*, 155.
- [38] I. Mayer, *Journal of Molecular Structure: THEOCHEM* **1987**, *149*, 81.
- [39] S. Pohl, B. Krebs, U. Seyer, G. Henkel, *Chem Ber* **1979**, *112*, 1751.
- [40] J. A. Dobado, H. Martínez-García, Molina, M. R. Sundberg, *J. Am. Chem. Soc.* **1998**, *120*, 8461.
- [41] A. E. Reed, P. v. R. Schleyer, *J. Am. Chem. Soc.* **1990**, *112*, 1434.
- [42] A. E. Reed, F. Weinhold, *J. Am. Chem. Soc.* **1986**, *108*, 3586.
- [43] D. A. Bors, A. Streitwieser, *J. Am. Chem. Soc.* **1986**, *108*, 1397.
- [44] W. Kutzelnigg, *Angew. Chem. Int. Ed.* **1984**, *23*, 272; *Angew. Chem.*, **1984**, *96*, 262.
- [45] J. Cioslowski, P. R. Surján, *Journal of Molecular Structure: THEOCHEM* **1992**, *255*, 9.
- [46] J. Cioslowski, S. T. Mixon, *Inorg. Chem.* **1993**, *32*, 3209.
- [47] R. E. Rundle, *J. Am. Chem. Soc.* **1947**, *69*, 1327.
- [48] R. E. Rundle, *J. Chem. Phys.* **1949**, *17*, 671.
- [49] B. Walfort, A. P. Leedham, C. A. Russell, D. Stalke, *Inorg. Chem.* **2001**, *40*, 5668.
- [50] D. Leusser, J. Henn, N. Kocher, B. Engels, D. Stalke, *J. Am. Chem. Soc.* **2004**, *126*, 1781.
- [51] J. Henn, D. Ilge, D. Leusser, D. Stalke, B. Engels, *J. Phys. Chem. A* **2004**, *108*, 9442.
- [52] D. Leusser, B. Walfort, D. Stalke, *Angew. Chem. Int. Ed.* **2002**, *41*, 2079; *Angew. Chem.*, **2002**, *114*, 2183.
- [53] S. L. Hinchley, P. Trickey, H. E. Robertson, B. A. Smart, D. W. H. Rankin, D. Leusser, B. Walfort, D. Stalke, M. Buhl, S. J. Obrey, *J. Chem. Soc., Dalton Trans.* **2002**, 4607.
- [54] J. Henn, D. Leusser, D. Stalke, *J. Comput. Chem.* **2007**, *28*, 2317.
- [55] S. Deuerlein, D. Leusser, U. Flierler, H. Ott, D. Stalke, *Organometallics* **2008**, *27*, 2306.
- [56] M. S. Schmøkel, S. Cenedese, J. Overgaard, M. R. V. Jørgensen, Y.-S. Chen, C. Gatti, D. Stalke, B. Iversen, *Inorg. Chem.* **2012**, *51*, 8607.
- [57] M. Fugel, L. A. Malaspina, R. Pal, S. P. Thomas, M. W. Shi, M. A. Spackman, K. Sugimoto, S. Grabowsky, *Chem. Eur. J.* **2019**, *25*, 6523.
- [58] I. Langmuir, *J. Am. Chem. Soc.* **1919**, *41*, 1543.

- [59] A. F. Holleman, E. Wiberg, N. Wiberg, *Lehrbuch der Anorganischen Chemie.*, 102. Aufl., Walter de Gruyter, Berlin, **2007**.
- [60] T. Chivers, R. S. Laitinen, *Chem. Soc. Rev.* **2017**, *46*, 5182.
- [61] J. K. Brask, T. Chivers, *Angew. Chem. Int. Ed.*, **2001**, *40*, 3960; *Angew. Chem.* **2001**, *113*, 4082.
- [62] P. P. Power, *Chem. Rev.* **2003**, *103*, 789.
- [63] J. K. Brask, T. Chivers, B. McGarvey, G. Schatte, R. Sung, R. T. Boéré, *Inorg. Chem.* **1998**, *37*, 4633.
- [64] Christina M. Legendre, *Magneto-structural correlations in molecular magnets containing the S–N motive*, Göttingen, **2021**.
- [65] D. Ilge, D. S. Wright, D. Stalke, *Chem. Eur. J.* **1998**, *4*, 2275.
- [66] R. Fleischer, D. Stalke, *Organometallics* **1998**, *17*, 832.
- [67] B. Walfort, T. Auth, B. Degel, H. Helten, D. Stalke, *Organometallics* **2002**, *21*, 2208.
- [68] E. Carl, D. Stalke, *Chem. Eur. J.* **2014**, *20*, 15849.
- [69] M. M. Meinholz, S. K. Pandey, S. M. Deuerlein, D. Stalke, *Dalton Trans.* **2011**, *40*, 1662.
- [70] S. Trofimenko, *Chem. Rev.* **1993**, *93*, 943.
- [71] S. Trofimenko, *J. Am. Chem. Soc.* **1966**, *88*, 1842.
- [72] S. Trofimenko, *J. Am. Chem. Soc.* **1967**, *89*, 3170.
- [73] K. Niedenzu, S. Trofimenko in *Topics in current chemistry Fortschritte der chemischen Forschung, Vol. 131* (Hrsg.: N. V. Alekseev, G. Heller, K. Niedenzu), Springer-Verlag, Berlin, Heidelberg, New York, **1986**, S. 1–37.
- [74] J. C. Calabrese, S. Trofimenko, J. S. Thompson, *J. Chem. Soc., Chem. Commun.* **1986**, 1122.
- [75] D. L. Reger, J. R. Gardinier, W. R. Gemmill, M. D. Smith, A. M. Shahin, G. J. Long, L. Rebbouh, F. Grandjean, *J. Am. Chem. Soc.* **2005**, *127*, 2303.
- [76] S. Trofimenko, J. C. Calabrese, J. S. Thompson, *Inorg. Chem.* **1987**, *26*, 1507.
- [77] A. A. Barney, A. F. Heyduk, D. G. Nocera, *Chem. Commun.* **1999**, 2379.
- [78] T. A. Betley, J. C. Peters, *Inorg. Chem.* **2003**, *42*, 5074.
- [79] M. A. Casado, V. Hack, J. A. Camerano, M. A. Ciriano, C. Tejel, L. A. Oro, *Inorg. Chem.* **2005**, *44*, 9122.
- [80] J. A. Camerano, M. A. Casado, M. A. Ciriano, C. Tejel, L. A. Oro, *Chem. Eur. J.* **2008**, *14*, 1897.
- [81] M. M. Meinholz, D. Stalke, *Eur. J. Inorg. Chem.* **2011**, *2011*, 4578.
- [82] R. G. Pearson, *J. Am. Chem. Soc.* **1963**, *85*, 3533.
- [83] R. G. Parr, R. G. Pearson, *J. Am. Chem. Soc.* **1983**, *105*, 7512.
- [84] R. G. Pearson, *J. Am. Chem. Soc.* **1985**, *107*, 6801.
- [85] T. Pugh, V. Vieru, L. F. Chibotaru, R. A. Layfield, *Chem. Sci.* **2016**, *7*, 2128.

- [86] L. E. Darago, M. D. Boshart, B. D. Nguyen, E. Perlt, J. W. Ziller, W. W. Lukens, F. Furche, W. J. Evans, J. R. Long, *J. Am. Chem. Soc.* **2021**, *143*, 8465.
- [87] C. M. Legendre, E. Damgaard-Møller, J. Overgaard, D. Stalke, *Eur. J. Inorg. Chem.* **2021**, 3108.
- [88] T. Pugh, F. Tuna, L. Ungur, D. Collison, E. J. L. McInnes, L. F. Chibotaru, R. A. Layfield, *Nat. Commun.* **2015**, *6*, 7492.
- [89] T. Pugh, N. F. Chilton, R. A. Layfield, *Chem. Sci.* **2017**, *8*, 2073.
- [90] J. M. Zadrozny, J. R. Long, *J. Am. Chem. Soc.* **2011**, *133*, 20732.
- [91] P. Evans, D. Reta, G. F.S. Whitehead, N. F. Chilton, D. P. Mills, *J. Am. Chem. Soc.* **2019**, *141*, 19935.
- [92] P.-H. Lin, N. C. Smythe, S. I. Gorelsky, S. Maguire, N. J. Henson, I. Korobkov, B. L. Scott, J. C. Gordon, R. T. Baker, M. Murugesu, *J. Am. Chem. Soc.* **2011**, *133*, 15806.
- [93] A. Eichhöfer, Y. Lan, V. Mereacre, T. Bodenstein, F. Weigend, *Inorg. Chem.* **2014**, *53*, 1962.
- [94] T. J. Pearson, M. S. Fataftah, D. E. Freedman, *Chem. Commun.* **2016**, 52, 11394.
- [95] J. M. Zadrozny, J. Telser, J. R. Long, *Polyhedron* **2013**, *64*, 209.
- [96] S.-M. Chen, J. Xiong, Y.-Q. Zhang, Q. Yuan, B.-W. Wang, S. Gao, *Chem. Sci.* **2018**, *9*, 7540.
- [97] B. Walfort, R. Bertermann, D. Stalke, *Chem. Eur. J.* **2001**, *7*, 1424.
- [98] T. Schulz, D. Stalke, *Eur. J. Inorg. Chem.* **2010**, 2185.
- [99] C. Selinka, D. Stalke, *Eur. J. Inorg. Chem.* **2003**, 3376.
- [100] J. Matussek, R. Herbst-Irmer, D. Stalke, *Eur. J. Inorg. Chem.* **2015**, 2015, 166.
- [101] C. Selinka, S. Deuerlein, T. Häuser, D. Stalke, *Inorg. Chim. Acta* **2004**, *357*, 1873.
- [102] C. Selinka, D. Stalke, *Z. Naturforsch. B* **2003**, *58*, 291.
- [103] J. T. E. Meyer, T. Schulz, S. K. Pandey, D. Stalke, *Inorg. Chem.* **2010**, *49*, 2743.
- [104] T. Schulz, S. Deuerlein, D. Stalke, *Eur. J. Inorg. Chem.* **2010**, 2178.
- [105] E. Carl, D. Stalke, *Eur. J. Inorg. Chem.* **2015**, 2015, 2052.
- [106] J. Matussek, R. Herbst-Irmer, I. Objartel, D. Stalke, *Dalton Trans.* **2014**, 43, 15944.
- [107] E. Carl, S. Demeshko, F. Meyer, D. Stalke, *Chem. Eur. J.* **2015**, *21*, 10109.
- [108] T. Gehrmann, M. Kruck, H. Wadepohl, L. H. Gade, *Chem. Commun.* **2012**, 48, 2397.
- [109] M. Bayram, D. Bläser, C. Wölper, S. Schulz, *Organometallics* **2015**, *34*, 3421.
- [110] S. V. Klementyeva, N. P. Gritsan, M. M. Khusniyarov, A. Witt, A. A. Dmitriev, E. A. Sutura, N. D. D. Hill, T. L. Roemmele, M. T. Gamer, R. T. Boéré, P. W. Roesky, A. V. Zibarev, S. N. Konchenko, *Chem. Eur. J.* **2017**, *23*, 1278.
- [111] F. Knösel, M. Noltemeyer, F. T. Edelmann, *Z. Naturforsch. B* **1989**, *44*, 1171.
- [112] T. Chivers, *A guide to chalcogen-nitrogen chemistry*, World Scientific, **2005**.
- [113] D. Gatteschi, R. Sessoli, J. Villain, *Molecular Nanomagnets*, Oxford Univ. Press, Oxford, **2006**.

- [114] M. Mannini, F. Pineider, P. Saintavitt, C. Danieli, E. Otero, C. Sciancalepore, A. M. Talarico, M.-A. Arrio, A. Cornia, D. Gatteschi, R. Sessoli, *Nat Mater* **2009**, *8*, 194.
- [115] R. Sessoli, D. Gatteschi, A. Caneschi, M. A. Novak, *Nature* **1993**, *365*, 141.
- [116] H. Coufal, L. Dhar, C. D. Mee, *MRS Bull.* **2006**, *31*, 374.
- [117] F. Donati, S. Rusponi, S. Stepanow, C. Wäckerlin, A. Singha, L. Persichetti, R. Baltic, K. Diller, F. Patthey, E. Fernandes, J. Dreiser, Ž. Šljivančanin, K. Kummer, C. Nistor, P. Gambardella, H. Brune, *Science* **2016**, *352*, 318.
- [118] M. N. Leuenberger, D. Loss, *Nature* **2001**, *410*, 789.
- [119] G. Aromí, D. Aguilà, P. Gamez, F. Luis, O. Roubeau, *Chem. Soc. Rev.* **2012**, *41*, 537.
- [120] M. J. Graham, J. M. Zadrozny, M. S. Fataftah, D. E. Freedman, *Chem. Mater.* **2017**, *29*, 1885.
- [121] A. Gaita-Ariño, F. Luis, S. Hill, E. Coronado, *Nat. Chem.* **2019**, *11*, 301.
- [122] L. Bogani, W. Wernsdorfer, *Nat Mater* **2008**, *7*, 179.
- [123] E. Coronado, *Nat Rev Mater* **2020**, *5*, 87.
- [124] M. Cinchetti, V. A. Dediu, L. E. Hueso, *Nature Materials* **2017**, *16*, 507.
- [125] K. V. Raman, A. M. Kamerbeek, A. Mukherjee, N. Atodiresei, T. K. Sen, P. Lazić, V. Caciuc, R. Michel, D. Stalke, S. K. Mandal, S. Blügel, M. Münzenberg, J. S. Moodera, *Nature* **2013**, *493*, 509.
- [126] H. L.C. Feltham, S. Brooker, *Coord. Chem. Rev.* **2014**, *276*, 1.
- [127] O. Kahn, *Molecular Magnetism*, Wiley-VCH, New York, **1993**.
- [128] A. Caneschi, D. Gatteschi, R. Sessoli, A. L. Barra, L. C. Brunel, M. Guillot, *J. Am. Chem. Soc.* **1991**, *113*, 5873.
- [129] R. Sessoli, H. L. Tsai, A. R. Schake, S. Wang, J. B. Vincent, K. Folting, D. Gatteschi, G. Christou, D. N. Hendrickson, *J. Am. Chem. Soc.* **1993**, *115*, 1804.
- [130] S. M. J. Aubin, M. W. Wemple, D. M. Adams, H.-L. Tsai, G. Christou, D. N. Hendrickson, *J. Am. Chem. Soc.* **1996**, *118*, 7746.
- [131] W.-P. Chen, J. Singleton, L. Qin, A. Camón, L. Engelhardt, F. Luis, R. E. P. Winpenny, Y.-Z. Zheng, *Nat. Commun.* **2018**, *9*, 2107.
- [132] A. M. Ako, I. J. Hewitt, V. Mereacre, R. Clérac, W. Wernsdorfer, C. E. Anson, A. K. Powell, *Angew. Chem. Int. Ed.* **2006**, *45*, 4926; *Angew. Chem.* **2006**, *118*, 5048.
- [133] C. J. Milios, A. Vinslava, W. Wernsdorfer, S. Moggach, S. Parsons, S. P. Perlepes, G. Christou, E. K. Brechin, *J. Am. Chem. Soc.* **2007**, *129*, 2754.
- [134] O. Waldmann, *Inorg. Chem.* **2007**, *46*, 10035.
- [135] F. Neese, D. A. Pantazis, *Faraday Discuss.* **2011**, *148*, 229–38; discussion 299–314.
- [136] E. Ruiz, J. Cirera, J. Cano, S. Alvarez, C. Loose, J. Kortus, *Chem. Commun.* **2008**, 52.
- [137] J. M. Frost, K. L. M. Harriman, M. Murugesu, *Chem. Sci.* **2016**, *7*, 2470.

- [138] G. Christou, D. Gatteschi, D. N. Hendrickson, R. Sessoli, *MRS Bull.* **2000**, *25*, 66.
- [139] G. A. Craig, M. Murrie, *Chem. Soc. Rev.* **2015**, *44*, 2135.
- [140] A. Sarkar, S. Dey, G. Rajaraman, *Chem. Eur. J.* **2020**, 14036.
- [141] D. E. Freedman, W. H. Harman, T. D. Harris, G. J. Long, C. J. Chang, J. R. Long, *J. Am. Chem. Soc.* **2010**, *132*, 1224.
- [142] N. F. Chilton, *Inorg. Chem.* **2015**, *54*, 2097.
- [143] J. D. Rinehart, J. R. Long, *Chem. Sci.* **2011**, *2*, 2078.
- [144] D. N. Woodruff, R. E. P. Winpenny, R. A. Layfield, *Chem. Rev.* **2013**, *113*, 5110.
- [145] J.-L. Liu, Y.-C. Chen, M.-L. Tong, *Chem. Soc. Rev.* **2018**, *47*, 2431.
- [146] S. Gómez-Coca, D. Aravena, R. Morales, E. Ruiz, *Coord. Chem. Rev.* **2015**, 289-290, 379.
- [147] S. Gomez-Coca, E. Cremades, N. Aliaga-Alcalde, E. Ruiz, *J. Am. Chem. Soc.* **2013**, *135*, 7010.
- [148] K. S. Pedersen, J. Dreiser, H. Weihe, R. Sibille, H. V. Johannesen, M. A. Sørensen, B. E. Nielsen, M. Sigrist, H. Mutka, S. Rols, J. Bendix, S. Piligkos, *Inorg. Chem.* **2015**, *54*, 7600.
- [149] N. Ishikawa, M. Sugita, T. Ishikawa, S.-Y. Koshihara, Y. Kaizu, *J. Am. Chem. Soc.* **2003**, *125*, 8694.
- [150] B. M. Day, F.-S. Guo, R. A. Layfield, *Acc. Chem. Res.* **2018**, *51*, 1880.
- [151] E. Moreno-Pineda, L. E. Nodaraki, F. Tuna, *Novel Magnetic Nanostructures* Elsevier, San Diego, **2018**, 1–50.
- [152] J. Tang, I. Hewitt, N. T. Madhu, G. Chastanet, W. Wernsdorfer, C. E. Anson, C. Benelli, R. Sessoli, A. K. Powell, *Angew. Chem. Int. Ed.* **2006**, *45*, 1729; *Angew. Chem.* **2006**, *118*, 1761.
- [153] J. D. Rinehart, M. Fang, W. J. Evans, J. R. Long, *J. Am. Chem. Soc.* **2011**, *133*, 14236.
- [154] J. D. Rinehart, M. Fang, W. J. Evans, J. R. Long, *Nat. Chem.* **2011**, *3*, 538.
- [155] J. Lu, M. Guo, J. Tang, *Chem. Asian J.* **2017**, *12*, 2772.
- [156] C. A. P. Goodwin, F. Ortu, D. Reta, N. F. Chilton, D. P. Mills, *Nature* **2017**, *548*, 439.
- [157] F.-S. Guo, B. M. Day, Y.-C. Chen, M.-L. Tong, A. Mansikkamäki, R. A. Layfield, *Angew. Chem. Int. Ed.* **2017**, *56*, 11445; *Angew. Chem.* **2017**, *129*, 11603.
- [158] F.-S. Guo, B. M. Day, Y.-C. Chen, M.-L. Tong, A. Mansikkamäki, R. A. Layfield, *Science* **2018**, *362*, 1400.
- [159] C. A. Gould, K. R. McClain, J. M. Yu, T. J. Groshens, F. Furche, B. G. Harvey, J. R. Long, *J. Am. Chem. Soc.* **2019**, *141*, 12967.
- [160] K. Randall McClain, C. A. Gould, K. Chakarawet, S. J. Teat, T. J. Groshens, J. R. Long, B. G. Harvey, *Chem. Sci.* **2018**, *9*, 8492.
- [161] N. Ishikawa, M. Sugita, T. Ishikawa, S.-Y. Koshihara, Y. Kaizu, *J. Phys. Chem. B* **2004**, *108*, 11265.
- [162] C. Benelli, D. Gatteschi, *Introduction to Molecular Magnetism*, Wiley-VCH, Weinheim, **2015**.
- [163] P. C. Bunting, M. Atanasov, E. Damgaard-Møller, M. Perfetti, I. Crassee, M. Orlita, J. Overgaard, J. van Slageren, F. Neese, J. R. Long, *Science* **2018**, *362*.

- [164] G. Wedler, *Lehrbuch der Physikalischen Chemie*, 5. Aufl., Wiley-VCH, Weinheim, **2004**.
- [165] C. E. Jackson, I. P. Moseley, R. Martinez, S. Sung, J. M. Zadrozny, *Chem. Soc. Rev.* **2021**, 50, 6684.
- [166] D. Gatteschi, R. Sessoli, *Angew. Chem. Int Ed.* **2003**, 42, 268; *Angew. Chem.* **2003**, 115, 278.
- [167] H. A. Kramers, *Proc. K. Ned. Akad. Wet.* **1930**, 33, 959.
- [168] R. Marin, G. Brunet, M. Murugesu, *Angew. Chem. Int. Ed.* **2021**, 60, 1728; *Angew. Chem.* **2021**, 133, 1752.
- [169] S. T. Liddle, J. van Slageren, *Chem. Soc. Rev.* **2015**, 44, 6655.
- [170] R. Orbach, *Proc. Math. Phys. Eng. Sci. A* **1961**, 264, 458.
- [171] L. Ungur, L. F. Chibotaru, *Inorg. Chem.* **2016**, 55, 10043.
- [172] M. A. Hay, C. Boskovic, *Chem. Eur. J.* **2021**, 27, 3608.
- [173] K. R. Meihaus, J. R. Long, *J. Am. Chem. Soc.* **2013**, 135, 17952.
- [174] P. Zhang, L. Zhang, C. Wang, S. Xue, S.-Y. Lin, J. Tang, *J. Am. Chem. Soc.* **2014**, 136, 4484.
- [175] J. M. Zadrozny, D. J. Xiao, M. Atanasov, G. J. Long, F. Grandjean, F. Neese, J. R. Long, *Nat. Chem.* **2013**, 5, 577.
- [176] E. Bill, *Nat. Chem.* **2013**, 5, 556.
- [177] J. M. Zadrozny, M. Atanasov, A. M. Bryan, C.-Y. Lin, B. D. Rekker, P. P. Power, F. Neese, J. R. Long, *Chem. Sci.* **2013**, 4, 125.
- [178] J. M. Zadrozny, J. Liu, N. A. Piro, C. J. Chang, S. Hill, J. R. Long, *Chem. Commun.* **2012**, 48, 3927.
- [179] M. S. Fataftah, J. M. Zadrozny, D. M. Rogers, D. E. Freedman, *Inorg. Chem.* **2014**, 53, 10716.
- [180] Y. Rechkemmer, F. D. Breitgoff, M. van der Meer, M. Atanasov, M. Hakl, M. Orlita, P. Neugebauer, F. Neese, B. Sarkar, J. van Slageren, *Nat. Commun.* **2016**, 7, 10467.
- [181] M. Craven, M. H. Nygaard, J. M. Zadrozny, J. R. Long, J. Overgaard, *Inorg. Chem.* **2018**, 57, 6913.
- [182] H. Andres, E. L. Bominaar, J. M. Smith, N. A. Eckert, P. L. Holland, E. Münck, *J. Am. Chem. Soc.* **2002**, 124, 3012.
- [183] Y.-F. Deng, Z. Wang, Z.-W. Ouyang, B. Yin, Z. Zheng, Y.-Z. Zheng, *Chem. Eur. J.* **2016**, 22, 14821.
- [184] Y.-F. Deng, T. Han, B. Yin, Y.-Z. Zheng, *Inorg. Chem. Front.* **2017**, 4, 1141.
- [185] F.-S. Guo, A. K. Bar, R. A. Layfield, *Chem. Rev.* **2019**, 119, 8479.
- [186] S. C. Coste, B. Vlasisavljevich, D. E. Freedman, *Inorg. Chem.* **2017**, 56, 8195.
- [187] L. R. Thomas-Hargreaves, M. J. Giansiracusa, M. Gregson, E. Zanda, F. O'Donnell, A. J. Wooles, N. F. Chilton, S. T. Liddle, *Chem. Sci.* **2021**, 12, 3911.
- [188] J. P. Durrant, J. Tang, A. Mansikkamäki, R. A. Layfield, *Chem. Commun.* **2020**, 56, 4708.
- [189] S.-D. Jiang, B.-W. Wang, H.-L. Sun, Z.-M. Wang, S. Gao, *J. Am. Chem. Soc.* **2011**, 133, 4730.

- [190] S. Scheuermayer, F. Tuna, E. M. Pineda, M. Bodensteiner, M. Scheer, R. A. Layfield, *Inorg. Chem.* **2013**, *52*, 3878.
- [191] S. Scheuermayer, F. Tuna, M. Bodensteiner, M. Scheer, R. A. Layfield, *Chem. Commun.* **2012**, *48*, 8087.
- [192] W. Lan, Z. Zhou, J. Li, Y. Dou, X. Hao, L. Yang, H. Liu, D. Li, Q. Liu, D. Zhang, *Acta Cryst. C* **2019**, *75*, 1475.
- [193] M.-G. Alexandru, D. Visinescu, S. Shova, M. Andruh, F. Lloret, M. Julve, *Eur. J. Inorg. Chem.* **2018**, *2018*, 360.
- [194] A. Mishra, W. Wernsdorfer, S. Parsons, G. Christou, E. K. Brechin, *Chem. Commun.* **2005**, 2086.
- [195] V. Chandrasekhar, B. M. Pandian, J. J. Vittal, R. Clérac, *Inorg. Chem.* **2009**, *48*, 1148.
- [196] S. Biswas, J. Goura, S. Das, C. V. Topping, J. Brambleby, P. A. Goddard, V. Chandrasekhar, *Inorg. Chem.* **2016**, *55*, 8422.
- [197] P. W. Anderson, *Phys. Rev.* **1959**, *115*, 2.
- [198] D. M. Pajerowski, Q. Li, J. Hyun, C. L. Dennis, D. Phelan, P. Yan, P. Chen, G. Li, *Dalton Trans.* **2014**, *43*, 11973.
- [199] M. Li, H. Wu, Z. Xia, V. Montigaud, O. Cador, B. Le Guennic, H. Ke, W. Wang, G. Xie, S. Chen, *Chem. Commun.* **2019**, *55*, 14661.
- [200] J. D. Hilgar, B. S. Flores, J. D. Rinehart, *Chem. Commun.* **2017**, *53*, 7322.
- [201] T. Gupta, T. Rajeshkumar, G. Rajaraman, *Phys. Chem. Chem. Phys.* **2014**, *16*, 14568.
- [202] S. Demir, I.-R. Jeon, J. R. Long, T. D. Harris, *Coord. Chem. Rev.* **2015**, *289-290*, 149.
- [203] S. Demir, M. I. Gonzalez, L. E. Darago, W. J. Evans, J. R. Long, *Nat. Commun.* **2017**, *8*, 2144.
- [204] S. Demir, J. M. Zadrozny, M. Nippe, J. R. Long, *J. Am. Chem. Soc.* **2012**, *134*, 18546.
- [205] C. A. Gould, E. Mu, V. Vieru, L. E. Darago, K. Chakarawet, M. I. Gonzalez, S. Demir, J. R. Long, *J. Am. Chem. Soc.* **2020**, *142*, 21197.
- [206] W. R. Reed, M. A. Dunstan, R. W. Gable, W. Phonsri, K. S. Murray, R. A. Mole, C. Boskovic, *Dalton Trans.* **2019**, *48*, 15635.
- [207] P. Zhang, M. Perfetti, M. Kern, P. P. Hallmen, L. Ungur, S. Lenz, M. R. Ringenberg, W. Frey, H. Stoll, G. Rauhut, J. van Slageren, *Chem. Sci.* **2018**, *9*, 1221.
- [208] S. Demir, M. Nippe, M. I. Gonzalez, J. R. Long, *Chem. Sci.* **2014**, *5*, 4701.
- [209] P. Zhang, Y.-N. Guo, J. Tang, *Coord. Chem. Rev.* **2013**, *257*, 1728.
- [210] I.-R. Jeon, J. G. Park, D. J. Xiao, T. D. Harris, *J. Am. Chem. Soc.* **2013**, *135*, 16845.
- [211] X. Ma, E. A. Suturina, M. Rouzières, M. Platunov, F. Wilhelm, A. Rogalev, R. Clérac, P. Dechambenoit, *J. Am. Chem. Soc.* **2019**, *141*, 7721.
- [212] A. E. Thorarinsdottir, R. Bjornsson, T. D. Harris, *Inorg. Chem.* **2020**, *59*, 4634.

- [213] G. Brauer, *Handbuch der Präparativen Anorganischen Chemie*, 3. Aufl., Band 1, F. Enke Verlag, Stuttgart, **1975**, S. 380.
- [214] G. Fraenkel, W. R. Winchester, P. G. Williard, *Organometallics* **1989**, *8*, 2308.
- [215] D. J. Peterson, *J. Organomet. Chem.* **1967**, *8*, 199.
- [216] C. Mantel, C. Baffert, I. Romero, A. Deronzier, J. Pécaut, M.-N. Collomb, C. Duboc, *Inorg. Chem.* **2004**, *43*, 6455.
- [217] P. J. Desrochers, J. Telser, S. A. Zvyagin, A. Ozarowski, J. Krzystek, D. A. Vicić, *Inorg. Chem.* **2006**, *45*, 8930.
- [218] H. I. Karunadasa, K. D. Arquero, L. A. Berben, J. R. Long, *Inorg. Chem.* **2010**, *49*, 4738.
- [219] S. Zein, C. Duboc, W. Lubitz, F. Neese, *Inorg. Chem.* **2008**, *47*, 134.
- [220] J. I. van der Vlugt, S. Demeshko, S. Dechert, F. Meyer, *Inorg. Chem.* **2008**, *47*, 1576.
- [221] C. M. Coates, S. R. Fiedler, T. L. McCullough, T. E. Albrecht-Schmitt, M. P. Shores, C. R. Goldsmith, *Inorg. Chem.* **2010**, *49*, 1481.
- [222] F. Boersma, A.M.C. Tinus, K. Kopinga, A. Paduan-Filho, R. L. Carlin, *Physica B+C* **1982**, *114*, 231.
- [223] E. Carl, *Metal complexes of a new polyimido sulfur phosphanyl ligand*, Georg-August-Universität Göttingen, Göttingen, **2014**.
- [224] M. Lappert, A. Protchenko, P. Power, A. Seeber, *Metal Amide Chemistry*, John Wiley & Sons, Ltd, Chichester, UK, **2008**.
- [225] R. E. Mulvey, S. D. Robertson, *Angew. Chem. Int. Ed.* **2013**, *52*, 11470; *Angew. Chem.* **2013**, *125*, 11682.
- [226] P. P. Power, *Chem. Rev.* **2012**, *112*, 3482.
- [227] D. C. Bradley, R. G. Copperthwaite, M. W. Extine, W. W. Reichert, M. H. Chisholm in *Inorganic Syntheses* (Hrsg.: B. E. Douglas), John Wiley & Sons, New York, **1978**, S. 112–120.
- [228] H. Bürger, U. Wannagat, *Mh. Chem.* **1964**, *95*, 1099.
- [229] H. Bürger, U. Wannagat, *Mh. Chem.* **1963**, *94*, 1007.
- [230] B. D. Murray, P. P. Power, *Inorg. Chem.* **1984**, *23*, 4584.
- [231] D. C. Bradley, M. B. Hursthouse, P. F. Rodesiler, *J. Chem. Soc. D* **1969**, 14.
- [232] K. J. Fisher, D. C. Bradley, *J. Am. Chem. Soc.* **1971**, *93*, 2058.
- [233] R. R. Fraser, T. S. Mansour, S. Savard, *J. Org. Chem.* **1985**, *50*, 3232.
- [234] A. Streitwieser, A. Facchetti, L. Xie, X. Zhang, E. C. Wu, *J. Org. Chem.* **2012**, *77*, 985.
- [235] A. M. Bryan, G. J. Long, F. Grandjean, P. P. Power, *Inorg. Chem.* **2013**, *52*, 12152.
- [236] D. L. J. Broere, I. Čorić, A. Brosnahan, P. L. Holland, *Inorg. Chem.* **2017**, *56*, 3140.
- [237] S. Trofimenko, *Polyhedron* **2004**, *23*, 197.
- [238] G. R. Fulmer, Alexander J. M. Miller, N. H. Sherden, H. E. Gottlieb, A. Nudelman, B. M. Stoltz, J. E. Bercaw, K. I. Goldberg, *Organometallics* **2010**, *29*, 2176.

- [239] P. P. Samuel, K. C. Mondal, N. Amin Sk, H. W. Roesky, E. Carl, R. Neufeld, D. Stalke, S. Demeshko, F. Meyer, L. Ungur, L. F. Chibotaru, J. Christian, V. Ramachandran, J. van Tol, N. S. Dalal, *J. Am. Chem. Soc.* **2014**, *136*, 11964.
- [240] T. Glaser, *Angew. Chem. Int. Ed.* **2011**, *50*, 10019; *Angew. Chem.* **2011**, *123*, 10195.
- [241] C. Rajnák, J. Titiš, O. Fuhr, M. Ruben, R. Boča, *Inorg. Chem.* **2014**, *53*, 8200.
- [242] R. Boča, J. Miklovič, J. Titiš, *Inorg. Chem.* **2014**, *53*, 2367.
- [243] Z.-Q. Zhang, Y.-M. Yao, Y. Zhang, Q. Shen, W.-T. Wong, *Inorg. Chim. Acta* **2004**, *357*, 3173.
- [244] Y. Yao, Y. Zhang, Q. Shen, K. Yu, *Organometallics* **2002**, *21*, 819.
- [245] C. Cui, A. Shafir, J. A. R. Schmidt, A. G. Oliver, J. Arnold, *Dalton Trans.* **2005**, 1387.
- [246] L. F. Sánchez-Barba, D. L. Hughes, S. M. Humphrey, M. Bochmann, *Organometallics* **2006**, *25*, 1012.
- [247] K. R.D. Johnson, A. P. Côté, P. G. Hayes, *J. Organomet. Chem.* **2010**, *695*, 2747.
- [248] S. V. Klementyeva, M. Y. Afonin, A. S. Bogomyakov, M. T. Gamer, P. W. Roesky, S. N. Konchenko, *Eur. J. Inorg. Chem.* **2016**, *2016*, 3666.
- [249] R. D. Shannon, *Acta Cryst. A* **1976**, *A32*, 751.
- [250] F.-M. Tesky, R. Mews, B. Krebs, M. R. Udupa, *Angew. Chem., Int. Ed.* **1978**, *17*, 677; *Angew. Chem.*, **1978**, *90*, 722.
- [251] F.-M. Tesky, R. Mews, B. Krebs, *Z. Naturforsch. B* **1981**, *36*, 1465.
- [252] N. K. Hansen, P. Coppens, *Acta Cryst. A* **1978**, *34*, 909.
- [253] R. F. W. Bader, *Atoms in Molecules: A Quantum Theory*, Clarendon Press, Oxford, New York, **1990**.
- [254] D. B. Chesnut, *J. Phys. Chem. A* **2003**, *107*, 4307.
- [255] Annika Münch, *Klassifizierung polarer Metall-Kohlenstoff-Bindungen in hauptgruppenmetall-organischen Verbindungen mittels experimenteller Elektronendichteanalyse*, Göttingen, **2020**.
- [256] W. Schlenk, A. Thal, *Chem. Ber.* **1913**, *46*, 2840.
- [257] T. T. Tidwell, *Angew. Chem. Int. Ed.* **2001**, *40*, 331; *Angew. Chem.* **2001**, *113*, 343.
- [258] Georg-August-University, "Virtuelles Labor I", **2014**.
http://www.stalke.chemie.uni-goettingen.de/virtuelles_labor/advanced/13_de.html
- [259] Georg-August-University, "Virtuelles Labor II", **2014**.
http://www.stalke.chemie.uni-goettingen.de/virtuelles_labor/nmr/de.html
- [260] G. Bodenhausen, D. J. Ruben, *Chem. Phys. Lett.* **1980**, *69*, 185.
- [261] A. Bax, M. F. Summers, *J. Am. Chem. Soc.* **1986**, *108*, 2093.
- [262] E. Bill, *JulX-2s*, **2013**.
- [263] D. Reta, N. F. Chilton, *Phys. Chem. Chem. Phys.* **2019**, *21*, 23567.
- [264] OriginLab Corporation, Origin(Pro), **2021**.

- [265] N. F. Chilton, D. Collison, E. J. L. McInnes, R. E. P. Winpenny, A. Soncini, *Nat. Commun.* **2013**, *4*, 2551.
- [266] P.-Å. Malmqvist, B. O. Roos, *Chem. Phys. Lett.* **1989**, *155*, 189.
- [267] C. Angeli, R. Cimraglia, J.-P. Malrieu, *Chem. Phys. Lett.* **2001**, *350*, 297.
- [268] F. Neese, *Wiley Interdiscip. Rev. Comput. Mol. Sci.* **2012**, *2*, 73.
- [269] F. Neese, *Wiley Interdiscip. Rev. Comput. Mol. Sci.* **2018**, *8*.
- [270] M. Atanasov, D. Ganyushin, K. Sivalingham, F. Neese in *Structure and Bonding*, Vol. 143 (Hrsg.: D. M. P. Mingos, P. Day, J. P. Dahl), Springer-Verlag, Heidelberg, Dordrecht, New York, **2012**, S. 149–220.
- [271] M. D. Hanwell, D. E. Curtis, D. C. Lonie, T. Vandermeersch, E. Zurek, G. R. Hutchison, *J. Cheminform.* **2012**, *4*, 17.
- [272] T. Kottke, D. Stalke, *J. Appl. Cryst.* **1993**, *26*, 615.
- [273] D. Stalke, *Chem. Soc. Rev.* **1998**, *27*, 171.
- [274] Georg-August-University, “Virtuelles Labor III”, **2014**.
http://www.stalke.chemie.uni-goettingen.de/virtuelles_labor/special/22_de.html
- [275] T. Kottke, R. J. Lagow, D. Stalke, *J. Appl. Cryst.* **1996**, *29*, 465.
- [276] T. Schulz, K. Meindl, D. Leusser, D. Stern, J. Graf, C. Michaelsen, M. Ruf, G. M. Sheldrick, D. Stalke, *J. Appl. Cryst.* **2009**, *42*, 885.
- [277] APEX2 v2.2012.2-0. APEX2, WI, USA, Madison, **2012**.
- [278] Bruker AXS Inc., APEX3. *Crystallographic Software Suite*, Madison, WI, USA, **2016**.
- [279] Bruker SAINT v8.30C. Bruker AXS Inst. Inc., WI, USA, Madison, **2013**.
- [280] L. Krause, R. Herbst-Irmer, G. M. Sheldrick, D. Stalke, *J. Appl. Cryst.* **2015**, *48*, 3.
- [281] G. M. Sheldrick, *TWINABS 2012/1*, Göttingen, **2012**.
- [282] L. Krause, R. Herbst-Irmer, D. Stalke, *J. Appl. Cryst.* **2015**, *48*, 1907.
- [283] G. M. Sheldrick, *XPREP in SHELXTL 2014/2*, Göttingen, **2014**.
- [284] G. Sheldrick, *Acta Cryst. A* **2008**, *64*, 112.
- [285] C. B. Hübschle, G. M. Sheldrick, B. Dittrich, *J. Appl. Cryst.* **2011**, *44*, 1281.
- [286] G. M. Sheldrick, *SHELXL in SHELXTL v2014/7*, WI, USA, Madison, **2014**.
- [287] P. Müller, R. Herbst-Irmer, A. L. Spek, T. R. Schneider, M. R. Sawaya, *Crystal structure refinement – A crystallographer’s guide to SHELXL*, 8. Aufl., Oxford University Press, Oxford, **2006**.